The University Of Sheffield.

Reinterpreting turbidity: new methodologies for suspended-sediment research

By:

Ben Gareth Brian Kitchener

A thesis submitted in partial fulfilment of the requirements for the degree of Doctor of Philosophy

The University of Sheffield
Faculty of Social Sciences
Department of Geography

August 2019

If you let cloudy water settle, it will become clear. If you let your upset mind settle, your course will also become clear.

Gautama Buddha

Declaration

I confirm that no part of the material presented in this thesis has been submitted previously by me or any other person for a degree in this or any other university. In all cases, where it is relevant, material from the work of others has been acknowledged.

The copyright of this thesis rests with the author. No quotation from it should be published without prior written consent and information derived from it should be acknowledged.

Signed:

Date:

Abstract

Reinterpreting turbidity: new methodologies for suspended-sediment research

Existing instruments for turbidity measurement vary considerably in terms of the principles of operation, the physical design, and the cost to the researcher. The operational methodologies of late twentieth century turbidity instruments have led to the development of new turbidity measurement standards, and the invention of new turbidity measurement units. These measurement units are invalid and do not have a sound footing with regard to the underlying physics of the scattering and absorption of light by suspended particles. A review of the turbidity literature has shown that the proliferation of these incommensurate units of measurement throughout the physical sciences has caused extensive misinterpretation of turbidity data, particularly concerning its use as a surrogate for suspended sediment concentration (SSC).

Turbidity is a complex phenomenon, and its measurement reported in terms of a single numeric quantity in some physically indeterminate units of measurement. It is not necessarily useful to reduce complex data to a single value, since this approach does not permit the researcher any *a posteriori* opportunity to reinterpret existing data in light of innovations in analysis methodology. This thesis proposes a new way to present turbidity data that will facilitate the cross-comparison of turbidity measurements made by different instruments on any type of suspended sediment. The creation of a new turbidity research instrument that illustrates the application of the new method for reporting turbidity data as a ratio of light attenuation values in decibels, promotes a positive change in direction away from the traditional measurement units. The design process focusses on the instrument calibration procedure. With a simple reinterpretation of the phase-function description of light scattering from suspended particles, measurements of light attenuation made at multiple angles with respect to the axis of the incident light beam, compare easily with the same measurements made using different wavelengths of incident light. This work goes on to introduce new nomenclature that requires the citing of measurement angle and wavelength of light to be an integral part of any recorded turbidity measurement.

A modelling approach is used in the evaluation of the new turbidity instrument. This modelling is important for three reasons. First, it identifies which instrument parameters affect the result of a turbidity measurement – the key parameter being the mathematical function that describes the spatial divergence of the incident light beam, which is important to measurement systems that employ incoherent light sources such as LEDs, rather than to laser-based systems. Secondly, the modelling reveals two fundamental theories of light scattering due to suspended particles, both of which are required to describe adequately the turbidity of sediment-laden water. These two theories are Mie scattering and geometric optics. Mie scattering is well accounted for by the developed model - geometric optics, less so. The extent to which the model predictions diverge from the empirical data is characterised by a metric related to the backscatter fraction, and the consistency and linearity of the model is established. Ideas for the improvement of the geometric optics feature of the model are discussed, as is the third reason for the importance of numerical modelling. This third reason relates to the use of multi-parameter turbidity measurements as a means to characterise the properties of a suspended sediment. By simulating precisely the measurement response of the turbidity instrument, then it is notionally possible to infer the properties of an unknown sediment by tuning the model parameters to match the empirical response of the unknown sediment. This tuning process could reveal information pertaining to particle size and shape.

Finally, potential applications for the new research instrument focus on improvements to the instrument itself and the methodology, and the further development of the turbidity data reporting nomenclature. Prototype methodologies that relate turbidity to suspended sediment concentration are suggested, which also consider ways in which the optical measurements can potentially classify the physical properties of a sediment.

Acknowledgements

I would like to thank my supervisors, Prof. Tony Parsons, Prof. John Wainwright and Prof. Mark Bateman, for introducing me to the field of physical geography (pun intended), and for providing me with the inspiration to explore this fascinating aspect of physical science. Thanks to Tony for generally improving my grammar, and for pulling me back from dangerous philosophical tangents. Thanks to John for his immense patience when responding to my deeply trivial technical questions. The review paper would not have seen the light of day without guidance from both of you. Thanks to Mark for stepping into the breach that is known as University Bureaucracy to sort out the paperwork, and for generally being sensible. Another thankyou goes to Mark for providing the loess sample upon which most of this thesis is based. Thanks also to Dr. Manoj Menon for providing feedback on some of my thesis chapters, and for his insights into sediments and soil science.

I would also like to thank all the people that have provided me with practical support throughout this project. Thanks to Tom Sullivan in the Department of Geography at the University of Sheffield for being my student services bureaucracy and general red-tape guidance counselor. Alan Smalley and Rob Ashurst, also in Sheffield, have been endlessly helpful with their practical support and guidance over the years, a trend that began well before my research project started. I dread to think how many beers I now owe them! Mark Foster in the Department of Civil Engineering in Sheffield kindly provided me with extra sediment samples. Simon Dixon and Kieren Howarth in the Department of Physics and Astronomy in Sheffield have provided crucial design support, without which the turbidity research instrument would not have been built. Thanks to Chris Orton in the Department of Geography at Durham University for his creative improvement of a number of the figures in this thesis.

Penultimate thanks go to my network of friends for all their moral support. Particular thanks go to Dr. Adam Anderson for all of our chats in the pub, and for the impartment of his numerical modelling knowledge via the medium of beer-mat diagrams. Many thanks go to the East family: Dr. Vince, Becky, and Georgie. Your friendship and support has cheered me up on many occasions. I have particularly enjoyed our sanity-realignment sessions involving beer and wooden spoons.

Finally, I would like to thank my family for their long-standing patience and encouragement throughout this process. I could not have completed this project without the love and support of the two most important people in my life, and so this thesis is dedicated to my wife Lucy and my son Rowan.

Contents

Contents

Contents

List of figures

List of figures

List of figures

List of figures

List of figures

List of figures

List of figures

List of figures

List of figures

List of tables

Notation

x	= dimensionless size parameter [dimensionless]
λ	= wavelength of light [nm]
ω	= single scattering albedo [dimensionless]
n	= refractive index [dimensionless]
Σ	= beam attenuation coefficient [m^{-1}]
T	= transmittance [dimensionless]
c	= concentration of absorbers [dimensionless]
l	= nominal optical path length [m]
δ	= beam divergence angle [° or rad]
ε	= absorptivity [m^2, or m^2 kg^{-1}] *or* beam divergence half-angle (ray emergence angle) [° or rad]
τ	= optical depth [m]
A	= absorbance [dimensionless]
I	= transmitted radiant intensity [mW sr^{-1}]
I_0 or $I_0(\theta, \lambda)$	= incident radiant intensity [mW sr^{-1}]
$V(\lambda)$	= photometric to radiometric conversion function [mW sr^{-1} mcd^{-1}]
m_{LED}	= LED coefficient of efficiency
I_{OUT}	= LED output radiant intensity [mW sr^{-1} or mcd sr^{-1}]
I_{IN}	= LED input current [mA]
T_λ	= ND filter wavelength-corrected transmittance [dimensionless]
S_V	= sensor voltage [V]
S_α	= sensor calibration coefficient [dimensionless]
α	= sensor number [dimensionless]
θ	= azimuthal (horizontal) scattering angle [° or rad]
I_θ or $I_\theta(\theta, \lambda)$	= measured angular radiant intensity [mW sr^{-1}]
I_n	= instantaneous radiant intensity [mW sr^{-1}]
φ	= altitudinal (vertical) scattering angle [° or rad]
Ω	= solid angle [$(°)^2$ or sr]
$\beta(\theta, \varphi, \lambda)$	= volume scattering function [m^{-1} sr^{-1}]
$\beta(\theta, \lambda)$	= volume scattering function (reduced form) [m^{-1} sr^{-1}]
ΔV	= infinitesimal volume element [m^3]
b or $b(\lambda)$	= scattering coefficient [m^{-1}]

Notation

$a(\lambda)$	= absorption coefficient [m^{-1}]
$\tilde{\beta}(\theta, \lambda)$	= scattering phase function [sr^{-1}]
$b_b(\lambda)$	= scattering coefficient for backscattering only [m^{-1}]
$B_b(\lambda)$	= backscatter fraction [dimenstionless]
$BAC(\theta, \lambda)$ or $c(\lambda)$	= beam attenuation coefficient [m^{-1}]
$AGF(\theta, \lambda)$	= angular gain function [dB]
$\boldsymbol{A}$	= a calibration standard [dimensionless]
$WAGF(\theta, \lambda, \boldsymbol{A})$	= weighted angular gain function [dB]
p_c	= ray-particle collision probability [dimensionless]
α_1	= Beta distribution shape parameter [dimensionless]
α_2	= Beta distribution shape parameter [dimensionless]
M_d	= Mie transition diameter [µm]
M_p	= Mie probability [dimensionless]
R_c	= number of rays for CLARITAS model convergence [dimensionless]
ρ_c	= sediment mass concentration [$g\ l^{-1}$]
B_{bp}	= predicted backscatter fraction [dimensionless]
B_{be}	= empirical backscatter fraction [dimensionless]
d	= sediment particle diameter [µm]
$\bar{C}_p$	= mean ratio of the mean normalised angular predicted radiant intensity to the mean normalised angular empirical radiant intensity [dimensionless]
$\tilde{I}_{PRED}(\theta)$	= mean normalised angular predicted radiant intensity [dimensionless]
$\tilde{I}_{EMP}(\theta)$	= mean normalised angular empirical radiant intensity [dimensionless]
L	Loess particle size distribution [µm]
V_S	Stokes settling velocity [$m\ s^{-1}$]
d_n	Particle size of PSD class bin n [µm]
γ_n	Normalised frequency of occurrence [dimensionless]
g	Acceleration due to gravity [$m\ s^{-2}$]
ρ_p	Loess particle density [$kg\ m^{-3}$]
ρ_m	Density of water [$kg\ m^{-3}$]
μ	Viscosity of water [$kg\ m^{-1}\ s^{-1}$]
t_S	Stokes settling time [s]
D_S	Stokes scale parameter [m]

$I_{\not\propto}$	Normalised Mie intensity distribution [dimensionless]
$L_{\not\propto}$	Loess-Mie intensity function [dimensionless]
$P_{P,\theta}$	Empirical primary intensity peak position [s]

Abbreviations

ADC	Analogue to Digital Converter
AGF	Angular Gain Function
APHA	American Public Health Association
ASTM	American Society for Testing and Materials
AU	Attenuation Unit
BAC	Beam Attenuation Coefficient
BRU	Backscatter Ratio Unit
BU	Backscatter Unit
CERN	European Organization for Nuclear Research
CLARITAS	ComputationaL Accumulator of Rays Invoking Tracing And Scattering
DGB	Device Baseline Geometry
DIGPOT	Digital Potentiometer
DIP	Dual Inline Package
DOF	Degree Of Flocculation
DPM	Discrete Particle Model
FAU	Formazin Attenuation Unit
FBRU	Formazin Backscatter Ratio Unit
FBU	Formazin Backscatter Unit
FMNU	Formazin Nephelometric Multibeam Unit
FNRU	Formazin Nephelometric Ratio Unit
FNU	Formazin Nephelometric Unit
GLI	Great Lakes Instruments
GOF	Goodeness Of Fit
IC	Integrated Circuit
IR	Infra-Red
ISO	International Organization for Standardization
KS	Kolmolgorov-Smirnov
LASER	Light Amplification by Stimulated Emission of Radiation
LED	Light Emitting Diode
LS	Loess-Mie
MSGM	Mie-Stokes Graphical Method
ND	Neutral Density
NI	National Instruments
NSE	Nash-Sutcliffe efficiency
NTMU	Nephelometric Turbidity Multibeam Unit
NTRU	Nephelometric Turbidity Ratio Unit
NTU	Nephelometric Turbidity Unit
OD	Optical Density

OHL	Open Hardware License
PCB	Printed Circuit Board
PDF	Probability Density Function
PGA	Programmable Gain Amplifier
PMF	Probability Mass Function
PSD	Particle Size Distribution
RMSE	Root Mean Square Error
SI	International System of Units
SMD	Surface Mount Device
SPI	Serial Peripheral Interface
SSC	Suspended Sediment Concentration
TARDIIS	Turbidity Assessment by Radially Distributed Illumination Intensity Sensing
TSS	Total Suspended Solids
US EPA	United States Environmental Protection Agency
WAGF	Weighted Angular Gain Function

Chapter 1 Introduction: *statement of aims*

1.1 Aims and objectives

The overall aim of this project is to improve our understanding of how turbidity relates to suspended sediment concentration (SSC), focusing on the measurement methodologies and the reporting of data. Five primary objectives are identified:

1. **Explain how turbidity measurement is done now, and how turbidity is related to SSC.**

   Turbidity is measured in many different ways for many different purposes, for example the assessment of drinking water quality or the quantification of water pollution. There is a plethora of commercially available turbidity-measurement instruments that operate according to a small set of core physical principles. Most of these instruments include a light source, such as coherent LASER light, or incoherent light sources such as incandescent bulbs (polychromatic), or monochromatic (or very narrow-band polychromatic) light emitting diodes (LEDs). Light-sensitive components (photomultiplier tubes, photodiodes etc.) are employed to detect the light that is transmitted and scattered by particulates suspended in the water. Sometimes these measurements of the emergent light are used to infer directly the concentration of the particulates. In the case of sediment-transport research, turbidity is often synonymous with SSC. However popular, this relationship is subjective – a fact that is recognised in some - but not all - of the turbidity literature.

2. **Explain what is wrong with these existing turbidity measurement methods.**

   Turbidity "standards" refer to two different entities. One is the physical suspension of particles that is used for the calibration of turbidity instruments. The other is the documentation that describes the turbidity measurement methodology. In both cases, the standards are based on incorrect principles. In the former, the physics is flawed, and in the latter (a derivative of the former), the methodology and the physics are flawed. The existing turbidity measurement methods report turbidity as a single metric in one of many different turbidity units of measurement – all based on flawed physics and methodology. Turbidity measurements performed in accordance with existing standards are mutually inconsistent, and therefore they are not cross-comparable.

3. **Design a new turbidity research instrument from first principles.**

   A new turbidity research instrument is described, which features user-selectable light sources and variable light-source intensity control. The photodiode-based light detectors are

situated at 10° intervals around the circumference of the large sample-cell, providing the user with a parameter-rich set of turbidity data. A calibration methodology based on the use of neutral density (ND) filters is suggested, as is the reporting of turbidity as the angular attenuation of light in decibels. The user is encouraged to experiment with the device, and to modify and improve it according to their own particular requirements.

4. **Test and evaluate the new turbidity research instrument.**
   The calibration methodology is improved upon, and the interpretation of the new parameter-rich turbidity data is explored. The benefits of numerical modelling are investigated in terms of the characterisation of suspended sediment, and in terms of the design of turbidity-instrument geometry. The potential to discover the inherent optical properties of suspended particles is discussed, as is the potential for the improved estimation of SSC.
5. **Suggest a new and better way to report turbidity data.**
   A new way to report turbidity data is suggested. This new method is based on the idea of angular light attenuation, and it facilitates the successful cross-comparison of turbidity data, given a set of rigorously defined pre-requisites. The methodology is expanded to the definition of application-specific turbidity measurements, thus obviating the temptation to make incommensurate comparisons between widely differing application domains.

1.2 Thesis structure

Chapter 2 presents a review of the turbidity and SSC literature, and has been published previously in Kitchener et al. (2017). The evolution of the accepted turbidity units is discussed, and the argument that they are not physically valid is presented. The issue that turbidity is used incorrectly as a surrogate for SSC is explained, as are the problems that arise due to the promotion of incommensurate measurement units by the accepted turbidity measurement standards (US EPA Method 180.1, ISO 7027, and GLI Method 2). It is suggested that new turbidity units based on the attenuation of light should be developed, and that they should report turbidity values in decibels.

Chapter 3 presents a newly designed turbidity research instrument (TARDIIS), for the offline investigation of light-attenuation by suspended sediment. Complete building instructions and basic calibration procedures are described. This work has been published previously in Kitchener et al. (2019).

Chapter 4 evaluates the new turbidity research instrument. The chapter begins by revisiting the calibration methodology, and introduces a number of optical parameters that are well established in the ocean sciences, but are less well known in other areas of turbidity research. These

parameters are the *volume scattering function*, the *scattering phase function*, and the *backscatter fraction*. A number of light-scattering experiments are described, which were performed under conditions of steady-state sediment suspension. The results of these experiments are used to exemplify a new parameter for the reporting of turbidity data. This parameter, called the *angular gain function* (AGF), is derived from a simple reinterpretation of the oceanographic optical parameters. A secondary parameter, the *weighted angular gain function* (WAGF) is also explained. The chapter concludes by suggesting the potential benefits of mathematical modelling to the study of turbidity, and to the design of turbidity instruments.

Chapter 5 is a first attempt to model the scattering and absorption of light due to the presence of suspended sediment in the TARDIIS sample cell. This new computational, process-based model (CLARITAS) is an example of a *discrete particle model* (DPM), which uses Mie scattering as the primary physical light-particle interaction process. A probabilistic approach to the modelling demonstrates the importance of knowing the precise mathematical form of the light-beam divergence, a parameter that comprises the fundamental geometry of the measuring instrument. It is shown that Mie scattering by itself does not adequately describe the empirical data taken during the steady-state sediment suspension experiments. The results of the modelling are improved considerably by the addition of a crude approximation to geometric optics into the computational algorithm. Finally, the backscatter fraction is employed as a metric for the evaluation of the CLARITAS model performance.

Chapter 6 suggests applications for the TARDIIS instrument, which could be the prototypes for future analysis methodologies. Data is presented in terms of the new AGF, WAGF, and other formats. Suggestions for further work are developed.

Chapter 7 presents the main conclusions of the thesis, and the implications for turbidity measurement and its relationship with suspended sediment concentration.

Chapter 2 A review of the principles of turbidity measurement

2.1 Declaration of originality

The article reproduced in this chapter, originally titled "A review of the principles of turbidity measurement" (Kitchener et al. 2017) is done so according to the University of Sheffield regulations relating to the "Alternative Format Thesis". I (Ben G. B. Kitchener) am the first author, and I confirm that the work is mine and is not plagiarised.

Signed:

Date:

Reference to the original article:

Kitchener, B.G.B., Wainwright, J. & Parsons, A.J., 2017. A review of the principles of turbidity measurement. *Progress in Physical Geography*, 41(5), pp.620–642. Available at: http://journals.sagepub.com/doi/10.1177/0309133317726540.

2.2 Abstract

Turbidity of water due to the presence suspended sediment is measured and interpreted in a variety of ways, which can lead to the misinterpretation of data. This paper re-examines the physics of light-scattering in water, and exposes the extent to which the reporting of turbidity data is inconsistent. It is proposed that the cause of this inconsistency is the fact that the accepted turbidity standards USEPA Method 180.1, ISO 7027 and GLI Method 2 are mutually inconsistent, as these standards give rise to a large number of measurement units that are not based on the optical properties of light absorption and scattering by suspensions in water, but by the arbitrary definition of the degree of turbidity being due to a concentration of formazin or other similar polymer-based calibration standard. It is then proposed that all turbidity-measuring devices should be calibrated with precise optical attenuators such as ND filters. Such calibration would allow for the definition of a beam attenuation coefficient (BAC) for every turbidity measuring instrument which would be cross-comparable with any other instrument calibrated in the same

way. The units for turbidity measurements should be based on attenuation and reported as dB m^{-1}. It is also proposed that a new standard should be drafted according to this attenuation-based method, and this new standard should also define the nomenclature for reporting data collected at any specific scattering angle in terms of an attenuation in dB m^{-1}. The importance of multi-parameter turbidity measurements for the improvement of the quality of turbidity data, and the application of parameter-rich data sets to new methods of sediment characterization are discussed. It is suggested that more research into multi-parameter turbidity measurements is needed, as these new methods will facilitate an increase in parity between turbidity and suspended sediment concentration (SSC), a relationship that is subjective.

2.3 Key words

Turbidity; Suspended Sediment; Sediment Transport

2.4 Introduction

The term "turbidity" is used widely throughout the physical sciences, and is interpreted in different ways in different contexts. It is commonly used to describe the optical clarity of a fluid (for example, the atmosphere), but for the purposes of this paper it refers to another common usage of the term which is the optical clarity of water. The presence of suspended particulates, dissolved inorganic chemical species, organic matter content and temperature can all affect the turbidity of a body of water. Investigators from different fields (waste water treatment; drinking water quality; forestry; civil engineering, aquaculture and ecology), and from the sub-disciplines within physical geography (fluvial; marine; glacial; coastal and estuarial) use turbidity measurement as a surrogate relative indicator of some other physical property, typically suspended sediment concentration (SSC) or total suspended solids (TSS). The amount of literature available on the subject of water turbidity is large, and a number of reviews have already been undertaken by investigators from some of the sub-disciplinary groups (Bilotta & Brazier 2008; Davies-Colley & Smith 2001; Kerr 1995; Ziegler 2003). There is however, some disagreement about what turbidity actually means, partly due to the different sub-disciplinary contexts in which the term is used, and partly because of the way in which the various measurement standards are assumed to be based on a correct a priori understanding of the physical processes of light-scattering and absorption.

Why is turbidity measurement important? The answer to this question depends on the perspective of the investigator. Some researchers are purely interested in the effect that the attenuation of light has on, for example, aquatic ecosystems, so that knowledge of the mass concentration of the suspended particles is not always the primary concern. In this case other

parameters of interest include the reduction of visual range in water (affecting the ability of predators to hunt), and the amount of light available for photosynthesis (Bilotta & Brazier 2008). Other investigators are concerned directly with the study of sediment-transport processes, in which case knowledge of the mass concentration of the suspended particles and other parameters such as the particle-size distribution (PSD) is highly desirable for a number of reasons. Turbidity measurement is important in this context, as although the turbidity measurement itself is heavily biased by the PSD (Gippel 1989), it is not specifically designed to provide detailed information about the PSD. For example, knowledge of particle size is important as the transport of fine sediment derived from different land uses through catchments will impact directly on ecosystem services, such as the provision of drinking water. Fine sediment delivery into river systems is also known to cause problems such as irritation to fish gills whilst it is in suspension (Davies-Colley & Smith 2001). Bilotta & Brazier (2008) summarize the effects of what they refer to as suspended solids (SS) on periphyton and macrophytes, invertebrates and salmonid fish species. The displacement of many fish species can often be due to an increase in turbidity caused by the cumulative effects of fine sediment introduced into the riparian environment as a direct result of human activities such as deforestation (Kerr 1995), or by natural events such as sediment-transport by stormwater runoff. The use of turbidity measurement as a surrogate indicator for parameters such as suspended sediment concentration has been explored by many researchers, as reviewed by Ziegler (2003). It has been shown that the particle size distribution (PSD) of a homogenous sediment can vary temporally from its source (e.g. hillslope runoff) as it is transported through a catchment into a stream, due to a variation in the relative proportion of aggregates (flocs) present in the measured flux (Slattery & Burt 1997). Therefore knowledge of how the PSD varies dynamically in this fluvial context due to a variability in the degree of flocculation (DOF) is important for the study of the transport processes of both sediment and organic species in flocs (Williams et al. 2007). There is clearly some variation in the importance given to the parameters of turbidity by the different sub-disciplinary groups, and so the aim of this paper is to evaluate how relevant turbidity measurement is to the study of sediment-transport processes specifically, and to propose methods for the improvement of the measurement and reporting of turbidity in a general context. The steps required to achieve this evaluation are given by the following list of objectives:

1. To analyse critically the measurement methodologies described in the literature including any inconsistencies in nomenclature of measurement principles.

2. To review briefly the physics of light absorption and scattering processes in water in order to provide an underpinning for the discussion of the definition of terms according to various investigators from different sub-disciplinary groups.

3. To present a critique of the measurement units, calibration methods and standards applicable to the measurement of turbidity, SSC and TSS, and to examine of the origins of the relationship between turbidity measurements and the implied properties of suspended sediment. This step is vital because the cross-comparability of turbidity data obtained in the field is often invalid due to a widespread reliance on the assumed integrity of Formazin calibration methods.

4. To propose, based on objective 3, that a new turbidity instrumentation standard is required, and to describe its fundamental content.

2.5 Turbidity measurement principles and nomenclature

The measurement of turbidity is split into two basic methodologies: *turbidimetry*, in which the degree of *transmission* of light is determined, and *nephelometry*, in which the degree of light-scattering is evaluated (see reviews by Ziegler, 2003 and Lawler, 2005). This division has its roots in the mathematical descriptions employed to model the various phenomena. In the case of turbidimetry, the appropriate theories are due to Beer (1852) and Lambert (1760) ; as for nephelometry, many theories and models have been developed to describe a range of scattering processes, and these models are mostly derived from Mie theory (Mie 1908). Nephelometry itself is sub-divided into three further categories which are *forward-scattering*, *side-scattering* and *back-scattering*. Side-scattering is generally accepted to be a measurement angle of 90° to the incident beam, although the existing standards impose different upper and lower bounds on that value (Table 2-3). Forward-scattering ($0° < \theta < 90°$) and Back-scattering ($90° < \theta < 180°$, often referred to as *optical back-scattering* or *OBS*) however, do not have a well-defined relative measurement angle. Different instruments employ different measurement angles, and these values are not always reported.

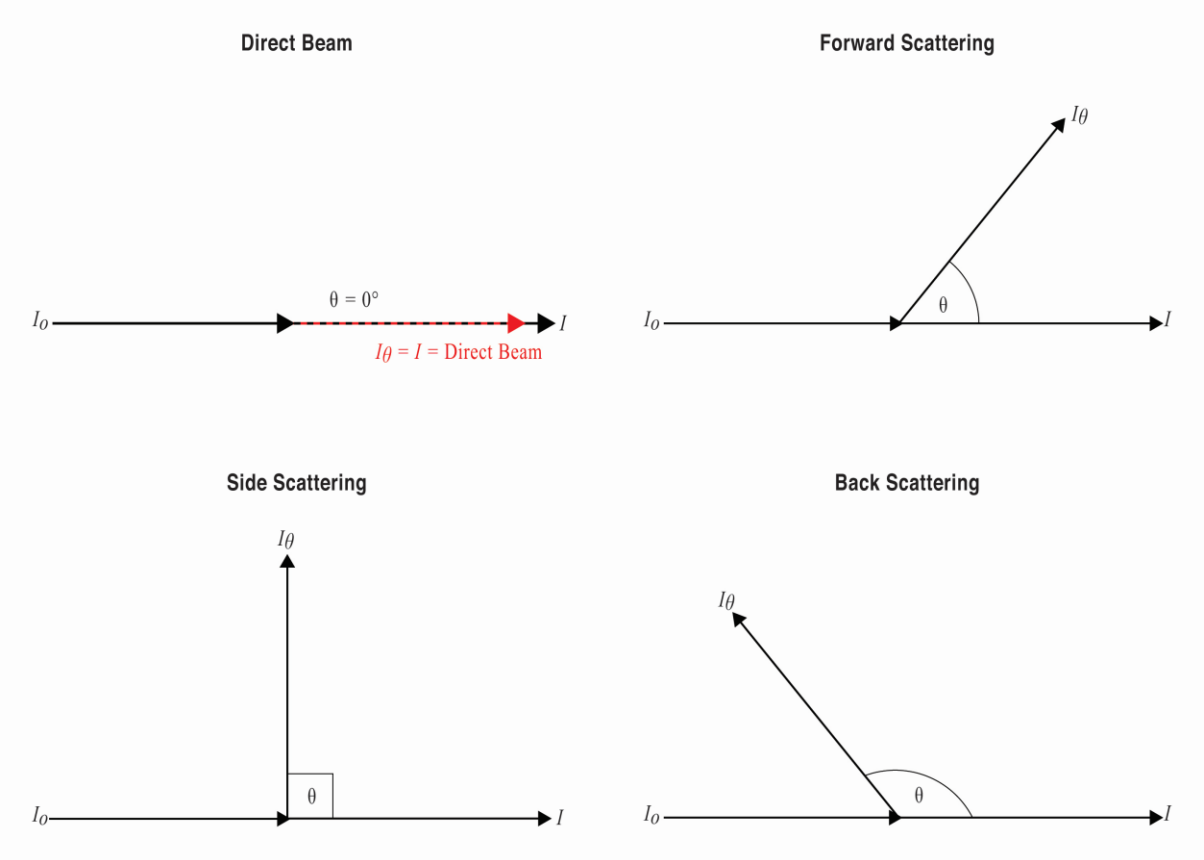

Figure 2-1. Illustrations of the light-scattering angle convention: the "direct beam" where $I_\theta = I$, forward-scattering, side-scattering and back-scattering. The incident beam is denoted I_0 and the direct transmitted beam at 0° to the incident beam is denoted I. The scattered beams are denoted I_θ, where θ is the scattering angle with respect to the incident beam.

Before continuing with the discussion another ambiguity in terminology must be addressed. The definition of the scattering angle in terms of where the 0° position is located spatially also varies throughout the literature (Table 2-1). For example in some cases a forward-scattering angle is stated, which *implies* that the transmitted (direct) beam is located at 0° (Agrawal et al., 2008 and Jansson, 1992). Contradictory to this position, Bilro et al. (2010) define the transmitted beam as being located at the 180° position. In one instance two contradictory diagrams are presented in the same paper (Sadar 2004, pp.8-9), and in many other cases the scattering-regime nomenclature is not associated with a specific scattering angle (e.g. Fugate & Friedrichs, 2002).

The interpretation that is adopted throughout this paper is that the scattering-angle is specified in terms of a detector placed at a position with respect to the incident beam *after* a physical interaction has occurred in the sample, i.e. the direct beam detector is placed at the 0° position (denoting "pure" attenuation measurement), forward-scattering detectors are placed anywhere

from 0° < θ < 90°, a side-scattering detector is placed at exactly 90°, and back-scattering detectors are placed at 90° < θ <= 180°.

Table 2-1. A selection of turbidity literature references illustrating the ambiguity associated with the assignment of scattering-regime nomenclature to the actual scattering-angle.

	Scattering-regime and scattering-angle referenced in the text.		
Reference	**Transmitted**	**Back-scattered**	**Forward-scattered**
Agrawal et al. (2008)	*Implied 0°*		<10°
Bilro et al. (2010)	180°		
Campbell et al. (2005)		180°	
Fugate & Friedrichs (2002)		Angle not defined	
Green & Boon (1993)		>150°	
Guillén et al. (2000)		Angle not defined	
Gumprecht & Sliepcevich (1953)	Angle not defined		
Jansson (1992)	*Implied 0°*		12°
Morais et al. (2006)	Angle not defined		
Pavanelli & Bigi (2005)		90°	
Sadar (2004, Fig.4, p.8)	180°		
Sadar (2004, Fig.5, p.9)	*Implied 0°*	140°	
Xu (1997)		Angle not defined	
Yang & Hogg (1979)	Angle not defined		

2.6 The physics of light absorption and scattering through turbid water

2.6.1 A brief review of optical theories

To understand the physics of light scattering by particles suspended in water, it is necessary to have some knowledge of the mathematical models employed to describe the various absorption and scattering processes. Fundamental theory and mathematical model development are continually progressing in this area, but the basic points of interest pertinent to the understanding of turbidity in water for the practical investigator are summarised in this section.

Three main theories are discussed: Rayleigh theory, Mie theory and geometric optics. Also discussed are two theories that can be considered as approximations to Mie theory for specific conditions. These are the *Fraunhofer diffraction theory* (FDT) and the *Anomalous diffraction theory* (ADT) of Van De Hulst (1957). The reason that these two theories are considered here is that they both yield computationally fast algorithms that are utilised by laser-based particle-sizing instruments. These instruments are used widely in suspended particle analysis (organic and inorganic) both in situ and off-line in laboratories, and are extensively employed for suspended sediment characterization.

2.6.2 Rayleigh and Mie scattering

The third Baron Rayleigh formulated his scattering theory to account for the blue colour of the sky (Strutt 1871). Rayleigh scattering involves particles that are much smaller than the wavelength of the incident light, and are also defined as being *optically soft* – meaning that the particles are limited to having a refractive index very close to 1 (air molecules in the case of Rayleigh's model). Rayleigh demonstrated that scattering from small particles is strongly wavelength dependent in favour of the shorter wavelengths and is spatially isometric (i.e. scattered equally in all directions), hence the blue colour of the sky. He determined that this blue colour is predominant because the scattered light intensity is inversely proportional to the fourth power of the incident light wavelength, i.e. the shorter wavelengths of light (e.g. blue end of the visible spectrum) are scattered more readily than the longer wavelengths of light (e.g. red end of the visible spectrum).

Gustav Mie originally developed his theory to explain the colouration of metals in the colloidal state (Mie 1908). Mie theory successfully explains the dominance of forward scattering where particles are of a similar size to or larger than the incident wavelength of light, unlike the case of isotropic scattering of light by much smaller particles as in Rayleigh scattering.

In order to get some sense of the particle size ranges that are applicable to the different scattering regimes it is first necessary to define the *dimensionless size parameter x*,

$$x = \frac{2\pi r}{\lambda} \qquad 2\text{-}1$$

where r is the spherical particle radius [m] and λ is the wavelength of the incident light [m]. Figure 2-2 shows how the forward-lobed nature of a set of light intensity distribution functions develops as x increases from 0.1 to 10. These spatial intensity distribution functions are also known as *scattering phase functions*, which are calculated using Mie theory.

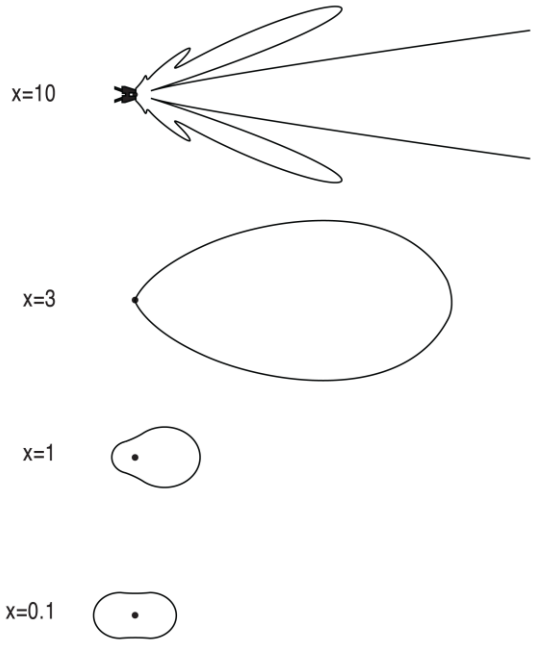

Figure 2-2. Scattering phase functions derived from Mie theory, with light incident from the left of the diagrams. Forward scattering becomes more pronounced as x increases.

2.6.3 Geometric optics

Geometric optics, otherwise known as ray optics, describes the light traversing a medium in terms of a straight path (hence "ray"). It explains *refraction*, in which there is a change in direction of a light ray at the interface between two regions with differing refractive indices. It also accounts for *reflection* and *absorption*, and is best applied in situations where the wavelength of light is much less than the size of the scattering particle. Figure 2-3 depicts a simplified diagram of scattering and absorption processes of a particle suspended in water as viewed from the perspective of ray optics.

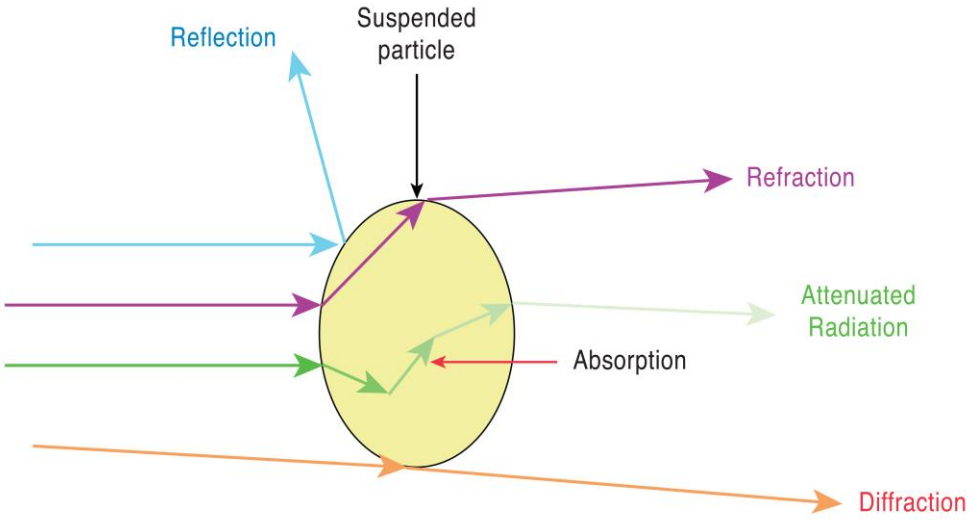

Figure 2-3. The scattering processes of reflection, refraction and diffraction, and the attenuation process of absorption of light due to a particle suspended in water.

2.6.4 Fraunhofer diffraction theory (FDT)

Fraunhofer diffraction occurs at small angles to the forward-scattered beam, i.e. <30°. Under these conditions of wavelength and scattering angle, FDT is a useful approximation to Mie theory, and is popular due to the relative simplicity of its algorithms. Due to the wavelength and particle size restrictions FDT cannot be applied to sub-micron sized particles. For example, the smallest sized sediment particle that could exhibit Fraunhofer diffraction when illuminated by a beam of red light (wavelength 630 nm) would be 6.3 µm, i.e. well above the sub-micron size limit.

2.6.5 Anomalous diffraction theory (ADT)

ADT (Van De Hulst 1957) is a computationally efficient method by which the scattering from small particles can be modelled. The caveat is that the particles must be optically soft as in Rayleigh scattering (i.e. they must have a refractive index close to 1), and they must also have a large size parameter $x >> 1$.

2.7 The single scattering albedo

The single scattering abledo, denoted ω, is a useful unitless quantity defined as the ratio of scattering efficiency to total extinction efficiency. If the attenuation observed by a detector placed in the "direct beam" configuration as in Figure 2-1 was due entirely to absorption, then $\omega = 0$. When the observed attenuation is due to scattering processes alone, then $\omega = 1$. The scattering albedo is useful when describing the particle size range that can be effectively modelled by the various regimes (Rayleigh, Mie etc.). A graph of scattering albedo (ω) versus size parameter (x) is

presented by Moosmüller & Arnott (2009, Fig.1, p.1031), which shows the particle size ranges covered by Rayleigh and Mie theory for particles with a refractive index of 1.55 (similar to that of silica). On this graph, the approximate scattering-model regime boundaries are observed, as shown in Figure 2-4 . The *large particle limit* of Mie theory is also shown, and the size parameter at which Mie theory converges with this limit is the point at which geometric optics (not shown on the graph) becomes an alternative scattering model (at $x \approx 2000$).

2.8 Light absorption and scattering by suspensions in water

In the terminology of physical optics absorption is a *non-parametric* process, i.e. one that is inherently lossy – meaning that energy is dissipated in the absorbing medium. The *parametric* processes that are to be considered do not involve any imparting of energy to the physical system through which the radiation is traversing, i.e. the wavelength of the scattered light is not altered (elastic scattering). The pertinence of these (and other) theories to the study of suspended particles in general, and suspended sediment specifically, must be considered. Rayleigh theory is applicable to small, non-absorbing (dielectric) spherical particles. Mie theory is the most ubiquitous of the models that is applied to the study of light scattering by suspensions in water. It represents a general solution to scattering from absorbing or non-absorbing spherical particles, with no limits on particle size. Rayleigh theory is less complex to apply than Mie theory, but is limited to small particles. The dimensionless size parameter x (Equation 2-1) for the scattering regimes, and the equivalent approximate particle size ranges are:

$x \ll 1$ Rayleigh scattering (2 nm to 75 nm)

$x \cong 1$ Mie scattering (20 nm to 765 μm)

$x \gg 1$ Geometric optics (>200 μm)

The graph of wavelength vs. particle diameter (Figure 2-4) shows the accepted boundaries between the various scattering regimes, as adapted from Lelli (2014) and confirmed by Moosmüller & Arnott (2009). Also plotted on the graph are the clastic sediment size ranges that are of interest in this paper.

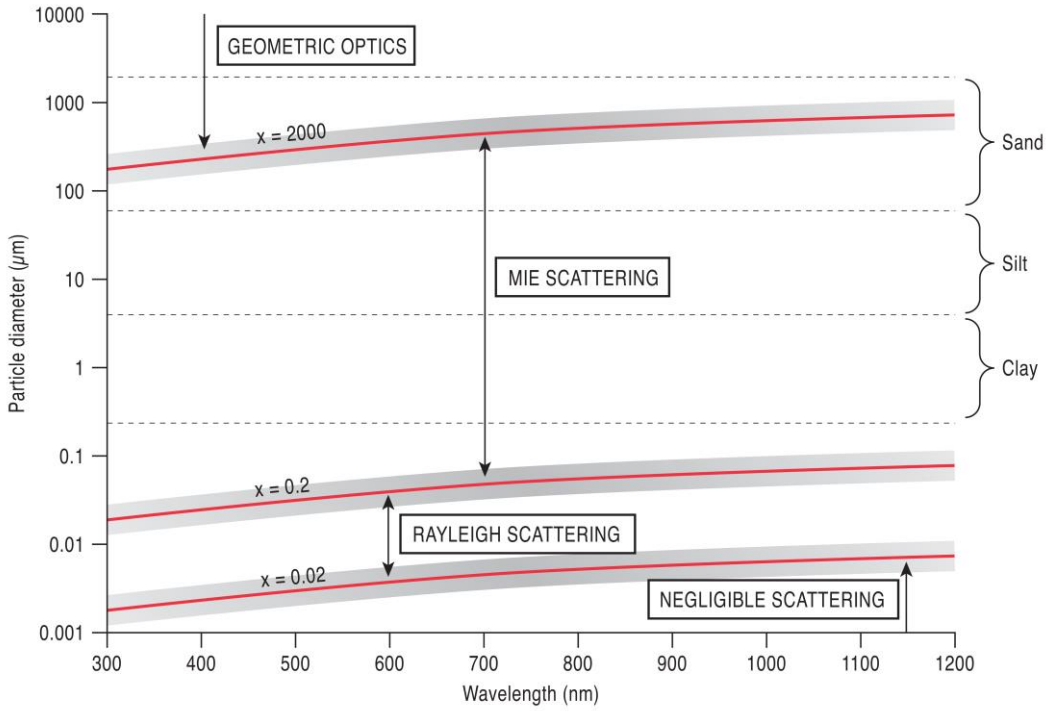

Figure 2-4. Light scattering theory regimes as a function of particle diameter and wavelength of light. Also shown are sediment particle size bands according to the American Geophysical Union Sediment Classification System.

Interpretation of this plot must however be considered carefully, as the data it represents are limited to a *single scattering event* from a *purely spherical* particle. The regime boundaries located at x=0.02, x=0.2 and x=2000 (Lelli 2014 and Moosmüller & Arnott (2009) are not strict demarcation lines (i.e. Mie theory includes Rayleigh theory as $x \rightarrow 0$), but are there to suggest the generally accepted view of where the various models are used with respect to particle size parameter x. These boundaries should be considered to be somewhat blurred when applied to multiple-scattering from non-homogenous suspended sediment particles. Considerable model development is needed to account for scattering from large, non-spherical sediment particles. This work will lead to a redefinition of the scattering regime boundaries as depicted in Figure 2-4, with new models specific to suspended sediment being represented on the graph. There would also be one omission from the graph, namely Rayleigh scattering. As far as light scattering from suspended sediment is concerned, this theory has no application due to the restrictions in particle size (i.e. very small: < 76.4 nm) and refractive index (i.e. $n \approx 1$). Although Mie theory is limited to small, spherical particles only, it has many extensions that describe much more complex scattering regimes (including multiple-scattering and scattering from small non-spherical particles), and also simpler scattering regimes such as FDT (valid for particle diameter $d \geq 10\ \lambda$,

and scattering angle $\theta \leq 30°$). Other theories such as ADT which as with Rayleigh theory was originally designed for optically soft particles (but in this case with a large *x* value), are also adaptable to cope with higher refractive indices and non-spherical particles (Liu et al. 1998).

There is clearly a need to find a light-scattering model framework that is consistent with both small and large particle scattering, and which is also extensible to many-particle analysis. In the case of back-scattering from suspended sediment it has been shown that the reflectivity of the sediment also has a direct effect on the scattered light intensity (Sutherland et al. 2000), suggesting that geometric optics may play a part in future model development. Without a comprehensive understanding of the complex manner by which particle size, shape and concentration affect the absorption and scattering of light, it will not be possible to interpret what a turbidity measurement actually *means*.

2.9 The definition of the beam attenuation coefficient

The attenuation coefficient Σ is commonly referred to as the *beam attenuation coefficient* (BAC) in the turbidity literature, but these two quantities are defined in different ways by different authors. It is important that the ambiguities in both the definition and application of the BAC as a method for comparing turbidity data obtained by different methods are appreciated, as these ambiguities can lead to the misinterpretation of that data. The following discussion focusses on how the *a priori* Σ is defined, and then leads on to a definition of the BAC as an expression of Σ in terms of observable quantities, i.e. a measured attenuation and the optical path-length of the measurement instrument.

2.9.1 The attenuation coefficient Σ

Light is absorbed by water and this absorption is a function of the wavelength of the incident light (Figure 2-5). The strongest absorption occurs at a wavelength of λ = 417.5nm (Pope & Fry 1997) which gives a maximum reduction in transmitted light intensity of 0.05% over a distance of 0.1 m, which is the typical limit to the optical path length of existing turbidity instruments. As this is the worst-case scenario, the absorption of light by water is considered to be negligible in the context of turbidity measurement.

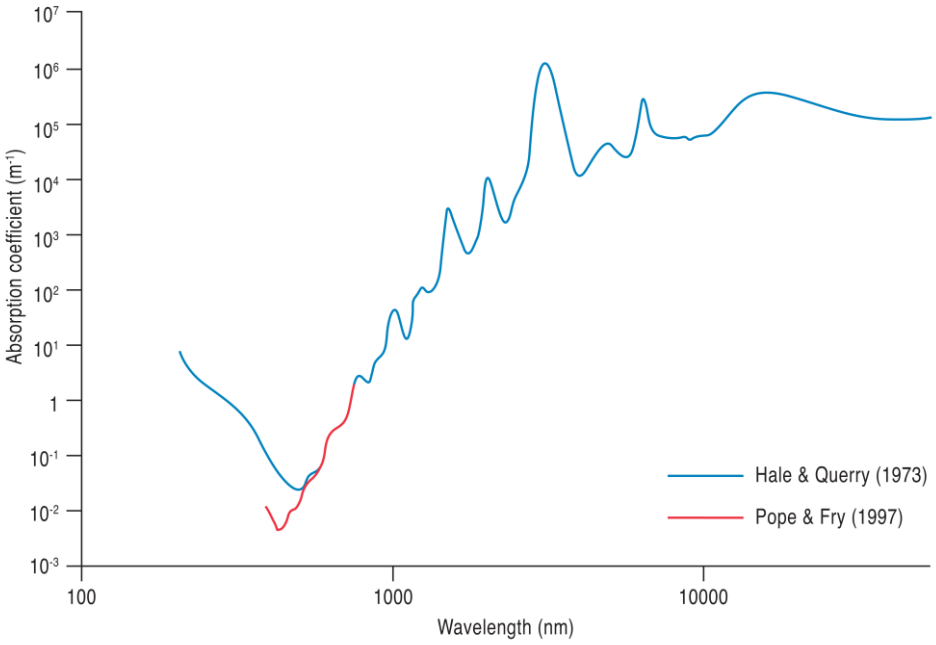

Figure 2-5. The light absorption spectrum of water. After Hale & Querry (1973) and Pope & Fry (1997).

Light is also absorbed by any other material that may be suspended in the water. In order to determine practically a value for absorption it is necessary to measure the amount of light transmitted through a given sample of water. This is termed the transmittance, T, which is defined as the ratio of the transmitted light intensity I to the light source intensity I_0, and has units of Wm^{-2}. The transmittance is also related to the optical depth (Equation 2-2), τ (effectively the opacity of the medium), and the *absorbance*, A:

$$T = \frac{I}{I_0} = e^{-\tau} = 10^{-A} \qquad 2\text{-}2$$

A quantitative measure of the optical depth τ can be expressed in terms of the natural logarithm of the transmittance or in terms of the absorbance (Equation 2-3). This in turn leads to a definition of absorbance with units of the Neper (Equation 2-4), or in terms of the base-ten logarithm (Equation 2-5) yielding a decibel quantity.

$$\tau = -\ln(T) = A\ln(10) \qquad 2\text{-}3$$

$$A = \frac{\ln(T)}{\ln(10)} = -\log_{10}(T) \qquad 2\text{-}4$$

$$A = -10 \log_{10}(T) \qquad 2\text{-}5$$

This definition of absorbance as a logarithmic function of transmittance is useful as it facilitates a linear relationship with the optical path-length. When a linear relationship between *transmittance* and *path-length* is established it then becomes theoretically easier to relate the *absorbance* to the *concentration* of a suspension, which will consequently itself be a linear function.

The *a posteriori* description of the attenuation of light through a homogeneous medium is credited to Bouguer (1729) and is also associated with Lambert. It has been called Bouguer's law, Lambert's law (Lambert 1760) and the Bouguer-Lambert law. It states that the attenuation is proportional to the distance travelled through the absorbing medium. The extension to this law which includes a term for the concentration of absorbers is known as Beer's law, or more ubiquitously as the Beer-Lambert law (Equation 2-6 and Equation 2-7), which states that the attenuation is proportional to the concentration of the absorbers (Beer 1852).

The Beer-Lambert law allows the absorbance to be stated under *ideal conditions*, including the assumption that there are *no scattering processes* occurring in the sample, and that the attenuation is linear along the light path. This law enables the absorbance to be directly related to the concentration of absorbers, *c*, and the path length *l* (Equation 2-6). Equation 2-7 expresses the same quantity as a transmittance:

$$A = \varepsilon c l \qquad 2\text{-}6$$

$$T = e^{(-\varepsilon c l)} \qquad 2\text{-}7$$

where ε is the absorptivity [m^2, or $m^2\ kg^{-1}$] of the absorbers in suspension, and is a constant dependent on the physical properties of the absorbers (i.e. dielectric properties). When defined in these terms, the *attenuation coefficient* Σ can be stated as the product of the absorptivity and the concentration of the absorbers:

$$\Sigma = \varepsilon c \qquad 2\text{-}8$$

Substituting Equation 2-8 into Equation 2-6 gives the absorbance in terms of the attenuation coefficient:

$$A = \Sigma l \qquad 2\text{-}9$$

The attenuation coefficient can be expressed in Naperian terms or as a decadic quantity (i.e. in decibels). The measured *luminance* (cd m^{-2}) represents the *power* delivered by the transmitted light beam per unit area. In electronic design it is more common to use decadic terminology to specify measurement instrument parameters such as those used for the determination of light attenuation. If Equation 2-7 is substituted into Equation 2-5, then the absorbance can alternatively be stated in decibels (Equation 2-10 and Equation 2-11).

$$A = 10\Sigma l \qquad 2\text{-}10$$

$$A = 10\varepsilon c l \qquad 2\text{-}11$$

It is worth noting that the absorbance A is a dimensionless parameter, and the attenuation coefficient Σ has units of reciprocal length (m^{-1}). However, the absorptivity ε may have different units depending on the context in which the concentration c is expressed (Equation 2-11). For example, in the case where the concentration is simply the number of absorbers N per unit volume, then the units of concentration are reciprocal volume, i.e. m^{-3} or l^{-1}. Therefore, absorptivity ε in this instance has units of m^2. In the case of suspended sediment, the absorptivity ε would have units of $m^2\ kg^{-1}$. It is important to recognise the units stated for absorptivity, as other nomenclature could potentially refer to the same physical quantity. For example, the *mass attenuation coefficient* used in chemistry also has units of $m^2\ kg^{-1}$. Hence it is prudent to examine the mathematical definition being used within a given text to determine what physical quantity is actually being discussed, and not to rely on the accuracy of the nomenclature at all. Another example of ambiguous nomenclature is highlighted by Figure 2-5, which shows the graph of the light absorption spectrum of water. The range of this function is referred to as the *absorption coefficient*, and as it has units of reciprocal length (m^{-1}) it is equivalent to the Σ of this discussion (i.e. the attenuation coefficient). This multiplicity of measurement units has the potential to cause confusion, since the absorption coefficient has the same units as the attenuation coefficient Σ. This is an important point as absorption is not the same as attenuation. Attenuation is the end result of the effects of the physical properties of the medium on the propagation of the light waves, and represents a loss of measureable light intensity. Any measured attenuation cannot be presumed to be due to absorption alone (Figure 2-3). Scattering of light can occur in all directions, and reflection and refraction of light can also distort any attenuation measurement. For example, Gumprecht & Sliepcevich (1953) suggested that *forward scattering* can distort a true attenuation measurement by *adding* to the transmitted light intensity observed by a detector. This forward-scattering component is referred to as the *extinction coefficient* by Clifford et al. (1995, p.774),

who describe it as "*the re-formation of light after scattering behind the particle*", and attribute this effect to the presence of suspended particles of diameter less than approximately 4 μm.

2.9.2 BAC – the beam attenuation coefficient

The attenuation coefficient Σ is defined for *ideal* conditions, i.e. situations in which the attenuation of light obeys the Beer-Lambert law and is thus concerned with absorption only, although some definitions of BAC include a term for light-scattering (Kirk 1985). However, light-absorption cannot be measured directly; only the *attenuation* of a light source can be determined by direct measurement of light transmitted through a sample. As this attenuation could be affected by other processes besides absorption (e.g. scattering), the absorption itself is not directly observable. The absorption and scattering processes that occur within the sample do not have any bearing on how a transmitted light intensity is measured at a given angle with respect to the incident beam, as the only available parameters are the measurement angle θ, and I / I_0 for each θ. It is crucial that the BAC is accepted only as a measurement of light *attenuation*, and it cannot by itself be used to infer any *a priori* mechanism of absorption or scattering. It is however conceptually convenient to consider the definition of the BAC as being based purely on the effects of absorption alone (i.e. the ideal conditions of the Beer-Lambert law). The measurement of transmissivity and hence the attenuation of light due to the turbidity of water is referred to in the literature as *turbidimetry* or *transmissometry*. The class of device for performing this measurement is consequently termed a *turbidimeter* or a *transmissometer*.

2.9.3 A practical definition of the BAC

Many devices exist for the measurement of optical transmissivity in water, and in this sense the word "transmissivity" is synonymous with *attenuation* and refers to the measurement of I / I_0 at an angle θ of 0° with respect to I_0, i.e. the "direct beam" (Figure 2-1). This measurement leads to the derivation of the BAC by application of Equation 2-4, such that the BAC in decibels per metre (dB m^{-1}) can be stated as

$$BAC = \frac{-10 \log_{10}(T)}{l} \qquad 2\text{-}12$$

where l is the optical path length (m) as determined by the particular instrument used for the measurement.

2.10 Turbidity measurement units, calibration methods and standards

2.10.1 A summary of the major turbidity standards

The following three standards are in common use throughout the sub-disciplines of water quality assessment. Although other standards do exist, these three are the most commonly cited by

researchers into the properties of natural waters. The summaries of these standards are presented in order to highlight some of the technical imprecision inherent in their measurement methodologies.

2.10.2 US EPA Method 180.1

This standard has been in use in various revisions since the early 1970s. The most recent revision being 2.0 (US EPA 1993), which states that it is applicable to the measurement of turbidity in "*drinking, ground, surface, and saline waters, domestic and industrial wastes*" (US EPA 1993, p.1). The standard employs the comparison between the light scattered by the test sample to the light scattered by a "*standard reference suspension*" (US EPA 1993, p.1). This reference suspension consists of a defined mixture of two chemicals, hydrazine sulphate and hexamethylenetetramine, to produce a "*stock standard suspension*" known as Formazin (US EPA 1993, p.3). A *primary standard suspension* is then created by diluting 10mL of stock standard in 100mL of reagent water. This concentration is defined as having a turbidity of 40 Nephelometric Turbidity Units (NTU). Another acceptable commercially available primary standard based on styrene divinylbenzene polymer is also stated.

The instrumentation parameters for the measurement of scattered light by this standard are the use of a tungsten light source with a colour temperature from 2200-3000K, and a beam path-length of not greater than 0.1 m. The detector response should peak at 400-600 nm, and the measurement angle should be 90° ± 30°. Note that this is a very broad range of light wavelengths and scattering angles which encompass forward-, side- and back-scattering geometries.

2.10.3 ISO 7027

This standard has been in effect in Europe since 1994. It relies in part on the use of light scattering and attenuation by standard suspensions for comparison with the same measurements in a test sample, as with EPA Method 180.1. A notable difference between the two standards is that ISO 7027 dictates the use of near infrared light (λ = 860 nm) for all measurements. The standard suggests that at wavelengths greater than 800nm the interferences caused by natural colouration of the water (e.g. by dissolved humic substances) can be significantly reduced, an effect which has been observed by Hongve & Akesson (1998).

In addition to the measurement of diffuse radiation (i.e. nephelometry) expressed in Formazin Nephelometric Units (FNU – in the range 0-40), the standard also defines a method for the "*measurement of the attenuation of a radiant flux, more applicable to highly turbid waters (for example waste or polluted waters)*" (ISO 1999). This measurement is expressed in Formazin Attenuation Units (FAU), in the range 40-4000 FAU.

2.10.4 GLI Method 2

This method is explicitly for the determination of turbidity in drinking water. It is a nephelometric *and* attenuation-based *ratio-metric* method based on infrared light of 860 nm wavelength, in common with ISO 7027. The use of dual-beam instruments that have two light sources and two detectors is specified. Each light source is pulsed sequentially, and for each measurement phase a 90° *active* intensity and a 0° *reference* intensity measurement is acquired (Figure 2-6). A ratio-based algorithm is then used to calculate an NTU value based on the four data points (i.e. two 0° and two 90° measurements). The accepted reason for employing this method is that it improves instrument stability due to interferences caused by the degradation of the light source, the fouling of sensor windows, and the effects of water colouration. It must be noted that the ratio algorithm is not defined in the standard, which implies that the implementation is left to the instrument designer (the topic of ratio methods is considered in greater detail later). As in the previously discussed standards, formazin suspensions are used for calibration. This is an example of a *multiple parameter* measurement method.

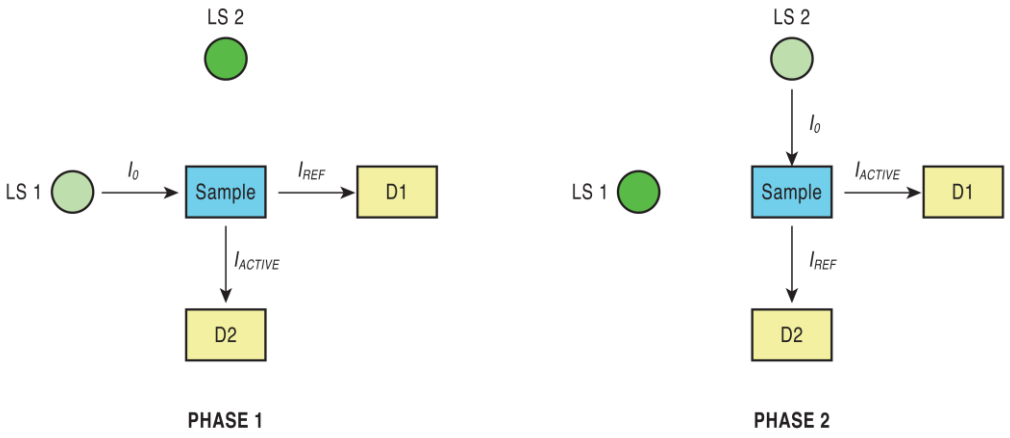

Figure 2-6. Beam-ratio process as described in GLI Method 2. LS 1 & LS 2 are the light sources; D1 and D2 are the detectors. I0 is the light beam incident on the sample; IACTIVE is the 90° scattered light and is considered to be the actual nephelometric measurement; IREF is the 0° transmitted light and is used purely as a reference value for use in a ratio-metric calculation.

2.11 A summary of turbidity measurement units

The U.S. Geological Survey has summarized currently used turbidity units and their associated standards as reproduced in Table 2-2 (USGS 2013), with amendments for the scattering angle convention in use throughout this paper .

Table 2-2. Units of Measurement for Turbidity Sensors, after USGS website (USGS 2013).

Units of Measurement for Turbidity Sensors		
	Wavelength of Light Source	
	White or broadband: peak spectral output of 400-680 nm	**Infrared, monochromatic: typical output in 780-900 nm range**
Single Illumination Beam Light Source		
90° to incident beam; single detector	**Nephelometric Turbidity Unit (NTU)**[a]	**Formazin Nephelometric Unit (FNU)**[b]
90° and other angles; multiple detectors; instrument algorithms use combination of detector readings and ratio techniques	Nephelometric Turbidity Ratio Unit (NTRU)	Formazin Nephelometric Ratio Unit (FNRU)
30°±15°to incident beam (backscatter)	Backscatter Unit (BU)	Formazin Backscatter Unit (FBU)
30°±15° and other angles; multiple detectors; instrument algorithms use combination of detector readings and ratio techniques	Backscatter Ratio Unit (BRU)	Formazin Backscatter Ratio Unit (FBRU)
0° to incident beam (attenuation)	Attenuation Unit (AU)	Formazin Attenuation Unit (FAU)
Multiple Illumination Beam Light Source		
90° and possibly other angles; multiple detectors; instrument algorithms use combination of detector readings	Nephelometric Turbidity Multibeam Unit (NTMU)	Formazin Nephelometric Multibeam Unit (FNMU)

[a] **NTU:** limited to instruments that comply with EPA Method 180.1.

[b] **FNU:** pertains to instruments that comply with ISO 7027, the European drinking-water protocol. This includes many of the most commonly used submersible turbidimeters.

Most of the material reviewed for this paper pertains to measurements taken by turbidity instruments that comply with either USEPA Method 180.1 or ISO 7027, and hence the measurement units that are most commonly encountered in the literature are NTU, FNU (specifically for drinking-water assessment) and FAU (specifically for waste-water assessment). The USGS considers these units to be the ones that are most commonly applied to submersible turbidimeters. The other units listed in Table 2-2 are rarely encountered in the turbidity literature. In addition to the USGS website, another useful summary containing greater detail

regarding the applications of the different turbidimeter designs is presented by Sadar (2004). A more concise summary of the standards discussed in this paper is presented by (Ziegler 2003), and this summary is reproduced here (Table 2-3) as it provides pertinent and useful aid to the context of this discussion.

Table 2-3. Summary of turbidity test methods after Ziegler (2003), where NTU are nephelometric turbidity units, FTU are formazin turbidity units, and FAU are formazin attenuation units.

Characteristic	**USEPA Method180.1 (non-ratio mode)**	**ISO Method 7027 (diffuse radiation)**	**ISO Method 7027 (attenuated radiation)**	**GLI Method 2**
Use of data	Drinking water	Drinking water	Wastewater	Drinking water
Range of method	0-40 NTU (dilution permitted)	0-40 FTU (dilution permitted)	40-4000 FAU	0-40 NTU (dilution permitted)
Light source	Tungsten lamp	Photodiode	Photodiode	Photodiode
Wavelength	400-600 nm	860 nm	860 nm	860 nm
Spectral bandwidth	Not specified	60 nm	60 nm	60 nm
Detector orientation measurement angle	90° ± 30°	90° ± 2.5°	90° ± 2.5°	Two sources, two detectors at 90° ± 2.5°
Aperture angle	Not specified	20°-30°	20°-30°	Unknown
Path length	Less than 0.1 m	Less than 0.1 m	Less than 0.1 m	Less than 0.1 m
Primary standards	Formazin polymer	Formazin polymer	Formazin polymer	Formazin polymer
Secondary standards	Polymer microspheres	Polymer microspheres	Polymer microspheres, cubes, or filaments	Polymer microspheres

2.12 The problem with formazin

Formazin is useful as a turbidity standard as it can be reproducibly prepared from raw materials to within ±1% , and comprises a wide range of particle shapes and sizes ranging from 0.1 μm to 10 μm (Buzoianu 2000). However, it also has a number of drawbacks as highlighted by Buzoianu (2000):

- The preparation temperature affects the resulting PSD.
- Formazin is carcinogenic.
- Formazin primary standards do not usually state the concentration uncertainty.
- The stability of formazin standards decreases as the concentration decreases (Table 4). The dilution ratio can be very high which leads to high uncertainty at low concentrations. This necessitates the use of secondary standards with longer shelf lives, and these standards can have poor repeatability of preparation, they are not formazin (eg latex), and they have different (narrow) PSDs. Hence, the use of secondary standards produces more variation in the response of different measurement instruments to the same nominal turbidity level.

Table 2-4. Stability of formazin standards, after Buzoianu (2000).

Formazin standard concentration	**Stability duration**
> 400 NTU	1 year
20 – 400 NTU	1 month
2 – 20 NTU	12 – 24 hours
< 2 NTU	<= 1 hour
<= 1 NTU	Difficult to prepare accurately

It is a key fact that all of the units described in the previous section (Table 2-2 and Table 2-3) are derived from a *chemical concentration level* of formazin or a secondary polymer-based standard. By this methodology an increase in concentration is defined as an increase in turbidity. *There is no defined relationship between the stated turbidity and the measured light intensity*. The word "concentration" has effectively been replaced by "turbidity" in the definition of these measurement units. For example section 7.3 of US EPA Method 180.1 states "Primary calibration standards: Mix and dilute 10.00 mL of stock standard suspension (Section 7.2) to 100 mL with reagent water. The turbidity of this suspension is defined as 40 NTU. For other values, mix and dilute portions of this suspension as required."

This definition is a serious issue as "turbidity" in these standard techniques no longer refers to an optical property of water, but rather a chemical concentration of what is in terms of particle classification an unknown distribution of both particle sizes and particle shapes. As the particle-size distribution (PSD) is not known, it is therefore not repeatable between measurements due to factors such as chemical degradation and flocculation during storage of the "stock standards". Also, the fact that it is deemed acceptable to use secondary standards that will not have the exact same optical response as formazin (Sethi et al. 1997, p.110) suggests a flaw in the methodology at its root, as these "stock standards" are clearly not consistent nor are they traceable.

The sphericity of the suspended formazin particles is also not quantified. Sadar (1999) states when describing formazin "*the polymer in solution consists of random shapes and sizes.*" Both PSD (Baker & Lavelle 1984, Ziegler 2003) and sphericity (Gibbs 1978) have been shown to have a significant effect on the light-scattering characteristics of a suspension. Referring back to Figure 2-2, the dimensionless size parameter x has a large effect on the scattering phase function. For example, nephelometric instruments are most sensitive to particles of <1 μm diameter as in this size-range there is a significant amount of side-scattering, yet the standards do not state the PSD limits required for reference solutions.

It has been demonstrated that different instruments measure different turbidity values when calibrated with the same primary standard, due to the differences in instrument design (Buzoianu 2000). This is a situation that can occur even when the different instruments are made to comply with the same measurement standard (e.g. EPA Method 180.1), due to the wide design tolerances (e.g. a measurement angle of 90° ± 30°). In view of the large uncertainties in the concentrations (and PSDs) of the calibration standards, augmented by the variation in measurement instrument response, there is then a scenario in which one stock standard and two different measurement instruments (made to the same or different standards) could potentially give rise to not *two*, but *multiple different* initial calibration results (Figure 2-7). An inaccurate surrogate model of turbidity has now effectively become synonymous with turbidity itself *by definition* in these standards. This calibration problem has implications for the measurement of turbidity in the field. The cross-comparability of measurements made by different researchers at different sites using different instrumentation is now questionable, even if each researcher has a self-consistent set of repeatable calibration data for their own particular measurement instrument. It is therefore necessary to take a step back and to re-define the chain of measurement at its first and weakest link, which is the Formazin standard, and to establish a new methodology based purely on the calibration of measurement instruments to well-defined light intensities at well-defined wavelengths.

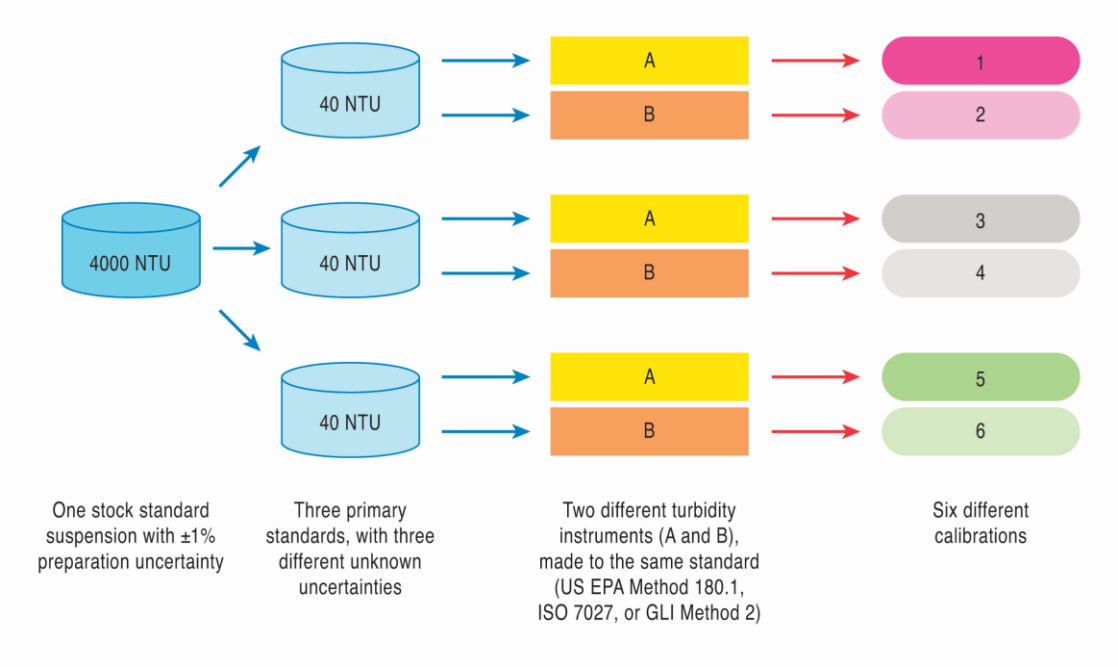

Figure 2-7. An example of the effect of indeterminate PSD due to identically defined but potentially physically dissimilar primary turbidity standards on the calibration of turbidity instruments. Results are further confounded by the variability in response between different instruments to the same PSD.

2.13 Towards a new turbidity instrumentation standard

In order to move towards a new standard for the design of turbidity instrumentation it is first necessary to take a step back from the accepted suspension-based calibration methods as prescribed by the existing standards. The following discussion attempts to clarify the misconceptions associated with the relationship between SSC, TSS and turbidity, and leads on to a proposed calibration methodology based on the measurement of light-attenuation due to the presence of optical neutral density (ND) filters in the optical beam path. To complete the new standard, a new nomenclature based on the BAC is proposed for the reporting of turbidity at multiple scattering angles and wavelengths of light. To conclude the discussion, some suggestions for the contents of potential secondary standards (based on the newly proposed instrumentation standard) for surrogate SSC determination are then outlined briefly.

2.14 Suspended sediment concentration (SSC) and total suspended solids (TSS): their relationship with turbidity and the importance of the PSD

The surrogacy of physical properties for intrinsic optical properties as is the case regarding *chemical concentration* becoming a surrogate for *optical turbidity* has raised the possibility of further misinterpretation, due to the undefined PSD of the calibration standards and the inconsistent response of different measurement instruments to the same PSD (Buzoianu 2000). In this section it is necessary to take a step back from turbidity to examine the meanings of the pre-existing terminology for suspensions (of sediment or otherwise) in water. It is important to understand this terminology as the descriptive acronyms actually refer to documented test methods for the determination of sediment concentration and suspended solids concentration. An understanding of these methods will then facilitate a deeper appreciation of the reasons for the conceptual conflation of sediment concentration with turbidity.

The US convention regarding the attribution of documented test methods to the acronyms "SSC" and "TSS" has been adopted in this paper. Regarding this terminology, as with that of turbidity, the differences in use in different disciplinary areas arises again. For example Holliday et al. (2003) suggest TSS to mean "total suspended sediment concentration", rather than "total suspended solids", i.e. the acronym SSC may have been a better choice.

The field techniques and laboratory methods for the measurement of SSC and TSS were reviewed by Gray et al. (2000), who cite Method D 3977-97 (ASTM 1998) for SSC and Method 2540 D (APHA 1971) for TSS. They describe the two different analytical methods as follows:

- SSC data are produced by measuring the dry weight of all the sediment from a known volume of a water-sediment mixture.
- TSS data are produced by several methods, most of which entail measuring the dry weight of sediment from a known volume of a subsample of the original.

After an analysis of 3235 paired SSC and TSS measurements was performed, it was concluded that SSC was the more reliable methodology (Gray et al. 2000), especially when the amount of sand in a sample exceeds approximately one quarter of the dry sediment mass. The main reason given for this disparity of results is that the SSC analytical method utilises the entire sample (including all sediment present), whereas the TSS methods typically involve the analysis of only a sub-sampled aliquot of the total sample. The decanting and pipetting techniques employed to obtain this aliquot do not capture a complete representation of the sediment population of the original sample. The resulting sub-sample is therefore sediment deficient, particularly of the

larger sand-sized sediment fraction. Gray et al. (2000) go on to suggest that the reason for this loss of sediment during TSS analysis arises from the fact that TSS methods were originally designed for analysis of waste-water samples that were to be collected *after* an initial settling phase, hence larger sediment particles were never intended to be part of the analysis. They finally conclude that SSC and TSS analysis of natural water samples are not comparable, and that SSC is the only viable method for the determination of the sediment concentration of natural waters.

In order to relate a subjective turbidity reading to a real physical property such as SSC, a calibration procedure is typically performed. This relationship between the optical properties of suspended sediment and its mass concentration must therefore be understood, requiring the characterisation of its lithology. The size of the sediment particle is frequently measured either directly (e.g. filtering and sieving), or analytically (by LASER diffraction) in the case of smaller size fractions. LASER-based particle size measurements give a *volume* concentration value, which then requires further knowledge of the specific density and mineralogy of the sample in order for an estimate of the *mass* concentration to be obtained. This process is known as *end-member calibration*.

The problem now arises that the detector response has been pre-calibrated to a primary standard, with arbitrary units for turbidity based on unstable calibration methods. It has already been suggested (Figure 2-7) that these units (NTU etc.) are not comparable between calibrations made on instruments constructed to the same standard. It is therefore highly unlikely that calibrations made by *different* instruments (constructed to the same or different standards) can ever be accurately compared due to the invalidity of these extrinsic turbidity units. It is therefore necessary to determine the true instrument response by a different method entirely. Only then can an end-member calibration have any chance of being meaningful.

Optical neutral density filters (ND filters) are regularly employed for the calibration of transmission-based optical instruments, but are seldom employed in turbidimetry or nephelometry. These filters provide a consistent optical density (OD) which in turn will attenuate a well-defined percentage of the transmitted light. One such example of an attempt to calibrate a turbidimeter against a known light attenuator is Finlayson (1985). By not only calibrating a turbidimeter against Formazin suspension, but also against ND filters, Finlayson has devised a method by which direct comparison between attenuation measurements made on the same sample by different devices could potentially be developed. It can be seen that Formazin concentration does not in fact have a linear relationship to measured light attenuation (Figure 2-8). Although the calibration data are sparse in the upper range of the instrument in this case (Finlayson 1985), there is a good fit of the data to a power law ($R^2 = 0.9954$). The only two useful

axes on this graph are "meter reading" and "neutral density filters", as these two alone are all that is required to accurately establish the response of the instrument to attenuation (Figure 2-9). Only when this detector attenuation curve has been established can further selective end-member calibrations be performed to determine the effect the PSD has on the response of a particular instrument to a given sediment. Each ND filter represents an optical density, *d*, which is directly equivalent to the absorbance *A*, as in Equation 2-4. So in order to calculate the BAC in dB m^{-1} for an instrument with path-length *l*, the following equation can be applied (Equation 2-13):

$$BAC = \frac{-10d}{l} = \frac{10ND}{l} \qquad 2\text{-}13$$

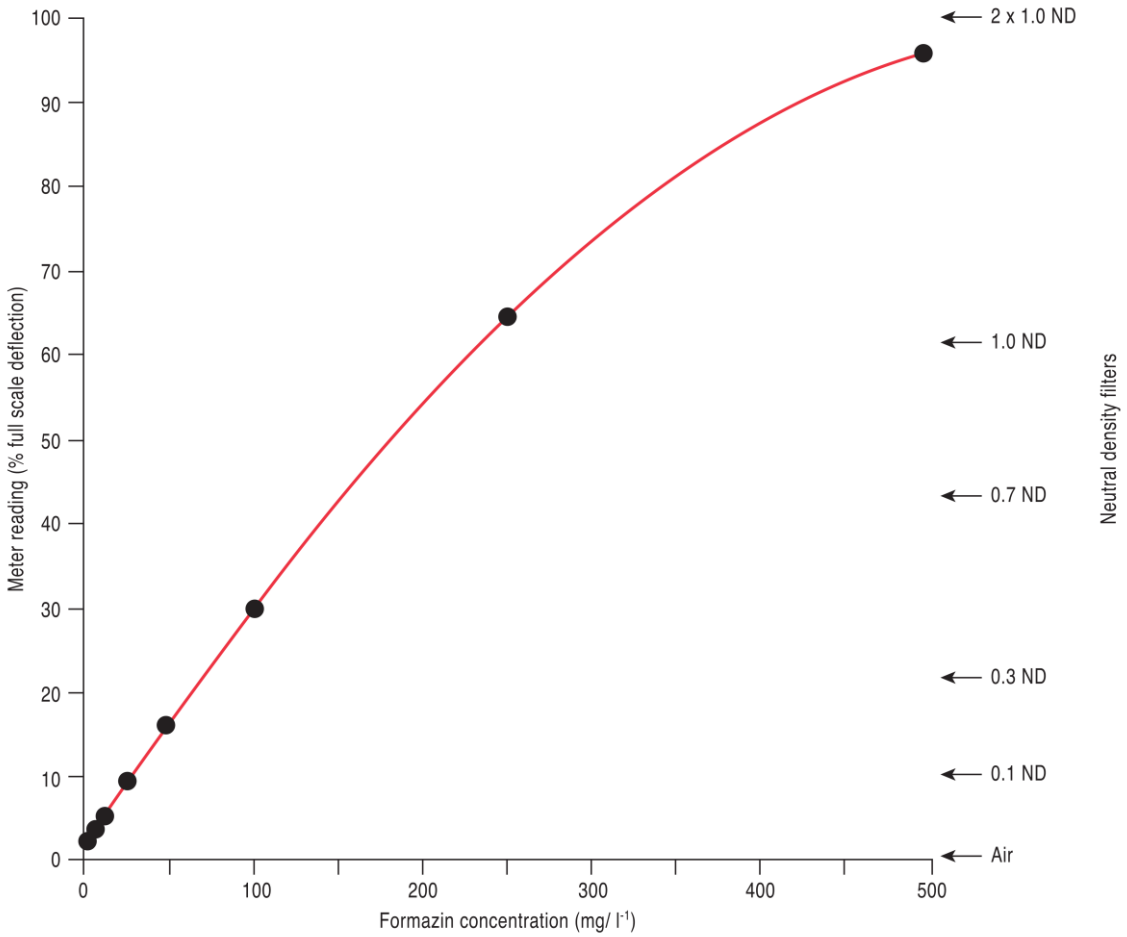

Figure 2-8. Laboratory calibration of a turbidity meter with Formazin standards. Meter readings of the neutral density filters used in the field are shown also (Finlayson 1985).

2.15 Instrumentation parameters and calibration methods

To arrive at a *consistent* methodology for the measurement of turbidity it is necessary to accept that the only quantity that can be readily measured optically in this context is the transmitted light intensity, and hence *attenuation* with respect to the light source (i.e. I / I_0). It is the methodology for taking this measurement that should be rigorously specified, regardless of the measurement angle θ with respect to I_0. The implementation section of the standard should address this methodology, and focus purely on the desired response of the instrument to light at defined intensities and wavelengths. This aspect of work would involve the definition of parameters such as sensor type, variable intensity light source specification (including coherence and polarization), detector amplifier gains and ranges, ND filter calibration procedure involving multiple beam paths, beam path-length and collimation arrangements. It is then necessary to decide which instrument parameters (e.g. θ, λ and l) should be specified as mandatory for all turbidity measuring instruments, and which ones should be considered as being application-specific.

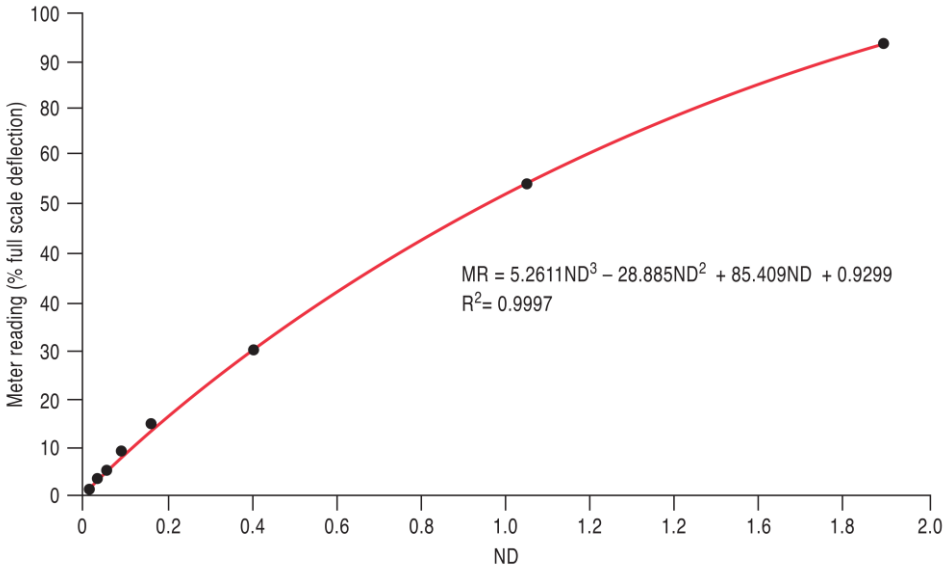

Figure 2-9. A reproduction of the data contained in Figure 2-8 showing the meter reading vs. the ND filter value (after Finlayson 1985). The ND value is equivalent to d, the optical density.

2.16 The reporting of turbidity measurement data

The standardization of the reporting of turbidity as attenuation data (Ziegler 2003) and the use of a more descriptive nomenclature is proposed, which will allow for the easy identification of application-specific data such that incompatible measurements will not be inadvertently compared to each other. It is suggested that significant progress could be made if the

measurement concepts for turbidimetry and nephelometry were unified, i.e. by treating them *both* as an attenuation process. The only difference being that for scattered light measurement the effective concentration of scatterers is *inversely proportional* to the BAC measured at a specific angle to the incident beam. However, for that to be achieved formulations of the BAC at specific angles must then be defined, for example BAC_0 for a standard transmissivity measurement and BAC_{90} for the nephelometric counterpart at 90°. For the nephelometric case the relationship between the scattered light intensity and the concentration could be viewed as an *inverse attenuation*, since a higher concentration of particles will produce stronger scattering (until the concentration is too high, at which point multiple-scattering and grain-shielding will dominate and interfere with the measurement of the side-scattered light). Measurement-instrument calibration now becomes somewhat critical, as any drift in the incident light intensity or the sensor response will affect the sensitivity of the system to the low light intensities that need to be detected due to side- or back-scattering. This nephelometric BAC_{90} measurement results in potentially larger percentage errors than those that are likely for measurements based on BAC_0, as greater electronic amplification is required to detect the weaker scattered-light signal which can be inherently noisy. In order to formulate a generic equation for the BAC as a function of measurement angle it is necessary to include two terms: one for attenuation and one for scattering. The use of these terms is in no way a new idea (e.g. Kirk 1985), however the interpretation of scattered light intensity as an *inverse absorbance* has not been previously considered. In this new method the same measurement units could be employed for practical comparison between data obtained under different conditions using different instruments, so long as those instruments complied with the same instrumentation standard, and the reporting of said data is consistent (Ziegler 2003). For example Kirk (1985) suggested using the correct description of the measurement method, such as “side-scattering”, when stating results – or preferably BAC_{90} in this case.

2.17 Standards for surrogate SSC determination

Further standards for the determination of surrogate properties such as SSC should refer to instruments that are specified according to the new instrumentation standard. In order to estimate SSC accurately, optical instruments must be capable of producing data rich enough to facilitate suspended sediment characterization. Methods for the determination of the PSD (and other properties) of a suspended sediment by multi-parameter measurements need to be developed, which could include the use of LASER diffraction techniques. Other potential methods of sediment characterization should also be explored more thoroughly.

2.18 Suspended sediment characterization

For a deeper understanding of sediment transport to be realized, it is essential to know how the different size-classes of sediment respond to different flow conditions, especially the larger sand-sized particles that can be transiently in suspension long enough to affect turbidity measurements. A knowledge of sediment particle shape in terms of *sphericity* and *roundness* can also provide an insight into the distance travelled by sediment particles that have previously been entrained in a flow of water. There is a clear need therefore to characterize the suspended sediment to determine the particle sizes present. This characterization can be achieved by traditional gravimetric sampling methods, but there is an increasing need to gather data for research purposes *in-situ* and quickly. In some cases, these measurements could be made "off-line" by optical means, which would still be much faster than can be achieved by gravimetric methods. LASER-based optical measurements are the most commonly employed for this purpose, although there have been attempts to derive particle-size information from multi-parameter turbidity measurements. The effect that particle shape has on such measurements could also be exploited as a characterization technique.

2.19 Measurement ratios and multi-parameter method development

The designers of some turbidity meters (i.e. any commercially available instrument that claims compliance with GLI Method 2) have adopted the use of multi-parameter measurements in order to improve instrument performance. This innovation has included the measurement of light intensities at multiple scattering angles, and the use of the ratios of those intensities to infer some of the physical properties of the scattering suspension, e.g. sphericity (Gibbs 1978), or to negate the effect of water colour as an interference to the turbidity measurement (Lawler 2005, Lambrou et al. 2009). An example of another multi-parameter approach to turbidity measurement is presented by Yang & Hogg (1979), wherein two different wavelengths of light are used to predict the PSD of the scattering suspension. These and other multi-parameter approaches to turbidity measurement should be the focus of further research, and will aid the development of new turbidity standards.

2.20 Conclusions

1. The use of turbidity purely as an indicator of water clarity is entirely acceptable assuming the development of more consistent standards. The problem is that the existing standards have introduced a set of measurement units that actually represent a surrogate for turbidity and therefore cannot be used to describe water clarity.

2. Simple turbidity measurements when used as a surrogate for suspended sediment concentration are only viable under highly constrained conditions. Bias toward the fine sediment fraction is usually considered unimportant, but this is not always the case.

3. Sand-sized sediment fractions are not consistently accounted for by existing turbidity measurements, due to their high settling velocities. The SSC method is also required in order to quantify the sand fraction fully.

4. The development of new light-scattering models will permit more sophisticated approaches to turbidity measurement, in particular by the use of parameter-rich data sets obtainable from multi-parameter methods. This approach will facilitate the improvement of turbidity standards, and could increase the accuracy of large sediment particle detection.

5. A new turbidity instrumentation standard needs to be drafted, based purely on the principle of attenuation for calibration and reporting purposes. It should specify the reporting of the BAC in dB m^{-1} (or derived units) for a range of measurement angles and wavelengths of light. This standard should be a root standard from which other secondary standards are derived, e.g. standards for suspended sediment characterisation or total suspended solids assessment by optical turbidity measurement.

6. A further standard for suspended sediment determination by simple multi-parameter turbidity measurements needs to be devised (leading on from point 4 above). This standard should include basic sediment characterisation as an outcome of optical turbidity measurements (e.g. PSD and sphericity).

Chapter 3 A low-cost device for turbidity measurement by radially distributed illumination intensity sensing at multiple wavelengths

3.1 Declaration of originality

The article reproduced in this chapter, originally titled "A low-cost device for turbidity measurement by radially distributed illumination intensity sensing at multiple wavelengths" (Kitchener et al. 2019) is done so according to the University of Sheffield regulations relating to the "Alternative Format Thesis". I (Ben G. B. Kitchener) am the first author, and I confirm that the work is mine and is not plagarised.

Signed:

Date:

Reference to the original article:

Kitchener, B.G.B., Dixon, S.D., Howarth, K.O., Parsons, A.J., Wainwright, J., Bateman, M.D., Cooper, J.R., Hargrave, G.K., Long, E.J. & Hewett, C.J.M., 2019. A low-cost bench-top research device for turbidity measurement by radially distributed illumination intensity sensing at multiple wavelengths. *HardwareX*, 5.

3.2 Abstract

Presented here is a new research device for the measurement of the optical turbidity of natural sediment-laden water samples. This prototype device employs 18 unique angular measurement positions and a variety of user-selectable LED light sources. The motivation for this project was the need to generate more parameter-rich data sets pertaining to the light-scattering properties of natural sediment suspensions, and to address the issues raised by Kitchener et al. [Progress in Physical Geography 41 (5), 620-642 (2017)] concerning the inconsistent calibration

methodologies currently employed to quantify suspended sediment concentration (SSC) by optical turbidity measurement. The mechanical design comprises re-purposed waste plastic materials and 3D-printed parts. The active light-source control and monitoring hardware and firmware executes on the open-source Arduino embedded microcontroller platform. The modular light sensors plug into any of the angular measurement positions, providing a 0-5V nominal output signal, which is readable by the user's choice of data-acquisition system. The device will facilitate the highly detailed characterization of suspended sediment samples, providing 18 voltage output channels for analysis by the user. The precise calibration of the light sensors is by the use of neutral density (ND) filters in conjunction with light-source electrical current measurements, providing light-source intensity values as required. The empirical data provided by existing turbidity meters are acquired using incommensurate methodologies, and therefore they are not cross-comparable. A new methodology, described here, facilitates the cross-comparability of turbidity measurements.

3.2.1 Keywords

Turbidity, suspended-sediment, sensors, Arduino, light-absorption, light-scattering, open-source hardware.

3.2.2 Specifications table

Table 3-1. Specifications

Hardware name	*TARDIIS (Turbidity Assessment by Radially Distributed Illumination Intensity Sensing).*
Subject area	• Environmental, Planetary and Agricultural Sciences • Educational Tools and Open Source Alternatives to Existing Infrastructure
Hardware type	• Measuring physical properties and in-lab sensors
Open Source License	CERN OHL, MIT
Cost of Hardware	450 GBP (ex. VAT)
Source File Repository	DOI: http://dx.doi.org/10.17632/sn3nh36k5k.1#folder-17b97de6-a196-477a-87e7-28298c3ab4b0

3.3 Hardware in context

Commercial instruments available for the purpose of optical turbidity measurement vary widely in design, operating principle, and cost. Turbidity instruments are now ubiquitous in the water supply sector, and operate widely throughout the physical and engineering sciences

(oceanography, fluvial and glacial sciences, civil engineering, chemical engineering etc.). These instruments are designed to operate either *in situ* (in a river, ocean, harbour etc.), or in a laboratory setting. They tend to be expensive, and they are inconsistent with regard to the measurement methodology (e.g. instrument geometry, wavelength of light source). Hence it is possible to obtain completely different and non-comparable measurements of the same water sample measured by two or more different instruments. The "turbidity units" reported by these devices are inconsistent and do not conform to the SI system of measurement, for example FNU (Formazin Nephelometric Units), NTU (Nephelometric Turbidity Units), FAU (Formazin Attenuation Units) [1].

Open-source and other public-domain instruments for turbidity measurement are available [2],[3],[4],[5],[6], but these devices only provide one or two measurement angles, and are limited to a single light source. In order to fully explore the limitations and capabilities of turbidity measurement it is necessary to investigate the physics of light scattering and absorption by suspended sediment, at a comprehensive range of scattering angles and wavelengths of light [1]. Designed for one specific application, these existent public-domain turbidity meters are not versatile research instruments. The list of devices presented in Table 3-2 is not exhaustive, but it is representative of the open-source state of the art.

Table 3-2. Public domain turbidity instrument designs.

Authors	Instrument Geometry	Light Source	Intended Measurement Application
Lawler & Brown [2]	Direct beam	LED, Green	Suspended sediment concentration in rivers, lakes and estuaries, *in situ*.
Lambrou et al. [3]	90° nephelometric	LASER diode, Red (670 nm)	Household drinking water quality, continuous *in situ* monitoring.
Bilro et al. [4]	90° nephelometric, direct beam	LED, Red (660 nm)	Suspended sediment concentration, laboratory samples.
Kelley et al. [5]	90° nephelometric	LED, Infrared (860 nm)	Drinking water quality assessment in low-resource communities, manual samples.
Orwin & Smart [6]	180° back-scatter	LED, Infrared (880 nm)	Suspended sediment concentration in proglacial streams, *in situ*.

Commercial instruments exist that not only measure turbidity, but also provide an estimate of the particle size distribution (PSD) of a suspension in water. In the case of suspended sediment, the determination of the PSD is by small-angle forward scattering measurements by LASER diffraction. These measurements require expensive (1000-20000 GBP) LASER diffraction devices, which can work *in situ* or on a bench top in a laboratory.

A low-cost research device for the exploration of the light-scattering properties of suspended sediment samples, and other water samples that could contain a proportion of settleable solids, does not presently exist. TARDIIS, as a laboratory research apparatus, will allow the user to observe the sediment-settling process from multiple scattering angles simultaneously, using any wavelength LED available in a 5mm package. The user is free to interpret the measurement data in their own way, and to gain their own insights into parameters such as the PSD. The user is also encouraged to customize and refine the design to accommodate their own particular measurement requirements, and to challenge the *status quo* in terms of turbidity measurement methodology.

With a knowledge of the LED light source characteristics and a direct measurement of the LED current, TARDIIS makes it possible to report the measured light intensity in terms of appropriate SI units (notionally mW sr^{-1}). This approach to the reporting of turbidity measurements will facilitate a more meaningful way to cross-compare measurements made on different samples by other similar devices.

3.4 Hardware description – TARDIIS

TARDIIS (Turbidity Assessment by Radially Distributed Illumination Intensity Sensing) is a prototype bench-top research device specifically for the examination of the light scattered by suspended sediment at multiple angles during the process of settling in a column of water, over a variable time. It is not, however, restricted to this single use-case.

TARDIIS offers:

- Turbidity measurement at 18 distinct scattering angles (with 1 LED light-source location and 35 potential sensor locations).
- Measurement of absorption and scattering in any water sample.
- User selectable light wavelengths.
- ND filter calibration.
- Data reporting in SI units (mW sr^{-1}), rather than using incommensurate turbidity units (NTU etc.). [1]
- Generation of a detailed "optical sedigraph" at multiple wavelengths.

3.5 Design files

The link to the top-level folder for this project on Mendelay Data is DOI:
http://dx.doi.org/10.17632/sn3nh36k5k.1#folder-17b97de6-a196-477a-87e7-28298c3ab4b0

3.5.1 Design Files Summary - TARDIIS Electronics Schematics & Drawings

Table 3-3. Design files summary - TARDIIS Electronics Schematics & Drawings.

Design file name	File type	Description	Open source license	Location of the file
Amplifier.dch	`DipTRACE Schematic.	Photodiode Amplifier DipTRACE schematic.	CERN OHL	DOI: http://dx.doi.org/10.17632/sn3nh36k5k.1#file-033bcadb-eb6d-4faf-b010-1004630e09bc
Amplifier.dip	DipTRACE PCB layout.	Photodiode Amplifier DipTRACE PCB layout.	CERN OHL	DOI: http://dx.doi.org/10.17632/sn3nh36k5k.1#file-18b6a683-3f32-4286-8d2b-abb31f5b8298

Design file name	File type	Description	Open source license	Location of the file
LED Driver Arduino Shield.dch	`DipTRACE Schematic.	LED Control & Monitoring Shield DipTRACE schematic.	CERN OHL	DOI: http://dx.doi.org/10.17632/sn3nh36k5k.1#file-91fba345-8b47-4b20-a740-fdab1ae48320
LED Driver Arduino Shield.dip	DipTRACE PCB layout.	LED Control & Monitoring Shield PCB DipTRACE layout.	CERN OHL	DOI: http://dx.doi.org/10.17632/sn3nh36k5k.1#file-3a49c4f4-b2a0-486c-a0b5-84bbaca56b5a
Turbidity.eli	DipTRACE schematic symbol library.	DipTRACE schematic symbol library for Photodiode Amplifier and the LED Control & Monitoring Shield.	CERN OHL	DOI: http://dx.doi.org/10.17632/sn3nh36k5k.1#file-2f97a2fb-05c4-4f87-b23a-94600e8658b8
Turbidity.lib	DipTRACE PCB symbol library.	DipTRACE PCB symbol library for Photodiode Amplifier and the LED Control & Monitoring Shield.	CERN OHL	DOI: http://dx.doi.org/10.17632/sn3nh36k5k.1#file-d90d4767-19c4-4af1-a15d-772e2f426d2e
1053131203.stp	STEP File.	Molex connector STEP file.	CERN OHL	DOI: http://dx.doi.org/10.17632/sn3nh36k5k.1#file-f1e182eb-fe4b-47cb-ac60-b3659dc099a6

The DipTRACE design files are provided so that the user can easily modify the existing circuits using the DipTRACE CAD package.

3.5.2 Design Files Summary – TARDIIS Electronics Gerbers

Table 3-4. Design Files Summary – TARDIIS Electronics Gerbers.

Design file name	File type	Description	Open source license	Location of the file
Active_LED_Control_Application	Gerber	Folder containing LED Control & Monitoring Shield Gerbers.	CERN OHL	DOI: http://dx.doi.org/10.17632/sn3nh36k5k.1#folder-c7770cfd-b5d9-415a-baf0-ec76d2acdc0a
Amplifier_Gerbers	Gerber	Folder containing Photodiode Amplifier Gerbers.	CERN OHL	DOI: http://dx.doi.org/10.17632/sn3nh36k5k.1#folder-6bdbf85c-8fe3-4efe-9df2-2b155f2dc179

The Gerber files can be sent directly to a manufacturer for PCB production.

3.5.3 Design Files Summary – TARDIIS LED Control & Monitoring Shield Firmware

Table 3-5. Design Files Summary – TARDIIS LED Control & Monitoring Shield Firmware.

Design file name	File type	Description	Open source license	Location of the file
Active_LED_Control_ Application.ino	Arduino source code	Active_LED_Control_Application Arduino Firmware	MIT	DOI: http://dx.doi.org/10.17632/sn3nh36k5k.1#file-ea7f2a61-7a4b-4fa9-83e8-a19ca04baffb

3.5.4 Design Files Summary – TARDIIS Mechanical – OpenSCAD Files

Table 3-6. Design Files Summary – TARDIIS Mechanical – OpenSCAD Files.

Design file name	File type	Description	Open source license	Location of the file
Amplifier_housing.scad	OpenSCAD	OpenSCAD source file for photodiode amplifier/LED housing.	CERN OHL	DOI: http://dx.doi.org/10.17632/sn3nh36k5k.1#file-ab9e9b4f-7d91-46c6-8f95-640a6c1317e1
Photodiode_ Calibrator.scad	OpenSCAD	OpenSCAD source file for photodiode calibrator.	CERN OHL	DOI: http://dx.doi.org/10.17632/sn3nh36k5k.1#file-4e142e20-d620-435c-acc6-7d40a5ab6076
Amplifier_housing	STL	Photodiode amplifier housing STL, created in OpenSCAD.	CERN OHL	DOI: http://dx.doi.org/10.17632/sn3nh36k5k.1#file-77fc7e42-5de2-4268-874f-abc9615594e2
Photodiode_Calibrator	STL	Photodiode calibrator STL, created in OpenSCAD.	CERN OHL	DOI: http://dx.doi.org/10.17632/sn3nh36k5k.1#file-a8ba5a56-95be-4938-b2ed-853ea9c6c34a

The 3D printed parts were originally created using OpenSCAD, which can be used to open and modify the designs. The STL files were generated by OpenSCAD, and can be directly uploaded to a 3D printer for printing. These designs have also been re-drawn in SolidWorks in order to produce 2D drawings (as PDF files (3.5.5)) of the parts, as this function is not available in OpenSCAD.

3.5.5 Design Files Summary – TARDIIS Mechanical – Drawings & SolidWorks Files

Table 3-7. Design Files Summary – TARDIIS Mechanical – Drawings & SolidWorks Files.

Design file name	File type	Description	Open source license	Location of the file
Amplifier Housing.pdf	PDF	Drawings of photodiode amplifier/LED housing.	CERN OHL	DOI: http://dx.doi.org/10.17632/sn3nh36k5k.1#file-4309487b-1d00-4825-ab4e-9fc4eec86253
Assembly.pdf	PDF	Drawings of the complete TARDIIS assembly.	CERN OHL	DOI: http://dx.doi.org/10.17632/sn3nh36k5k.1#file-720a42ab-4a33-41ee-ba96-27fc175d1a89
Photodiode_Calibrator Part 1.pdf	PDF	Drawings of the photodiode calibrator module receptacle sections.	CERN OHL	DOI: http://dx.doi.org/10.17632/sn3nh36k5k.1#file-98e5acba-36b4-416b-8e03-6ec6bd0c898d
Photodiode_Calibrator Part 2.pdf	PDF	Drawings of the photodiode calibrator module ND filter housing section.	CERN OHL	DOI: http://dx.doi.org/10.17632/sn3nh36k5k.1#file-68102f66-ca28-456f-83c2-c1eee9ed2d41
Base.pdf	PDF	Drawings of TARDIIS base section.	CERN OHL	DOI: http://dx.doi.org/10.17632/sn3nh36k5k.1#file-8b46d655-79fa-4c5a-9843-d23d5c8f4414
Sensor collar.pdf	PDF	Drawings of TARDIIS sensor collar section.	CERN OHL	DOI: http://dx.doi.org/10.17632/sn3nh36k5k.1#file-d4a9723a-095e-474c-a90a-125d674e4b9d
Sensor Ring.pdf	PDF	Drawings of TARDIIS sensor ring section.	CERN OHL	DOI: http://dx.doi.org/10.17632/sn3nh36k5k.1#file-4bc72e51-08ea-490b-ae22-543aebd59ef6
Amplifier Housing.sldd	SLDD	SolidWorks Drawings of photodiode amplifier/LED housing.	CERN OHL	DOI: http://dx.doi.org/10.17632/sn3nh36k5k.1#file-ac049fce-69ad-4e83-9759-ef609a57cb0a
Assembly.sldd	SLDD	SolidWorks Drawings of the complete TARDIIS assembly.	CERN OHL	DOI: http://dx.doi.org/10.17632/sn3nh36

				k5k.1#file-1cb6d8db-1993-4038-beff-fe1e677e2cbf
Photodiode_Calibrator Part 1. sldd	SLDD	SolidWorks Drawings of the photodiode calibrator module receptacle sections.	CERN OHL	DOI: http://dx.doi.org/10.17632/sn3nh36k5k.1#file-eabf0021-5443-4109-a0bd-f211932f4ac0
Photodiode_Calibrator Part 2. sldd	SLDD	SolidWorks Drawings of the photodiode calibrator module ND filter housing section.	CERN OHL	DOI: http://dx.doi.org/10.17632/sn3nh36k5k.1#file-08be4caa-2d8b-48db-be89-f88fc9542322
Base.sldd	SLDD	SolidWorks Drawings of TARDIIS base section.	CERN OHL	DOI: http://dx.doi.org/10.17632/sn3nh36k5k.1#file-8b46d655-79fa-4c5a-9843-d23d5c8f4414
Sensor collar.sldd	SLDD	SolidWorks Drawings of TARDIIS sensor collar section.	CERN OHL	DOI: http://dx.doi.org/10.17632/sn3nh36k5k.1#file-284e41c6-4481-4c7b-86ac-aceec1ebcc5d
Sensor Ring.sldd	SLDD	SolidWorks Drawings of TARDIIS sensor ring section.	CERN OHL	DOI: http://dx.doi.org/10.17632/sn3nh36k5k.1#file-08edcc93-3ab4-451c-8d12-0982bb06e067

The PDF design files can be handed directly to a machinist for production of the parts. Alternatively, the SolidWorks files will allow the user to make modifications to the designs using the SolidWorks CAD package.

3.6 Bill of Materials

3.6.1 Bill of Materials – TARDIIS Mechanical (see Figure 3-1 drawing designations).

Table 3-8. Bill of Materials – TARDIIS Mechanical (see Figure 3 1 drawing designations).

Designator	Component	Number	Cost per unit - GBP	Total cost - GBP	Source of materials	Material type
#1, #3, #4 *	PVC Grey Sheet 500 x 250 x 20mm	1	26.16	26.16	https://www.directplastics.co.uk/pvc-sheet	Polymer
#2a	(100/94) 100mm x 3mm x 500mm Clear Acrylic Tube (Extruded)	1	10.83	10.83	http://clearplastictube.co.uk/index.php?route=common/home	Polymer

Designator	Component	Number	Cost per unit - GBP	Total cost - GBP	Source of materials	Material type
#2b	100mm DIA x 3mm thick Clear Acrylic Disc	1	2.10	2.10	http://clearplastictube.co.uk/index.php?route=common/home	Polymer
#2c	EMA Plastic Weld 57ml	1	4.99	4.99	http://clearplastictube.co.uk/index.php?route=common/home	Organic
#5	RS Pro Stainless Steel, Hex Nut, M8	1 bag of 50 (6 needed)	8.79	8.79	https://uk.rs-online.com/web/p/hex-nuts/0189608/	Metal
#6	Stainless Steel Plain Washer, 1mm Thickness, M8 (Form B), A4 316	1 bag of 50 (6 needed)	4.78	4.78	https://uk.rs-online.com/web/p/plain-washers/0189664/	Metal
#7	RS Pro Plain Stainless Steel Threaded Rod, M8, 1m	Each in a pack of 5 (2 needed)	3.81	19.05	https://uk.rs-online.com/web/p/threaded-rods-studs/0280408/	Metal
#8 **	RS Pro 1.75mm Black PLA 3D Printer Filament, 300g	1	10.42	10.42	https://uk.rs-online.com/web/p/3d-printing-materials/8320406/	Polymer
			Subtotal:	**87.12 (ex VAT)**		

** The base, sensor collar and sensor ring could all potentially be manufactured from this material. Other similar materials could be substituted (e.g. nylon).*

*** This is an example of PLA filament used for 3D printing the sensor/LED housing and the photodiode calibrator. The filament chosen for this purpose must be compatible with the particular 3D printer used for making any parts.*

3.6.2 Bill of Materials – TARDIIS Electronics – LED Control & Monitoring Shield.

Table 3-9. Bill of Materials – TARDIIS Electronics – LED Control & Monitoring Shield.

Designator	Component	Number	Cost per unit - GBP	Total cost - GBP	Source of materials	Material type
ARD1	Arduino UNO	1	16.64	16.64	https://uk.rs-online.com/web/p/processor-microcontroller-development-kits/7154081/	Other: Electronics
U1	STMicroelectronics LM317P Linear Voltage Regulator, 1.5A, Adjustable, 1.2 → 37 V 3-Pin, TO-220FP	Each in a pack of 10 (1 needed)	0.62	6.20	https://uk.rs-online.com/web/p/linear-voltage-regulators/6869717/	Semiconductor
U2	MCP4261-502E/P - Non Volatile Digital Potentiometer, 5 kohm, Dual, SPI, Linear, ± 20%, 2.7 V	1	0.94	0.94	http://uk.farnell.com/microchip/mcp4261-502e-p/ic-dgtl-pot-5k-2ch-14dip/dp/1840760	Semiconductor
U3	MAX1416EPE+ - Analogue to Digital Converter, Low Power, 16 bit, 500 SPS, Single, 2.7 V, 3.6 V, DIP	1	6.26	6.26	http://uk.farnell.com/maxim-integrated-products/max1416epe/adc-2-ch-sigma-delta-16bit-dip/dp/2513557	Semiconductor
U4	MAX6225ACPA+ - Voltage Reference Series - Fixed, 2.5V reference, ± 1ppm/°C, DIP-8	1	5.16	5.16	http://uk.farnell.com/maxim-integrated-products/max6225acpa/voltage-ref-series-2-5v-dip-8/dp/2511205	Semiconductor
J1, J2	105313-1203 - Wire-To-Board Connector, Right Angle, 2.5 mm, 3	2	0.78	1.56	http://uk.farnell.com/molex/105313-1203/connector-header-3pos-	Metal / Polymer

Designator	Component	Number	Cost per unit - GBP	Total cost - GBP	Source of materials	Material type
	Contacts, Header, Nano-Fit Series, Through Hole				1row-2-5mm/dp/2576867	
Connector housing for sensors & LEDs	105307-1203 - Connector Housing, TPA Capable, Nano-Fit Series, Receptacle, 3 Ways, 2.5 mm	30*	0.22	6.60	http://uk.farnell.com/molex/105307-1203/receptacle-housing-3pos-nylon/dp/2576853	Metal / Polymer
Pins for Molex connectors	105300-1200 - Contact, 6.5A / 300V, Nano-Fit Series, Socket, Crimp, 24 AWG, Gold Plated Contacts	100	0.14	14.00	http://uk.farnell.com/molex/105300-1200/contact-socket-26-24awg-crimp/dp/2576850	Metal
R1	Vishay RN65 Series Axial Metal Film Fixed Resistor 250Ω ±0.1% 0.5W ±50ppm/°C	1	0.75	0.75	https://uk.rs-online.com/web/p/through-hole-fixed-resistors/8500696/	Metal
R2	TE Connectivity LR1 Series Axial Metal Film Fixed Resistor 100Ω ±1% 0.6W ±50ppm/°C	Each in a pack of 10 (1 needed)	0.08	0.80	https://uk.rs-online.com/web/p/through-hole-fixed-resistors/0148269/	Metal
R3	http://uk.farnell.com/bourns/pwr220t-20-1r50f/resistor-thick-film-1-5ohm-1-to/dp/2328253	1	4.82	4.82	http://uk.farnell.com/bourns/pwr220t-20-1r50f/resistor-thick-film-1-5ohm-1-to/dp/2328253	Metal
C1, C2, C6	KEMET 100nF Multilayer Ceramic Capacitor MLCC 50V dc ±10% X7R	Each in a pack of 5 (3 needed)	0.19	0.57	https://uk.rs-online.com/web/p/ceramic-multilayer-	Ceramic

Designator	Component	Number	Cost per unit - GBP	Total cost - GBP	Source of materials	Material type
	Dielectric Radial, Max. Temp. +125°C				capacitors/5381310/	
C3	Murata 10µF Multilayer Ceramic Capacitor MLCC 50V dc ±20% X7R Dielectric Radial Through Hole, Max. Temp. +125°C	Each in a pack of 5 (1 needed)	1.65	8.25	https://uk.rs-online.com/web/p/ceramic-multilayer-capacitors/8118373/	Ceramic
C4, C5	Murata 2.2µF Multilayer Ceramic Capacitor MLCC 50V dc ±15% X7R Dielectric Radial Through Hole, Max. Temp. +125°C	Each in a pack of 10 (2 needed)	0.31	3.10	https://uk.rs-online.com/web/p/ceramic-multilayer-capacitors/8410758/	Ceramic
Cable for sensors & LEDs	9533 - Multicore Screened Cable, Computer, EIA RS-232, Per Metre, 3 Core, 24 AWG, 0.2 mm^2, Chrome	Per metre (15 metres needed**)	1.06	15.90	http://uk.farnell.com/belden/9533/cable-9533-3core-per-m/dp/1218691	Metal / Polymer
Header for Arduino UNO connection	RS Pro, 2.54mm Pitch, 36 Way, 1 Row, Straight Pin Header, Through Hole	1	0.37	0.37	https://uk.rs-online.com/web/p/pcb-headers/2518632/	Metal / Polymer
			Subtotal:	**91.92 (ex VAT)**		

**Number depends on requirements, for example 24 are needed for making 18 sensor modules and 6 LED modules, with 6 spare.*

***Number depends on requirements. For example, 15 metres is enough for 18 sensor modules with 50 cm cable lengths, plus 6 LED modules and some spare for making a power cable.*

3.6.3 Bill of Materials – TARDIIS Electronics – Photodiode Amplifier.

Table 3-10. Bill of Materials – TARDIIS Electronics – Photodiode Amplifier.

Designator	Component	Number	Cost per unit - GBP	Total cost - GBP	Source of materials	Material type
U1	MCP6491T-E/OT - Operational Amplifier, Single, 1 Amplifier, 7.5 MHz, 6 V/µs, 2.4V to 5.5V, SOT-23, 5 Pins	18*	0.84	15.12	http://uk.farnell.com/microchip/mcp6491t-e-ot/op-amp-5-5v-7-5mhz-6v-us-5sot23/dp/2306614	Semiconductor
R1**	RC0805JR-07100ML - SMD Chip Resistor, 100 Mohm, RC Series, 150 V, Thick Film, 0805 [2012 Metric], 125 mW	18* (20 min order)	0.12	2.40	http://uk.farnell.com/yageo/rc0805jr-07100ml/res-thick-film-100m-5-0-125w-0805/dp/9236511	Metal
C1***	AVX 22pF Multilayer Ceramic Capacitor MLCC 200V dc 0805, Max. Temp. +125°C	18* (100 min order)	0.073	7.30	https://uk.rs-online.com/web/p/ceramic-multilayer-capacitors/1356624/	Ceramic
C2***	Kemet-BHC 100nF Multilayer Ceramic Capacitor MLCC 100V dc ±10% X7R Dielectric 0805 Solder, Max. Temp. +125°C	18* (100 min order)	0.06	6.00	https://uk.rs-online.com/web/p/ceramic-multilayer-capacitors/1744482/	Ceramic
PD1	SFH213 - Photodiode, 10 °, 1 nA, 850 nm, T-1 3/4 (5mm)	18* (20 - multiples of 5)	0.56	11.20	http://uk.farnell.com/osram-opto-semiconductors/sfh213/photodiode-850nm-10-t-1-3-4-5mm/dp/1212761	Semiconductor
			Subtotal:	**42.02 (ex VAT)**		

**Number depends on requirements. We recommend purchasing 50% more of these than are required by the design, as they are easy to break or lose.*

***The resistor R1 determines the gain of the amplifier. We used the 100M value listed here for a very high gain; however, the user is free to use lower resistances to achieve lower gains.*
****These capacitors are optional. We did not use them in our application. The values here are examples.*

3.6.4 Bill of Materials – TARDIIS Electronics – Sundry Items.

Table 3-11. Bill of Materials – TARDIIS Electronics – Sundry Items.

Designator	Component	Number	Cost per unit - GBP	Total cost - GBP	Source of materials	Material type
3.0 ND	3.0 OD 25mm Diameter, Reflective ND Filter Stock #43-812	1	40.38	40.38	https://www.edmundoptics.co.uk/p/30-od-25mm-diameter-reflective-nd-filter/5303/	Glass/Metal
4.0 ND	4.0 OD 25mm Dia., NIR ND Filter Stock #36-266	1	80.75	80.75	https://www.edmundoptics.co.uk/p/40-OD-25mm-Dia-NIR-ND-Filter/37226/	Glass/Metal
			Subtotal:	**121.13 (ex VAT)**		

3.7 PCB Fabrication

The PCBs used in this project were fabricated by Ragworm [7]. The price per PCB depends on its size, and the number ordered. We purchased two of the LED Control & Monitoring Shield PCBs for 31.83 GBP (one was a spare). We also purchased 50 of the Photodiode Amplifier PCBs for 39.06 GBP.

3.8 Build Instructions – Mechanical

3.8.1 Sample cell, sensor collar and mounting system

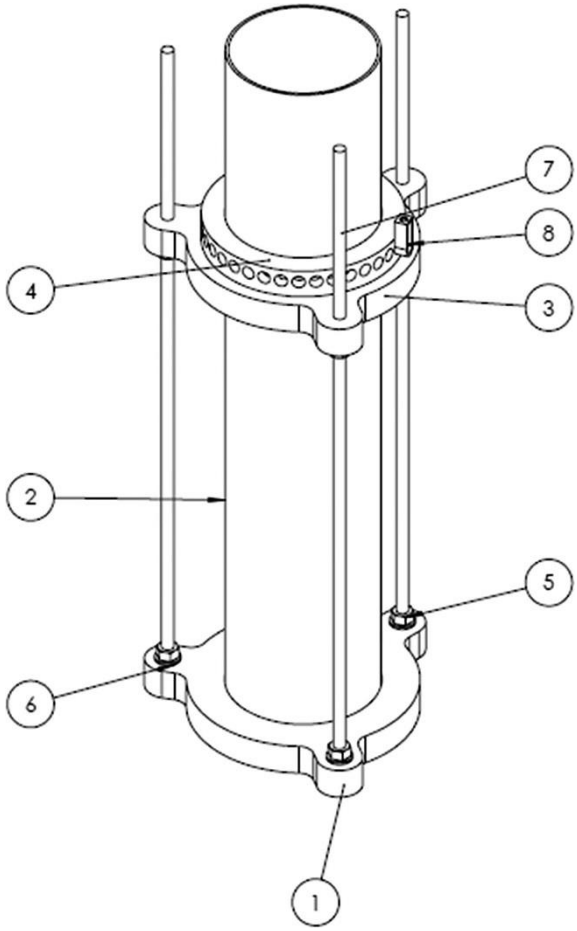

Figure 3-1. TARDIIS assembly drawing. #1) Base. #2) Tube (sample cell). #3) Sensor collar. #4) Sensor ring. #5) M8 nut. #6) M8 washer. #7) Threaded rod. #8) Amplifier housing.

The sample cell (#2) consists of an extruded acrylic tube (#2a) 491mm in length, with an internal diameter of 93mm, and an external diameter of 100mm. An acrylic disc (#2b) is glued (#2c) to one end of the tube to close it and form the watertight bottom of the sample cell. The sample cell then sits in the recessed base (#1) of the mounting system, surrounded by the three support columns (#7). The height of the nuts (#5 – see Figure 3-2 for positions) on the support columns can be adjusted to alter the height of the sensor collar (#3) containing the sensor ring (#4) above the base plate, which slots onto the support columns and encapsulates the circumference of the sample cell (Figure 3-1, Figure 3-2). This arrangement allows turbidity measurements to be performed at any height in the water column containing the sediment sample. The amplifier housing (#8) may contain either a photodiode amplifier PCB, or an LED.

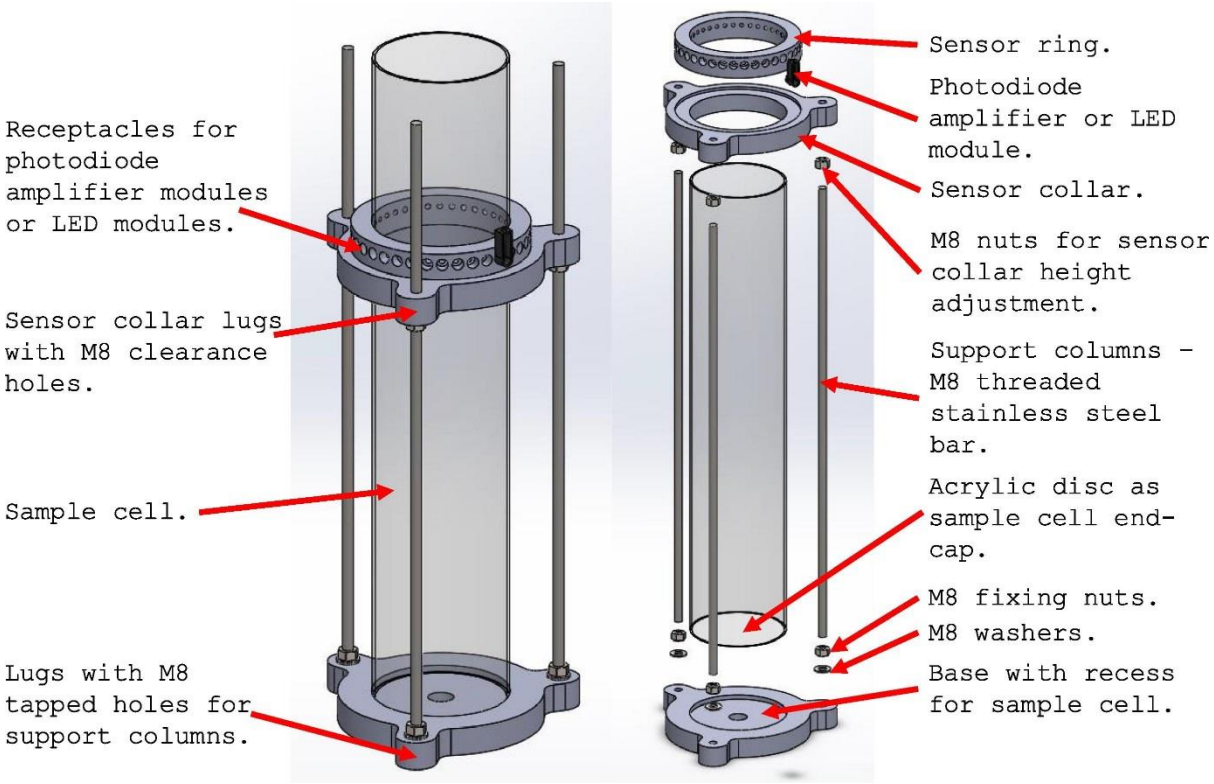

Figure 3-2. TARDIIS instrument assembly (left) and exploded view (right) showing the mounting system with support columns for the sensor collar containing the sensor ring.

3.8.2 Sample cell

The sample cell is made from an extruded acrylic tube (#2a), and has an acrylic disc glued (#2b) to one end to form the bottom of the cell. We found that the acrylic disc had a slightly larger diameter than the acrylic tube. After gluing the disc onto the tube, we had to perform some manual filing of the disc circumference to bring it flush with the tube diameter. This was necessary to allow the whole tube to fit easily through the sensor collar, thus allowing clearance for its lifting in and out of the instrument assembly without snagging on the sensor ring.

3.8.3 Sensor ring

The sensor ring (Figure 3-3) fits over the outer diameter of the sample cell to facilitate the connection of LED light modules and sensor modules at any of the 36 receptacle positions around the circumference of the ring, at 10° intervals. The receptacle positions each consist of an 8.7mm diameter hole in the outer surface of the ring, bored to a depth of 10mm. This hole allows a 3D-printed sensor housing (which could contain either a photodiode amplifier or an LED) to be slotted in and held in place by an interference fit. A second concentric hole of 3mm diameter then penetrates through the remaining thickness of the sensor ring wall and breaks through to the inner surface of the sensor ring, to form a collimated light path. This collimator hole helps to

eliminate stray light when a sensor module is connected, and provides a consistent angle of maximum beam divergence for any given type of LED utilized as a light source.

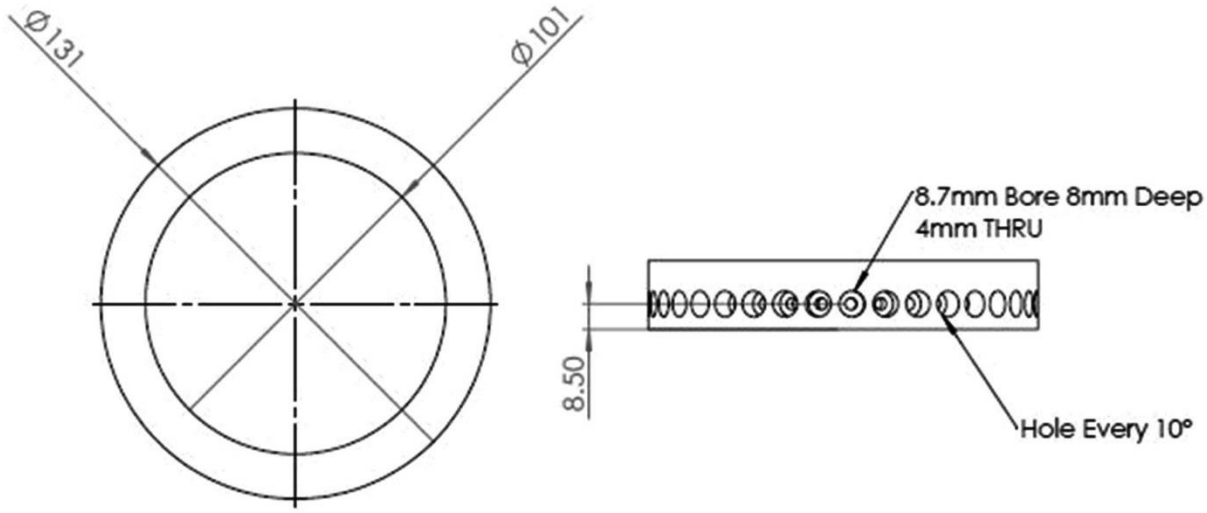

Figure 3-3. Sensor ring drawings.

The sensor ring was machined from waste nylon plastic (Figure 3-4), and the sensor collar into which it fits was made from waste PVC, although both parts could be made from the same stock. Alternative materials could be used to create these parts, e.g. wood or MDF, or any suitably rigid and machineable material.

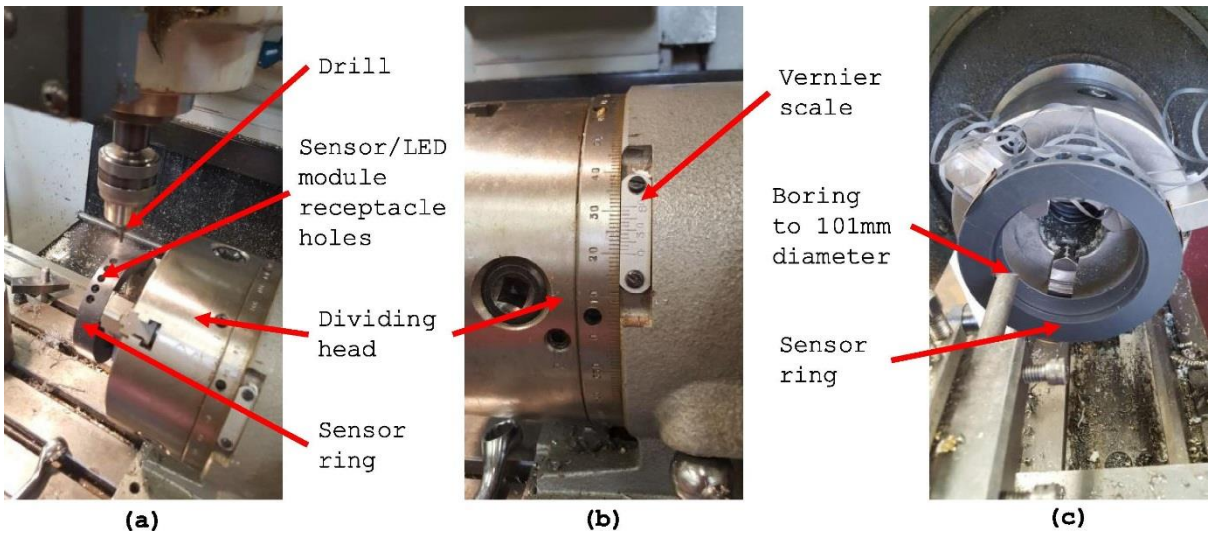

Figure 3-4. a) Drilling of sensor/LED module receptacle holes in the sensor ring, shown mounted in a dividing head to produce a regular separation angle of 10°. Centre drilled through at 4mm diameter (inner collimator hole), and then counter bored at 8.7mm diameter to 8mm depth (module receptacle hole). b) The Vernier scale on the dividing head showing the setting required to

achieve the 10° separation angle. c) The boring of the internal diameter of the sensor ring to 101mm so that it will fit over the 100mm outer diameter of the sample cell.

3.8.4 Sensor collar

The sensor collar (Figure 3-5) has lugs with M8 clearance holes that allow it to slot onto the support columns of the main assembly, thus allowing the sensor ring to encircle the sample cell when contained by the collar (Figure 3-6).

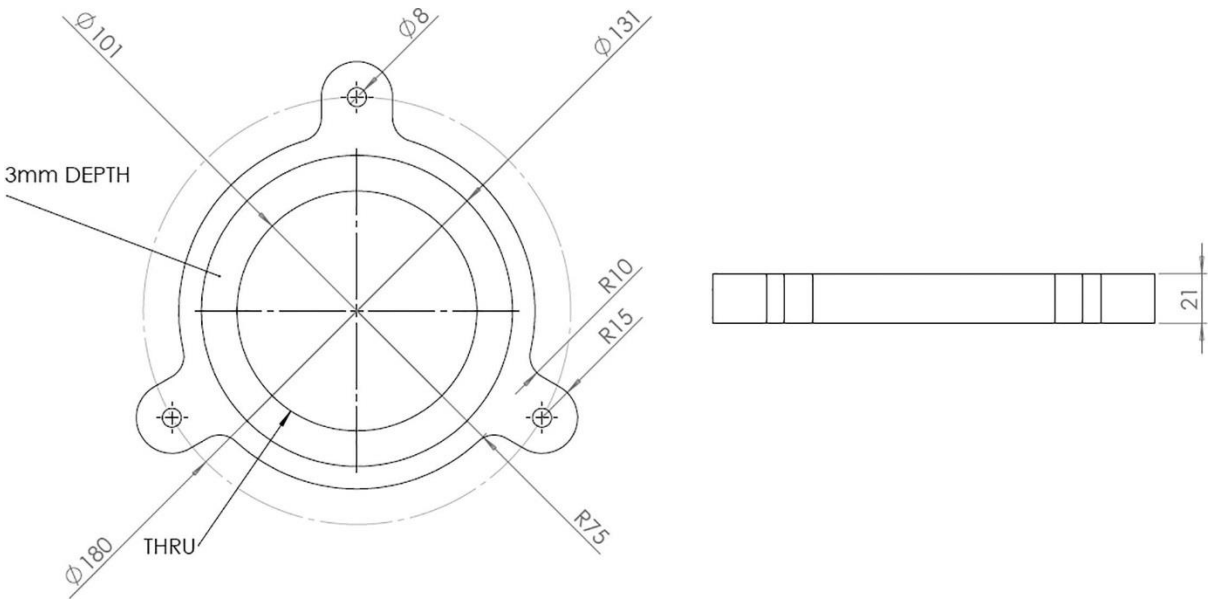

Figure 3-5. Sensor collar drawings.

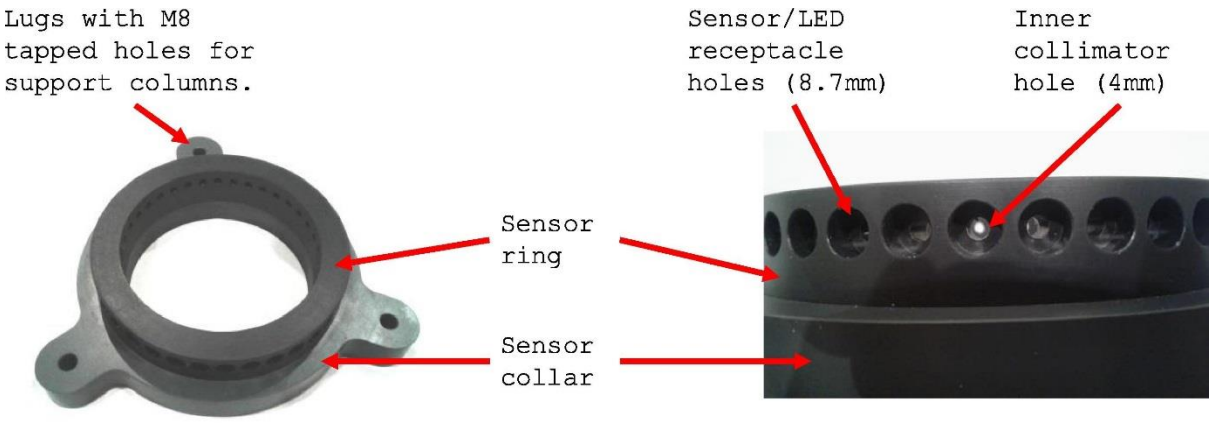

Figure 3-6. The sensor ring mounted in the sensor collar. The sensor/LED module receptacle holes (8.7mm diameter) are shown along with the concentric 4mm diameter inner collimator holes.

3.8.5 Base

The base (Figure 3-7) has lugs with M8 threaded holes that allow the support columns to be screwed in and then locked in place with M8 nuts and washers. A 5 mm deep recess allows for sample cell lateral retention at the bottom end.

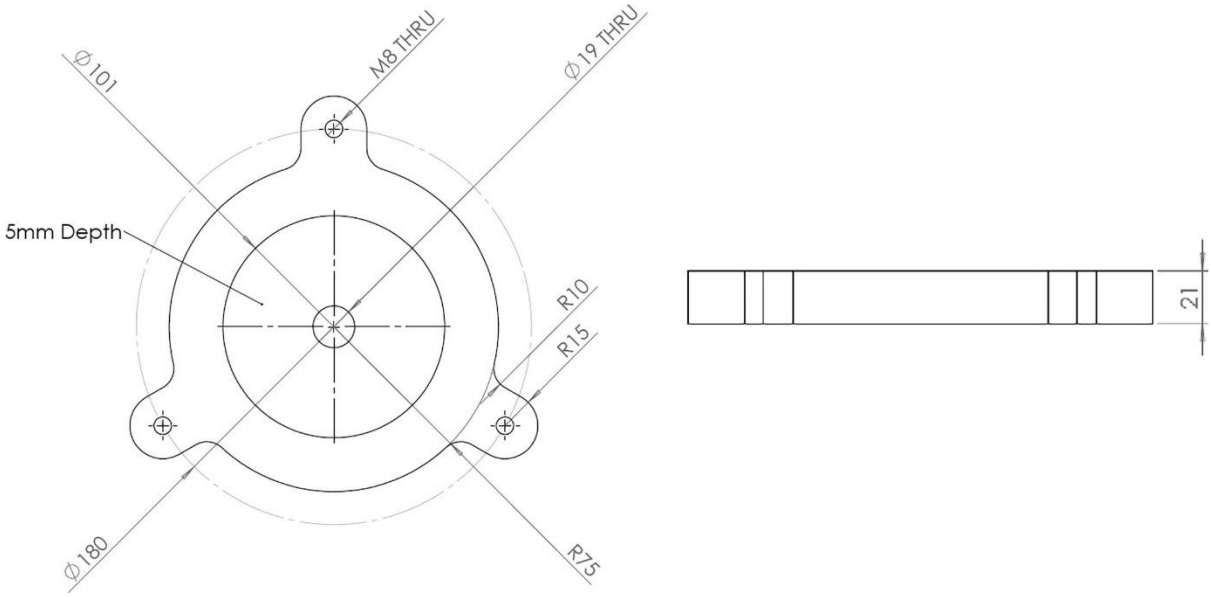

Figure 3-7. Base drawings.

3.8.6 Sensor and LED modules

The small form-factor of the sensor/LED housing measuring only 27.5 x 10.5 x 13.5 mm, as shown in Figure 3-8.

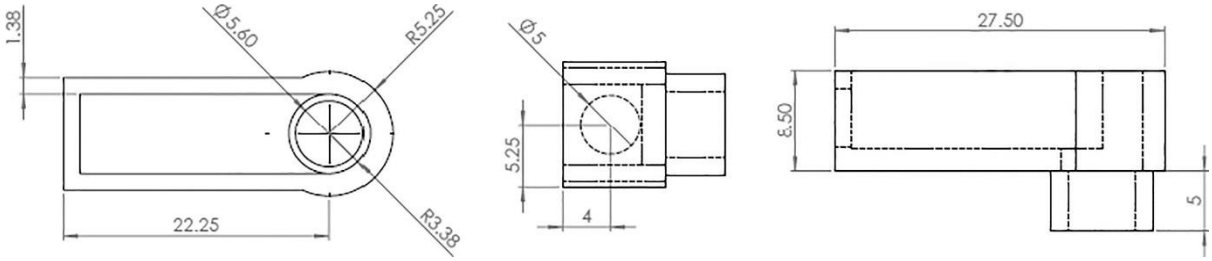

Figure 3-8. Sensor or LED module housing drawings.

The sensor module consists of the photodiode amplifier board and a plastic housing for it, which was designed using OpenSCAD [8] and printed on a Makerbot 3D printer from PLA plastic (Figure 3-9). As the photodiode amplifier utilises an SFH213 photodiode in a standard 5mm package, the same plastic module can be used to house an LED with the same standard 5mm package.

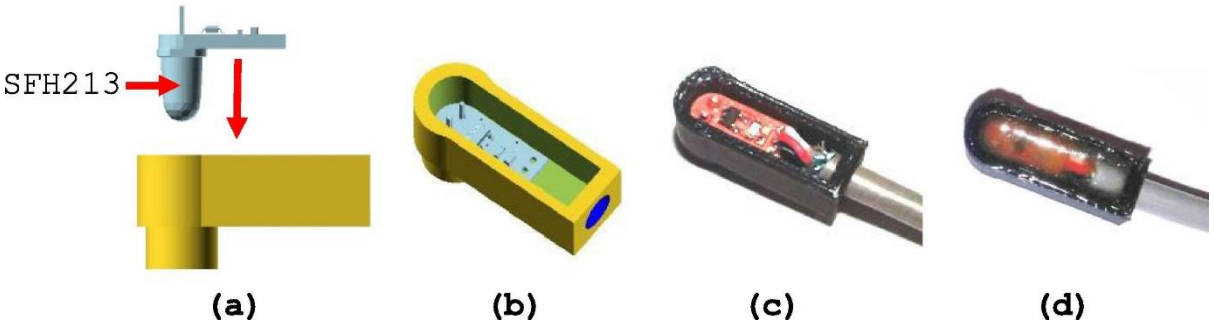

Figure 3-9. a) CAD model showing the photodiode amplifier PCB insertion into the module housing. b) A CAD model of the PCB located in the housing. c) The actual photodiode amplifier located in the 3D-printed module housing with cable attached. d) The module potted with epoxy resin.

3.8.7 Photodiode calibrator and ND filters

The principle of operation of the optical calibrator is the measurement of the attenuation of a light source by the placing of an optical neutral density filter (ND filter) between the light source (LED module) and the detector (sensor module), as in Figure 3-10. It is worth noting that the filter number *ND* is synonymous with absorbance, *A* (see Kitchener et al., p.628 for an explanation of absorbance [1]).

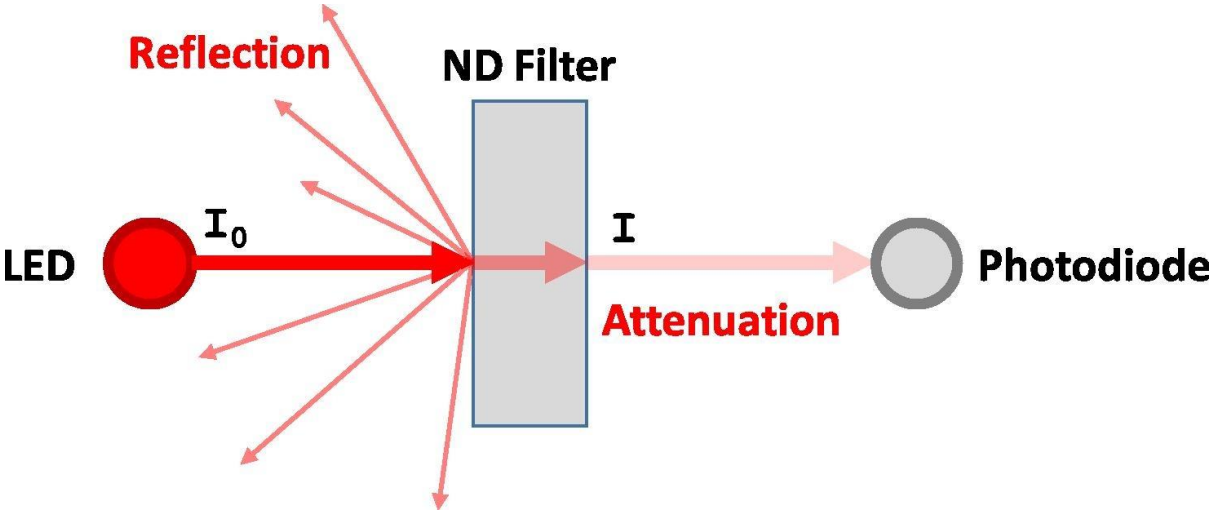

Figure 3-10. Attenuation of incident beam I_0 *by ND filter to give transmitted beam* I.

The percentage of light transmitted by an ND filter is *T*:

$$\frac{I}{I_0} = T(\%) = 10^{-ND} \times 100 \qquad 3\text{-}1$$

For example, a 3.0 ND filter will transmit 0.1% of the incident light, whereas a 0.3 ND filter will transmit 50.12% of the incident light. The transmission formula in terms of the ND filter number is:

$$ND = -\log\frac{T(\%)}{100} \qquad 3\text{-}2$$

The photograph in Figure 3-11 demonstrates the logarithmic nature of the relationship between percent transmission and ND filter number.

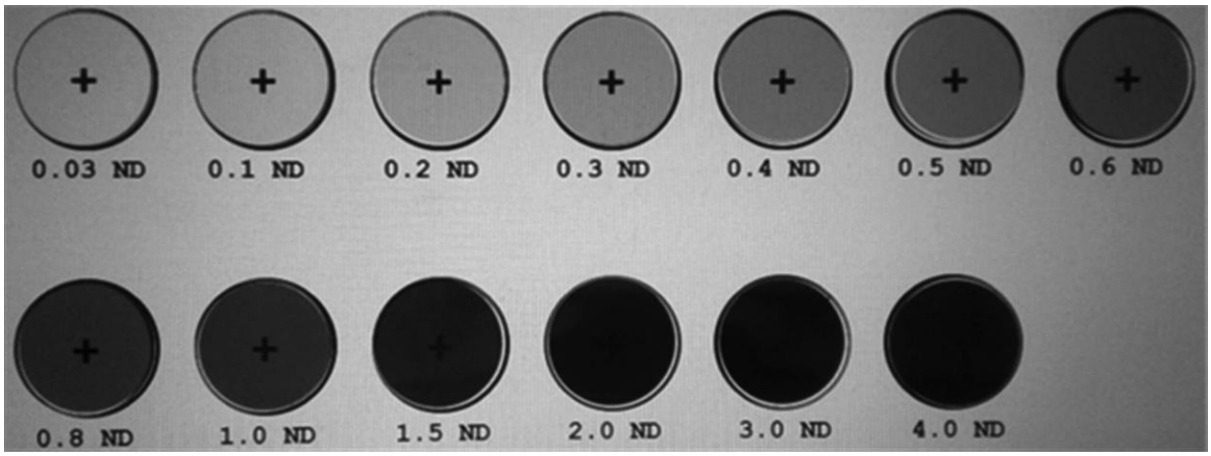

Figure 3-11. Neutral density (ND) filters placed on the horizontally oriented monitor of a laptop PC. The 25mm ND filters attenuate the light from the PC screen.

3.8.8 Photodiode calibrator design

The photodiode calibrator consists of two different parts, designed to be printed separately on a filament type 3D printer. Part 1 (Figure 3-12) is a receptacle for a photodiode/LED module. Two of these parts form the ends of the calibrator. Sandwiched between them is part 2 (Figure 3-13). This section forms the housing for an ND filter.

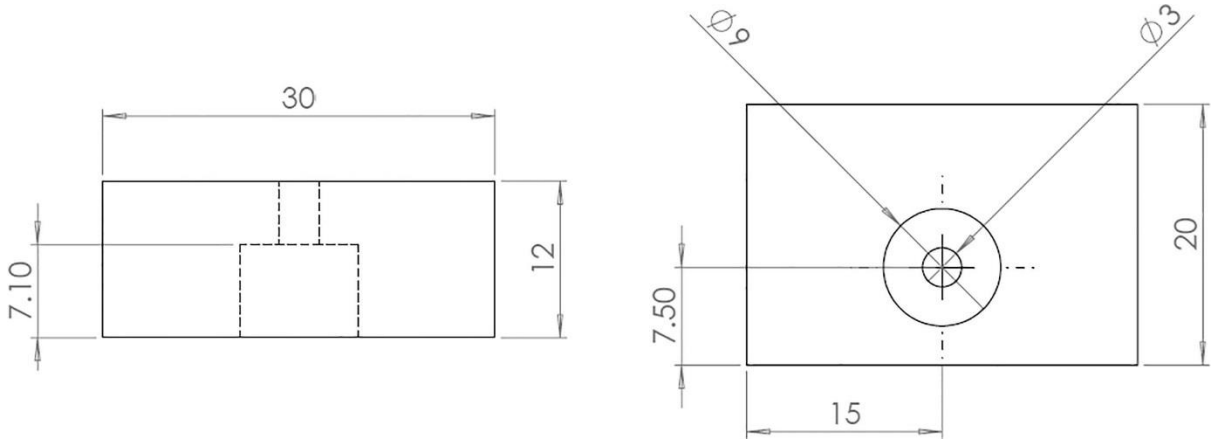

Figure 3-12. Photodiode calibrator part 1 – module receptacle.

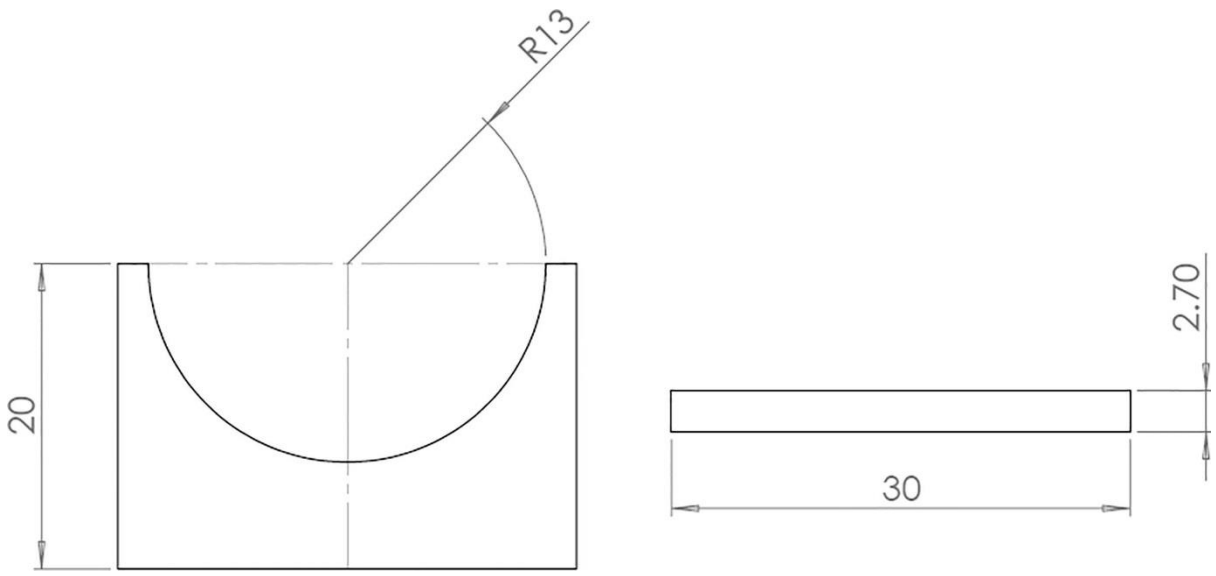

Figure 3-13. Photodiode calibrator part 2 – ND filter housing.

The optical calibrator model was produced using OpenSCAD [8], and printed by a Makerbot 3D printer from PLA plastic filament (Figure 3-14). The orientation of part 1 (2 off) and part 2 (1 off) as shown in Figure 3-14(a) is flat. This is to optimize the dimensional precision in the 3D printing of the holes and circular sections.

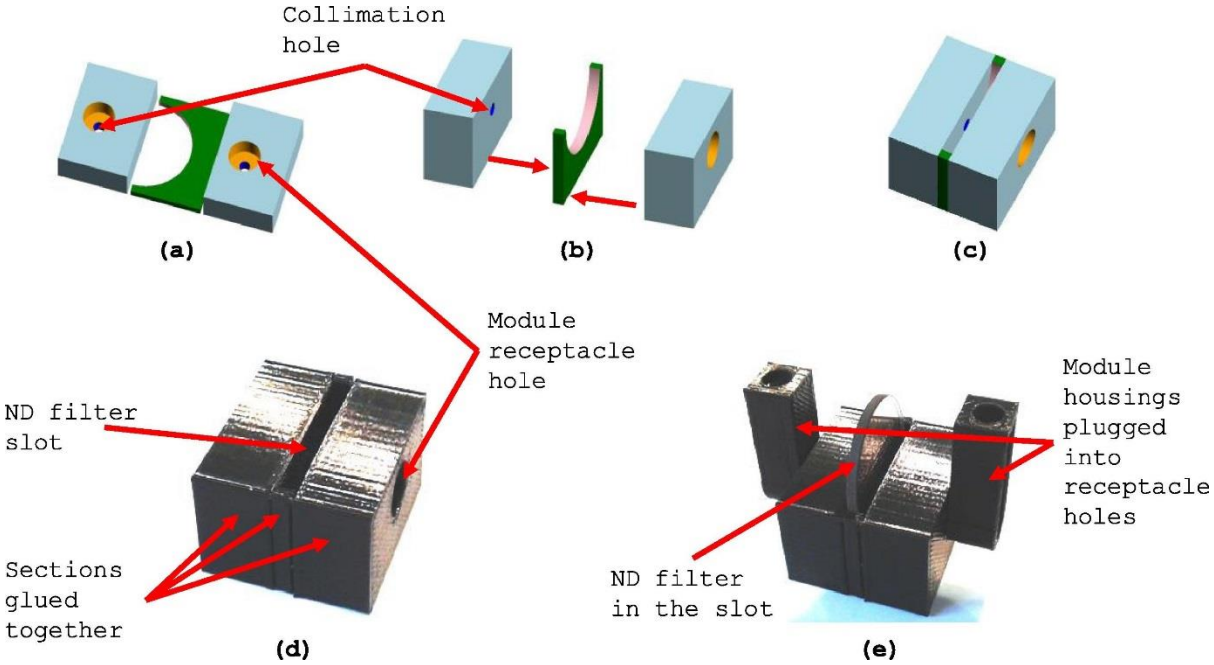

Figure 3-14. The optical calibrator. a) CAD model optimised for printing of individual sections on a plastic filament extruding 3D printer. b) CAD model showing the assembly of the separate parts for gluing together. c) CAD model of the assembled unit. d) Photograph of the glued-together optical calibrator unit, showing slot for ND filter insertion and the hole for the LED or sensor module. e) The optical calibrator with two modules plugged in (notionally one LED module and one sensor module), and a 25mm ND filter located in the slot.

3.9 Build Instructions – Electronics & Firmware

3.9.1 Active LED control and current monitoring system

In order to perform precise measurements of optical attenuation using light detectors to measure the transmitted light intensity through a sample, it is first necessary to know precisely the intensity of the LED light source, since the optical transmittance T through a sample is equal to the ratio of the measured light intensity I to the incident light intensity I_0. An instantaneous value for I_0 can be derived from a measurement of the current passing through the LED. The light intensity can then be determined from the luminous intensity vs. forward current graph on the appropriate LED data sheet. This instantaneous current value is required as the current passing through the LED will drift over time due to thermal effects in the control circuit. A simple circuit based around a ubiquitous LM317 voltage regulator with a digitally controllable feedback section has been designed (Figure 3-6) to allow the user to select a desirable LED current, which the circuit will then attempt to establish and maintain over time. Digital control of the active elements in the feedback section is provided by an Arduino UNO microcontroller board running a simple

active control algorithm. These active elements are two digital potentiometers (DIGPOTs) and an analogue to digital converter (ADC). The user can communicate with the Arduino UNO via USB to send commands, e.g. the desired current (set-point). The instantaneous LED current measurement can also be polled repeatedly by the user interface, for use in light transmittance calculations.

3.9.2 Conceptual circuit diagram

The diagram in Figure 3-15 illustrates the architecture of the active LED control and current monitoring system, which comprises a control algorithm (Figure 3-16) and an electronic circuit (Figure 3-17). This circuit is implemented as a "shield" PCB for the Arduino UNO (Figure 3-18), where "shield" refers to a secondary "daughter" PCB that can be stacked on top of the "parent" Arduino board and electrically connected by means of SIL headers.

Control of the feedback to the voltage regulator is achieved by the adjustment of two feedback resistors connected in parallel. These feedback resistors are digital potentiometers designated W0 and W1. Each potentiometer wiper can be digitally set to one of 256 discreet values, where the value 0 notionally represents zero resistance, and the value 255 indicates maximum resistance (5KΩ in this case). This scale provides a resistance resolution of $5000/256 = 19.53\Omega$ per step. By fixing the value of one potentiometer (W0, or "fine adjust") and then searching for the optimum value of the second potentiometer (W1, or "coarse adjust"), it is possible to achieve the desired set-point current. When the LED current is close to the set point, the control algorithm (Figure 3-16) maintains the current level and compensates for drift continuously (for example see Figure 3-20). This level of control can be difficult at low currents, i.e. below 1mA, due to potentiometer resolution limits, or the presence of protective Zener diodes in the LED package. In addition, the forward-voltage to current characteristics of the LED can have a steep gradient in this region (especially so where infrared LEDs are concerned). The minimum load threshold of the voltage regulator is 3.5 mA, and so operating at load currents below this level is outside the specification of the device, adding to the unpredictability of current control in this low current range (Figure 3-20), an effect that is further confounded by the increased dominance of voltage measurement noise in this region. However, for most turbidity measurements this effect will not be problematic, as a higher LED intensity would be more desirable for suspended sediment experiments. It will present some small challenges with respect to sensor calibration, however, as low light intensities are useful for the calibration of the high-gain sensors utilised in this application. An obvious solution to the problem of generating a calibration curve at low light levels is to ramp the LED current from a high intensity level to a low intensity level with a high-value ND filter between the LED and the photodiode. We have found that a 3.0 ND filter is ideal

for determining the full measurement range of the photodiode amplifier (4.0 ND for λ = 940 nm) whilst keeping the LED at a well-controlled intensity.

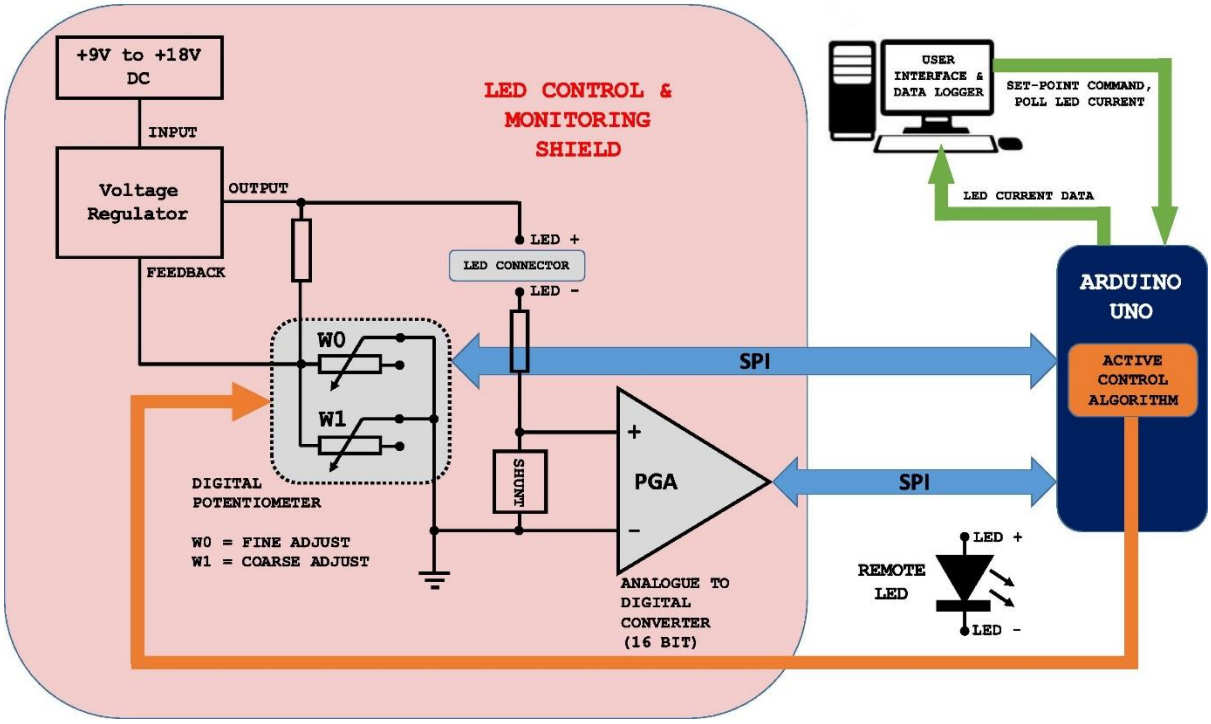

Figure 3-15. Conceptual circuit diagram of the LED control system. SPI is the serial peripheral interface for two-way communication between the Arduino UNO and the two chips (the DIGPOT chip and the ADC chip). W0 and W1 are the two potentiometer-wiper positions, controlled digitally via the SPI interface with the Arduino UNO. PGA is the programmable gain amplifier built into the front end of the ADC chip. The box labelled "SHUNT" is the shunt resistor across which the ADC measures a voltage drop. The active control algorithm converts the measured voltage into the LED current measurement.

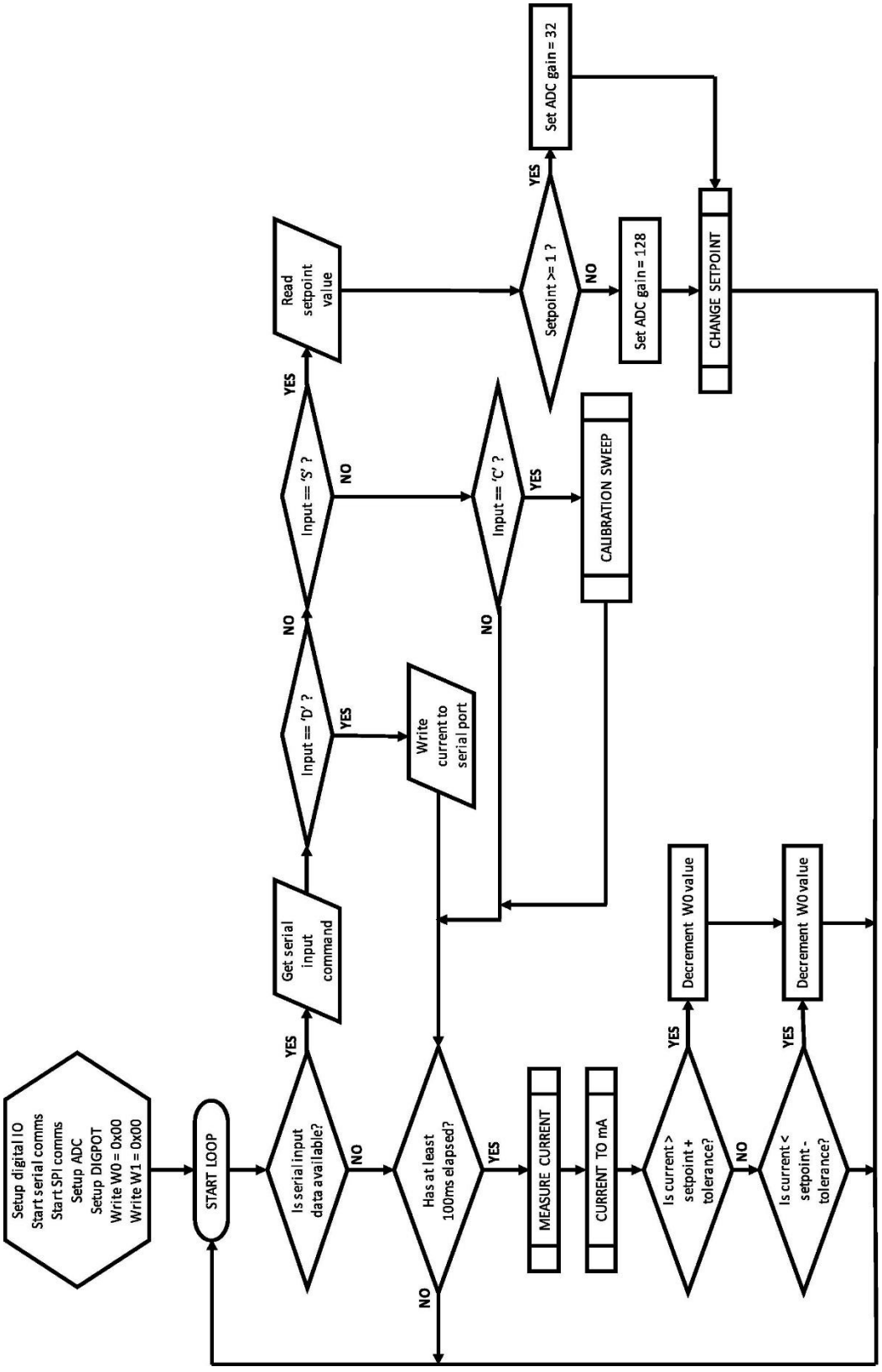

Figure 3-16. LED Control algorithm flowchart for Arduino UNO. Shows setup operations and main loop.

3.9.3 Circuit schematic

The components used for the LED control and monitoring shield were chosen primarily for ease of assembly, i.e. no surface mount devices (SMDs), only dual-in-line (DIP) package integrated circuits (ICs) and through-hole passive components were chosen. The voltage regulator is an adjustable LM317P [9] in a TO-220FP package, which can be operated from a DC differential input voltage of up to 40V. The suggested input voltage range for this application is +9V to +18V with respect to a common ground, as these voltages can notionally be provided by one or two 9V batteries connected in series (if portability is required). However, for development and testing purposes a bench power supply was used to provide a nominal 12V input to the voltage regulator via a Molex connector (J1).

The circuit board has a second Molex connector for plugging a remote LED into the output of the voltage regulator (Figure 3-18, J2). This connector puts the LED in series with stabilisation resistor R2, and shunt resistor R3. The shunt resistor provides a ground-referenced measurement to the ADC [10]. This voltage measurement represents the feedback signal to the control algorithm on the Arduino UNO (sent via SPI bus), which can then adjust the values of the two DIGPOTs on board the MCP4261 chip [11] - also via the SPI bus - thus forming direct feedback to the voltage regulator. The MAX6225ACPA+ [12] is a precision 2.5V voltage reference and is required by the ADC for correct operation.

Figure 3-17 shows the net names of all the connections, including to the headers on the Arduino UNO (ARD1). The schematic was created using DipTrace [13], for which a 300-pin limited freeware version is available for non-commercial use.

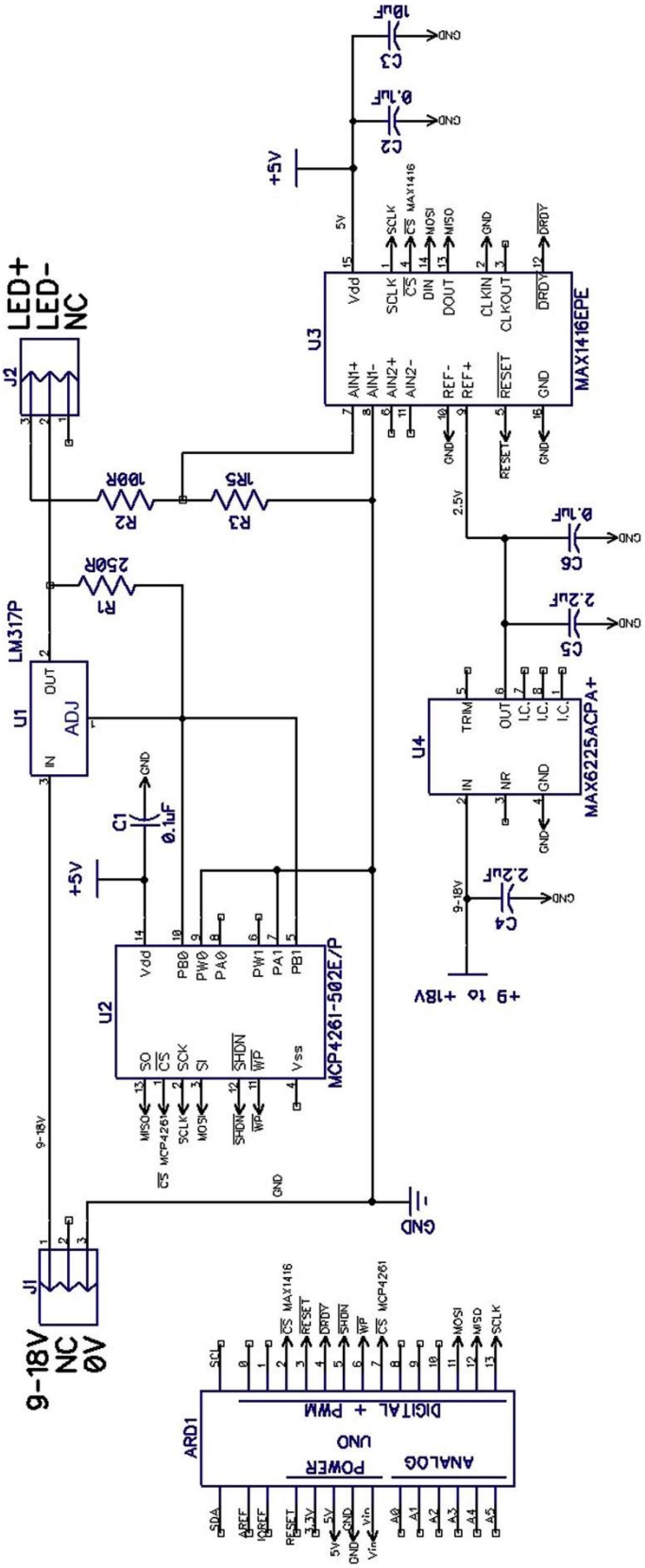

Figure 3-17. Circuit schematic of LED control and monitoring shield for Arduino UNO.

3.9.4 Arduino Uno shield PCB

The circuit described by Figure 3-17 is realized as a PCB "shield" for the Arduino Uno microcontroller board (Figure 3-18). This shield PCB is designed to have the same footprint as the Arduino Uno PCB, and stacks on top of the Arduino by means of SIL headers (2.54mm pitch), as in Figure 3-19.

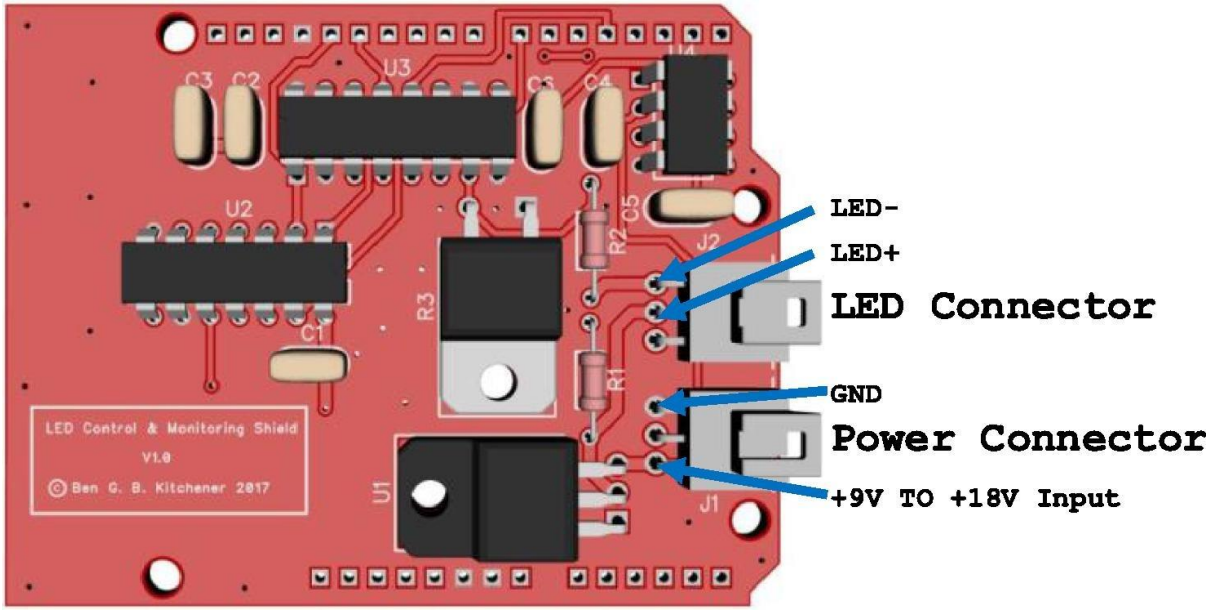

Figure 3-18. LED Control & Monitoring Shield PCB for the Arduino UNO.

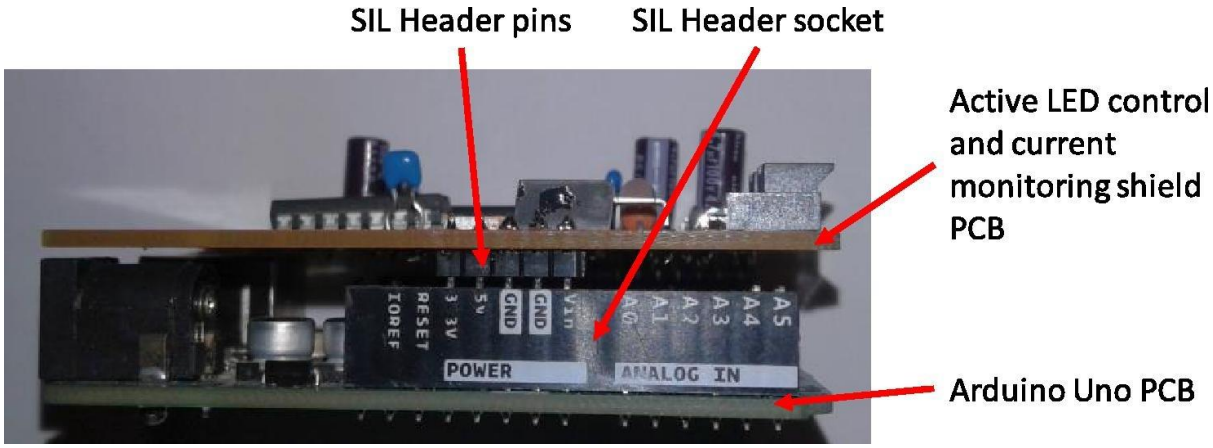

Figure 3-19. Active LED control and current monitoring shield PCB stacked on top of an Arduino Uno.

3.9.5 Photodiode amplifier design

The photodiode amplifier is a simple transimpedance amplifier that converts the photodiode current into a voltage output. It was designed to be as small as possible to fit in the constrained

space available for each of the 18 sensor positions on the outside circumference of the sensor ring. The basic design consists of the SFH213 photodiode [14], an MCP6491 operational amplifier [15], a gain resistor (R1 = 100MΩ), and two optional capacitors C1 and C2 (Figure 3-20). Given the size constraints, a surface-mount design was implemented (Figure 3-21), although a through-hole design would be preferable for ease of construction. It is however possible to solder manually the SMD components onto the PCB with a steady hand and a good pair of tweezers.

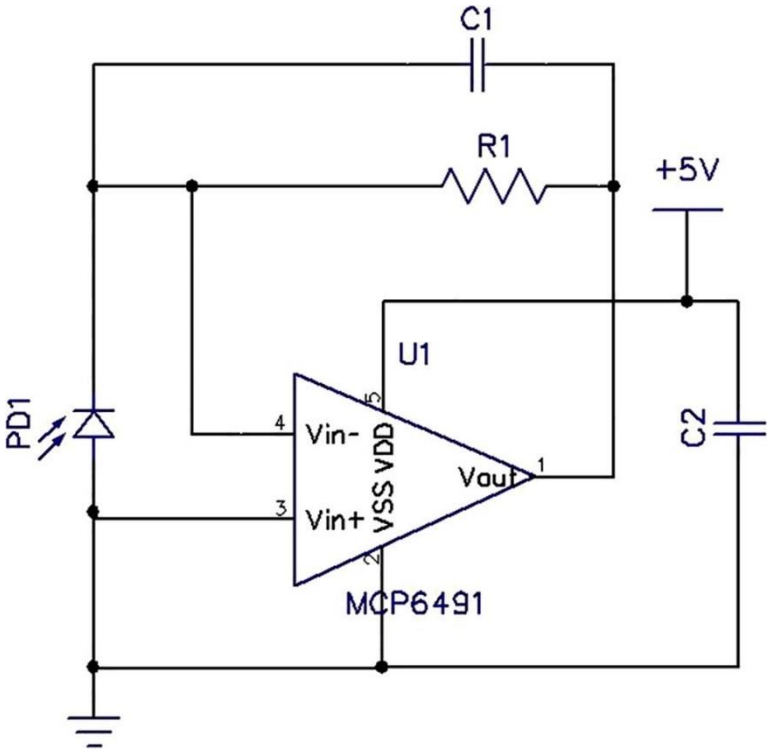

Figure 3-20. Photodiode amplifier schematic.

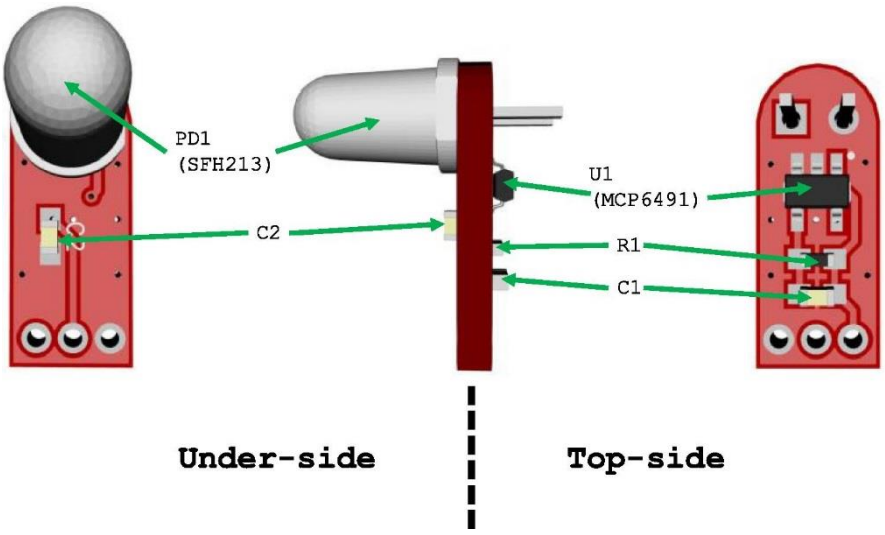

Figure 3-21. Photodiode amplifier PCB.

Solder one end of a short, screened 3-core cable (3.6.2 – Cable for sensors & LEDS) to the photodiode amplifier PCB. Solder a Molex connector (3.6.2 - Connector housing for sensors & LEDs) to the other end, and connect the LED module to the LED Control & Monitoring shield via PCB Molex connector (3.6.2 – J2), as in Figure 3-22.

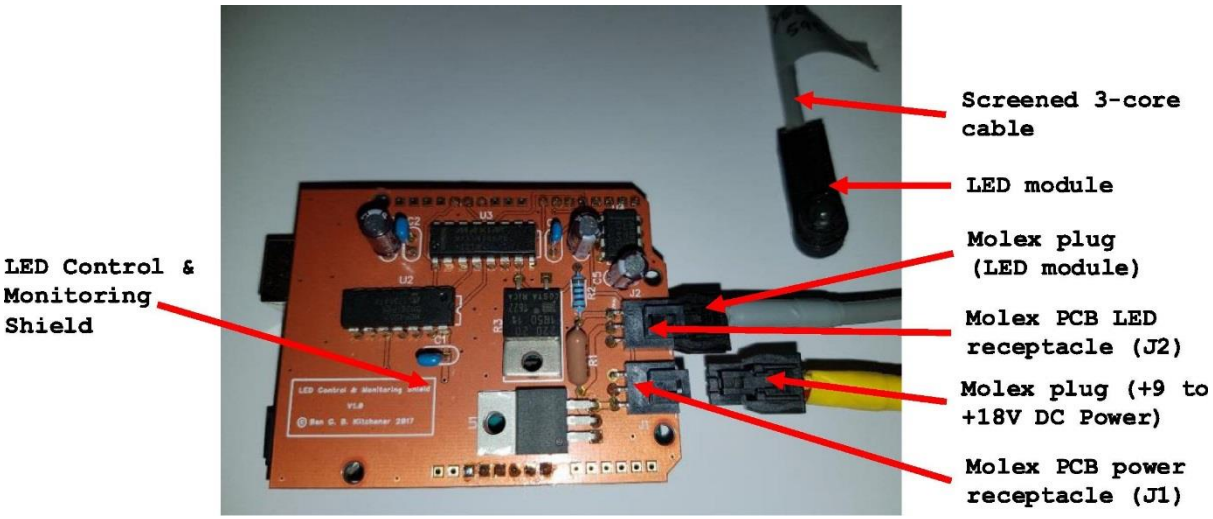

Figure 3-22. LED Control & Monitoring Shield showing LED module connection to J2, and power connection to J1.

3.10 Build Instructions – DAQ Hardware & Software Requirements

3.10.1 Sensor instrumentation and data logging requirements

The photodiode amplifier is particularly sensitive to ambient electric fields due to its high gain configuration. In this design, the amplifier is encased in plastic and potted with epoxy resin. Although this design approach is low-cost, it does not instil any degree of RFI or EMC protection into the circuit. During development, it was observed that the amplifier is particularly sensitive to the presence of ambient 50 Hz interference when a human operator places their hand in close proximity (within a few cm) to the device. The human body is a very good radiator of this background artefact of the domestic power distribution system, hence leaving the device undisturbed during operation is recommended. A countermeasure to this undesirable effect is to sample the photodiode amplifier signal at a rate of 10k samples per second (SPS), allowing for the application of a digital low-pass filter to remove 50Hz power line interference and other transients (3rd –order Butterworth infinite impulse response (IIR) filter with 1Hz cut-off frequency). We applied this approach to all 18 data channels, but only recorded the filtered data to disk at a rate of one sample per second. Also recorded at a rate of 1 SPS was the instantaneous LED current as measured by the active LED control and current monitoring system (Figure 3-23).

This measurement allows each of the 18 measured data points to be compensated for LED intensity, as inferred from the recorded LED current value.

The resolution at which the sensor voltage is measured is recommended to be less than 1 mV if possible. In some situations, the side-scattered signal from suspended sediment will lead to some very small responses in the detectors situated around the 90° position, so to see any structure in the recorded time-domain signal the best voltage resolution possible is desirable. We used a DAQ system with a voltage input range of ±10 V, and an ADC resolution of 16 bits. This system gave us a voltage measurement resolution of 0.305 mV. However, if the voltage input range of the DAQ were to be limited to 0-5 V, then the exact same voltage resolution could be achieved with only 14 bits of ADC resolution.

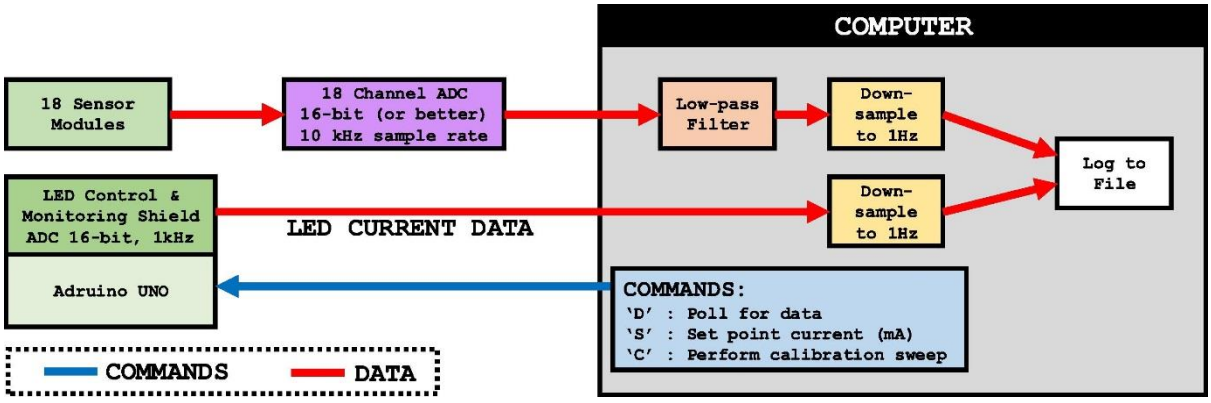

Figure 3-23. Suggested generic data-acquisition and logging arrangement.

3.10.2 User DAQ

This article does not describe a data acquisition and logging system. The operators must therefore select their own system. The data presented in this article were obtained using National Instruments (NI) DAQ equipment, and was programmed using NI LabVIEW graphical programming environment [16]. The production of a low-cost, open-source DAQ system is the subject of future work.

3.10.3 Example LabVIEW GUI

The DAQ system that we implemented using NI equipment has a LabVIEW GUI (Figure 3-24) that controls the operation of the LED Control & Monitoring system and reads the instantaneous LED current. It also logs 18 channels of data from the connected NI DAQ hardware, which was in this case 16 channels from an NI USB-6211 [17] plus 2 channels from an NI myDAQ [18].

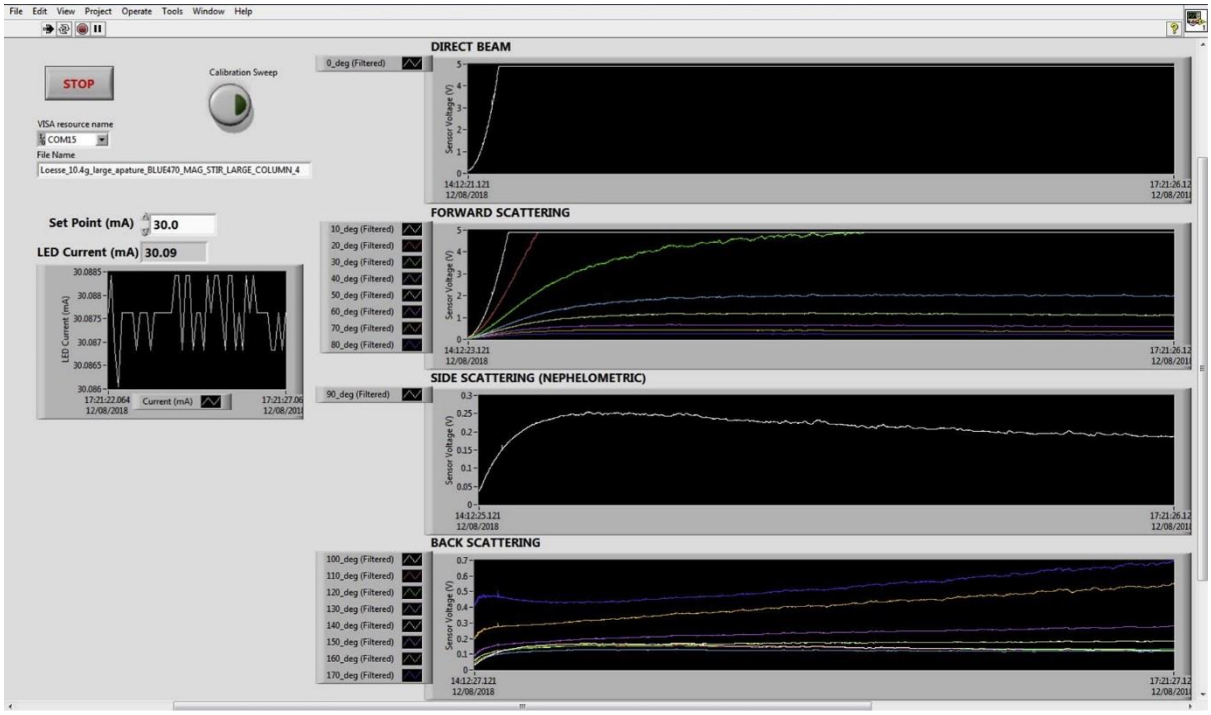

Figure 3-24. Example LabVIEW GUI for TARDIIS.

3.11 Operation Instructions – Experimental Methodology & Data Logging

3.11.1 Hazards associated with high-brightness LEDs

Warning: All LEDs that emit focused IR or UV light can be dangerous to the eyes, and UV LEDs can potentially damage the skin. Even the visible light LEDs when operated at nominal currents (e.g. 30 mA) can cause damage to the eye due to high output intensities (sometimes tens of thousands of millicandela). It is therefore recommended that anyone operating high-intensity visible, IR or UV LEDs should never look directly into the lens of the LED. This is of paramount importance where IR LEDs are concerned, as they will appear to be un-powered even when operating at nominal intensity, since IR light is not visible to the human eye. As such the human eye will have no pupil reflex with which to attenuate the incoming light, and permanent damage can be caused to the retina – including blindness. It is good practice to treat high- brightness LEDs with the same caution as one would a LASER light source.

3.11.2 Sensor calibration

The following list is a complete calibration example. The operations are to be performed in this order:

1. Connect DAQ system together, wire up all sensors etc., apply power and test all DAQ channels and functionality.

2. Choose a light source. In this example an IR LED (λ = 940 nm) has been selected [19]. Plug it into J2 on the Control & Monitoring shield.

3. Determine the relationship between LED current and output light intensity in mW sr^{-1} by extracting information from the LED data sheet. In Figure 3-25 the radiant intensity is stated in milli Watts per steradian (mW sr^{-1}). If the radiant intensity is stated in photometric units of millicandela (mcd), then the mcd value must be multiplied by the conversion factor *V(λ)* to obtain the radiometric value in mW sr^{-1} (equation 3-3). Wavelength λ is stated in nm [20], [21]:

$$V(\lambda) = 1.019e^{-285.4(0.001(\lambda-559))^2} \qquad 3\text{-}3$$

For example, a blue LED of wavelength 470 nm, *V(λ)* = 0.106264. This conversion is necessary since the candela is weighted according to the wavelength-dependent sensitivity of the human eye to light. Since photodiodes do not have this non-linear human-eye response, photometric units such as candelas (or mcd) must not be used to report the measured light intensities.

$$I_{mW\ sr^{-1}} = \frac{I_{mcd}}{V(\lambda)} \qquad 3\text{-}4$$

Using data extracted from the graph in Figure 3-25, the relationship between the applied current and the 940 nm LED light output can be stated: I_{OUT} (mW sr^{-1}) = 1.978 x I_{IN} (mA), as shown in Figure 3-26. The constant multiplier 1.978 shall be referred to as m_{LED}. So the expression for the input current to output light intensity is:

$$I_{OUT} = m_{LED} I_{IN} \qquad 3\text{-}5$$

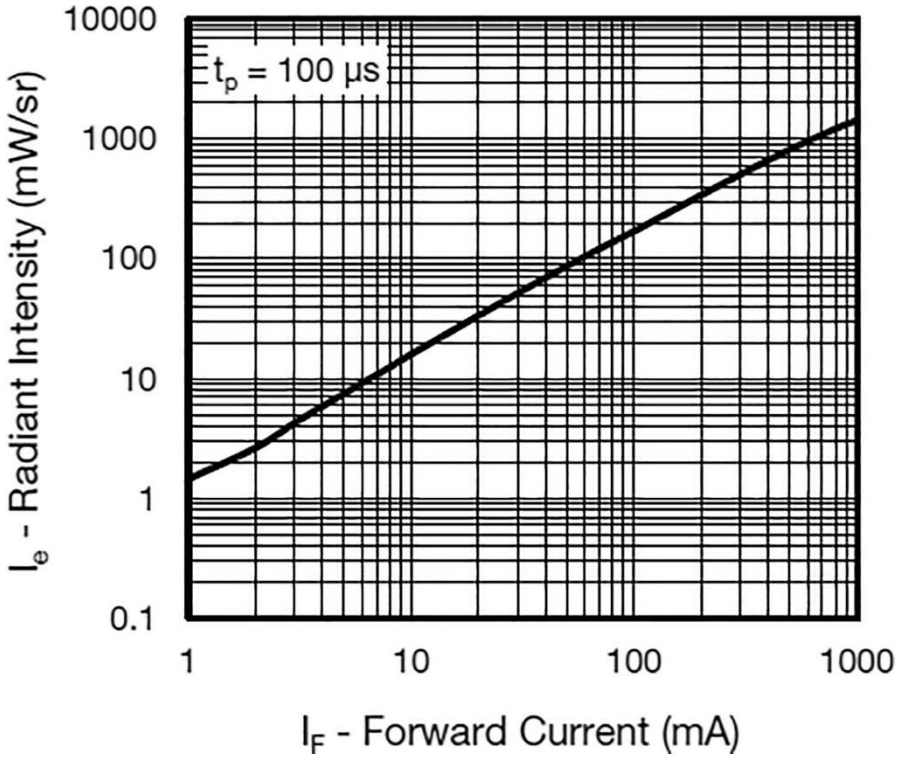

Figure 3-25. Radiant intensity vs. forward current. Extracted from Vishay TSAL6100 data sheet [19].

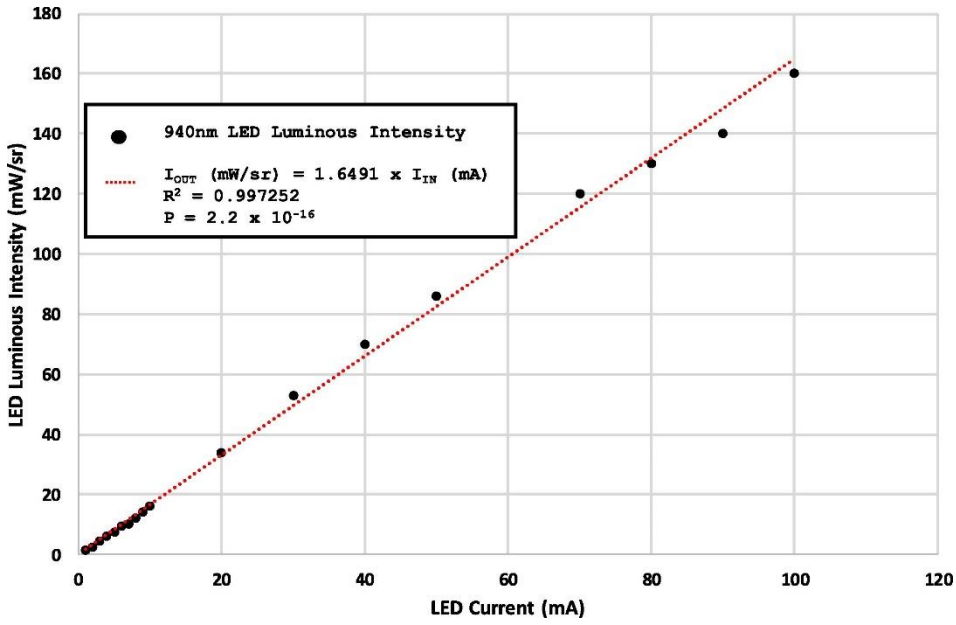

Figure 3-26. LED current input vs. light output intensity as derived from Vishay TSAL6100 data sheet [19]. The data points were extracted from the data sheet "by eye". Even so, there is a good fit

to a linear regression (R^2 = 0.9947, p = 2.2 x 10^{-16}) making the data suitable for calibration purposes.

4. Obtain a value for the transmittance through the chosen ND filter by examining the calibration graph supplied by the manufacturer and correcting for wavelength to arrive at transmission T_λ. The nominal transmittance of a 4.0 ND filter is 0.0001 (0.01%). Correcting for wavelength response at 940 nm from the manufacturer's ND calibration data, this value is modified to become T_{940nm} = 0.00038 (0.038%). Applying equation 3-2, the 4.0 ND filter value becomes 3.42 ND_{940nm}. Extending equation 3-5 to include the attenuation by the ND filter gives equation 3-6 below:

$$I_{OUT} = m_{LED} I_{IN} T_\lambda \qquad 3\text{-}6$$

5. Determine the response of each individual sensor module to the light source using the optical calibrator, and plot the relationship between sensor voltage and incident light level (mW sr^{-1}). The Arduino software has a "calibration sweep" function that performs a stepwise drop in LED current from the present set point. The current dwells at each step for one second for stabilization, thus allowing a calibration graph to be plotted. The gradient of the linear regression fit of sensor voltage S_V to the measured light intensity I_θ (θ is the scattering angle) yields the sensor calibration coefficient S_α where α is the sensor number. The measurements shown in Figure 3-27 were made with a 4.0 ND (3.42 ND_{940nm}) filter in place to attenuate the beam (otherwise the sensor output would saturate).

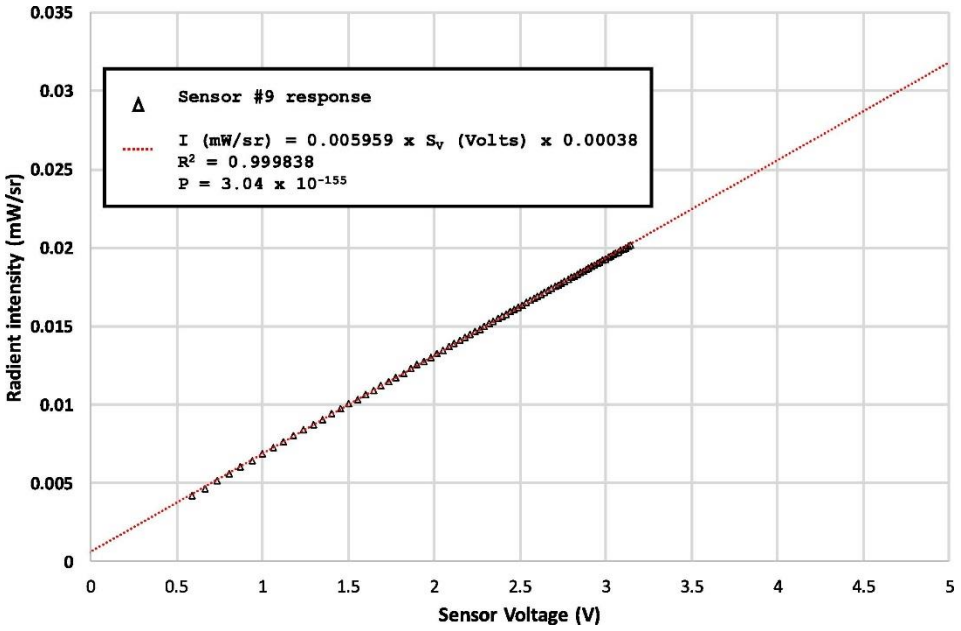

Figure 3-27. Response of sensor #9 to 940 nm light. Data generated using 'calibration sweep' function with optical calibrator and 4.0 ND filter, starting at 30mA LED current.

We now have a general calibration equation that can be applied to experimental data to give I_θ at a given scattering angle θ in mW sr^{-1}:

$$I_\theta = S_\alpha S_V \qquad 3\text{-}7$$

The calibration sweep was performed by starting at an initial LED current of 30mA and ramping the current down from there. Applying general calibration equation 3-7 we now obtain a specific calibration equation for sensor #9 at the 90° position on the sensor ring:

$$I_{90} = S_9 S_V = 0.005959 S_V \qquad 3\text{-}8$$

The I_{90} equation (3-8) will be used in the experimental measurement section.

6. With all the sensor modules in position around the sensor ring, add clean water to the sample cell (in this case tap water). Remove all ambient light (i.e. total darkness) and measure the response of all the sensor modules to the LED light source located at the 180° position. Any response measured at sensor locations from 10° to 170° are due to internal reflections within the instrument (Figure 3-28).

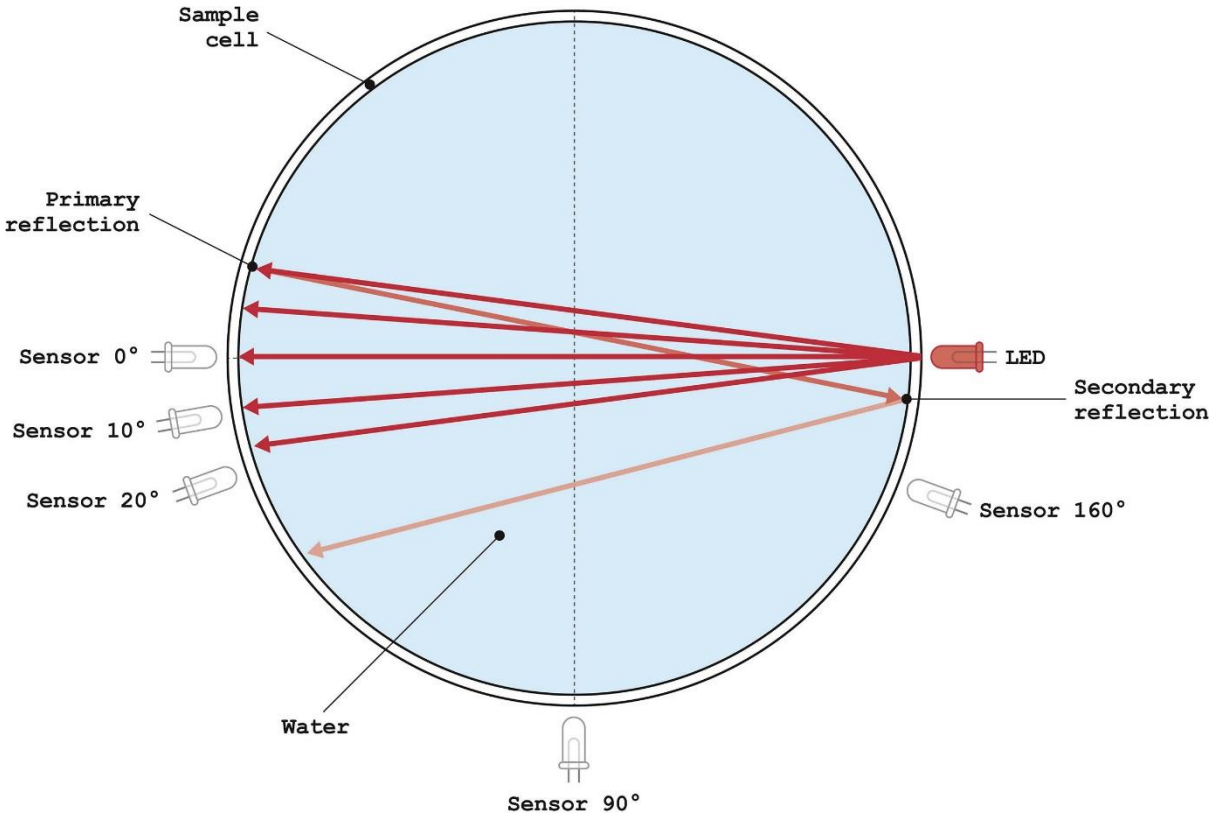

Figure 3-28. Reflections from the internal surfaces of the sample cell.

The response of the sensor at the 0° position is due to the direct beam, and is likely to cause the sensor to saturate. This effect could also be apparent at high beam intensities at the 10° and 20° positions (and other forward-angle positions), due to the divergence of the incident beam. The LED intensity can be stepped from high to low in order to generate a device geometry baseline (DGB_λ) dataset for each sensor. The "calibration sweep" function in the Arduino firmware can be used again to achieve this functionality. Figure 3-29 shows data for high (29.02 mA) and low (5.38 mA) LED intensities. Scattering angles θ_0 and θ_{10} have saturated detector responses at both intensities. The effect of the beam divergence on the forward-scattering sensors can be seen to drop off as θ approaches 90°. The effects of internal reflections can be seen to increase in the back-scattering sensors as θ approaches 170°. The sensors are numbered from 0 to 17, and are placed at corresponding θ x 10° angular positions around the sensor ring. For example, sensor #9 at 90° (Figure 3-27) is located at the θ_{90} position.

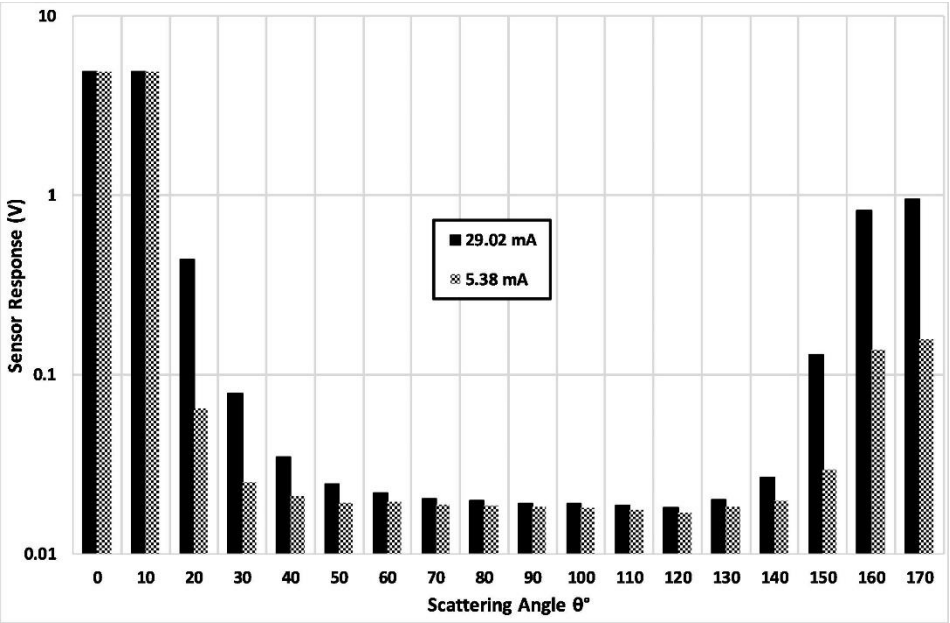

Figure 3-29. Water-only calibration of the TARDIIS sample cell, referred to as the Device Geometry Baseline (DGB_{940nm}) data set. Two LED currents are shown (29.02 mA and 5.38 mA), representing high and low LED intensities. In this example the 0° and 10° sensor responses have saturated.

3.11.3 Performing a sediment-settling experiment

1. Choose a light source. In this example a 940 nm LED (infrared) was selected, at a nominal operating current of 30 mA. The diagrams (Figure 3-30 and Figure 3-31) illustrate the experiment using blue light for clarity, since infrared light is not visible to the human eye.

2. Perform an experiment on a suspended sediment sample. The experiment design is at the discretion of the user, for example the choice of initial agitation method (e.g. stirring, dropping sediment into the water column, shaking the sample, measurement frequency, duration of experiment). The sample was stirred with a magnetic stirrer until a consistent degree of suspension was achieved. The settling experiment begins when the stirrer is switched off.

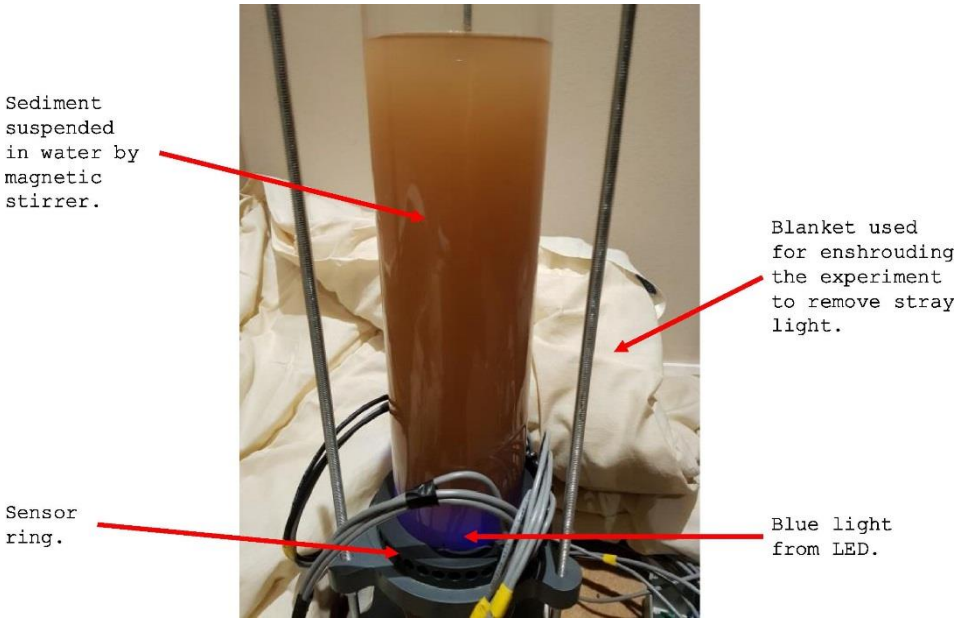

Figure 3-30. Photograph of a sediment settling experiment.

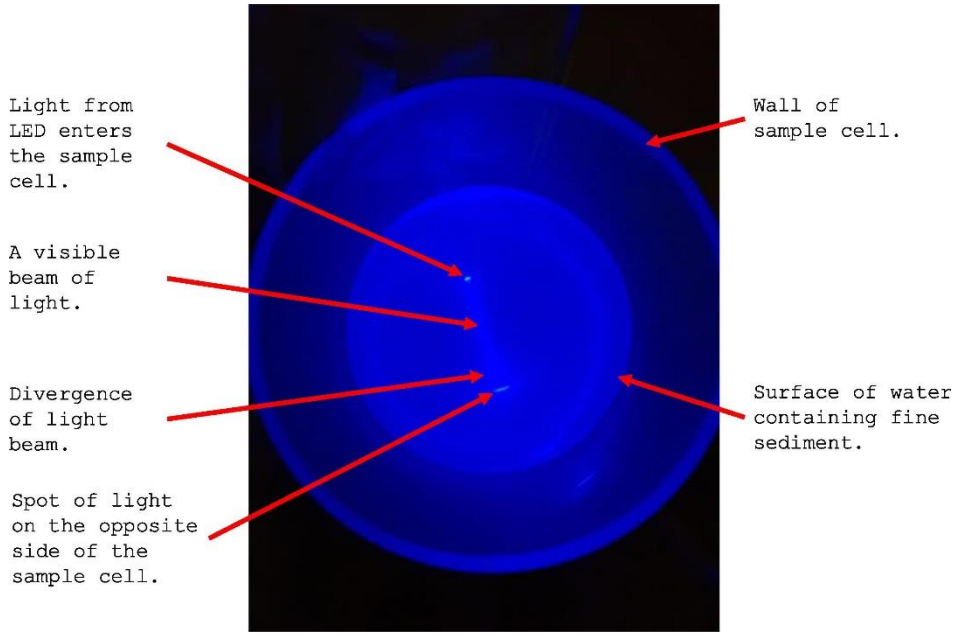

Figure 3-31. Top view of the sample cell. Side-scattering from the beam of blue light is evident, as are various reflections from the inner surface of the sample cell.

3.11.4 Preparing the data

It is important to know what events have been recorded during the experiment, and to know when the settling process begins. In our experiments, the entire process including the agitation phase is recorded. Thus, it is necessary to remove manually the beginning section of each data set in order to remove the effects of the stirring process. Also during this start-up phase, the LED is

ramping up to its set-point current, and so this initial data is not meaningful. Only when the LED is at a stable current and the stirring has stopped can the data considered to be at the *time = 0* position, t_0 (Figure 3-32).

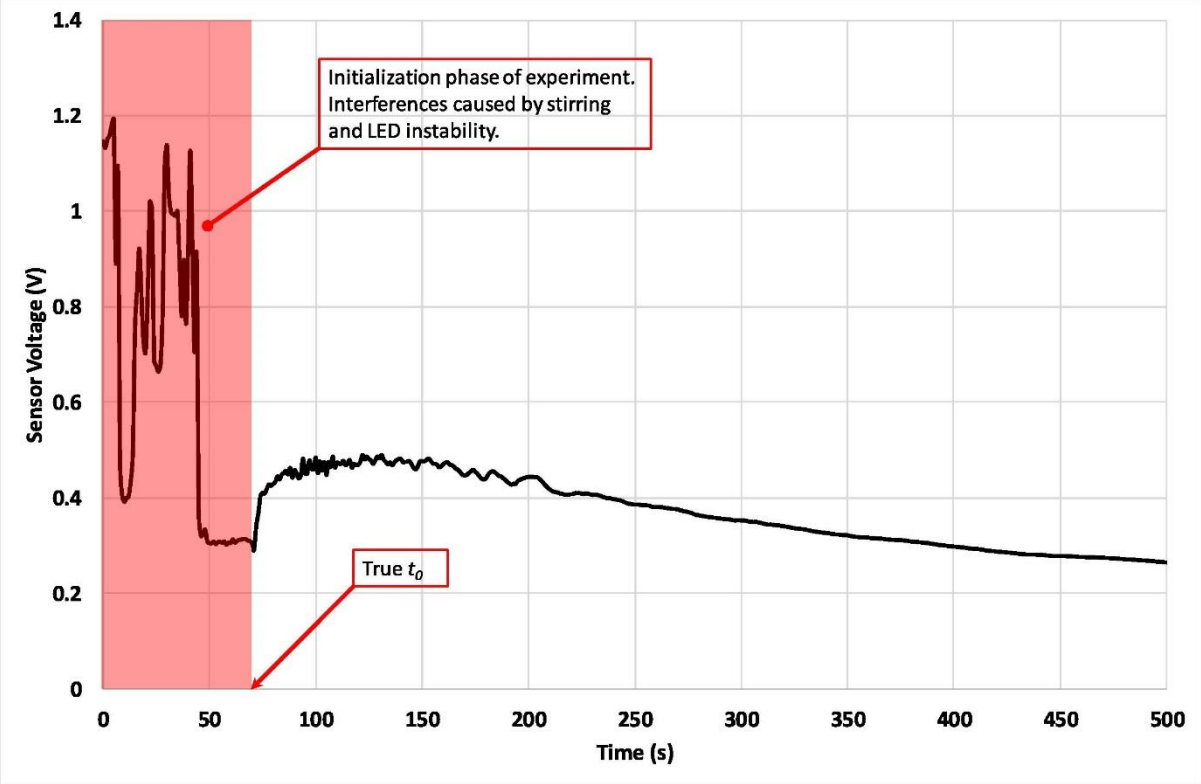

Figure 3-32. Graph showing the initialization phase of a sediment-settling experiment. λ = 940 nm, θ = 30°. The sediment used is loess, at a density of 0.5168 gl^{-1}. The hight of the water column is 426 mm and the sensor ring height is 102 mm.

3.12 Validation, characterization and modelling

TARDIIS allows the researcher to obtain a rich and diverse set of data about sediment as it settles in a column of water. These data do not however show directly the concentration of sediment at a particular height in the water column. The only way to measure *exactly* the characteristics of the sediment at different positions in the settling column and at different times during the settling process, is by physically sampling the column. Then, by the use of traditional sediment analysis methods, it is possible to determine the concentration, the PSD, the grain shapes, the degree of flocculation (DOF) and so on. The researcher must accept that there is not a well-defined link between sediment properties and turbidity in general. With this acceptance, the researcher may then challenge existing approaches to turbidity measurements, and use TARDIIS to establish new models that are based on the physics of light scattering and absorption.

3.12.1 Assessment of the active LED control and current monitoring system

The instantaneous current was measured throughout the settling experiment, thus allowing for the correction of the calculated I_0 value. The current is plotted against time (Figure 3-33) and shows that the drift in I_0 is very small – i.e. not greater than 72μA – over the 10.67 hour duration of the example experiment. There is a small amount of noise present in the signal; however, the overall degree of drift shows that the Arduino control system is performing very well, as the desired current is 30 mA in this case. There is an overall offset error of approximately 40 μA.

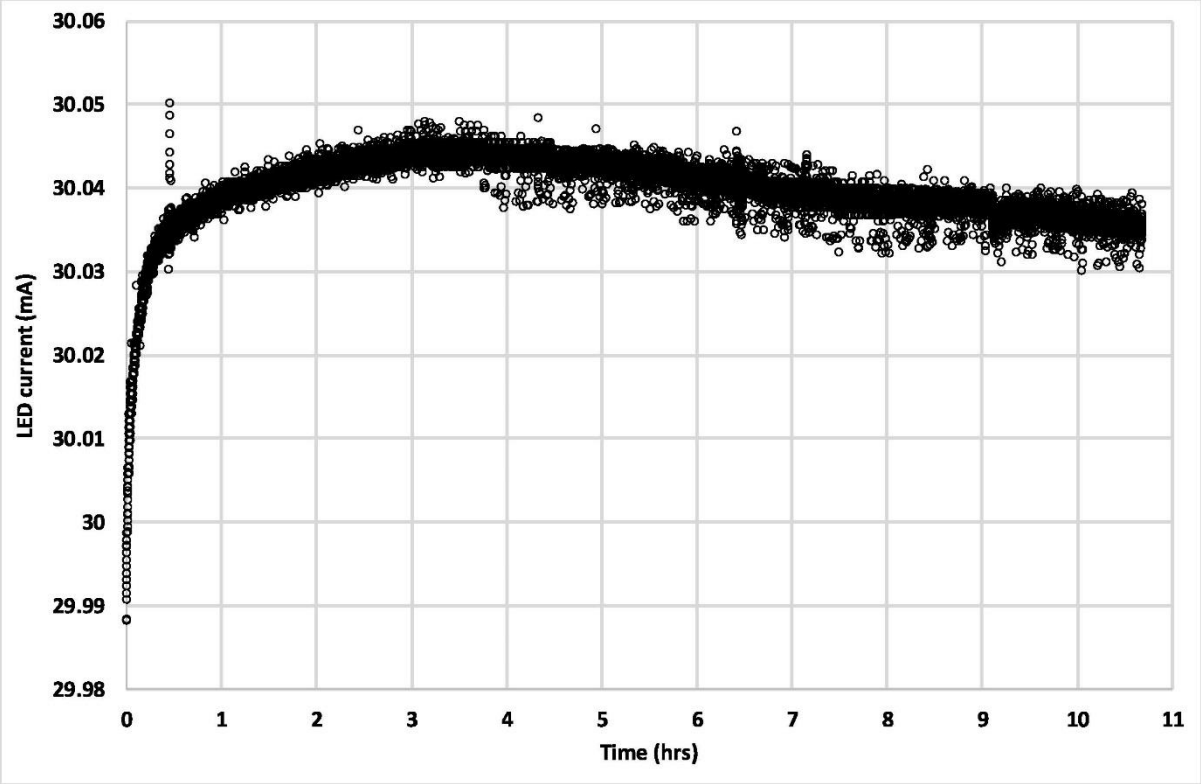

Figure 3-33. LED current drift.

3.12.2 Linearity of device geometry baseline measurements

It has been shown that the response of a specific sensor (#9) to incident light is linear (Figure 3-27) when calibrated using an ND filter. We must now check that the response function is linear when TARDIIS is operational. Using data that was collected to produce Figure 3-29, we can now show that the same linearity is present under device geometry baseline (DGB) conditions, with only water present in the sample cell. The responses of sensors #6, #9 and #12 are shown as I_{60}, I_{90} and I_{120} respectively in Figure 3-34, which confirms that the linearity is present. This DGB linearity must be tested for all sensors at all wavelengths of light that are to be used during settling experiments.

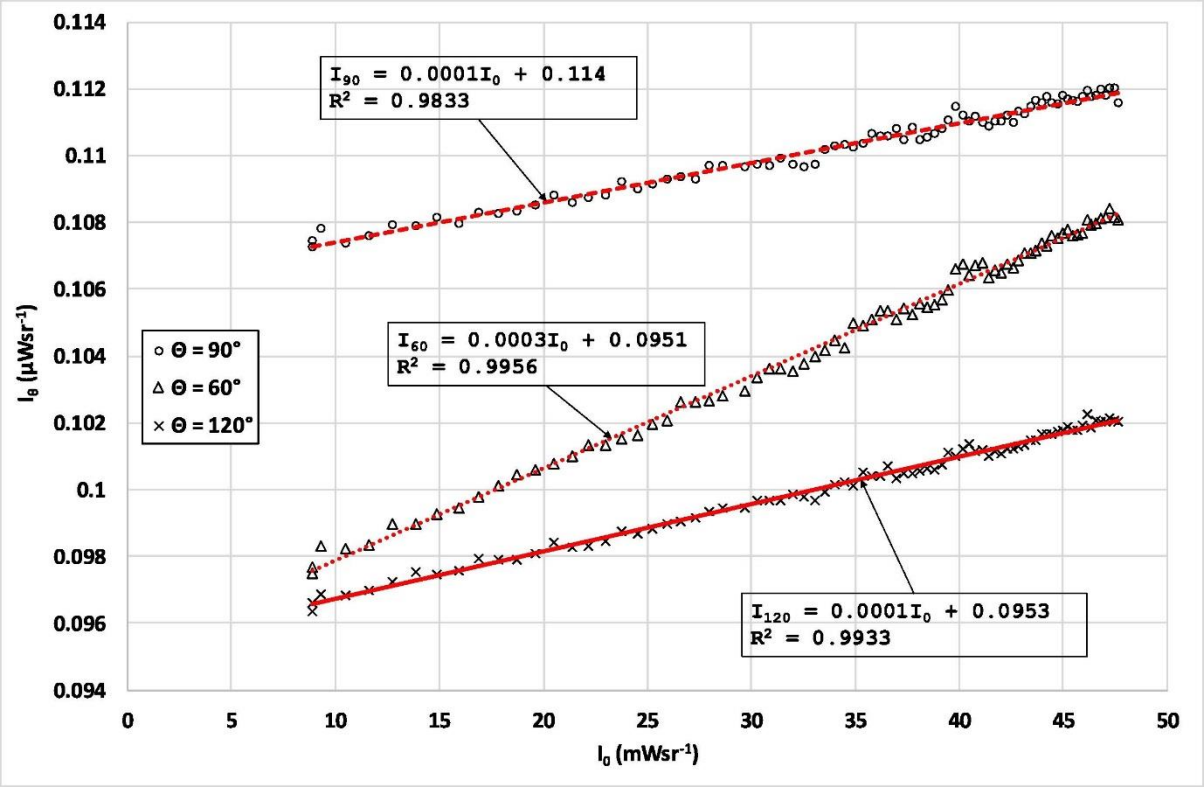

Figure 3-34. Linearity of DGB measurements I_{60}, I_{90} and I_{120}.

3.12.3 Example of sediment-settling data

The data in Figure 3-35 show the measured light intensity at three of the 18 available scattering angles during a sediment settling experiment. The initial peak that occurs at around 30 seconds into the experiment is due to turbulence in the water column after the magnetic stirrer is switched off. By analysing data gathered in this way at multiple scattering angles and wavelengths of light, the researcher may then:

- Develop models of light scattering by particles in suspension, and gain new insights into the effects of grain shape and PSD.
- Explore the impact that water colour has on turbidity measurement.
- Investigate the conditions under which the particle settling velocities deviate from Stokes Law.
- Enquire as to the suitability of the recognized turbidity standards.
- Apply new knowledge to future field measurements.

The "optical sedigraphs" shown in Figure 3-35 look as if they may be giving an indication of Stokes-like settling behaviour. In order to explore this possibility, the researcher must design their experiments carefully, and then develop suitable numerical models to make predictions

based on empirical data obtained using TARDIIS. This detailed analysis and model development is however beyond the scope of this article.

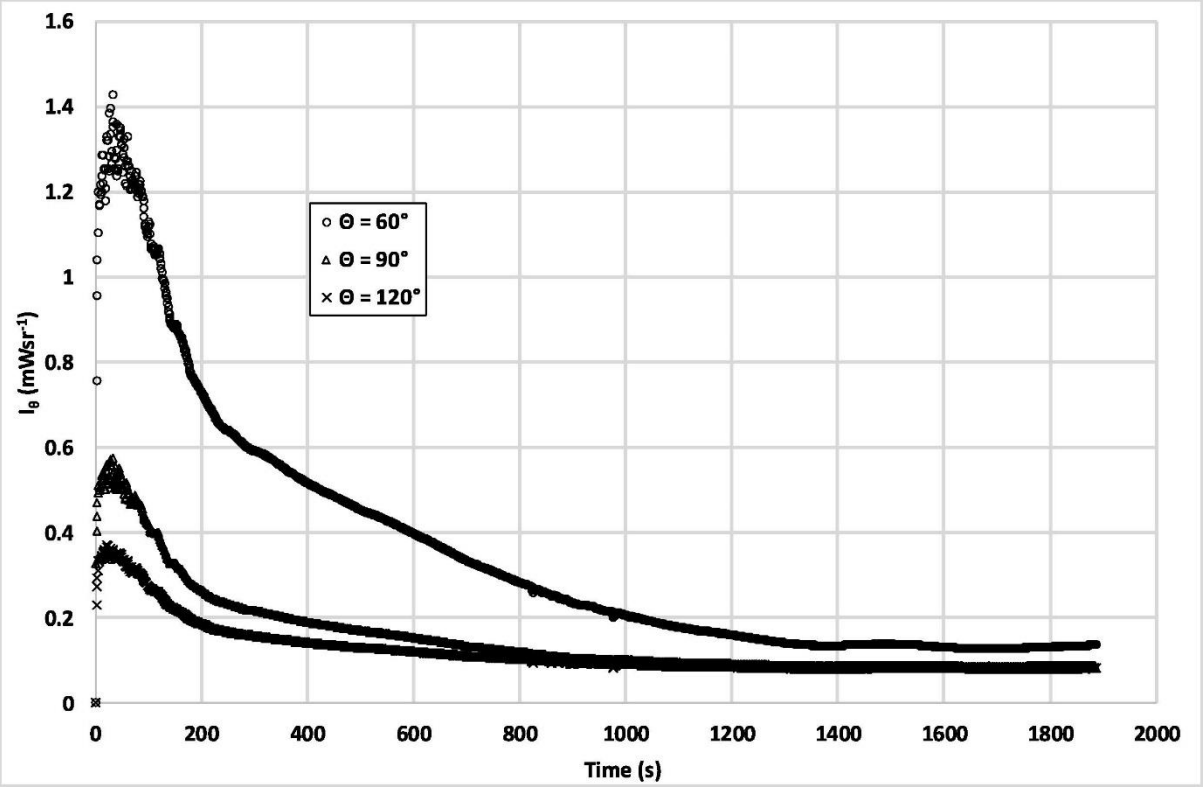

Figure 3-35. A sediment settling experiment using a loess concentration of 0.5168 gL^{-1}. λ = 940 nm.

3.13 Declaration of Interest

Declarations of interest: none.

3.14 Acknowledgements

This research was supported by NERC Grant No. NE/H006176/1.

The authors are grateful for the insights into numerical modelling and data interpretation strategies offered by Dr Adam Anderson at Ansys UK Ltd. We would also like to thank Alan Smalley and Rob Ashurst from the Department of Geography at the University of Sheffield for all their kind practical support and advice throughout this project, and Chris Orton at Durham University for his artistic improvement of the figures.

Chapter 4 TARDIIS: *Instrument evaluation and data analysis*

This chapter presents an evaluation of the TARDIIS instrument. To begin with, the calibration of the instrument is revisited. The effects due to variations in the construction quality of the TARDIIS components on the instrument response are considered. Experiments are carried out using a range of LED intensities in order to develop an optimal operational procedure. A new methodology for the reporting and comparison of turbidity data is developed. Finally, the collection of more data is recommended, along with suggestions for the future development of TARDIIS.

4.1 Calibration of the instrument

The published article reproduced in chapter 3 refers to the design, construction, and calibration of the TARDIIS research instrument. The calibration procedure, was detailed with regard to the voltage response, and progressed to the expression of the measured angular data as radiant intensities in units of milliwatts per steradian (mW sr^{-1}). Although these units are factually correct, the reporting of turbidity data as absolute values of radiant intensity is not necessarily conducive to the effective conveyance of any associated physical interpretation of that data. The calibration procedure must therefore be expanded upon, and a new methodology invented for the consistent reporting of turbidity data, which was a research goal suggested by the published review article reproduced in chapter 2.

The example data used in the calibration explanation in chapter 3 was adequate in terms of reporting absolute radiant intensity values, but it was not exemplary with regard to the new turbidity reporting methodology. The reason for this inconsistency is that the data collected in chapter 3 included some sensor responses, which were saturated during the calibration procedure. It is a requirement of the new reporting methodology that this situation cannot be allowed, and so a new set of data was taken at low incident light intensities to avoid this problem. A small, but necessary backward explanatory step is taken for the sake of clarity; hence, the development of the new turbidity data reporting idea begins in the voltage domain.

4.1.1 Baseline voltage response of the sensors to light

The sensors (photodiode amplifier modules) are very sensitive to background light, and as such all experiments need to be conducted under identical conditions, with external lighting being kept

to a minimum. Full details of the calibration procedure for individual sensors were given in chapter 2 (section 8.2), and will not be repeated here. However, a more detailed explanation of the overall instrument calibration is needed. As can be seen in Figure 4-1, the baseline voltages under the best achievable conditions of complete darkness are slightly greater than zero. Sensors S0 to S15 (at the 0° to 150° positions) have baseline voltages of approximately 38 to 42 µV. There is a distinct difference in the baseline voltages of S16 and S17 at the 160° and 170° positions, i.e. they are considerably higher at 98 to 99 µV. This difference in baseline response can only be attributed to differences in the construction of the photodiode amplifier modules. S0 to S15 were built using electrically shielded signal cable, which was no longer available by the time S16 and S17 were being constructed. The remaining two modules used a cheaper, unshielded brand of signal cable, which may account for the response observed in Figure 4-1.

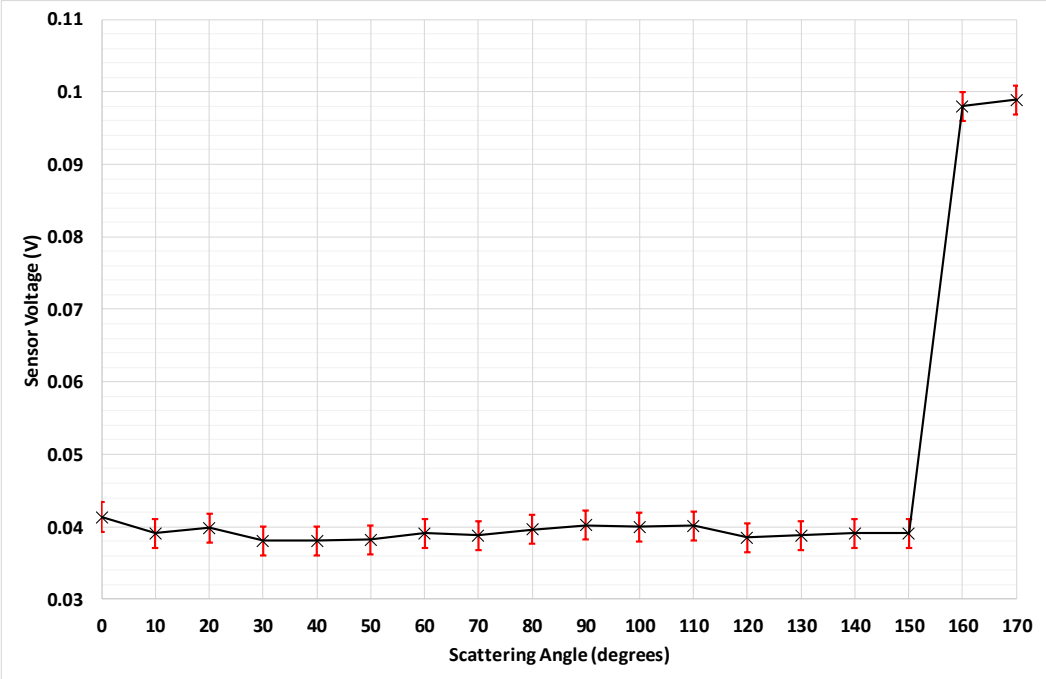

Figure 4-1. Sensor voltages under conditions of near total darkness.

4.1.2 Choice of LED intensity

There is a trade-off between light source brightness and measurement range. In order to perform experiments involving high concentrations of suspended sediment, it is necessary to use a high brightness level. To measure lower concentrations, a lower intensity light is required if sensor saturation is to be avoided. A number of experiments were performed using a high brightness level (with an LED current at the maximum of 30 mA). Although some useful data were collected, it was later realised that sensor saturation in the forward-angle detectors (0° to 30°) meant that it was not possible to calculate correctly the *backscatter fraction*, the *beam attenuation coefficient, or the angular gain function* - parameters that are important later on in this discussion. Therefore,

it was decided to use only a low intensity light-source, and to limit the upper limit of sediment concentration to 4.0 g l^{-1}.

4.1.3 Water-only baseline calibration

The sample chamber was set up using household tap water that was left for several hours to reach ambient room temperature. The calibration experiment was then executed in conditions of near total darkness. Using a 622 nm (red) LED at a nominal current of 1 mA gave a response in the 0° (direct-beam) sensor that only just achieved the maximum readout voltage, thus making sensor saturation impossible. The effects due to the instrument geometry then become apparent (Figure 4-2), which shows the sensor responses with the "dark voltages" (Figure 4-1) subtracted. There is a significant response in the 10° sensor, which is due to the divergence of the direct light beam. This divergence forms a "spot" centred on the 0° position, which radially diffuses outward toward the 10° and 20° positions.

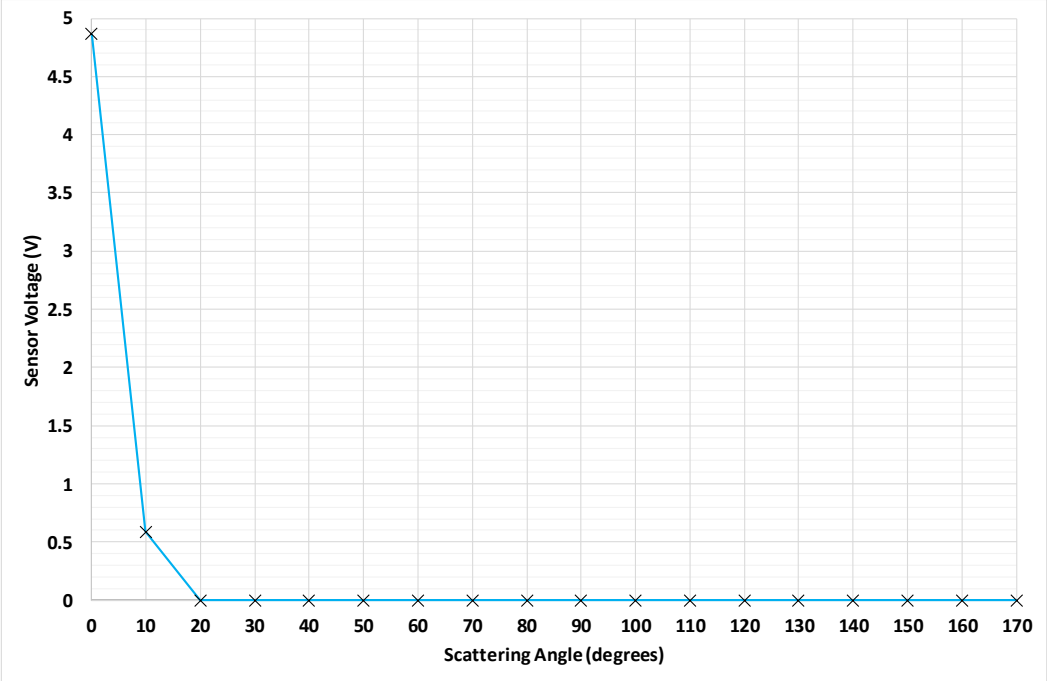

Figure 4-2. Sensor response to water only in the sample cell, using a 622 nm LED at 1 mA nominal current.

4.1.4 Conversion to radiant intensity

The remainder of this discussion will refer to light intensities in units of mW sr^{-1}, rather than sensor voltages. When the neutral density (ND) filter calibration method described in chapter 2 is applied to the baseline sensor voltages of Figure 4-2, the sensor calibration graph (SCG) is obtained (Figure 4-3).

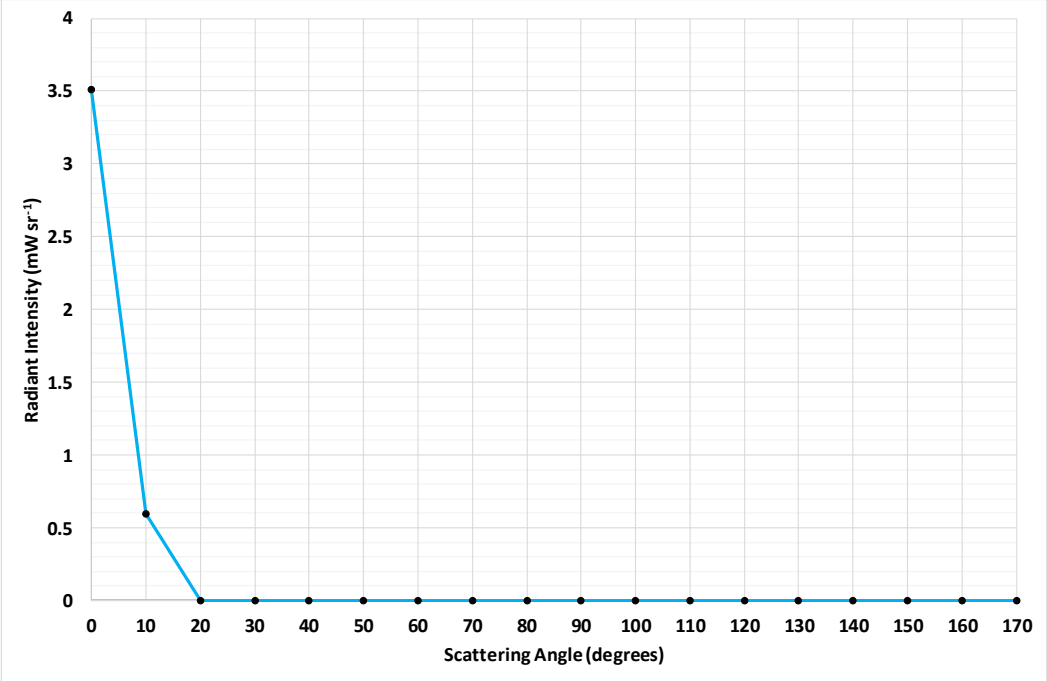

Figure 4-3. Sensor calibration graph (SCG). Water baseline calibration by ND filter method. 622 nm LED at 1 mA nominal current.

4.1.5 Interpretation of TARDIIS measurements

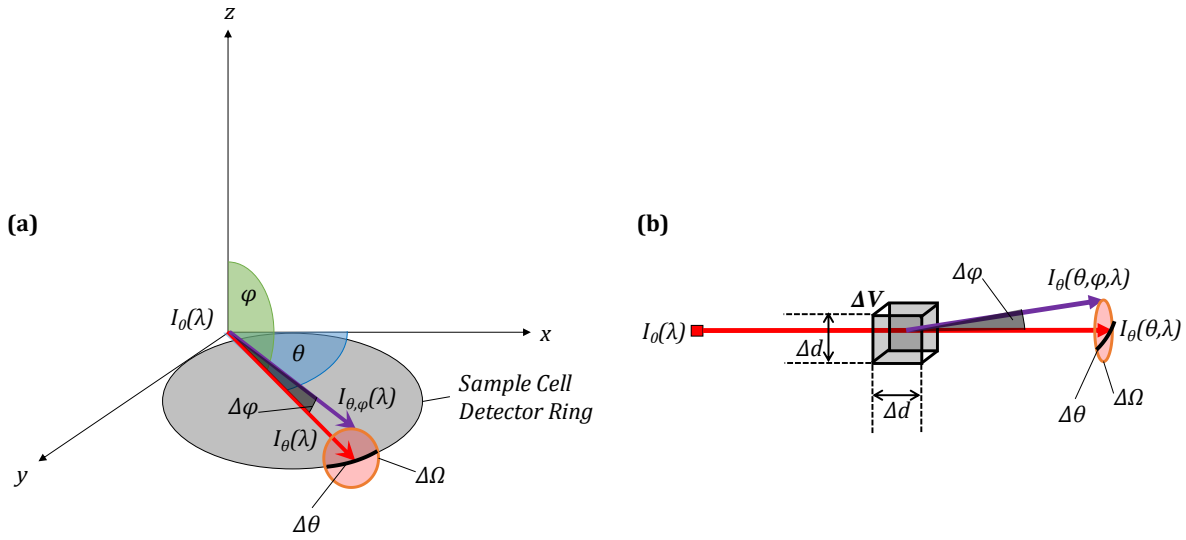

Figure 4-4. Light scattering geometry in the TARDIIS sample cell.

The angular measurements of radiant intensity I_θ provided by TARDIIS represent a direct measurement of the volume scattering function (VSF), $\beta(\theta, \varphi, \lambda)$. The VSF describes how light scatters from an infinitesimal volume element ΔV, in which θ is the azimuthal angle with respect to the volume centre, and φ is the angle of altitude with respect to the volume centre (Figure 4-4b). The light is scattered into solid angle Ω, which is bounded by θ and φ, and has units of

reciprocal steradians (sr^{-1}). The beam has an incident radiant intensity $I_0(\lambda)$ mW sr^{-1}, and has a resultant radiant intensity of $I_\theta(\theta, \varphi, \lambda)$ mW sr^{-1} after scattering. However, since TARDIIS only effectively measures the radiant intensity in a plane centred on ΔV, the geometry is simplified (Figure 4-4a). The altitude angle φ becomes *infinitesimal* as the geometry becomes planar, and is written as $\Delta\varphi$. This implies that the solid angle Ω is also *infinitesimal*, becoming $\Delta\Omega$. Likewise, as the infinitesimal volume element $\Delta V \rightarrow 0$, its "thickness" in the two of the orthogonal cubic planes also approaches zero ($\Delta d \rightarrow 0$), and the dimensionality is reduced from m^3 to m. Although the geometry has reduced from spherical to planar, the physical scattering processes are notionally occurring in a three-dimensional volume. However, it is now more meaningful to visualise the solid angle $\Delta\Omega$ (sr) as an arc, $\Delta\theta$ (rad). The scattered radiant intensity can now be written as $I_\theta(\theta, \lambda)$. Hence, the VSF is defined as equation 4-1, with units of m^{-1} sr^{-1} (or m^{-1} rad^{-1}),

$$\beta(\theta,\lambda) \equiv \lim_{\Delta d \rightarrow 0}\left(\frac{I_\theta(\theta,\lambda)}{I_0(\lambda)\,\Delta d}\right) \qquad 4\text{-}1$$

which reduces to:

$$\beta(\theta,\lambda) = \frac{I_\theta(\theta,\lambda)}{I_0(\lambda)} \qquad 4\text{-}2$$

The alternative units of measurement (m^{-1} rad^{-1}) that can be applied to the VSF in this derivation are different (but contextually correct) from the measurement units that are typical throughout the turbidity literature, i.e. m^{-1} sr^{-1}. The difference (per radian instead of per steradian) is essentially a case of mathematical semantics. In this application only, the two units are effectively interchangeable, since the solid angle $\Delta\Omega$ (measured in steradians - Figure 4-4) has *zero height*, hence reducing it to an arc $\Delta\theta$ (measured in radians). This simplification reduces the problem as a whole from three-dimensional to two-dimensional, which is useful for understanding the geometry of the practical measurements. However, in real terms, light-scattering events can only occur physically in three-dimensional space, and so the correct units should be, therefore, m^{-1} sr^{-1}. Since the radiant intensities of the light sources used in the TARDIIS experiments are stated in mW sr^{-1} and not mW rad^{-1}, it is mathematically convenient to stick with the accepted measurement units for the VSF and adhere to convention in this case.

The scattering coefficient b (m^{-1}) defines the amplitude of the total light removed from the beam by scattering. The scattering coefficient is simply the integral of the VSF over all angles in the plane (specifically the *xy* plane of Figure 4-4a). Since the VSF is symmetrical, it is adequate to consider only the semicircle (0 to π radians or 0° to 180°) and arrive at Equation 4-3.

$$b(\lambda) = \int_{0^\circ}^{180^\circ} \beta(\theta, \lambda) \sin\theta \, d\theta \qquad 4\text{-}3$$

In practical terms, the sensors sample the continuous integral defined as equation 4-3 at discrete angular positions (i.e. at 10° intervals), and so when integrated b becomes an approximation (4-4).

$$b(\lambda) \cong \sum_{0^\circ}^{180^\circ} -\beta(\theta, \lambda) \cos\theta \qquad 4\text{-}4$$

In terms of radiant intensities, substituting for $\beta(\theta, \lambda)$ (equation 4-2) gives Equation 4-5.

$$b(\lambda) \cong \frac{1}{I_0(\lambda)} \sum_{0^\circ}^{180^\circ} -I_\theta(\theta, \lambda) \cos\theta \qquad 4\text{-}5$$

It is also common practice in the literature to extract a *scattering phase function* (sr^{-1}) from equation 4-3, which gives the normalised angular distribution of the light field within the sample (4-6).

$$\tilde{\beta}(\theta, \lambda) = \frac{\beta(\theta, \lambda)}{b(\lambda)} \qquad 4\text{-}6$$

It is useful to visualise the shape of the instrument response as a phase function on a polar chart, as in this format the data is easy to compare with other results, such as those obtained from scattering at a different wavelength of light. In that case, the normalised $\tilde{\beta}(\theta, \lambda)$ values can be plotted on the same chart for direct comparison.

The water itself is considered to have negligible scattering and absorption properties in the context of this work. In other contexts, e.g. the measurement of very low turbidities for the assessment of drinking water quality (beyond the measurement capabilities of TARDIIS), the inherent optical properties of the water would have a measurable effect. In that case, consistent use of de-ionised water would be recommended.

Figure 4-5 shows the baseline phase function $\tilde{\beta}(\theta, \lambda)$, for θ = 0° to θ = 350° and λ = 622 nm. The θ = 180° value is omitted since TARDIIS cannot provide a measurement at that position. The 350° to 190° values are simply the mirror-image of the 10° to 170° values.

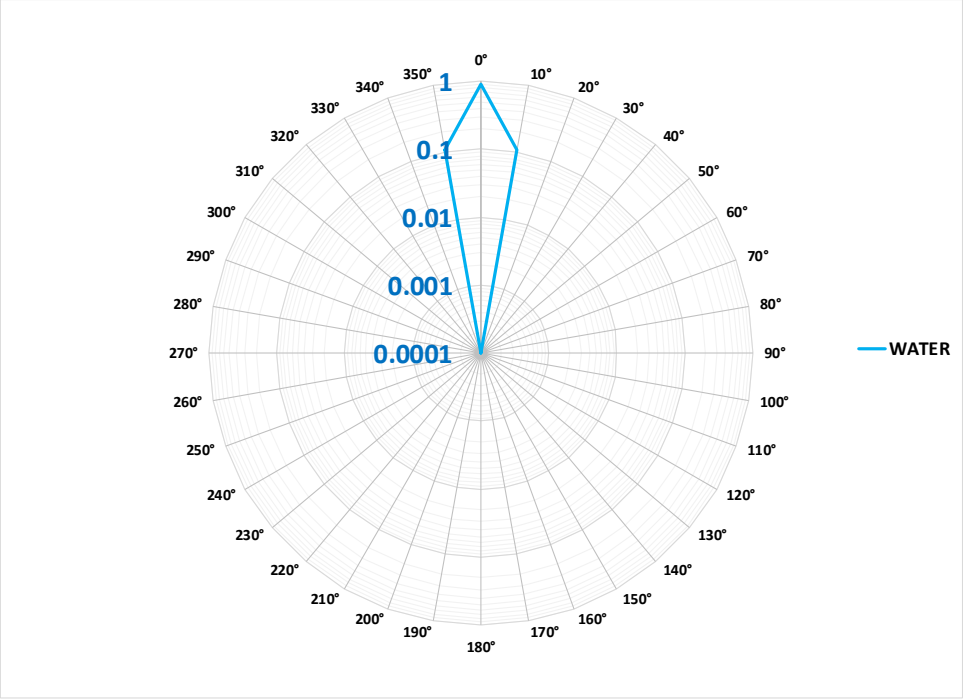

Figure 4-5. Baseline phase function $\tilde{\beta}(\theta, 622\ nm)$ (sr^{-1}) for TARDIIS sample cell containing only water. 622 nm LED at 1 mA nominal current.

4.1.6 Data reduction: expressing angular data as the backscatter fraction

The scattering coefficient for backscattering only, $b_b(\lambda)$, is the fraction of the total backscattering coefficient $b(\lambda)$ summed from 90° to 180° (Equation 4-7).

$$b_b(\lambda) \cong \frac{1}{I_0(\lambda)} \sum_{90^\circ}^{180^\circ} -I_\theta(\theta, \lambda) \cos\theta \qquad 4\text{-}7$$

The backscatter fraction $B_b(\lambda)$ is a simple metric that represents the symmetry of the VSF as a single parameter (Equation 4-8), for example a value of 0.5 would indicate that the amount of forward scattering is equal to the amount of backscattering. This metric is useful since it is independent of the light source intensity, suggesting that $B_b(\lambda)$ for a given value of λ could be used to compare different sediments (measured using different instruments), since different PSDs will result in different VSFs. Similarly, for a given sediment, a set of simple characterisation metrics could be generated by measuring the VSF at different wavelengths, and presenting the reduced data as a set of $B_b(\lambda)$ for multiple values of λ.

$$B_b(\lambda) = \frac{b_b(\lambda)}{b(\lambda)} \qquad 4\text{-}8$$

4.2 Observations of the steady-state loess suspension

4.2.1 Steady-state experimental setup

The intension of the steady-state experiments was to determine the effects due to varying concentrations of suspended sediment on the response of the TARDIIS system. To maintain the steady-state of the nominal concentration, a magnetic stirrer system was used to prevent the sediment from settling and to maintain a constant concentration level (Figure 4-6).

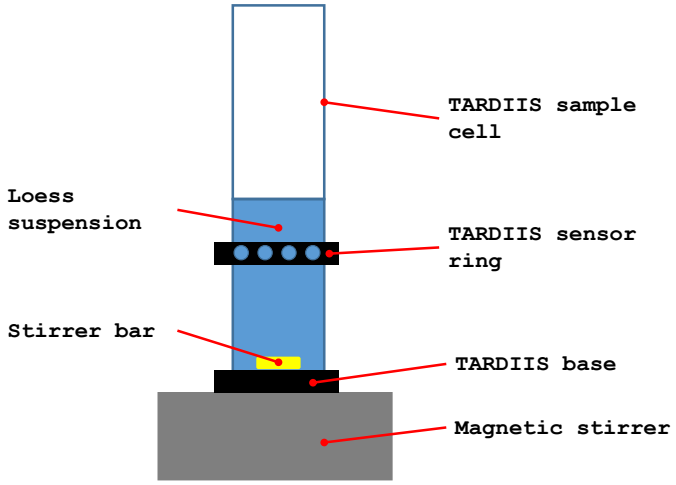

Figure 4-6. Experimental setup for steady-state loess suspension experiments. Sensor height = 93 mm, water height = 142 mm.

The voltage responses of the TARDIIS sensors (e.g. Figure 4-7) were time-averaged to arrive at values representative of the steady-state signals for each nominal concentration of loess. The mean percentage error for each loess concentration is the mean of the standard deviations of each sensor's time-averaged signal. The mean percentage error for the 1.0 g l^{-1} experiment (Figure 4-7) is 1.5%.

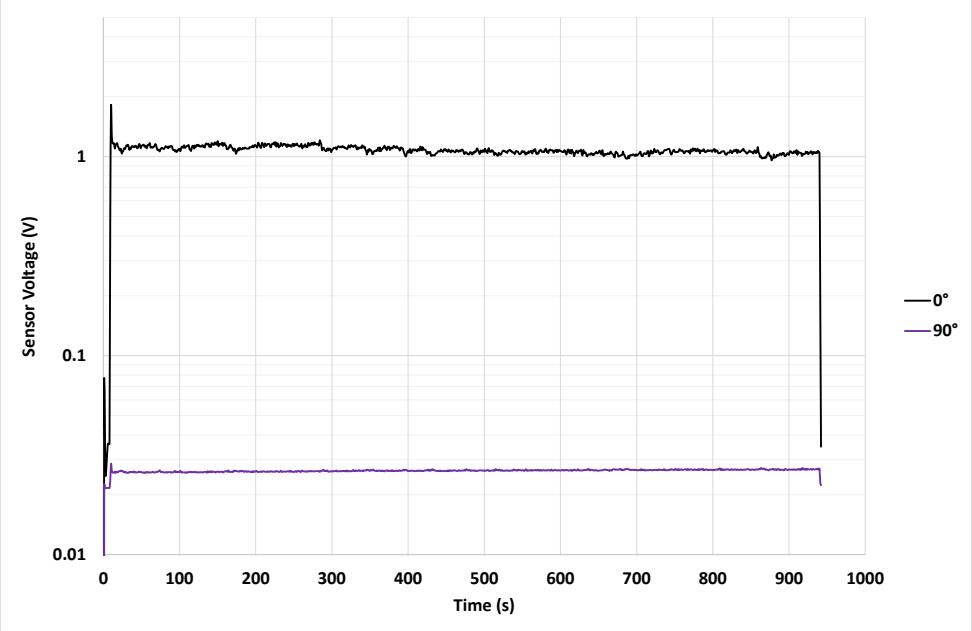

Figure 4-7. Example of steady-state experiment sensor responses, in this case from a loess concentration of 1.0 g l^{-1}.

The errors are likely to be due to interferences caused by the agitation method employed to maintain sediment suspension. One factor that could potentially bias the experimental results is the alignment of non-spherical sediment particles with the horizontal direction of the flow. However it is not possible to quantify the effect in this type of experiment, (a similar problem occurs in tranquil settling experiments, in which case the non-spherical particles will favour alignment with the vertical axis due to gravity). Another side effect of the agitation method is the formation of a vortex in the top of the water column. If the apex of the vortex projects downwards into the plane of the sensor ring, then reflections from the vortex meniscus could distort the light-scattering measurements. The velocity of stirring must be consistent to maintain sediment suspension whilst not allowing the vortex to become too large (Figure 4-8).

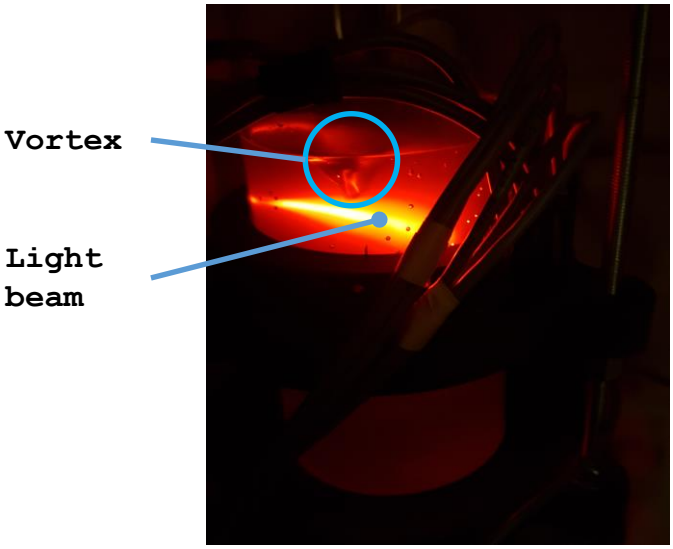

Figure 4-8. Vortex formation during steady-state suspended sediment experiments.

4.2.2 Results of the steady-state loess concentration experiments

The following figures (Figure 4-9 to Figure 4-16) show the evolution of the phase function for loess as the concentration increases from 0.5 g l^{-1} to 4.0 g l^{-1}, with the 0° to 10° lobe decreasing and the 20° to 130° signals increasing significantly. The details present in the shape of the phase function can potentially reveal information about the properties of the sediment, for example, there is a noticeable trough in the phase function at the 150° position, which seems to be independent of sediment concentration. The baseline calibration condition, i.e. water only (no sediment) indicates the lower limit of measurement of the TARDIIS instrument.

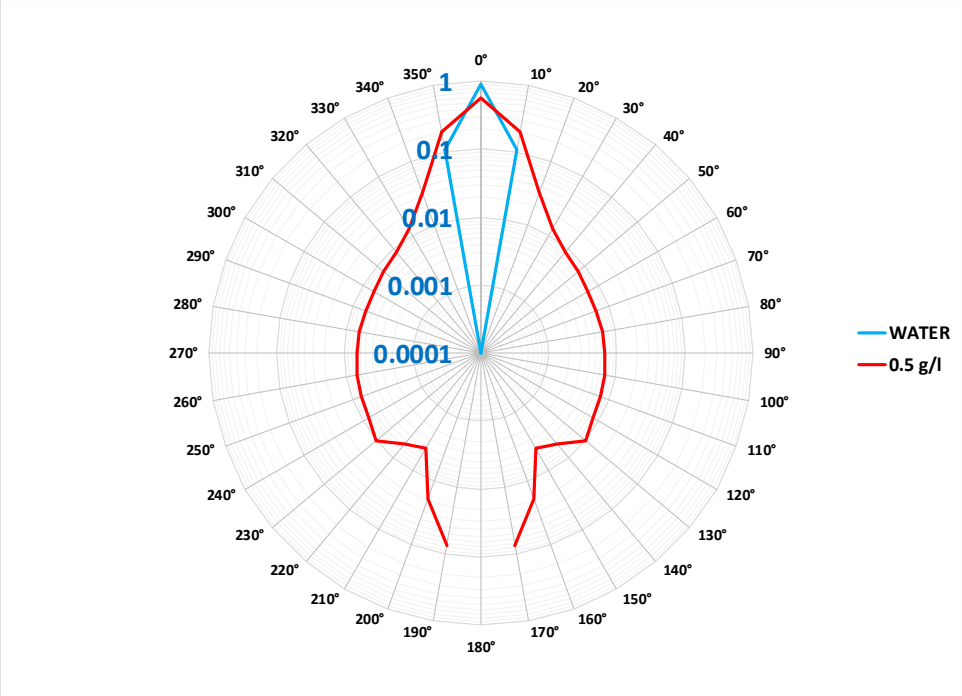

Figure 4-9. Phase function $\tilde{\beta}(\theta, 622\ nm)$ (sr^{-1}) of loess at 0.5 g l^{-1} concentration. The baseline calibration condition (labelled "WATER") is shown for comparison.

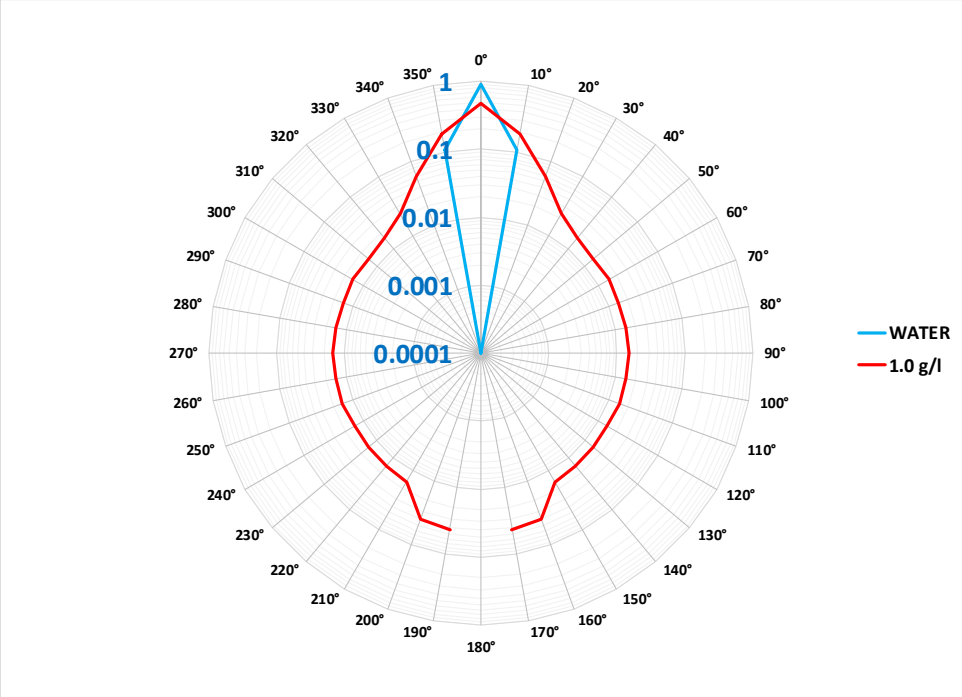

Figure 4-10. Phase function $\tilde{\beta}(\theta, 622\ nm)$ (sr^{-1}) of loess at 1.0 g l^{-1} concentration. The baseline calibration condition (labelled "WATER") is shown for comparison.

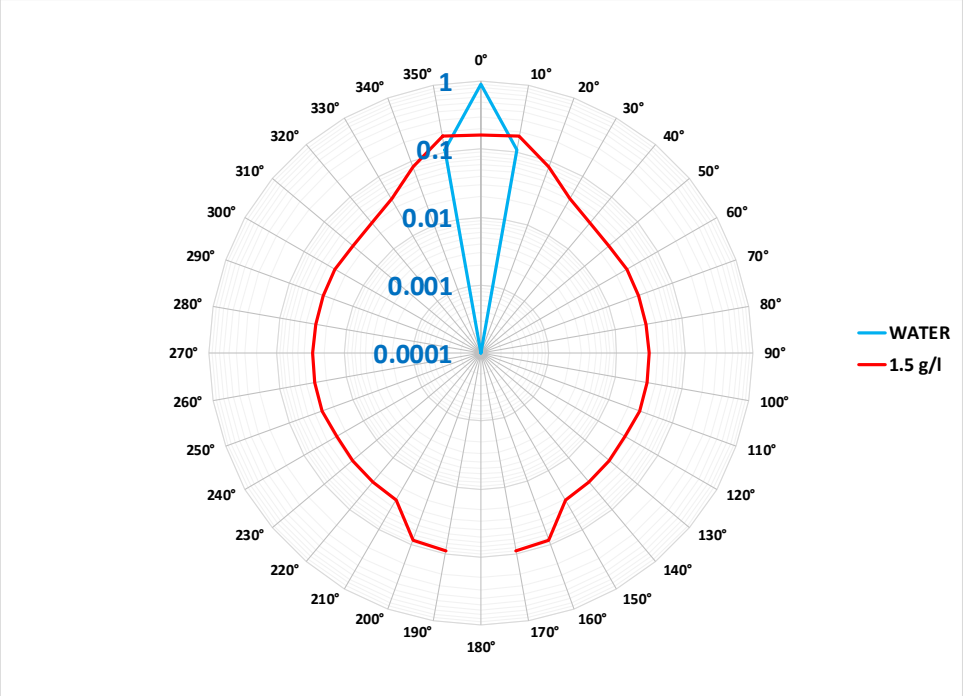

Figure 4-11. Phase function $\tilde{\beta}(\theta, 622\ nm)$ (sr^{-1}) of loess at 1.5 g l^{-1} concentration. The baseline calibration condition (labelled "WATER") is shown for comparison.

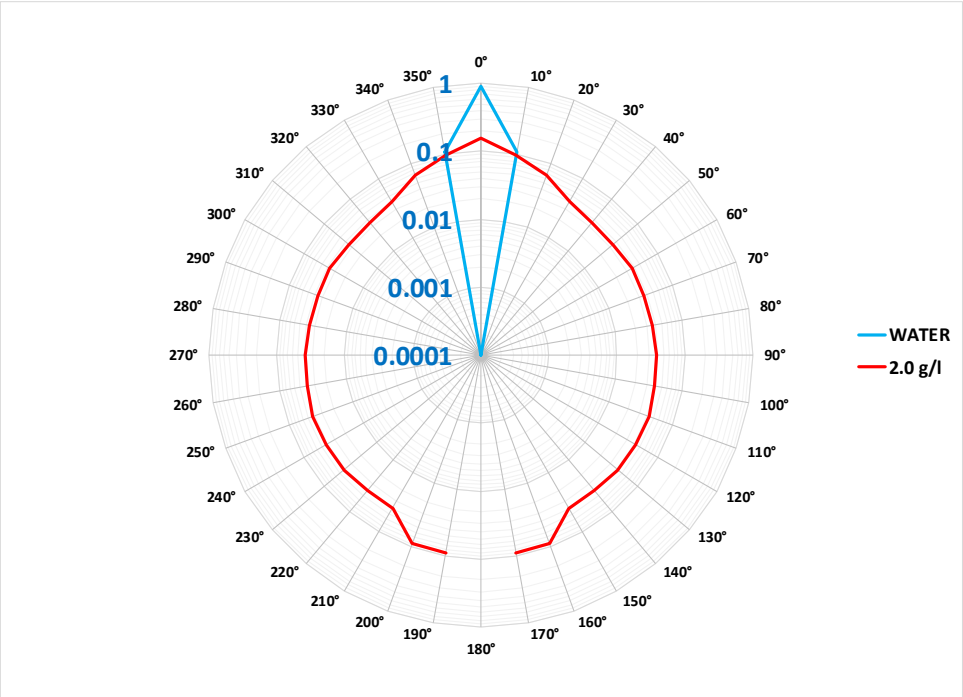

Figure 4-12. Phase function $\tilde{\beta}(\theta, 622\ nm)$ (sr^{-1}) of loess at 2.0 g l^{-1} concentration. The baseline calibration condition (labelled "WATER") is shown for comparison.

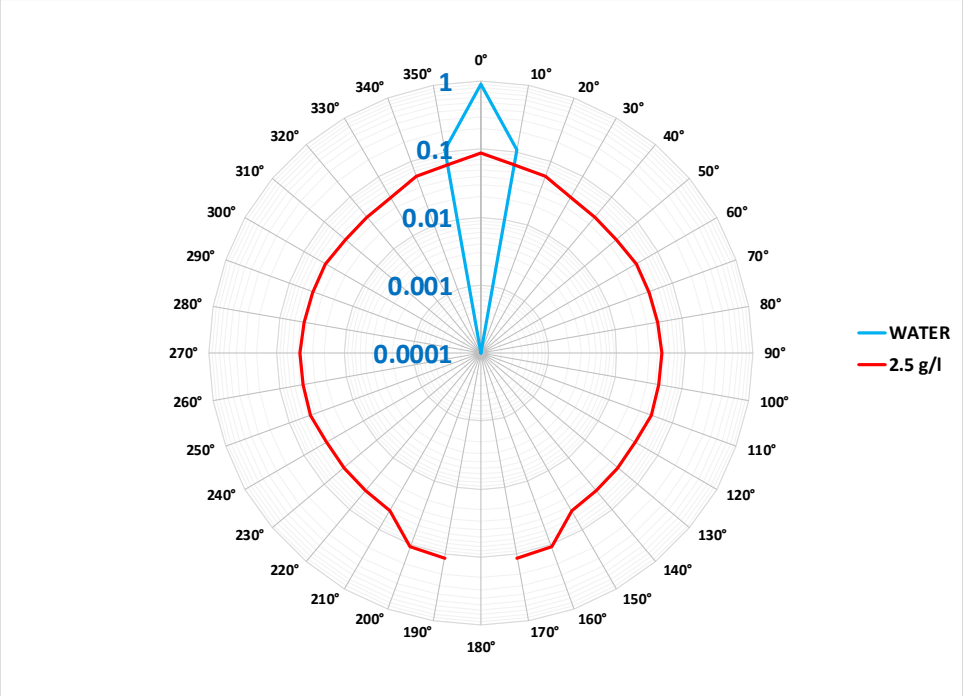

Figure 4-13. Phase function $\tilde{\beta}(\theta, 622\ nm)$ (sr^{-1}) of loess at 2.5 g l^{-1} concentration. The baseline calibration condition (labelled "WATER") is shown for comparison.

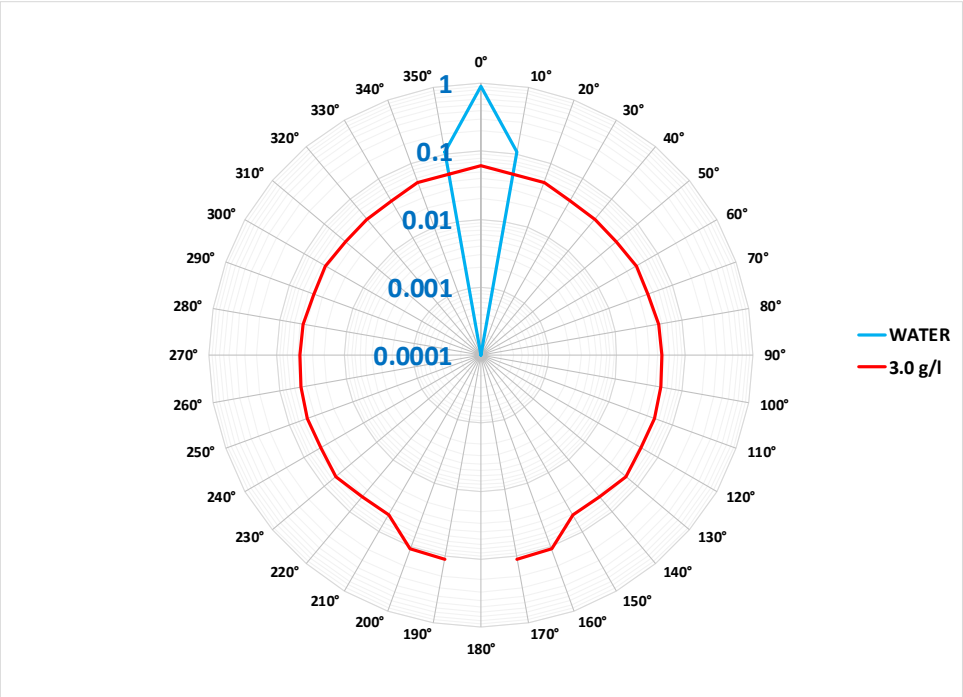

Figure 4-14. Phase function $\tilde{\beta}(\theta, 622\ nm)$ (sr^{-1}) of loess at 3.0 g l^{-1} concentration. The baseline calibration condition (labelled "WATER") is shown for comparison.

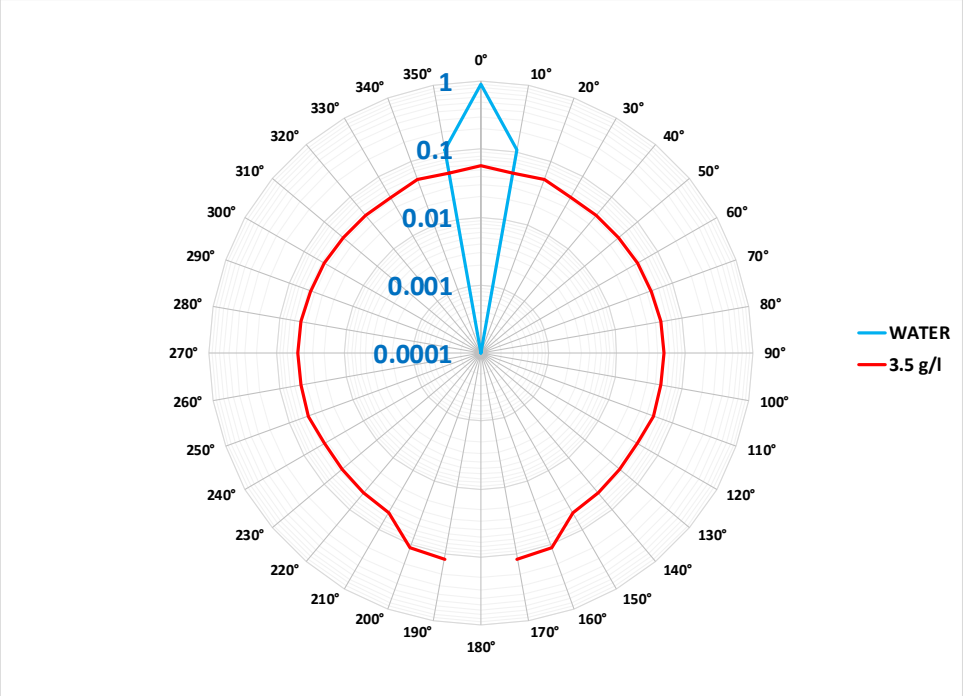

Figure 4-15. Phase function $\tilde{\beta}(\theta, 622\ nm)$ (sr^{-1}) of loess at 3.5 g l^{-1} concentration. The baseline calibration condition (labelled "WATER") is shown for comparison.

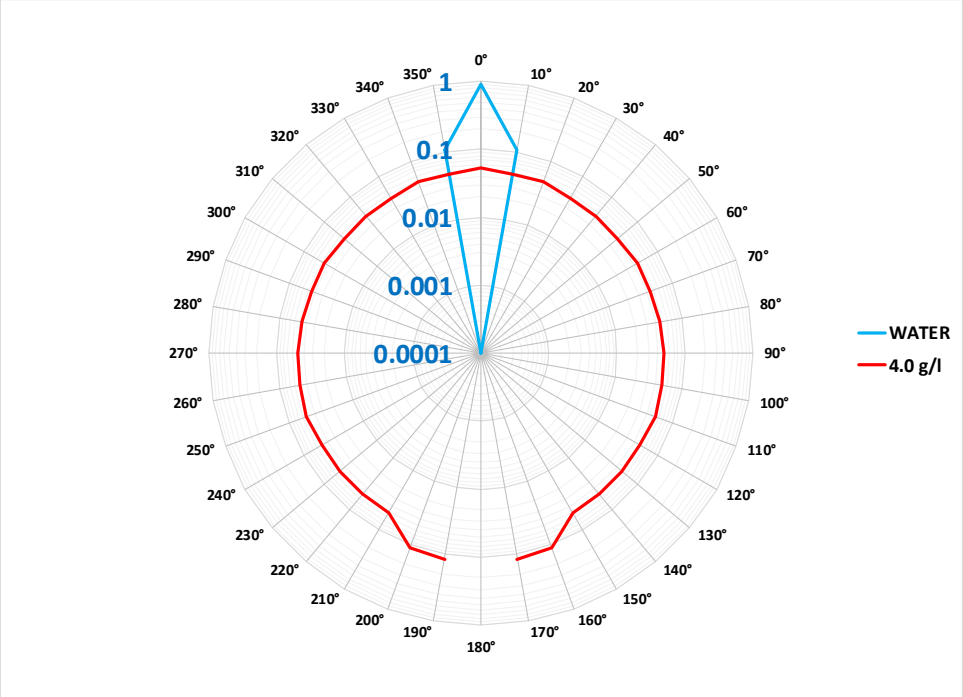

Figure 4-16. Phase function $\tilde{\beta}(\theta, 622\ nm)$ (sr^{-1}) of loess at 4.0 g l^{-1} concentration. The baseline calibration condition (labelled "WATER") is shown for comparison.

4.3 Reporting and comparing data

4.3.1 The angular gain function

In chapter 2, section 2.9.3 "A practical definition of the BAC", the beam attenuation coefficient (BAC) was defined by Equation 2-12. This equation of the BAC expresses the measurement of light attenuation based on the base-ten logarithm of the ratio of incident light intensity to the measured light intensity at a given angular position, divided by the optical path length, l (Equation 4-9). The numerator is a logarithmic function of the angular transmission, and the denominator l is the nominal beam path length in metres, which in the case of TARDIIS is 0.098 m. The BAC has units of dB m^{-1}.

$$BAC(\theta,\lambda) = \frac{-10\log[I_\theta(\theta,\lambda)/I_0(\lambda)]}{l} \qquad 4\text{-}9$$

Although the BAC is a useful quantity, it requires further development to enable the direct comparison of data obtained from different instruments. A new function is therefore required that will allow this comparison to be made. This function is termed the *angular gain function* (AGF), and is analogous to the concept of power gain in electronic circuits. The AGF (Equation 4-10) compares two BAC quantities: the *measurement* quantity and the *reference* quantity. The measurement quantity represents the BAC relating to a sediment suspension (BAC_M), and the reference quantity is the BAC measured under *baseline conditions*, i.e. water only in the sample cell (BAC_W). Assuming that the BAC is a root-power quantity (ISO 2006) as it is a function of distance, the AGF (Equation 4-10) is a power-gain formula based on the ratio of two BACs, and has units of decibels (dB). An AFG(θ, λ) of 3 dB represents a doubling of the measured light intensity as compared to the baseline (water only) value. Similarly, an AFG(θ, λ) of -3 dB represents a halving of the measured light intensity as compared to the baseline (water only) value. The AGF is analogous to voltage gain in an electronic amplifier.

$$AGF(\theta,\lambda) = -20\log\left(\frac{BAC_M(\theta,\lambda)}{BAC_W(\theta,\lambda)}\right) \qquad 4\text{-}10$$

The AGF provides a measurement that is independent of the incident light intensity, and that is independent of the instrument geometry (i.e. beam path length), with the caveat that the calibration procedure that produced BAC_W did not permit any sensor saturation. The results of the loess steady-state concentration experiments presented in section 4.2.2 are transformed into *AGF(θ, λ)* values and graphed in Figure 4-17. It is easy to compare visually the data for different sediment concentrations. Similar graphs are plotted to show differences in the AGF due to different wavelengths of incident light (Figure 4-18 shows λ=940 nm, and Figure 4-19 shows λ=470 nm).

An interesting feature of the angular gain function is the demarcation between negative and positive values. Conceptually, the negative AGF values are measurements in which the effects of the light absorption processes dominate over the effects due to the light scattering processes occurring in the sample cell. This *negative gain* is a *positive attenuation*. Conversely, the positive AGF gains indicate that the measured signals are greater than the baseline condition, and hence the contribution to the AGF of the light scattering from suspended sediment particles outweighs the contribution due to light absorption by those particles. In this case, the gain is *positive* (equivalent to a somewhat ambiguous *negative* attenuation).

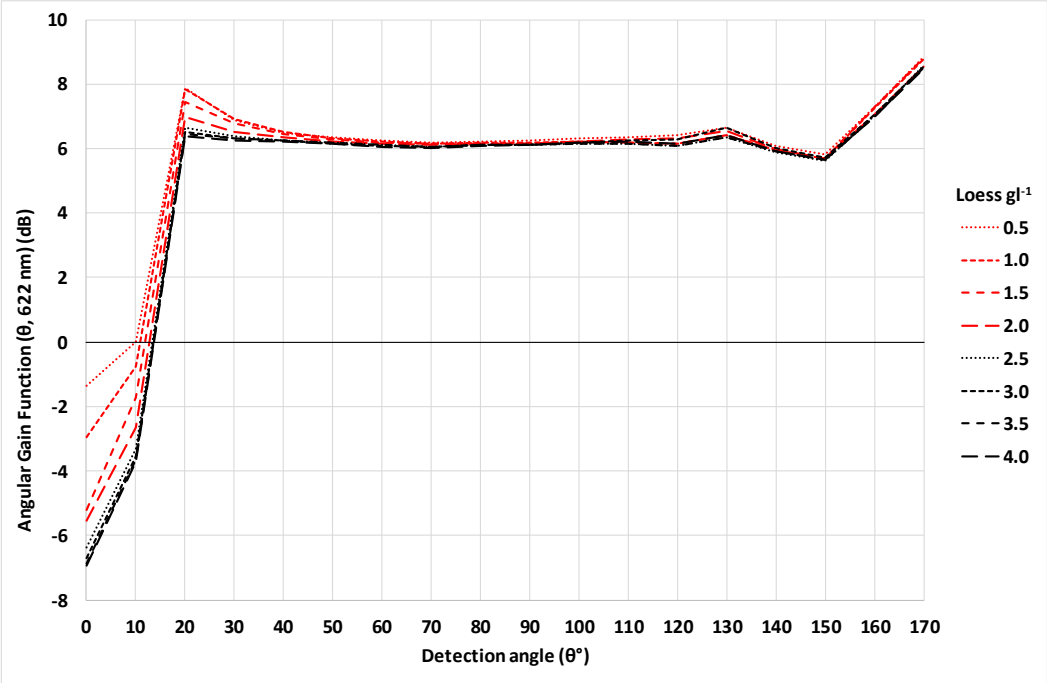

Figure 4-17. AGF(θ, 622 nm) for loess concentrations of 0.5 g l^{-1} to 4.0 g l^{-1}.

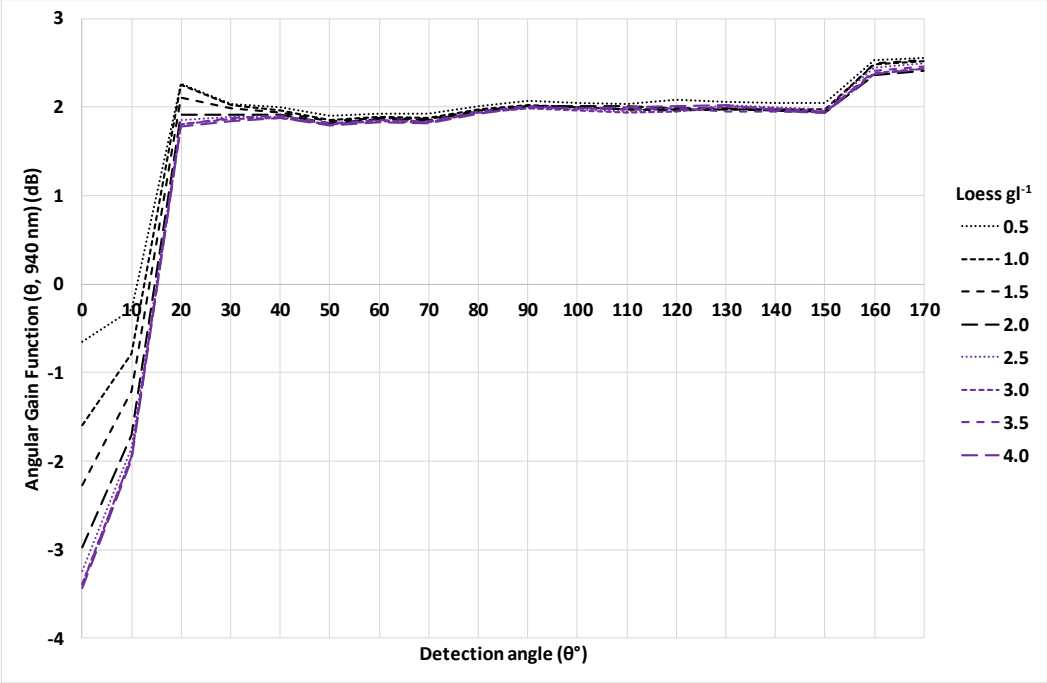

Figure 4-18. AGF(θ, 940 nm) for loess concentrations of 0.5 g l^{-1} to 4.0 g l^{-1}.

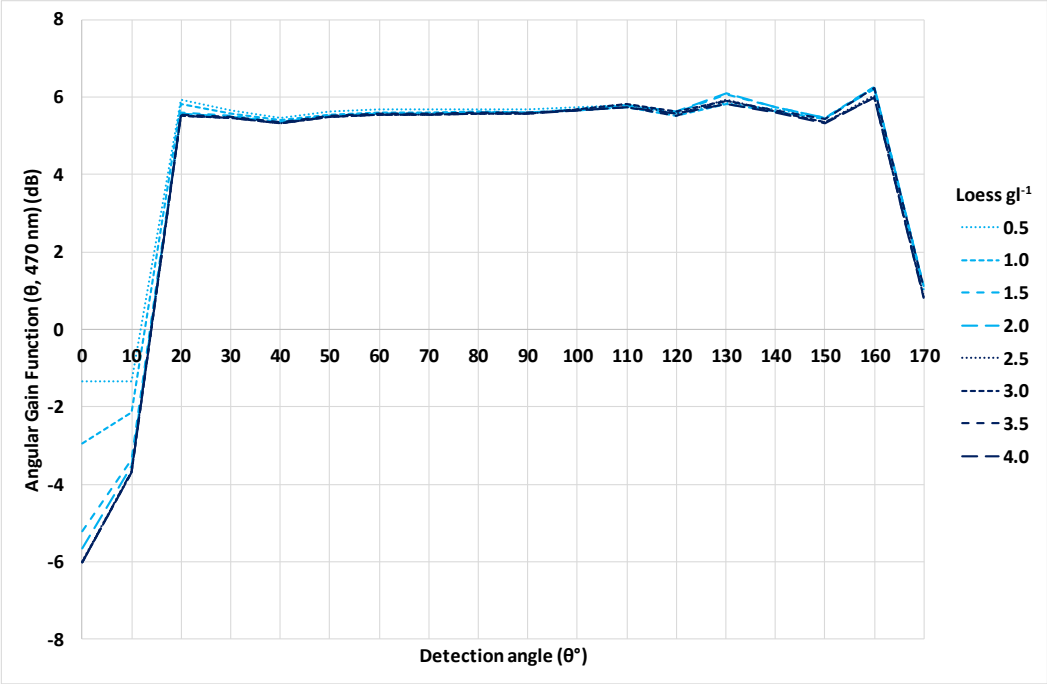

Figure 4-19. AGF(θ, 470 nm) for loess concentrations of 0.5 g l^{-1} to 4.0 g l^{-1}.

4.3.2 Using the AGF to determine sediment concentration

It is clear from Figures 4-17 to 4-19 that the AGF sensitivity to sediment concentration varies considerably with respect to detection angle θ. All of the steady-state measurements made using TARDIIS have been within the concentration limits of 0.5 g l^{-1} to 4.0 g l^{-1}. In order to summarise effectively this change in sensitivity to sediment concentration, the AGF dynamic range within these concentration limits (0.5 g l^{-1} to 4.0 g l^{-1}) is plotted against θ (Figure 4-20). It is useful to show the sensitivity to sediment concentration at two different PSDs, and so the dynamic ranges for loess sediment and kaolin clay are presented (refer to Chapter 6, Figure 6-4 for details of the PSDs of loess and kaolin).

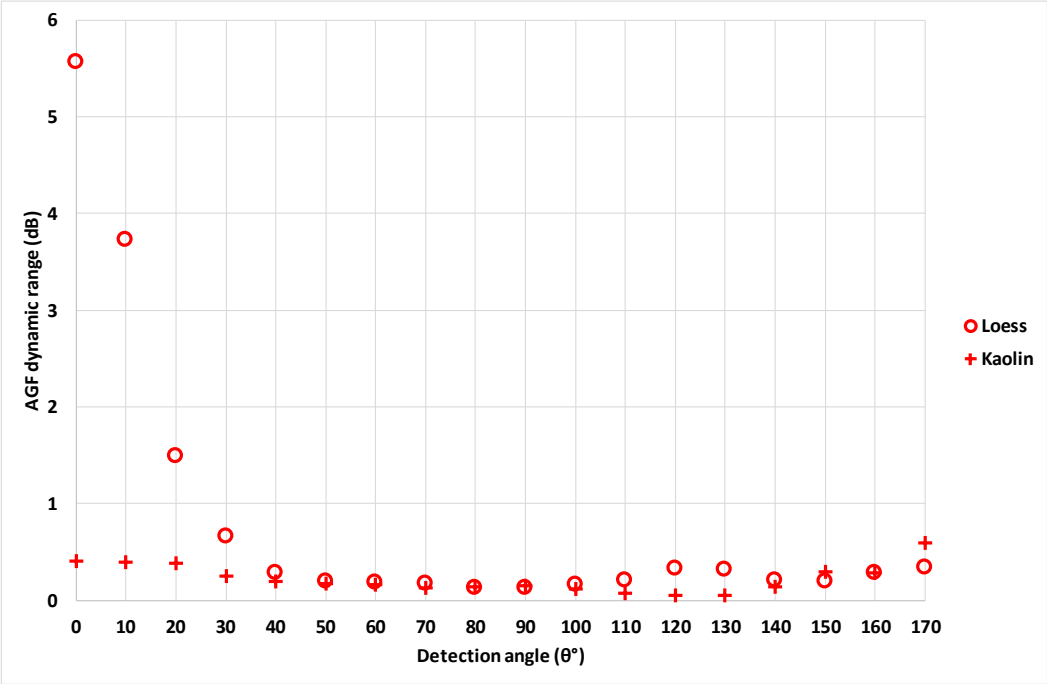

Figure 4-20. Dynamic range of TARDIIS measurements at 622nm within sediment concentration limits of 0.5 g l^{-1} to 4.0 g l^{-1}, for loess and kaolin.

It is notable that the AGF dynamic ranges of loess and kaolin are almost identical at the 90° detection angle. This result is interesting, since loess and kaolin have vastly different PSDs (with loess having large particles >20 µm diameter present in its distribution), and it implies that the gradients m of the AGF versus concentration curves should also be very similar. A crude test shows that the AGF versus concentration curves are reasonably linear, and almost identical - with $m = -0.03$ for loess and $m = -0.04$ for kaolin. Using the 90° detection position to determine concentration has the disadvantage that the measurement dynamic range is very low, and so high instrument sensitivity is required. However, it has the advantage of being less sensitive to the effects of PSD (maximum 0.17 dB difference in AGF between loess and kaolin over the 0.5 g l^{-1} to

4.0 g l^{-1} concentration range), and so reasonable estimates of SSC can be made irrespective of the PSD of the sediment.

Conversely, the AGF dynamic ranges of loess and kaolin diverge considerably in the forward-angle detection positions as $\theta \rightarrow 0$. Using, for example, the 0° detection position by itself to determine sediment concentration could give misleading results, since it is highly influenced by PSD (maximum 5.13 dB difference in AGF between loess and kaolin over the 0.5 g l^{-1} to 4.0 g l^{-1} concentration range, with $m = -1.51$ for loess and $m = -0.11$ for kaolin). However, when used in conjunction with the 90° detector data, the forward-angle measurements reveal the degree to which larger particles are present in the sediment PSD.

There is an implication for the precision of turbidity measurements made in compliance with USEPA Method 180.1 (US EPA 1993). This standard describes a method for nephelometric turbidity measurement, and specifies a detection angle of 90° ± 30°. When taking into consideration the data presented in Figure 4-20, it is clear that the 30° tolerance in the detector position will introduce significant errors into calibrations that aim to determine SSC from turbidity data. In particular, the backscatter angles of 100° to 120° reveal a relatively high sensitivity to PSD, compared with the less significant PSD sensitivity at the 90° position. Therefore, the ± 30° instrument design tolerance should be ideally removed from the USEPA Method 180.1 standard, i.e. only 90° measurements should be used for nephelometric turbidity measurement.

4.3.3 BAC reference standards and the WAGF

Equation 4-10 defines the angular gain function as a logarithmic ratio of two angular beam attenuation coefficients. In this definition, the reference BAC is that of the baseline condition, i.e. water only (BAC_W). As such, the AGF actually represents a *change*, i.e. the difference between two physical conditions – the first case in which there is no sediment present, and the second case in which there *is* sediment present. For example, Figure 4-21 shows the changes in the AGF response to loess sediment during a settling experiment.

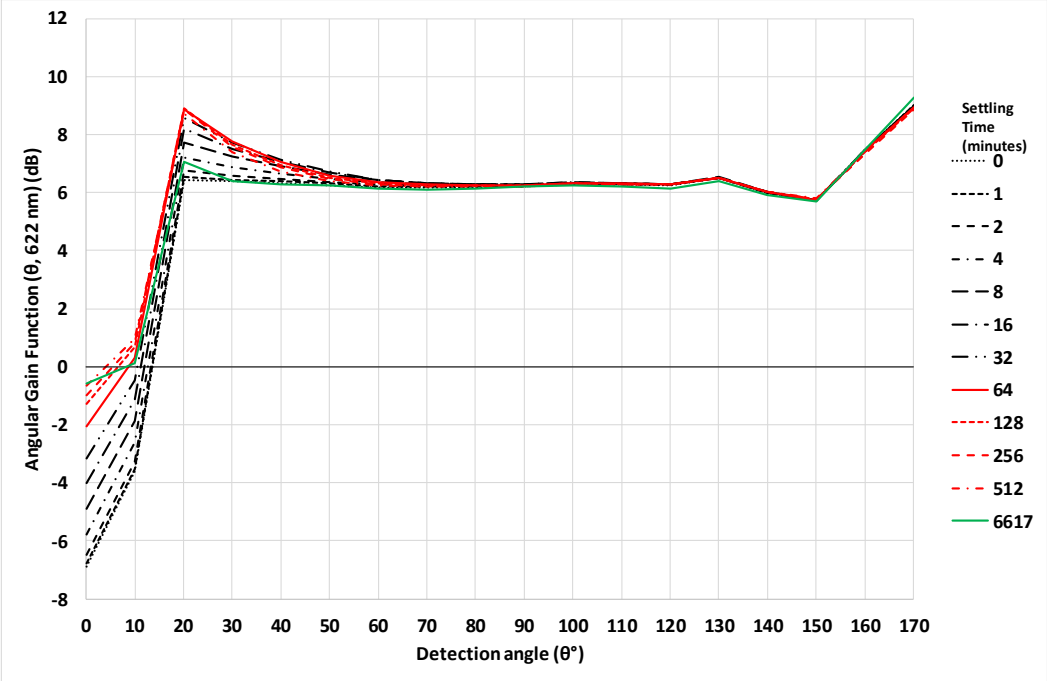

Figure 4-21. The AGF of a loess sediment settling experiment, with an initial loess concentration of 4.0 g l^{-1}. Information intrinsic to the light scattering properties of the loess (embedded in the VSF) are visible in the angular data.

It could potentially prove to be useful in some applications to base the AGF measurement on a *reference standard*, with the same good intentions that the doomed Formazin standards were designed for (see section 2.12). However, the use of particulate calibration standards could yet prove to be an effective way to enhance the comparison of certain turbidity measurements. There are some caveats to the correct use of calibration standards in turbidity calibrations:

1. The baseline calibration to *water only* conditions must happen **first**.
2. The *calibration standard* must **not** be derived from chemical reaction media, as in the case of Formazin.
3. The calibration standard must have a **well-defined PSD**.
4. The calibration standard must have **well-defined particle roundness**.
5. The calibration standard must have **well-defined colour**.
6. The calibration standard must have a **well-defined refractive index**.
7. The calibration standard must have **well-defined reflectivity**.
8. The BAC(θ, λ) data for the calibration standard must be provided (by the manufacturer) for a wide range of θ, λ, and concentration.

If the caveats above are met, then the *weighted angular gain function* (WAGF) is defined as Equation 4-11, where *A* is a particular calibration standard.

$$WAGF(\theta,\lambda,\boldsymbol{A}) = -20\log\left(\frac{BAC_M(\theta,\lambda)}{BAC_{\boldsymbol{A}}(\theta,\lambda)}\right) \qquad 4\text{-}11$$

An alternative use of the WAGF is in *comparative sediment analysis*, in which a sediment *end-member* that contains **the full representative PSD** of the sediment, provides the data for the reference BAC. For example, if the sediment end member is **loess at 4.0 g l^{-1}** concentration, then the WAGF is Equation 4-12. The reference type of the weighting could be introduced into the decibel measurement units in much the same way as in which weighted sound pressure levels (SPLs) are reported, e.g. dB(A), dB(B), dB(C) etc., except that in the case of reporting turbidity as an AGF, *A*, *B*, and *C*, would refer to specific calibration standards. For example, the initial ***S*** could represent the idea of a *self-referencing* measurement, such that the units of Equation 4-12 would become dB(S).

$$WAGF\left(\theta,\lambda,\boldsymbol{S}=[\boldsymbol{loess},\boldsymbol{4.0\ gl^{-1}}]\right) = -20\log\left(\frac{BAC_M(\theta,\lambda)}{BAC_{\boldsymbol{S}}(\theta,\lambda)}\right) \qquad 4\text{-}12$$

Applying Equation 4-12 to the sediment settling experiment of section 4.2.1, the settling data represents the changes over time from the nominal starting condition of loess at 4.0 g l^{-1} concentration (Figure 4-22).

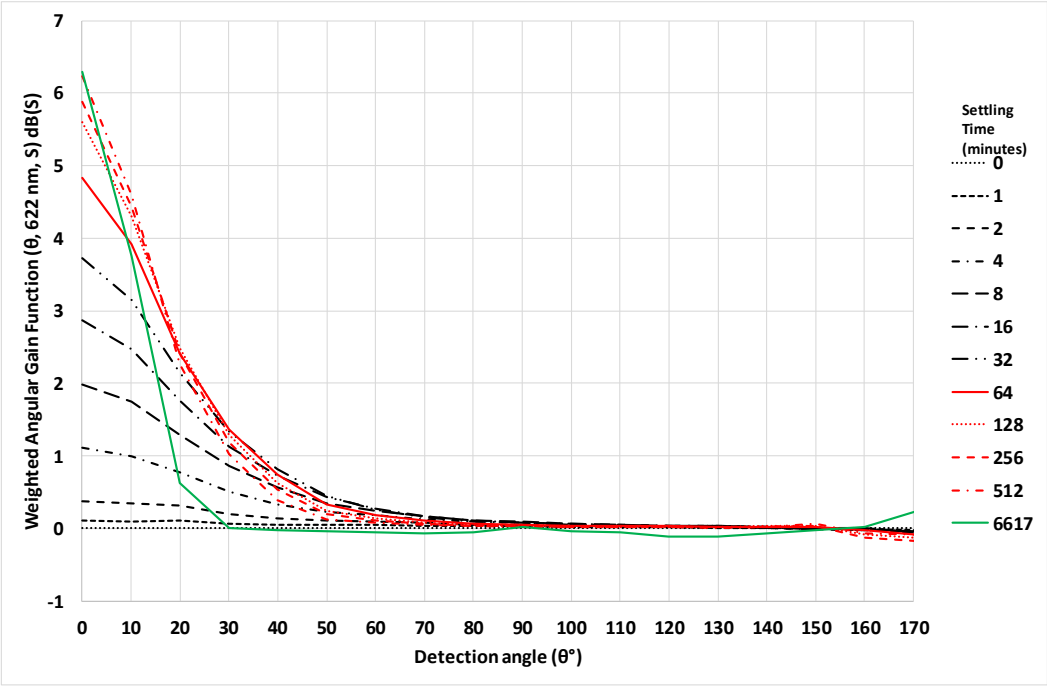

Figure 4-22. The weighted angular gain function as a way to visualise the changes in the optical profile of a loess sediment as it settles over time. No intrinsic light scattering information is available: only relative differences are discernible.

4.3.4 Summary of the AGF and the WAGF

The AGF allows turbidity measurements to be reported in decibels after calibration to a *baseline* condition, which will typically be the clean water into which the sediment is to be added. It is effectively an *absolute* representation of the turbidity of a sample. However, since the baseline water samples are not likely to be *exactly* the same, it can be at best described as being a *pseudo-absolute* measurement. It would therefore be prudent to stipulate a precise definition for *all* baseline water samples, to some particular grade of de-ionised water, for example.

The WAGF is useful for comparison of turbidity measurements with a particular calibration standard, which could potentially facilitate the extraction of particle size and particle shape data. For example, if a calibration standard with a particularly well-defined mono-modal PSD with highly spherical particles were used as the baseline, then any deviations from the baseline response would indicate differences in PSD and particle shape. This approach does however require a considerable prior knowledge of how different PSDs and particle shape profiles compare to that particular calibration standard. The complex data would require equally complex analysis in order to extract new data pertaining to a previously uncharacterised sediment.

The measured turbidity data could even be compared with multiple different calibration standards as part of a generalised characterisation procedure. Another use for the WAGF is to compare measured turbidity data with itself. Experiments that involve a variable flux of sediment concentration over a period of time could utilise the WAFG to highlight changes in the PSD, given detailed knowledge of the initial PSD. An example of this type of experiment is the sediment settling experiment described in this chapter. The main features of both quantities are summarised in Table 4-1.

Table 4-1. Features of the AGF and the WAGF.

Use-case	AGF	WAGF
Application type	Represents instrument sensitivity	Comparison & relative characterisation
Data type	Absolute (pseudo-absolute)	Relative
Calibration	Instrument baseline	Calibration standard or self-referencing
Units	dB	dB(x), where x is the weighting function

4.4 The importance of the instrument geometry

4.4.1 LED intensity and beam divergence

The data obtained in section 4.3 involved the selection of an LED intensity such that under baseline conditions (i.e. water only in the sample cell) the output voltage of the direct-beam sensor (0°) was only just generating its maximum value. It is important that the direct-beam sensor is not driven into saturation, because as the beam intensity increases, the spatial divergence of the beam changes (it becomes broader). This change in beam divergence affects the response of the entire system when sediment is present in the water, since the probability of light scattering into the forward angles is increased by a more disperse beam. In Figure 4-23, photograph (a) shows the beam spot with an LED current of 1 mA – the case in which the current is optimal. Photograph (b) shows the 4 mA beam spot with its brighter centre. The difference between the 1 mA and the 4 mA case is easier to see in photographs (c) and (d), which are copies of (a) and (b) with the same degree of colour and contrast enhancement applied. The 4 mA beam spot in photograph (d) shows clearly how the spatial divergence of the beam has changed, as a markedly brighter central region is centred on the 0° position, with its outer circumference encroaching on the 10° positions on either side of it.

(a) 1 mA (b) 4 mA

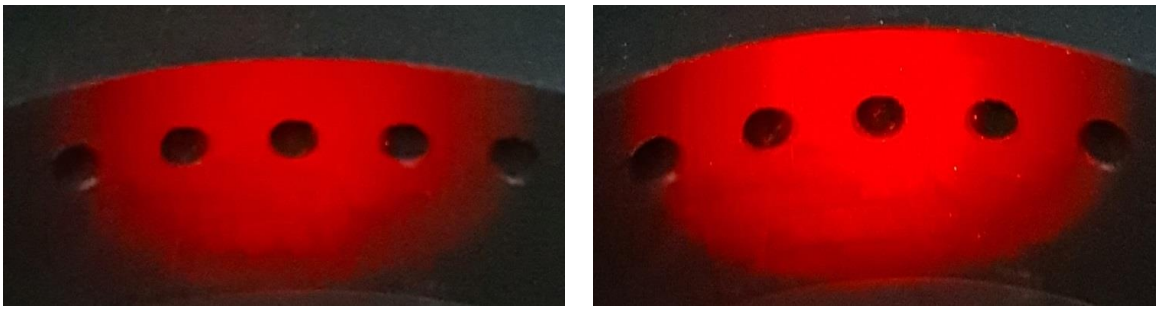

(c) 1 mA enhanced (d) 4 mA enhanced

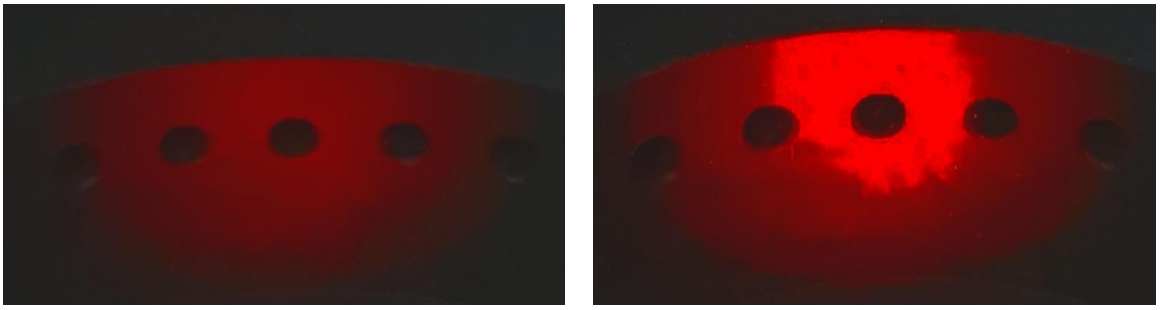

Figure 4-23. Photographs of the inner surface of the sample ring showing the illumination from the 622 nm LED with the sample-cell removed. (a) 1 mA, (b) 4 mA, (c) 1 mA enhanced, and (d) 4 mA enhanced.

The effect that the beam divergence (and intensity) has on the TARDIIS system response is illustrated in Figure 4-24. The increased brightness of the LED has altered the spatial divergence of the light beam, effectively changing the geometry of the experiment. The application of the correct calibration procedure and the maintenance of a precise and stable LED current is therefore crucial to the reproducibility of TARDIIS measurement results.

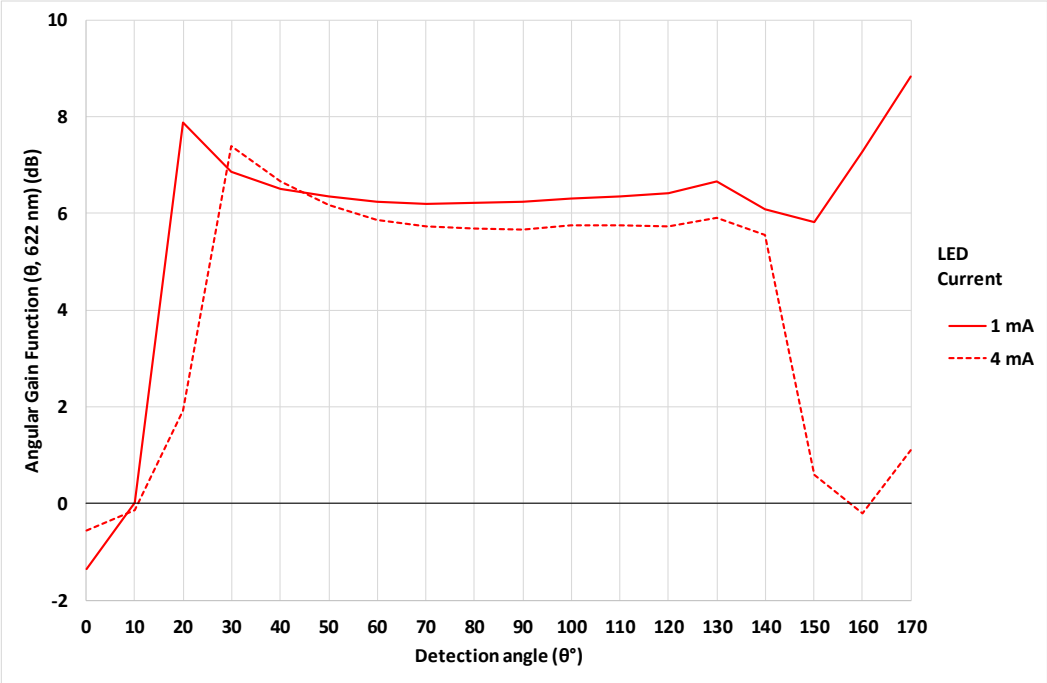

Figure 4-24. AGF(θ, 622 nm) for loess concentration 0.5 g l^{-1} at LED currents of 1 mA and 4 mA.

4.4.2 The relationship between sediment concentration and the backscatter fraction

The backscatter fraction B_b (Equation 4-8) was plotted for each concentration of loess (Figure 4-25). The general trend is that B_b is logarithmically proportional to concentration. Observing the backscatter fraction data at three different wavelengths (470 nm, 622 nm, and 940 nm), the three curves have the same general logarithmic shape (power-law, exponential and linear fits were also attempted, all of which resulted in much lower coefficients of determination). Although the 470 nm curve and the 940 nm curve are almost identical, this similarity is likely to be a *felix culpa*. The 470 nm data clearly displays a marked divergence from the logarithmic form at 1.5 g l^{-1}, the 2.0 g l^{-1}, and the 4.0 g l^{-1} positions in particular, which is reflected in the value of the coefficient of determination (Table 4-2).

Table 4-2. Logarithmic fits to backscatter fraction vs. concentration data, where ρ_m is the mass concentration of the loess suspension.

Wavelength (nm)	R^2	*p-slope*	Function	
470	0.824	0.0119	$B_b = 0.2403 \ln(\rho_c) + 0.3447$	*4-13*
622	0.957	0.00020	$B_b = 0.2762 \ln(\rho_c) + 0.3183$	*4-14*
940	0.951	0.00029	$B_b = 0.2375 \ln(\rho_c) + 0.3449$	*4-15*

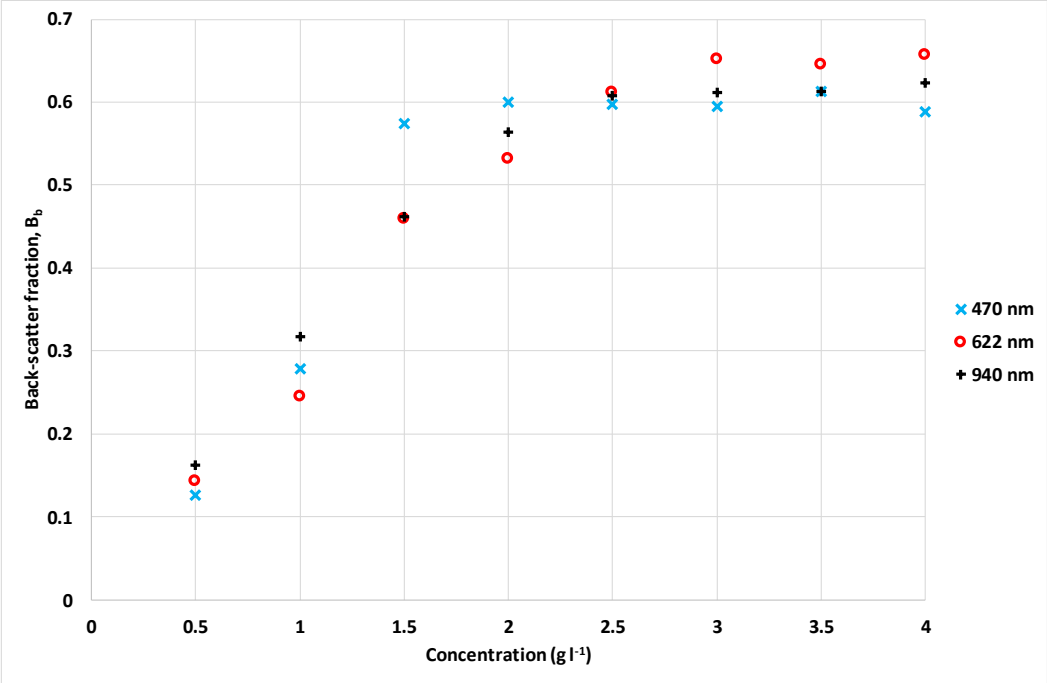

Figure 4-25. Steady-state backscatter fraction B_b as a function of loess concentration, as measured using TARDIIS at 470 nm, 622 nm, and 940 nm incident light wavelengths.

The increased backscatter fraction in the 470 nm data at a loess concentration of 1.5 g l^{-1} is explained by the presence of intensity peaks at 110°, 130° and 170° (Figure 4-26). The relatively larger degree of forward scattering in the 622 nm and 940 nm data at the 0° to 20° positions is also evident in the figure. As the concentration reaches 2.5 g l^{-1} there is a convergence in the backscatter fraction at all three wavelengths (Figure 4-25). The peaks in the 470 nm phase function are still present, but the general shape of the phase function has become more rounded at all wavelengths (Figure 4-27). Only the 622 nm phase function has any pronounced forward scattering relative to the other two signals.

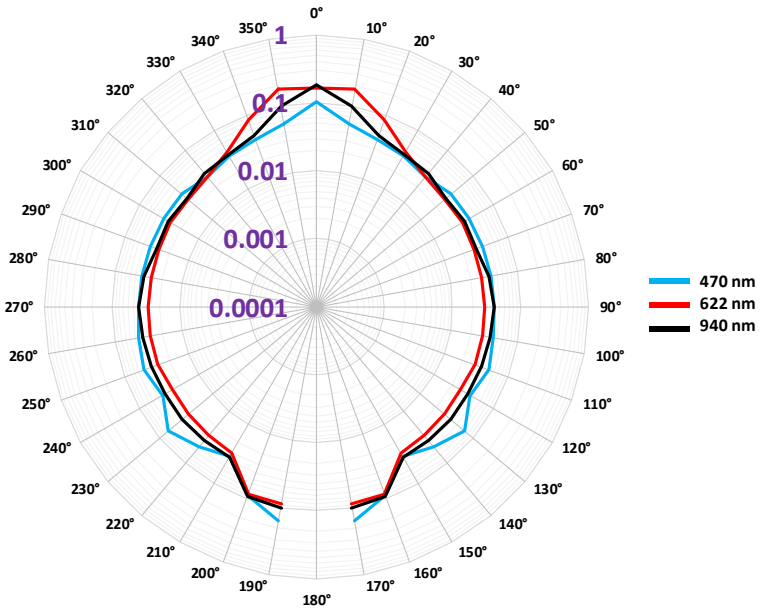

Figure 4-26. Loess scattering phase functions at 1.5 g l^{-1}.

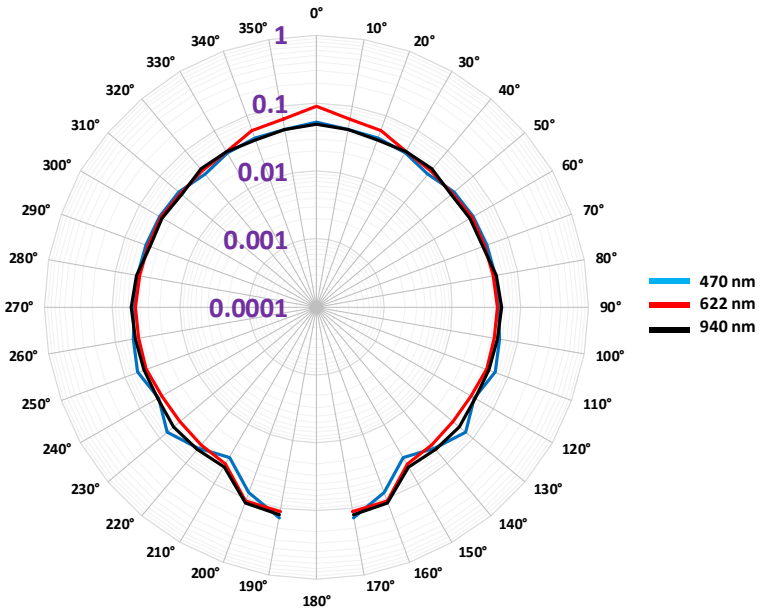

Figure 4-27. Loess scattering phase functions at 2.5 g l^{-1}.

When the loess concentration is 4.0 g l^{-1}, the backscatter fraction is lower than the logarithmic predictions for all wavelengths (Figure 4-25). The slight intensity minima at the 150° position that has been present in all three phase functions has become progressively smaller in the 470 nm

signal (relative to the other two wavelengths) as the concentration has increased to 4.0 g l^{-1} (Figure 4-28). A reduction in the 160° intensity is also apparent in the 470 nm phase function.

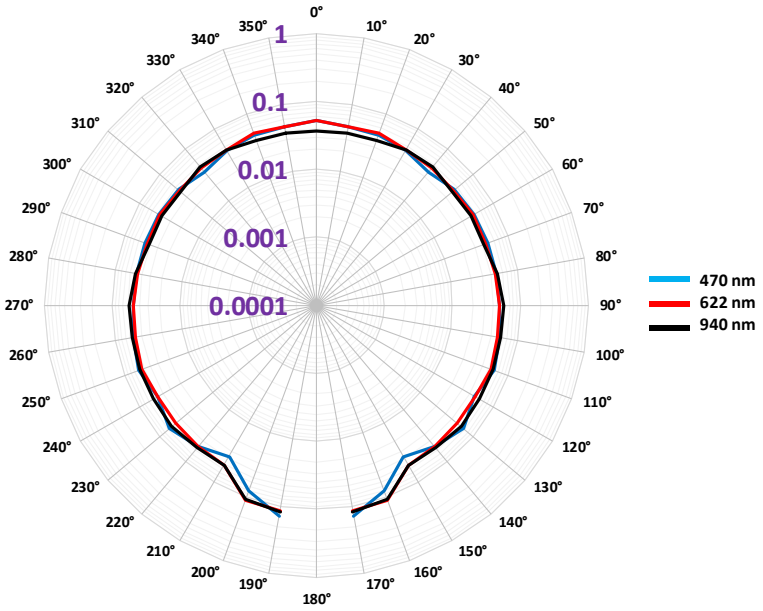

Figure 4-28. Loess scattering phase functions at 4.0 g l^{-1}.

It is clear that the suspended-sediment concentration affects the backscatter fraction such that higher concentrations of suspended sediment show proportionally more backscattering than the lower concentrations do. However, this relationship does not precisely adhere to any simple mathematical rule. A logarithmic function notionally describes the measured data – more so at wavelengths of 940 nm and 622nm than at 470 nm (Table 4-2). The deviations from the logarithmic form are important, since they highlight the presence of features in the scattering phase function. However, some proportion of the variation from a continuous function could be due to errors in the measurements. These errors could arise from small imperfections in the homogeneity of the sediment distribution within the sample cell during stirring. The small differences would become more apparent at higher concentrations, as the efficiency of the stirring (in terms of the ability of the generated vortex to hold a greater mass of sediment) could decline. This effect may be manifesting as measurement noise in the 3.0 g l^{-1} to 4.0 g l^{-1} region of Figure 4-25.

4.5 Summary of the observations.

I. The beam divergence is a function of the particular LED. The suspended sediment also affects the beam divergence, and hence the geometry of the turbidity measurement.

II. By finding the mathematical form of the beam divergence, it should be possible to model numerically the light scattering from suspended sediment.

III. There is a relationship between the sediment concentration and the backscatter fraction. This relationship may not have a well-defined mathematical form, meaning that the backscatter fraction does not precisely indicate concentration.

IV. The relationship between beam divergence and backscatter fraction is dependent upon sediment properties. These properties cause incident light to interact in a complex manner that is not proportional to the concentration of the sediment.

V. The ratio of the backscatter fractions measured at different incident wavelengths of light does not change in a predictable way as the sediment concentration increases linearly.

VI. The phase function evolves from being biased towards forward scattering at low concentrations, to becoming more directionally homogeneous (i.e. rounded) at higher concentrations.

VII. At low concentrations, there are many notable differences between the phase functions at different wavelengths. At high concentrations, those differences become restricted to the 0° to 20° forward scattering angles, and the back-scattering angles - particularly from 110° to 170°.

VIII. The AGF and the WAGF are potentially a better way to quantify turbidity than are the existing measurement units, and could potentially provide a backbone for future measurement standards.

IX. Some modifications to the basic TARDIIS design would be beneficial. For example, the added facility to incorporate ND filters into some of the forward detection angles, combined with a facility to vary the amplifier gains, would allow a wider dynamic range of turbidities to be explored. More precise control of very low LED currents would improve calibration errors. Ambient light rejection can be improved by enhancing the amplifier electronics, and by the inclusion of an enclosure for the instrument.

4.6 Discussion

The evaluation of TARDIIS as an instrument for measuring the turbidity of water due to the presence of suspended sediment, has shown that it is fit for purpose. During the evaluation process, a new methodology for the reporting and comparison of turbidity data has emerged, with many potential applications. This outcome produced the definitions of the *angular gain function*

(AGF) and the *weighted angular gain function* (WAGF), thus fulfilling a key aim of this thesis. The AGF notionally suggests that a *positive* decibel value indicates that *scattering* processes dominate the measurement, and that a *negative* decibel value indicates that *absorption* processes dominate the measurement (Figure 4-29).

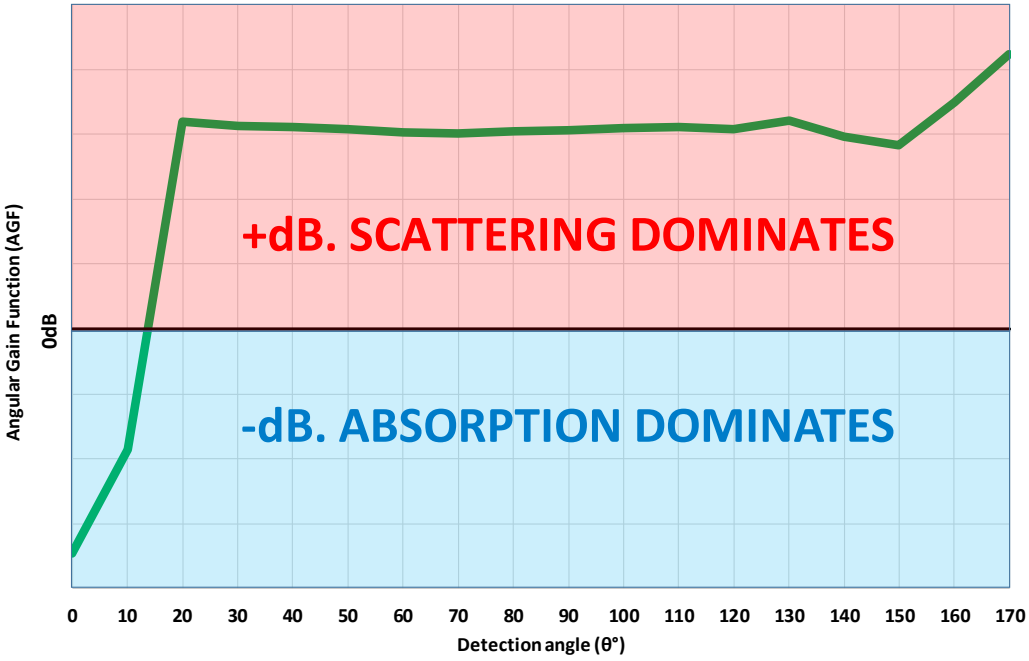

Figure 4-29. How the AGF implies the dominance of light-scattering or light-absorption.

The analyses presented in this chapter were based on a small number of data sets. Only one type of sediment has been examined thus far (loess). Clearly it is not possible to present a thorough statistical error budget, given the minimal data. However, reasonable efforts have been made to quantify the errors where possible. The future continuation of this work requires heavy investment in data collection from a range of diverse samples. Never the less, the data that *do* exist have proved invaluable as a means to the development of new methodology.

Moving forward, the data mining of the complex data sets generated by TARDIIS has to be considered. Many observations of the turbidity data show potential correlations, and yet it has proved to be extremely difficult to extract precisely what those correlations are, and how they are defined mathematically. Two main strategies are suggested, both of which could provide feedback into the instrument design process.

a. Empirical data-driven modelling, using machine-learning and deep-learning algorithms.
b. Numerical modelling of the physical processes associated with turbidity measurement.

4.6.1 Empirical data modelling

Data-driven approaches to modelling in physical geography can extract useful knowledge from diverse data sets obtained in the various sub-disciplines: e.g. hydroinformatics (Solomatine et al. 2009); soil science (Arya & Paris 1981); river water quality (Burchard-Levine et al. 2014); oceanography (Collin et al. 2011, Kim et al. 2014); and drinking water quality (Juntunen et al. 2013). In the case of TARDIIS, the data-driven modelling approach by the application of machine-learning methodologies - given enough carefully selected data - may reveal hard-to-reach information about particle-size and particle-shape distributions in unknown sediment samples. The knowledge derived from the modelling would inform the instrument design, thus creating an "intelligent" turbidity instrument.

4.6.2 Numerical modelling

The spatial divergence of the light beam implies that the optical path length l does not have a single fixed value based solely on the geometry of the sample cell. The sediment suspension itself therefore affects the geometry of the turbidity measurement in a complex interaction with the incident light beam. Knowing the mathematical form of the light-beam divergence would potentially enable a more detailed calibration of the TARDIIS instrument.

A process-based numerical model of the light scattering from suspended sediment that has a number of parameters relating to the physical properties of the sediment (such as the PSD and particle shape) could be developed. The beam divergence must be modelled correctly in order for the processes-based model to perform adequately. This approach could potentially provide new insights into sediment characterisation methodology, and enable the optimization of the TARDIIS instrument. Calibrations based on sediments with well-known PSDs and particle shape profiles could facilitate the characterisation of unknown sediments, since the model could predict the expected output of TARDIIS.

Chapter 5 Modelling the instrument response

This chapter aims to act upon one of the suggestions in conclusion to the literature review at the beginning of this thesis. Section 2.20, point 4 stated:

"*The development of new light-scattering models will permit more sophisticated approaches to turbidity measurement, in particular by the use of parameter-rich data sets obtainable from multi-parameter methods. This approach will facilitate the improvement of turbidity standards, and could increase the accuracy of large sediment particle detection.*"

The numerical model presented here is just the first step in the development of a new and comprehensive light-particle interaction model that will be capable (ultimately) of accurately describing the turbidity of water due to the presence of suspended sediment. The main aim of this first development step is to determine whether the Mie theory of light scattering (Mie 1908) is capable of modelling the response of the TARDIIS instrument to a suspended sediment. To that end, a detailed analysis of the TARDIIS instrument response is presented, incorporating the effects due to geometry of the instrument and the light-particle interactions according to Mie theory.

A systems-integration approach to model construction is described, which incorporates pre-computed Mie interactions via a third-party software application (Laven 2018). The core functionality of the model is implemented as a ray-tracing code, incorporating a statistical description of the spatial distribution of the light beam. The suspended sediment PSD is provided as an empirical distribution function based on Horiba LA950 particle size analyser data. This modular approach to model construction reduces the iterative calculation complexity, and hence increases the speed of computation.

5.1 Developing the model from first principles

The accepted definition of the beam attenuation coefficient c (Equation 5-1) divides it into scattering (b) and absorption (a) components (e.g. Kirk 1985, Davies-Colley & Smith 2001, Smith & Davies-Colley 2002).

$$c(\lambda) = a(\lambda) + b(\lambda) \qquad 5\text{-}1$$

This model presents an infinitesimal scattering volume of water in which light rays interact with suspended particles (Figure 5-1). The language used to describe these interactions suggests that

light detected in the 0° direct-beam position is the only light in the system that experiences absorption by the suspended particles, referred to as attenuated light. Similarly, the light detected at all other angular positions is referred to as scattered light, suggesting that the detected light has only experienced a scattering event, i.e. no absorption. It can be speculated that the reason for the choice of the labels "attenuation" and "scattering" as described in Figure 5-1, is that those words describe what is observed at only one key measurement position, i.e. directly opposite the light source. From this perspective, there is only one attenuation measurement. Light scattering away from the direct beam or being absorbed in the path of the direct beam causes this attenuation. A problem with this use of language arises when measurements of light intensity are made at other angular positions, i.e. not directly opposite the light source. In this case, it is "scattering" that is being measured, and not "attenuation". This labelling is clearly not correct since a light sensor can only provide an absolute measure of light intensity. This intensity, when compared with the intensity of the light source, is termed *attenuation*.

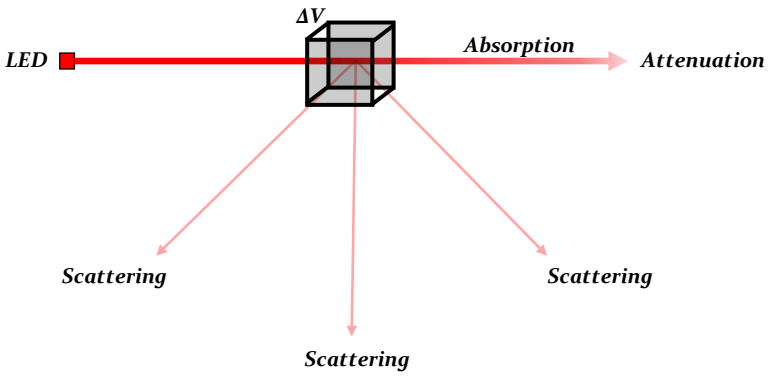

Figure 5-1. The generally accepted model of light scattering by a suspension of particles. ΔV represents an infinitesimal volume containing suspended particles. This representation defines the measurands as attenuation and scattering, and suggests that absorption is the only process occurring within the sample volume.

It is more accurate to note that the light detected at *every* angular position has been attenuated in some way by the medium through which it has passed, and should therefore be labelled as "attenuation". Each angular attenuation measurement is the sum of multiple absorption *and* scattering interactions. Figure 5-2 shows how light rays are attenuated in a complex set of interactions with suspended particles. The work described in sections 4.1.5 and 4.3.3 is based on this interpretation of light propagation. The traditional concept of the scattering coefficient $b(\lambda)$ and the absorption coefficient $a(\lambda)$ have been encapsulated into a definition of the *angular beam attenuation coefficient* $BAC(\theta, \lambda)$, defined in Equation 4-9.

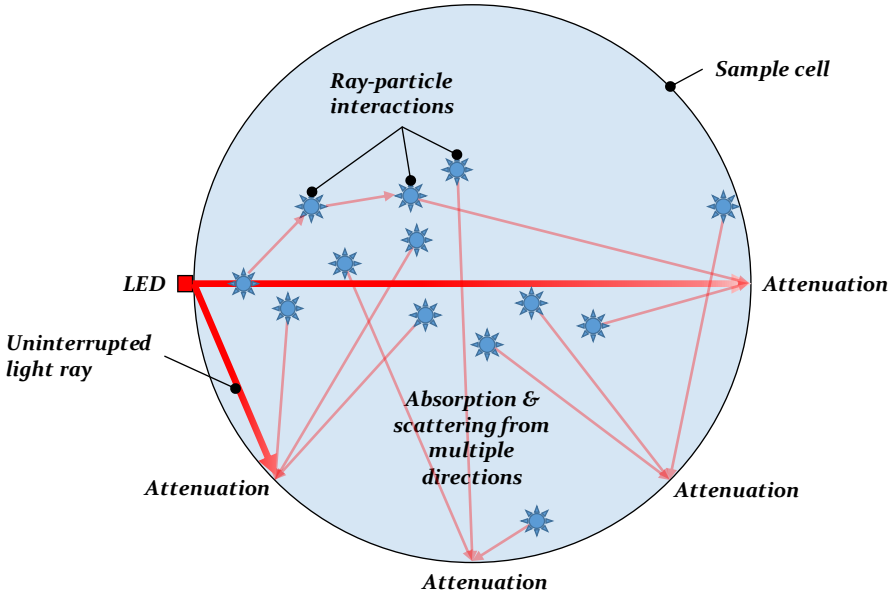

Figure 5-2. The interaction between light rays (red arrows) and suspended particles (blue stars).

This new definition of the angular beam attenuation coefficient is correct from the perspective of the actual measurements of light intensity, and does not imply any specific cause for the attenuation of the incident light due to the misleading use of language. The processes that cause the attenuation of the incident light can now be examined in an unbiased way. Process-based conceptual models of light-rays interacting with suspended particles can be developed that do not report data with pre-imposed meaning due to mislabelling. By using $BAC(\theta, \lambda)$ to report angular light-attenuation data (measured outside the sample volume), the scattering and absorption processes (occurring inside the sample volume) can be examined in isolation. A practical way to create a process-based model is by numerical simulation in computer software. By comparing the outputs of the numerical simulation with empirical data, some insight into the scattering and absorption processes may be achieved.

5.2 CLARITAS (ComputationaL Accumulator of Rays Invoking Tracing And Scattering): A process-based model of light interactions with suspended particles

5.2.1 Model geometry and basic operational principles

Full details of the model geometry are available in Appendix 1. The following discussion has minimal references to the model geometry and model parameters, for the sake of readability.

CLARITAS is a simple numerical model that generates arbitrary "rays" of light that are "fired" from a simulated LED at a probabilistically determined emergence angle δ into a simulated sample cell. Each ray has a property of direction and an initial radiant intensity I_0 (mW sr^{-1}). As

the TARDIIS instrument geometry is symmetrical about the beam axis, the beam emergence angle is simplified to half-angle ε (Figure 5-3).

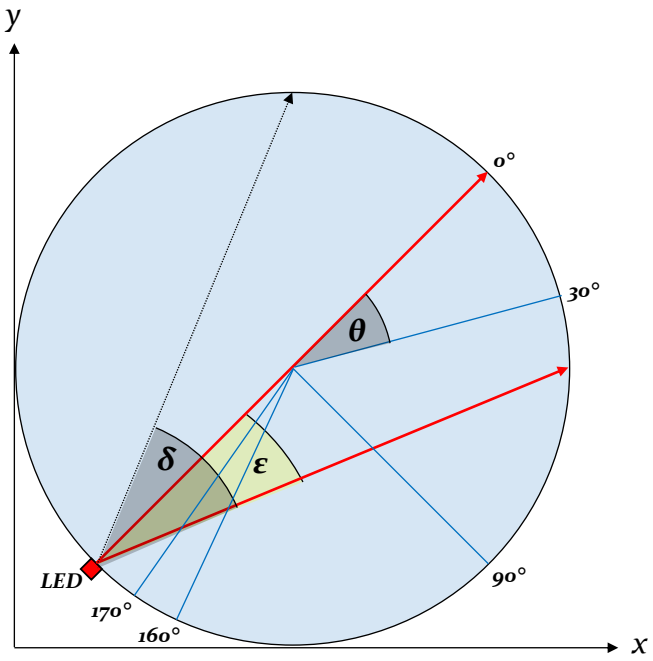

Figure 5-3. Diagram showing xy plane of TARDIIS sensors (top view). LED beam divergence δ is symmetrical, and is simplified to half-angle ε. Several of the sensor locations are shown (θ = 0°; θ = 30°; θ = 90°; θ = 160° and θ = 170°), and the red square is the LED light source. The red arrows are examples of light rays.

In ray-tracing mode, the simulated sample cell contains only water (i.e. no suspended particles), which has no effect on the passage of the simulated rays. Either the rays will hit one of the 18 simulated sensors (at 10° intervals of θ° around the circumference of the simulated sample cell) and are accumulated (i.e. the number of hits is counted per sensor, and total radiant intensity is recorded per sensor), or they will exit the sample volume and are lost. User-definable parameters allow for the possibility of internal reflection from the wall of the sample cell for those rays that do not hit sensor positions.

In light-scattering mode, CLARITAS becomes a *discrete particle model* (DPM). A pre-computed suspended particle distribution now populates the sample cell, and a collision probability p_c is calculated for the ray (Equation 5-2), which travels step-distance d_r through the sample cell (where V_T is the total volume of the sediment distribution [m^3]) during each iteration of the algorithm. If a ray collides with a suspended particle, it will scatter (i.e. change direction) according to a pre-computed Mie code. Its instantaneous radiant intensity value I_n decreases

according to a Beer-Lambert attenuation calculation (n is the incremental number of particle collisions experienced by the ray).

$$p_c = V_T d_r \qquad 5\text{-}2$$

In either mode, the convergence criterion can be pre-set to be dependent on either the achievement of a target radiant intensity at a selectable scattering angle, or by the achievement of a target number of rays emerging from the virtual LED. The latter approach is depicted in Figure 5-4.

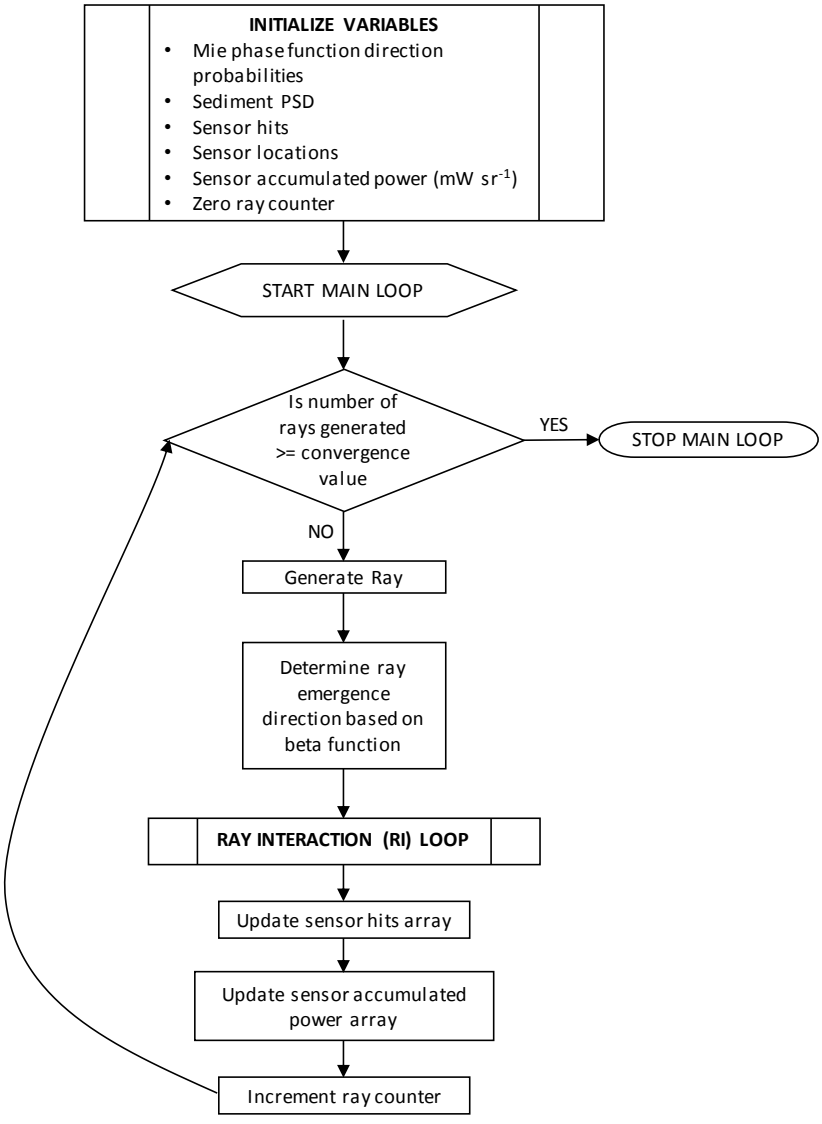

Figure 5-4. CLARITAS main program algorithm for modelling ray-particle interactions at a pre-defined wavelength of light. The ray interaction loop describes how a single ray iteratively traces a path through the sample volume.

CLARITAS reports data as the absolute radiant intensity at each detection angle $\theta°$. The user provides an arbitrary initial ray intensity and a step distance across which a simulated ray will traverse in one iteration of the ray interaction loop (Figure 5-5). In the development of the CLARITAS model, some optimal values for those parameters were determined manually. It would be beneficial in future work to include these parameter optimisations in an automated procedure (see section 5.3).

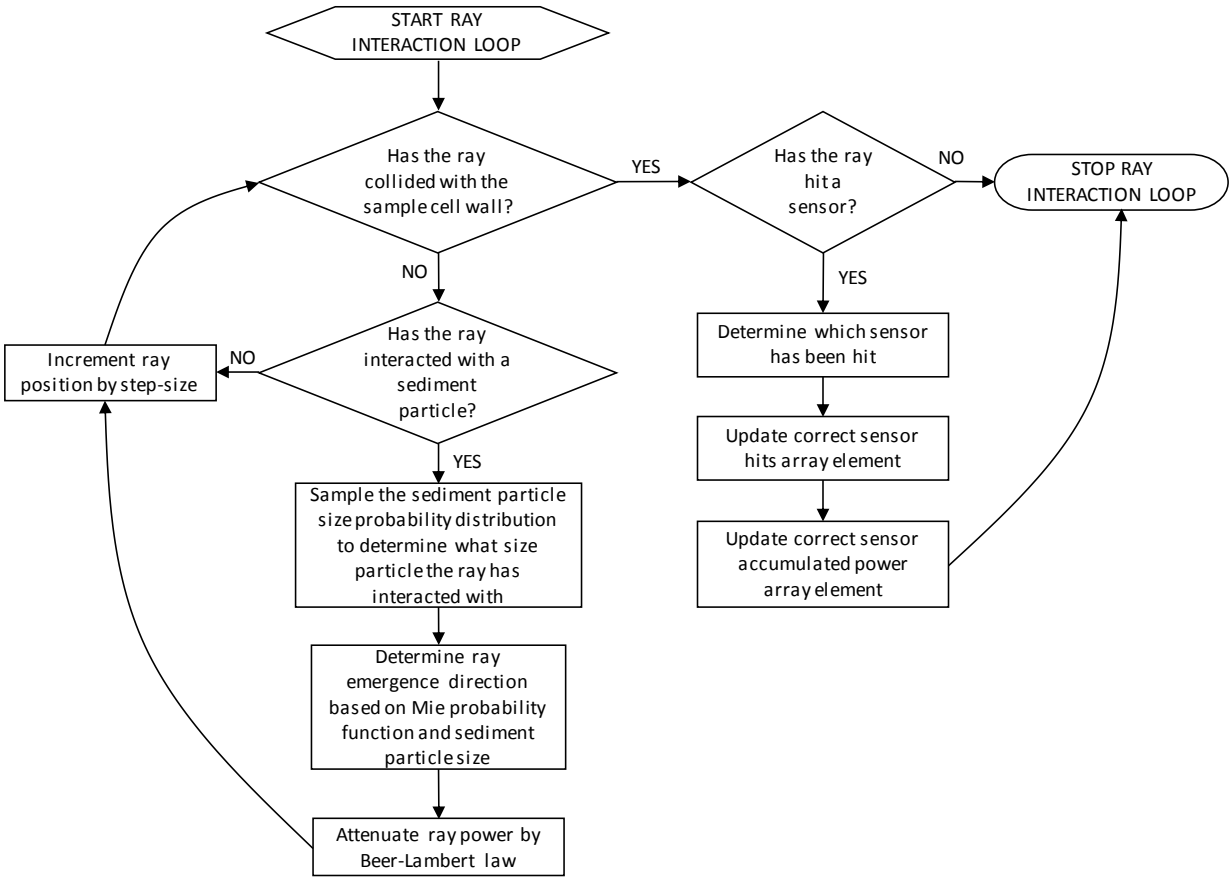

Figure 5-5. CLARITAS ray interaction (RI) loop, describing the path that a single ray takes through the sample volume.

5.2.2 Modelling the loess PSD

The particle size distribution of the loess sediment used in the steady-state experiments of Chapter 4 was measured by a Horiba LA950 particle size analyser (results reported to 1 nm precision by Horiba software). The probability mass function (PMF) of the size distribution (Figure 5-6) has a bimodal shape, with the largest peak at 51.471 μm, and a smaller peak at 17.377 μm.

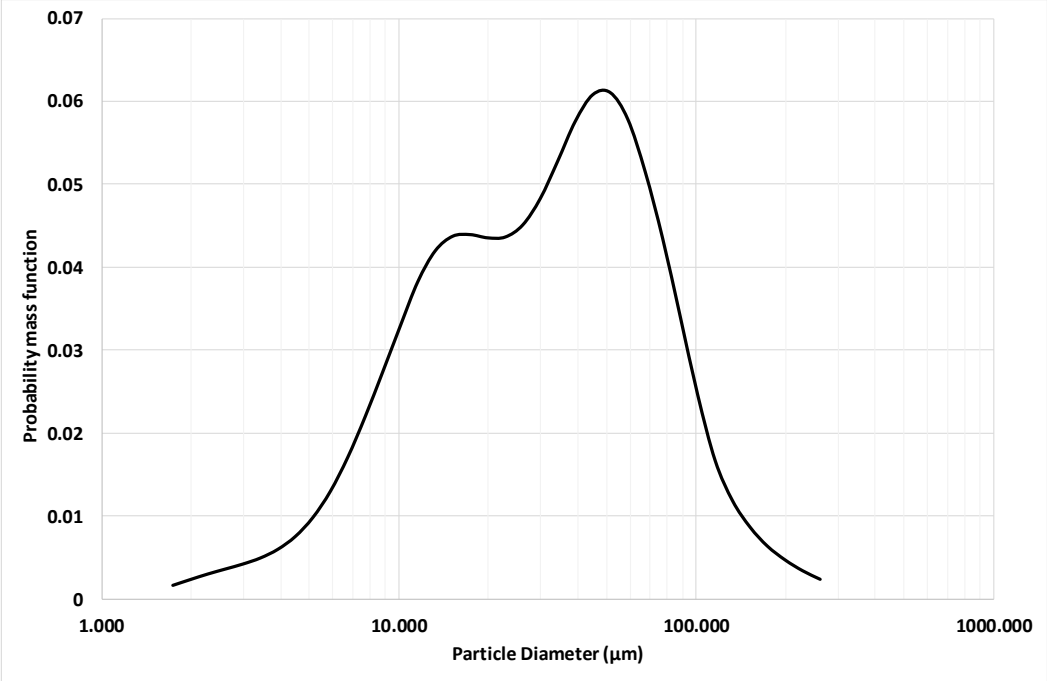

Figure 5-6. PMF of loess PSD.

In terms of sediment size classification, the Horiba software produced the following percentages (Table 5-1):

Table 5-1. Size classification of loess sediment.

Sediment size class	**Percentage of total sample (%)**
Medium sand	0.1
Fine sand	18.4
Silt	79.0
Clay	2.5

In the CLARITAS model, when a light ray interacts with a sediment particle, a function for selecting the size of the particle from the size distribution of the loess sediment is needed. That function is dependent upon the PMF described in Figure 5-6, and returns a probability that is not equal for all particle sizes (e.g. the size most often encountered will be the peak value of 51.471 µm). The function takes a weighted sample of the particles in the discrete size bins as provided by the Horiba. So the loess PSD is now represented as an empirical distribution function, rather than as a continuous PMF. There are now 38 discrete particle sizes available to the CLARITAS model (Figure 5-7).

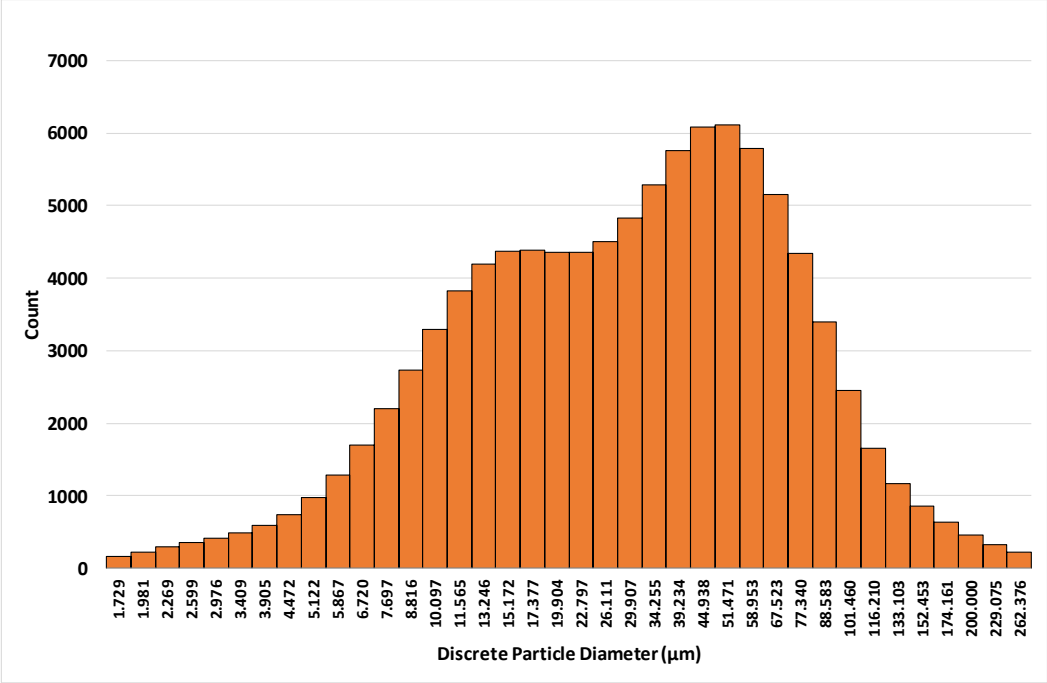

Figure 5-7. Empirical distribution function of the loess sediment particle sizes.

5.2.3 Modelling the beam divergence

The spatial distribution of the light-cone emitted by an LED is difficult to define mathematically. For the CLARITAS model to have any chance at succeeding to simulate the empirical data, the beam divergence characteristics must be known. Sometimes there are data available in the documentation for a particular LED that give some indication of how the light field is spatially distributed, but this is not always the case. Even when the data are available, they are only valid for a specific set of test conditions (e.g. nominal current), and are not easily convertible into a mathematical form suitable for a probabilistic simulation.

The beam divergence was modelled as a probability density function, such that sampling from that distribution would provide the direction from which a newly emitted light ray would exit the virtual LED. This emergence direction is parameterised by the *horizontal beam emergence angle*, ε, (Figure 5-3) which ranges from 0° (directly forward) to 90° relative to the LED. Now the question is which PDF to use?

The initial way to answer this question was to make guesses at the model parameters and rely on trial-and-error, refining the parameters with each iteration. This approach was fundamentally difficult due to the time required. Depending on the model parameters, one simulation could take anywhere from 5 to 48 hours to run. Initial investigations showed that the Uniform distribution and the Normal distribution were not suitable candidates for the beam emergence PDF, as they could not replicate the centrally very narrow spatial distribution of the light beam. The Beta

distribution is a continuous distribution with two shape parameters, α_1 and α_2. This distribution gives a reasonable and physically meaningful "shape" to the beam divergence. After considerable refining of the CLARITAS model parameters, a Beta distribution with shape parameters $\alpha_1 = 0.25$ and $\alpha_2 = 5.0$ was chosen as the best achievable manual result. In future development of the CLARITAS model, the beta function could be included in an automatic optimisation procedure (see section 5.3). Alternatively, a completely different arbitrary distribution function could be used to model the beam divergence.

The PDF is initially calculated on the interval [0, 1], and then normalised and mapped onto the interval [0°, 90°] (Figure 5-8).

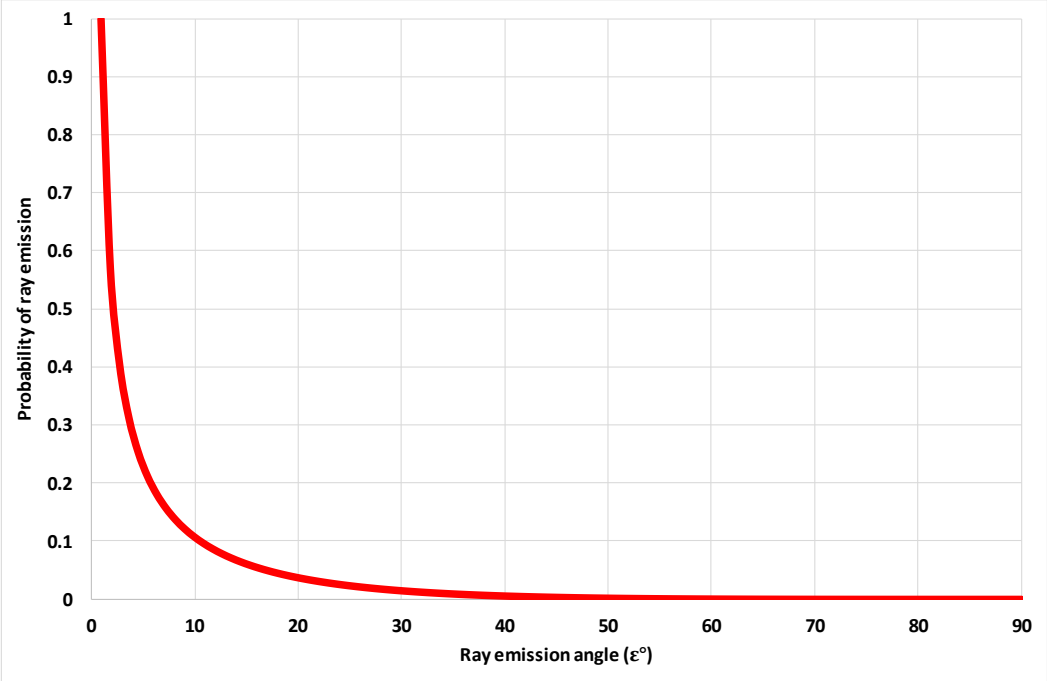

Figure 5-8. PDF of light ray emission angle probability in the CLARITAS model. Normailsed beta function with shape parameters $\alpha_1 = 0.25$ and $\alpha_2 = 5.0$.

5.2.4 Absorption of light by suspended particles

Each time a ray interacts with a particle, its radiant intensity is attenuated by a Beer-Lambert function in CLARITAS. A user-definable absorbance parameter A is utilised, such that:

$$I_{n+1} = I_n 10^{-A} \qquad 5\text{-}3$$

where I is the radiant intensity of the light ray, and n is the number of ray-particle interactions experienced by the ray (i.e. RI loop iteration number, see Figure 5-5). The use of the simple absorbance parameter A does not assume any prior knowledge of particle properties, and the user must provide an arbitrary value. One very practical reason for not providing a precise value

for the absorbance of a given sediment, is that it is not always possible to find a suitable value in the literature. By the use of automated optimisation in future versions of the CLARITAS model (see section 5.3), it should be possible to derive the correct value of absorbance for a given sediment. At this stage in the model development, however, it is necessary to estimate the parameter.

5.2.5 Mie scattering by suspended particles

For every ray-particle interaction in the CLARITAS model, the resultant ray direction must be determined. This scattering direction is calculated according to Mie theory (Mie 1908). The computational approach to implementing the Mie scattering function is to pre-calculate the Mie-scattering phase-function using a third-party external application called MiePlot (Laven 2018). The phase-function is computed for each discrete sediment particle size (as per Figure 5-7) at a given wavelength of light, and the data are tabulated for use by CLARITAS. All of the calculations using MiePlot assumed values for the refractive index of the sediment (1.65), and the refractive index of the water in which it was suspended (1.33).

5.2.6 Initial results of the modelling

MiePlot assumes that all of the particles in the loess PSD are spherical. It is expected that there will be some differences between the modelled data and the empirical data due to the loess particles being imperfect spheres. The predicted result displays ten times more than the measured amount of forward scattering, and ten times less than the measured amount of back scattering.

These initial results suggest that Mie theory by itself (at least according to Laven, 2018) does not adequately model the light-particle interactions between rays emitted by a 622 nm LED light source, and a loess sediment suspension of concentration 4.0 g l^{-1} in the TARDIIS sample cell. The usual application of Mie theory –which works very well - is to single particle simulations, or to narrowly distributed particle size populations of spheres. The process-based approach to the modelling of multiple scattering performed by CLARITAS suggests that the repeated application of Mie theory over relatively large distances, when constrained by the instrument geometry, does not adequately describe the gross instrument response on a larger scale.

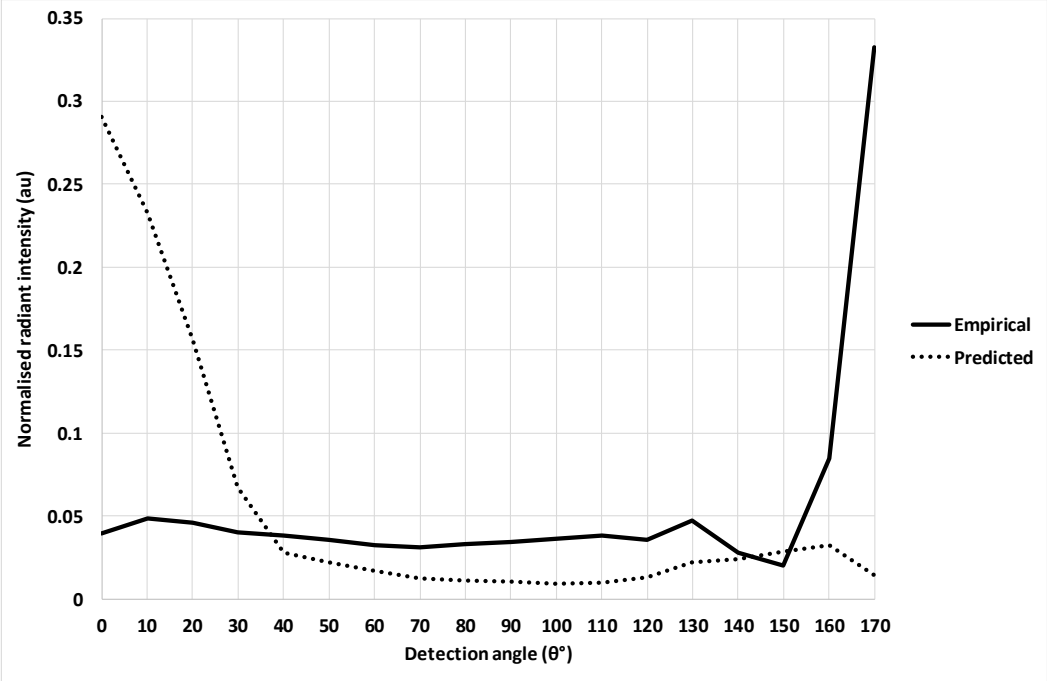

Figure 5-9. Graph showing the normalised output of TARDIIS at 622 nm. The differences between the empirical results (loess at 4.0 g l^{-1}) are compared with the CLARITAS model prediction.

5.2.7 Improving the initial results by the addition of a geometric optics parameter

The CLARITAS model is modular in design, and so a relatively simple upgrade was performed which improved the model output. By the addition of a simple term to approximate the effects of geometric optics, the output shown in Figure 5-10 was achieved using the same empirical data.

The model output now has the correct form (or shape), i.e. it generally follows the line of the empirical data. The improved fit to the empirical data has RMSE = 0.0534. The model is still slightly under-predicting the output in the 0° to 130° range, and over-predicting the output at the 140° to 170° positions. The CLARITAS model is normalised to the total area under the empirical curve.

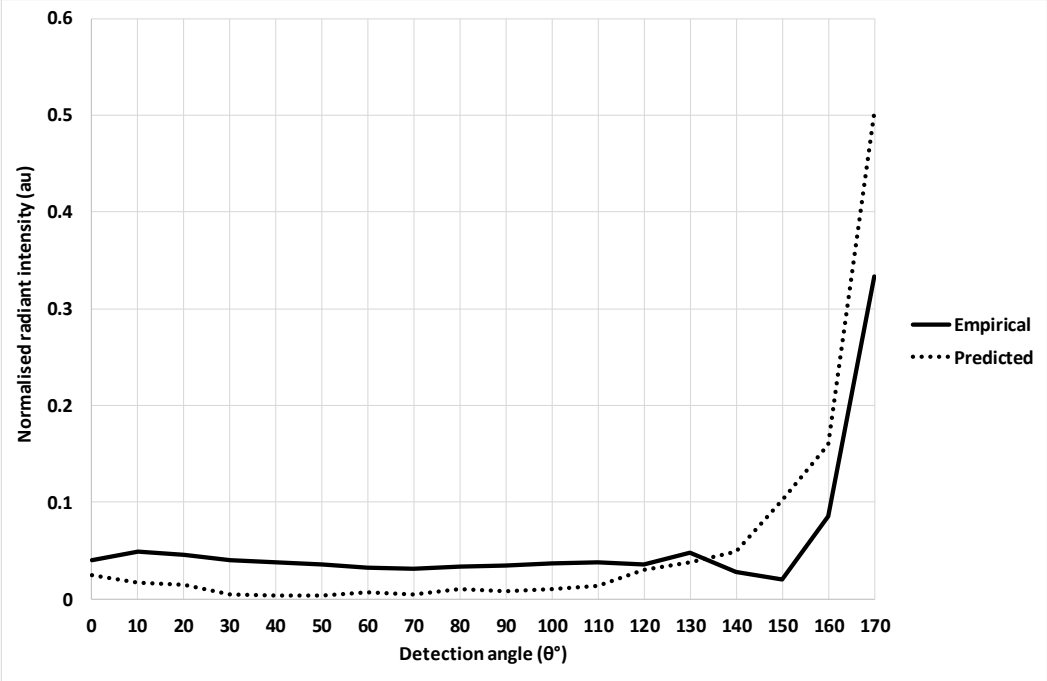

Figure 5-10. Graph showing the normalised output of TARDIIS at 622 nm. The differences between the empirical results (loess at 4.0 g l^{-1}) are compared with the improved CLARITAS model prediction.

5.2.8 Geometric optics in the CLARITAS model

The complete modelling of the geometric optics interpretation of ray-particle interactions is very complex, involving reflection, internal particle refraction, internal absorption, diffraction from edges, and diffraction from particle surface features. CLARITAS is not equipped to perform those calculations. Instead, a gross approximation to geometric optics is provided. This approximation involves treating a small proportion of the sediment particles of diameter $d \geq M_d$ as *randomly oriented planar reflectors* (i.e. mirrors). The parameter M_d is the *Mie transition diameter*, such that particles with diameters equal to or above this threshold are treated as planar reflectors. The probability that any particle that is greater than or equal to the Mie transition diameter will be treated as a Mie scatterer, is parameterised as the *Mie probability,* M_p. Therefore the probability of such a particle behaving as a planar reflector is $1\text{-}M_p$. For example, in Figure 5-9 the probability of Mie scattering is $M_p = 1.00$, and M_d is not relevant in that model since there is only Mie scattering. However, in Figure 5-10 $M_p = 0.962$ and $M_d = 200\ \mu m$. This means that for any ray-particle interaction in which the particle diameter is greater than or equal to 200 μm, there is a 3.8% chance that planar reflection will be the mode of scattering, rather than Mie scattering which will occur 96.2% of the time. The choice of 200 μm for the Mie transition value is as a result of the discussion about scattering regime boundaries in Chapter 2 (Kitchener et al. 2017).

5.2.9 Results of modelling with the inclusion of geometric optics

Multiple iterations of the CLARITAS model were run with λ = 622 nm, α_1 = 0.25, α_2 = 5.0, and M_d = 200 µm, over a range of loess sediment concentrations ranging from 0.5 g l^{-1} to 4.0 g l^{-1}. This range of parameters matched the concentration range over which empirical data from TARDIIS measurements were available. Eight data sets were obtained that were similar to (and including) the data depicted in Figure 5-10. As the model parameter M_p was selected manually, several iterations were required in order to obtain a data set that was considered to have a reasonable goodness of fit (GOF) to the empirical data, as determined by the root mean square error (RMSE). Since all the data are normalised radiant intensity, the range of the dependent variable is from 0 to 1. As it is known, the model is not fully representative of the real physical situation - in particular, due to the approximation regarding geometric optics - an RMSE value of < 0.1 was considered a reasonable fit. In the imperfect case summarised by Table 5-2, an RMSE of < 0.1 was considered to be a reasonable point at which to stop iterating the model, considering that each data set took approximately five hours to acquire. All of the models generated $R_c = 10^5$ virtual rays. Plots of the data listed in Table 5-2 are shown in Figure 5-11 to Figure 5-18. All of the CLARITAS model outputs are normalised to the area under the empirical curve in each case, since that value represents the integrated light intensity of the VSF.

Table 5-2. Goodness of fit of ray-particle models to empirical data, for loess suspensions at λ = 622 nm. $R_c = 10^5$.

Concentration (g l^{-1})	**M_p**	**RMSE**
0.5	0.992	0.020
1.0	0.988	0.036
1.5	0.976	0.031
2.0	0.974	0.030
2.5	0.970	0.036
3.0	0.967	0.041
3.5	0.964	0.047
4.0	0.962	0.053

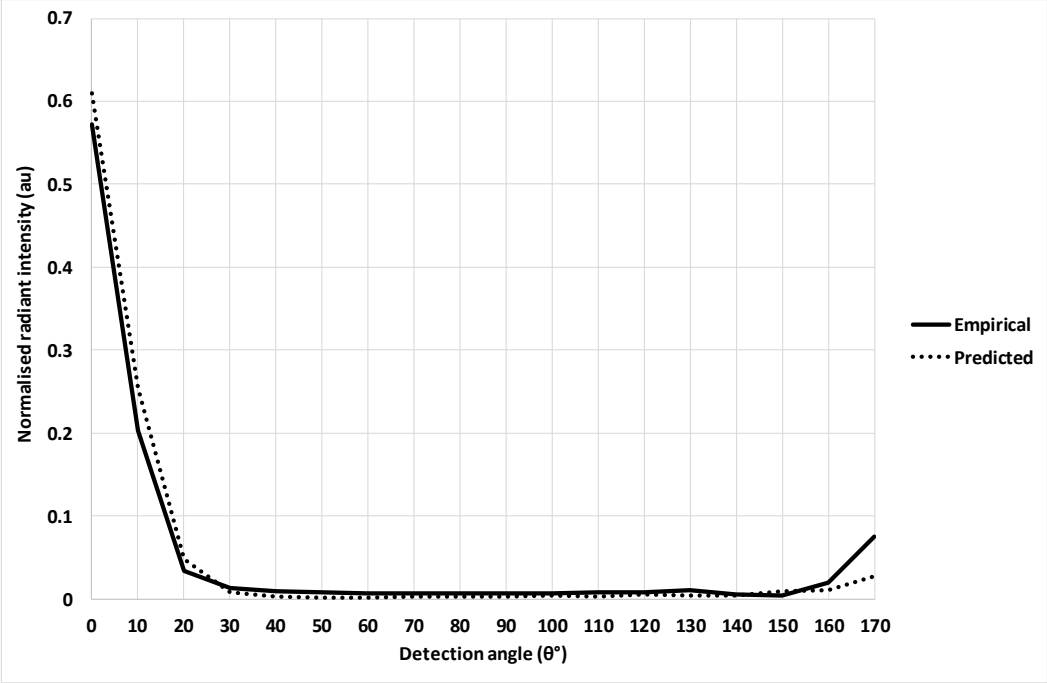

Figure 5-11. Graph showing the normalised output of TARDIIS at 622 nm, M_p = 0.992. The differences between the empirical results (loess at 0.5 g l^{-1}) are compared with the improved CLARITAS model prediction.

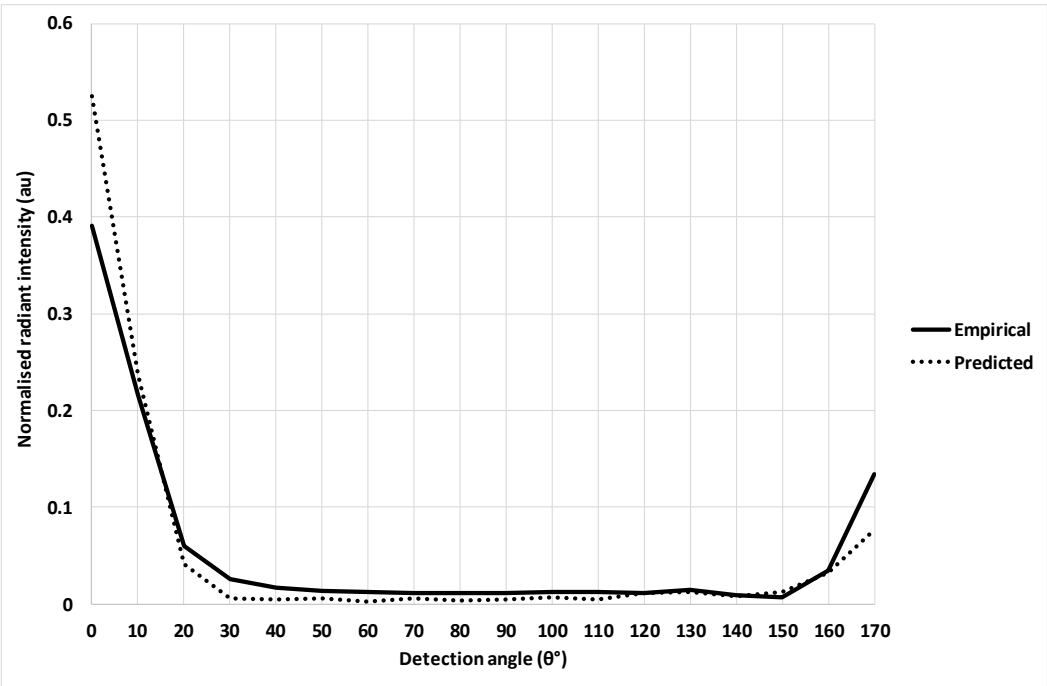

Figure 5-12. Graph showing the normalised output of TARDIIS at 622 nm, M_p = 0.988. The differences between the empirical results (loess at 1.0 g l^{-1}) are compared with the improved CLARITAS model prediction.

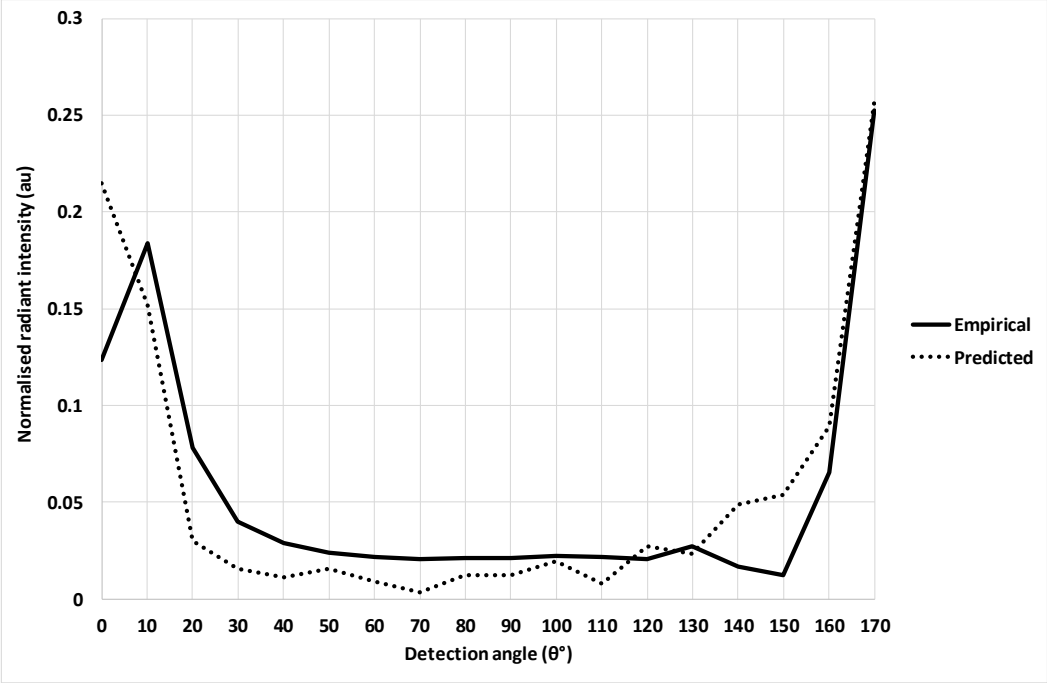

Figure 5-13. Graph showing the normalised output of TARDIIS at 622 nm, M_p = 0.976. The differences between the empirical results (loess at 1.5 g l^{-1}) are compared with the improved CLARITAS model prediction.

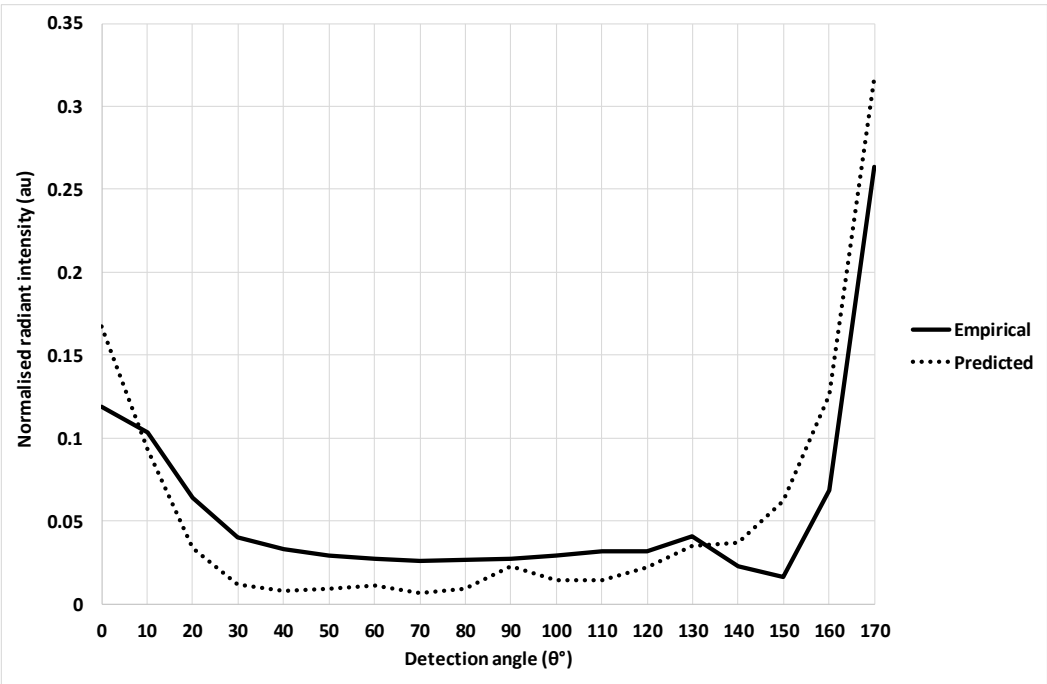

Figure 5-14. Graph showing the normalised output of TARDIIS at 622 nm, M_p = 0.974. The differences between the empirical results (loess at 2.0 g l^{-1}) are compared with the improved CLARITAS model prediction.

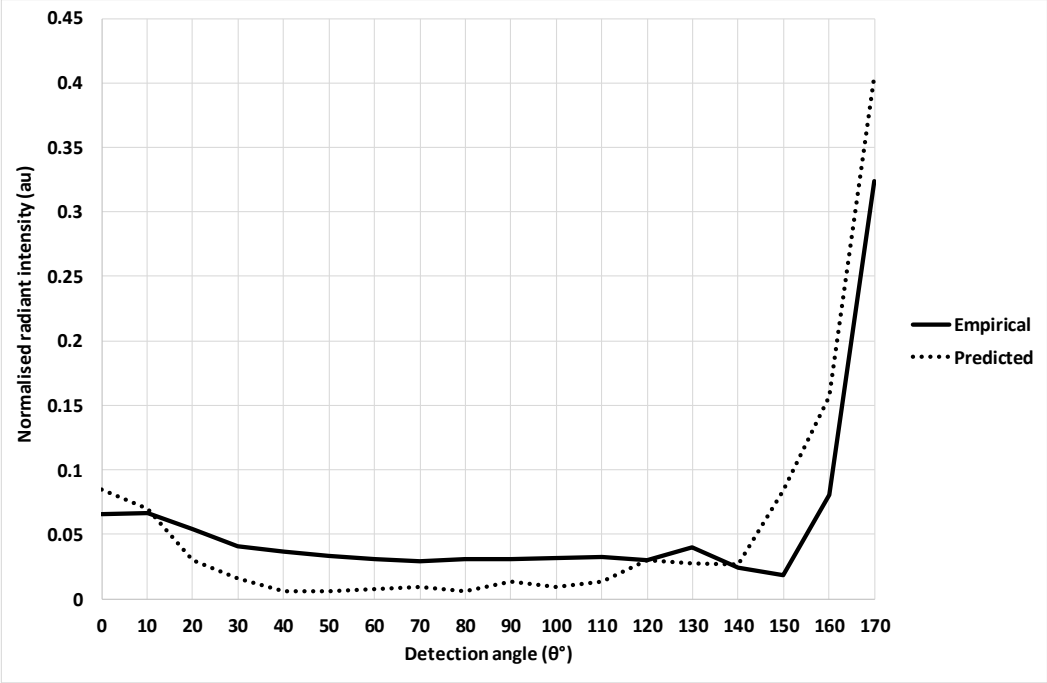

Figure 5-15. Graph showing the normalised output of TARDIIS at 622 nm, M_p = 0.970. The differences between the empirical results (loess at 2.5 g l^{-1}) are compared with the improved CLARITAS model prediction.

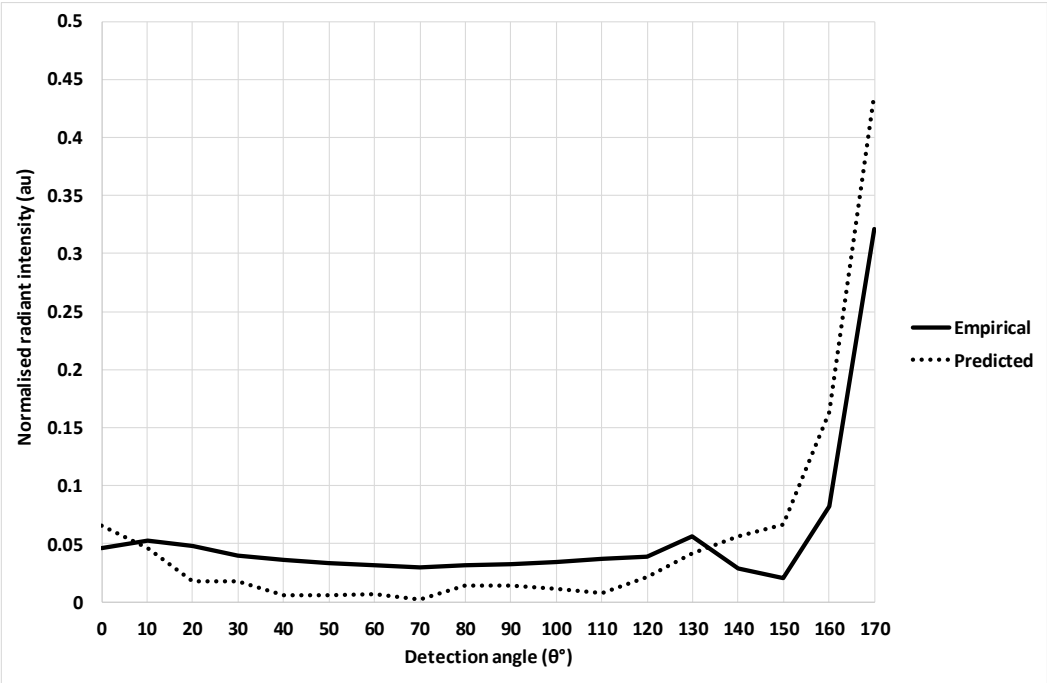

Figure 5-16. Graph showing the normalised output of TARDIIS at 622 nm, M_p = 0.967. The differences between the empirical results (loess at 3.0 g l^{-1}) are compared with the improved CLARITAS model prediction.

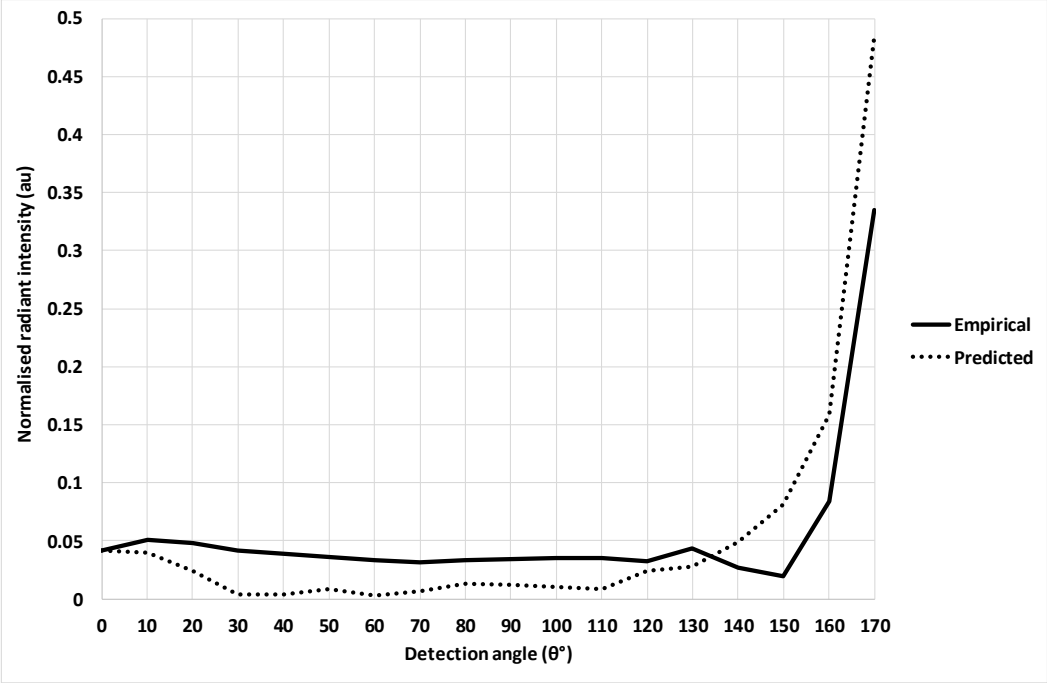

Figure 5-17. Graph showing the normalised output of TARDIIS at 622 nm, M_p = 0.964. The differences between the empirical results (loess at 3.5 g l^{-1}) are compared with the improved CLARITAS model prediction.

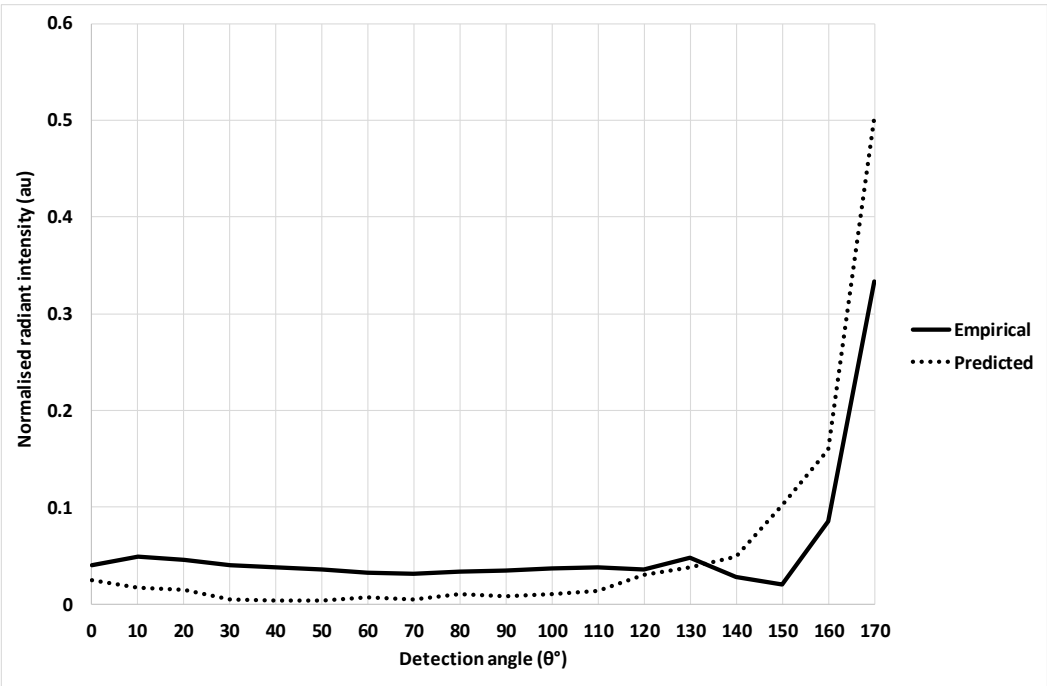

Figure 5-18. Graph showing the normalised output of TARDIIS at 622 nm, M_p = 0.962. The differences between the empirical results (loess at 4.0 g l^{-1}) are compared with the improved CLARITAS model prediction.

The relationship between the loess concentration and the Mie probability, M_p, is tabulated in Table 5-2, and plotted in Figure 5-20. A manual tuning of M_p was used to minimise the RMSE of the corresponding CLARITAS model fits to the empirical data over a range of loess concentrations (see Figure 5-11 to Figure 5-18). There is a clear logarithmic relationship (R^2 = 0.967, p-slope = 0.0000113, p-intercept = 9.87 x 10^{-17}) between the loess concentration and the Mie probability (equation 5-4). Equation 5-4 shows the Mie probability M_p, where ρ_c is the sediment mass concentration (g l^{-1}).

$$M_p = -0.035 \ln \rho_c + 0.9838 \qquad 5\text{-}4$$

The relationship described by Equation 5-4 suggests that geometric optics theory could become more important as the sediment concentration increases, as plotted in Figure 5-20. The relative amount of approximated geometric optics required by the CLARITAS model to achieve the minimum acceptable RMSE increases with sediment concentration. By looking at the relationship between the RMSE and the sediment concentration (Figure 5-19), a positive linear correlation is evident (R^2 = 0.824, p-slope = 0.00185, p-intercept = 0.00250). However, although the p-value of the slope term in the linear regression is within the 95% confidence limit (0.0019 < 0.05), it suggests that the RMSE minimisation could be improved. This suggestion is confirmed by a visual inspection of the graph (Figure 5-19), in which the first three RMSE values (0.5 g l^{-1}, 1.0 g l^{-1}, and 1.5 g l^{-1}) appear to be biasing what would otherwise be a better linear fit. If those three values were omitted from the linear regression, the regression statistics would be R^2 = 0.999, p-slope = 0.0000062, and p-intercept = 0.0012, indicating an almost prefect linear regression (99.9999% confidence on the slope coefficient). Furthermore, if the values of M_p for the loess concentrations 0.5 g l^{-1}, 1.0 g l^{-1}, and 1.5 g l^{-1} are considered, they show the largest deviations from the regression line described by Equation 5-4, as shown in Figure 5-20.

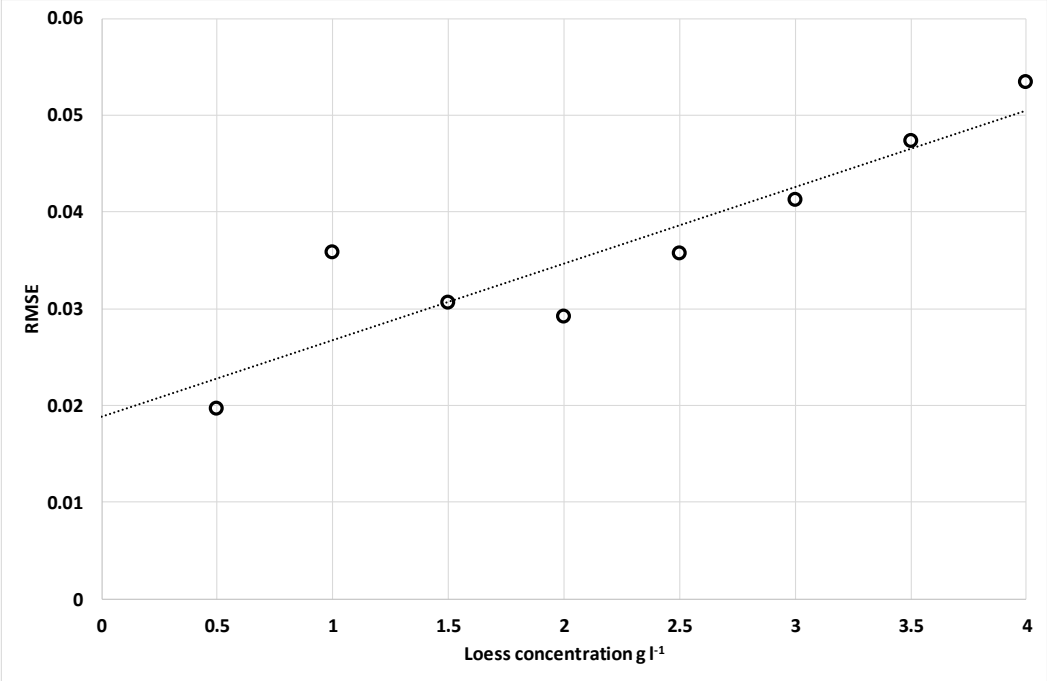

Figure 5-19. The minimised RMSE values of the CLARITAS model fitting as a function of loess concentration (g l^{-1}), after multiple iterations of manual optimisation of the M_p parameter. Line of best fit has R^2 = 0.824, p-slope = 0.00185, and p-intercept = 0.00250.

Since the chosen acceptance threshold for the RMSE value of a CLARITAS model datum was RMSE < 0.1, it is permissable to stop the optimisation process and accept the model in its present form. Given the results discussed from section 5.2.6 onward, several conclusions can be drawn:

1. Some representation of geometric optics (specifically the reflection of rays from suspended particles) is required for the CLARITAS model to provide any meaningful results. The reflectivity of the sediment particles and hence geometric optics theory is a prerequisite for the successful modelling of ray-particle interactions.
2. It is possible that the deviation from linearity exhibited at low sediment concentration (ρ_c < 2.0 g l^{-1}) is in part caused by larger than average errors in the empirical measurements, and is not solely a consequence of CLARITAS modelling errors.
3. The correct general form of the model output is observed.
4. The relationship between the error in the CLARITAS model (the RMSE) and the loess concentration is compounded systematically in a linear fashion; therefore, the formulation of the geometric optics aspect of the CLARITAS model must be refined in order to improve the overall performance.

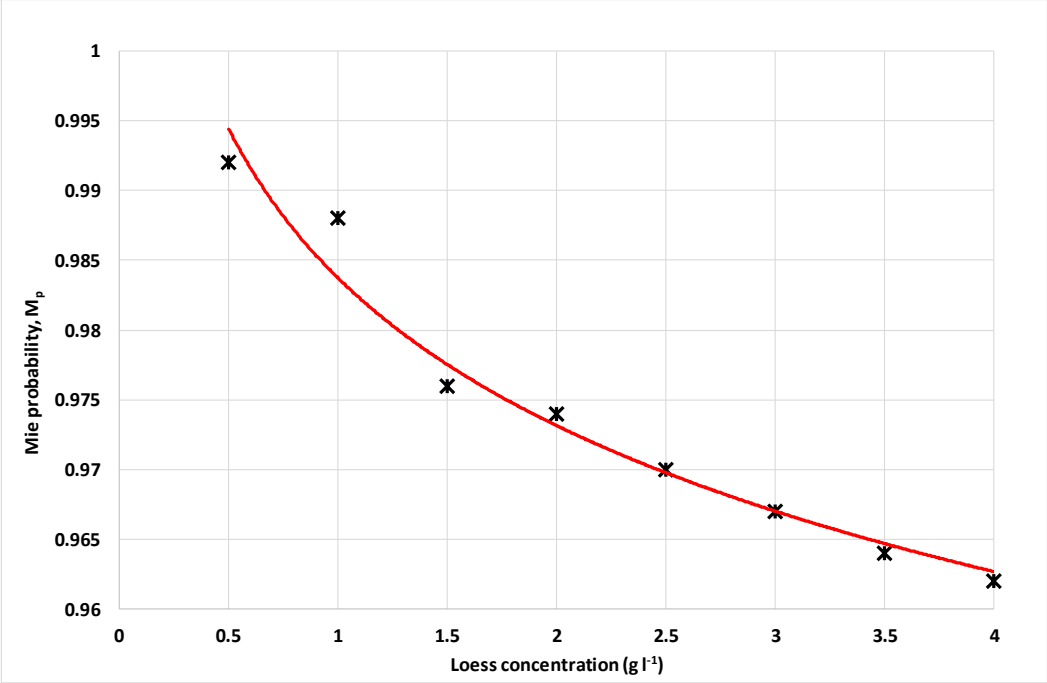

Figure 5-20. Relationship between the manually optimised Mie probability (M_p) and CLARITAS model outputs with RMSE < 0.1. Shows loess mass concentration ρ_c vs. M_p at wavelength λ = 622 nm, M_d = 200 µm, α_1 = 0.25, and α_2 = 5.0, and nominal LED current of 1 mA.

5.2.10 The backscatter fraction as a measure of CLARITAS model performance

If the predicted backscatter fraction B_{bp} is plotted against the measured (empirical) backscatter fraction B_{be}, then the model prediction can be compared directly with the ideal situation in which the two parameters are equal (line of equality in Figure 5-21). The ideal response is a straight line with a gradient of 1. The predicted response is a straight line (R^2 = 0.993) with a slope of 1.56. The p-value on the intercept is 0.0013 << 0.05, indicating that the line of best fit does not pass through the origin (Equation 5-5).

$$B_{bp} = 1.5567 B_{be} - 0.1640 \qquad 5\text{-}5$$

This result suggests that for the loess sediment used throughout this work, and with an incident light wavelength of 622 nm, that the transition between the over-prediction and the under-prediction of the backscatter fraction in the CLARITAS model happens somewhere in the concentration range 1.5 g l^{-1} > ρ_c > 1.0 g l^{-1}. The linearity of the model output as shown in Figure 5-21 provides some confidence that CLARITAS has taken a reasonable approach to modelling the turbidity of suspended sediment, but the model-tuning is still an issue. There is clearly a bias in the data (Figure 5-21) that is a function of sediment concentration (as discussed in section 5.2.9).

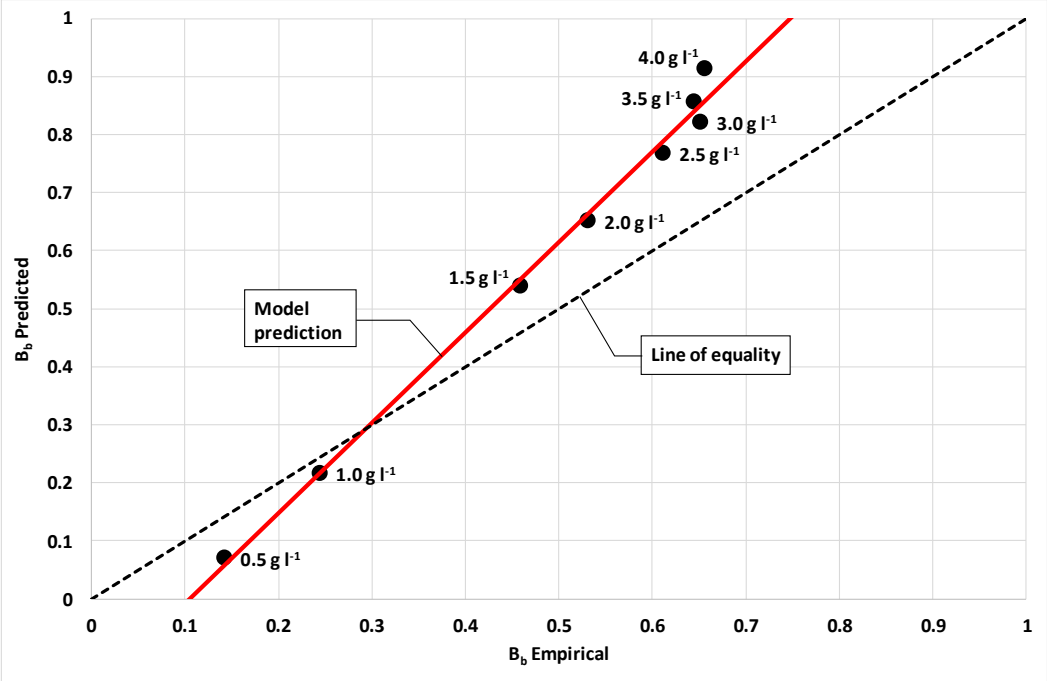

Figure 5-21. Measured backscatter fraction vs. predicted backscatter fraction. Loess sediment, λ = 622 nm, M_d = 200 µm, α_1 = 0.25, and α_2 = 5.0. The M_p values associated with each data point have been tuned individually by hand.

By defining the *mean coefficient of prediction* ($\bar{C}_p$) as the mean ratio of the mean normalised angular predicted radiant intensity $\tilde{I}_{PRED}(\theta)$ to the mean normalised angular empirical radiant intensity, $\tilde{I}_{EMP}(\theta)$ (Equation 5-6), it is possible to see where the prediction biases occur in terms of measurement angle θ°.

$$\bar{C}_p = \frac{\sum_{\theta=0°}^{\theta=170°} \tilde{I}_{PRED}(\theta)/\tilde{I}_{EMP}(\theta)}{N_\theta} \qquad 5\text{-}6$$

N_θ = 18, which is the number of measurements (angular detection positions) from which the mean is calculated. $\tilde{I}_{PRED}(\theta)$ and $\tilde{I}_{EMP}(\theta)$ are averaged over all values of loess concentration, 0.5 g l^{-1} to 4.0 g l^{-1}. Figure 5-22 shows how a large peak centred at the 150° detection angle explains the tendency of the CLARITAS model in general (i.e. averaged over all values of sediment concentration) to over-predict the backscatter fraction. The line of equality at $\bar{C}_p = 1$ indicates the demarcation between over-prediction and under-prediction. Plotting the averaged angular data in this format (Figure 5-22) serves to summarise and exaggerate the differences between the CLARITAS model predictions and the TARDIIS empirical measurements described by Figure 5-11 to Figure 5-18. The measurement locations that on average give the best predictions due to their proximity to the line of equality occur at 0° (23.5% over-prediction), 10° (10.8% under-prediction), 120° (16.0% under-prediction), and 170° (9.1% over-prediction).

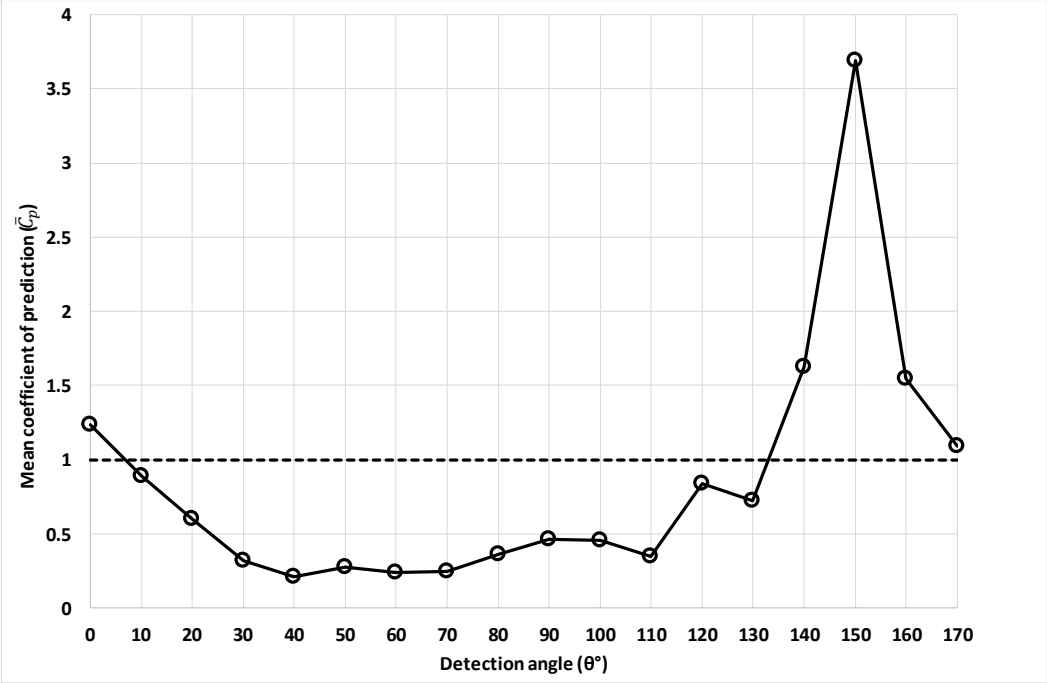

Figure 5-22. The mean coefficient of prediction of the CLARITAS model against TARDIIS empirical data for loess sediment, λ = 622 nm, M_d = 200 μm, α_1 = 0.25, and α_2 = 5.0. ρ_m ranges from 0.5 g l^{-1} to 4.0 g l^{-1}. M_p ranges from 0.962 to 0.992. The dashed line shows the boundary between the regions of over-prediction and under-prediction of the CLARITAS model.

5.3 Discussion

The approach taken to the modelling of the light-scattering processes in the TARDIIS sample cell is that of systems integration. For example, CLARITAS has taken pre-calculated data using a third-party mathematical modelling application (Laven 2018), and has integrated them into a simple computational framework in order to reduce program complexity, and to increase the speed and efficiency of the algorithm. The model has served a useful purpose in fulfilling the main aim of this chapter. CLARITAS has revealed that the ability of Mie theory to model the ray-particle interactions involving suspended sediment is likely to be a function of sediment concentration. At low concentrations ($\rho_c \leq 0.5$ g l^{-1}), Mie theory requires only a very small supplementation by geometric optics theory to be able to model well the response of the TARDIIS instrument at λ = 622 nm. However, as the concentration increases toward 4.0 g l^{-1}, this supplementary requirement also increases.

The geometric optics theory discussed throughout this chapter is in reality only a gross approximation to one aspect of that theory – reflection. It is known that the sensitivity of optical backscatter measuring devices is highly sensitive to particle size (Green & Boon 1993). It is also known that the colour of sediment has a strong effect on the backscatter intensity (i.e. a wavelength dependency), and that the reflectivity of the sediment is also important – particularly at infrared wavelengths (Sutherland et al. 2000). By incorporating a small probability that larger

particles will behave as reflectors of an incident ray, the CLARITAS model has demonstrated that Mie theory is only part of the modelling solution. However, CLARITAS does not yet adequately model the particle size dependency or the particle colour dependency of the ray-particle interactions in terms of the geometric optics theory. The oversimplification of this aspect of the CLARITAS model is the likely explanation for the large over-prediction peak centred at the 150° measurement position (Figure 5-22). The correct implementation of geometric optics theory will also obviate the need for the oversimplification of the absorbance term in the CLARITAS model, i.e. the Beer-Lambert approximation – which does not take into account the particle size, shape, or colour.

Moving forward to future work, the ongoing development of the CLARITAS model should be considered. The following actions are suggested:

1. Determine if similar relationship exists between M_p and ρ_c at wavelengths of light other than 622 nm.
2. The development of a test framework to facilitate the automatic tuning of the CLARITAS model, using recognised optimisation methodologies.
3. A more detailed investigation into ways to model the spatial beam divergence of different LEDs.
4. The development of CLARITAS into a hybrid model incorporating Mie theory and fully implemented geometric optics theory.
5. The alternative development of CLARITAS into a purely geometric optics model.
6. Repeat the modelling exercises with an improved version of CLARITAS.
7. The backscatter fraction may not be the best assessor of CLARITAS model performance. Other potential metrics should be discovered and investigated.
8. Develop an extension to the CLARITAS model (or a separate model) to simulate the sediment dynamics occurring in the water column. The agitation method used to maintain sediment suspension should be modelled in order to provide a refined estimate of the sediment PSD that is subsequently modelled by CLARITAS.

This chapter deepens the primary aims laid out in Chapter 1, in particular aim 3 and aim 4, which involved the design and evaluation of a turbidity research instrument. It has illustrated that numerical modelling is integral to the understanding of the act of turbidity measurement in a holistic manner. Specifically, it has suggested that the geometry of the measurement instrument and its response to a suspended sediment are mutually dependent. Key to the understanding of the instrument response is a precise knowledge of the spatial distribution of the light beam generated by the light source. Not only will effective process-based modelling be useful for the

characterisation of suspended sediment – it will be a crucial part of the design process of future turbidity instruments.

Chapter 6 TARDIIS: *Applications and future work*

This chapter expands upon some of the experimental ideas that were introduced in chapter 4. Experiments involving the steady-state suspension of sediment are discussed in the first section, and then the effects that sediment settling over time has on the turbidity of the suspension are investigated in the second section. Throughout the discussion, a number of hypotheses are presented, some of which are also tested to some extent. Strategies for testing all of the hypotheses (the untested ones and the partially tested ones) are presented in the final section of the chapter (6.3 – Future work). In this last section, suggestions for future work are put forward that involve all aspects of turbidity measurement and method development, including the numerical modelling strategies discussed in chapter 5.

6.1 Steady-state suspended sediment experiments

6.1.1 A method for estimating the SSC

The steady-state concentration can be estimated from measurements of AGF(0°, λ). The logarithmic functions fitted to the AGF data in Figure 6-1 can be used to calculate the concentration (Table 6-1). The AGF values at 470 nm begin to level out at around 2.5 g l^{-1}, and at around 3.0 g l^{-1} for the 622 nm and 940 nm data. This levelling out of the AGF at higher concentrations could be an indication of the limit of measurement being reached at those wavelengths with the LED currents chosen for the experiment (nominally 0.06 mA for 470 nm, 1.00 mA for 622 nm, and 1.14 mA for 940 mA). It could also potentially indicate that the agitation method (magnetic stirring bar) is not adequately lifting the sediment into the plane of the sensors at higher concentrations. It is possible to run the experiments again at higher beam intensities in order to investigate higher sediment concentrations. However, this approach would also require the addition of intensity-compensating features into the TARDIIS design to prevent saturation of the forward-angle sensors.

Table 6-1. Equations for calculating the loess concentration ρ_c given AGF(0°, λ).

Wavelength (nm)	R^2	p-intercept	p-slope	Concentration Calculation	
470	0.899	2.89 x 10^{-5}	0.000338	$\rho_c = e^{-(AGF(0°,470\ nm)+3.3848)/5.5187}$	*6-1*
622	0.965	2.62 x 10^{-6}	1.33 x 10^{-5}	$\rho_c = e^{-(AGF(0°,622\ nm)+3.4376)/6.574}$	*6-2*
940	0.970	2.00 x 10^{-6}	9.27 x 10^{-6}	$\rho_c = e^{-(AGF(0°,940\ nm)+1.7088)/3.3207}$	*6-3*

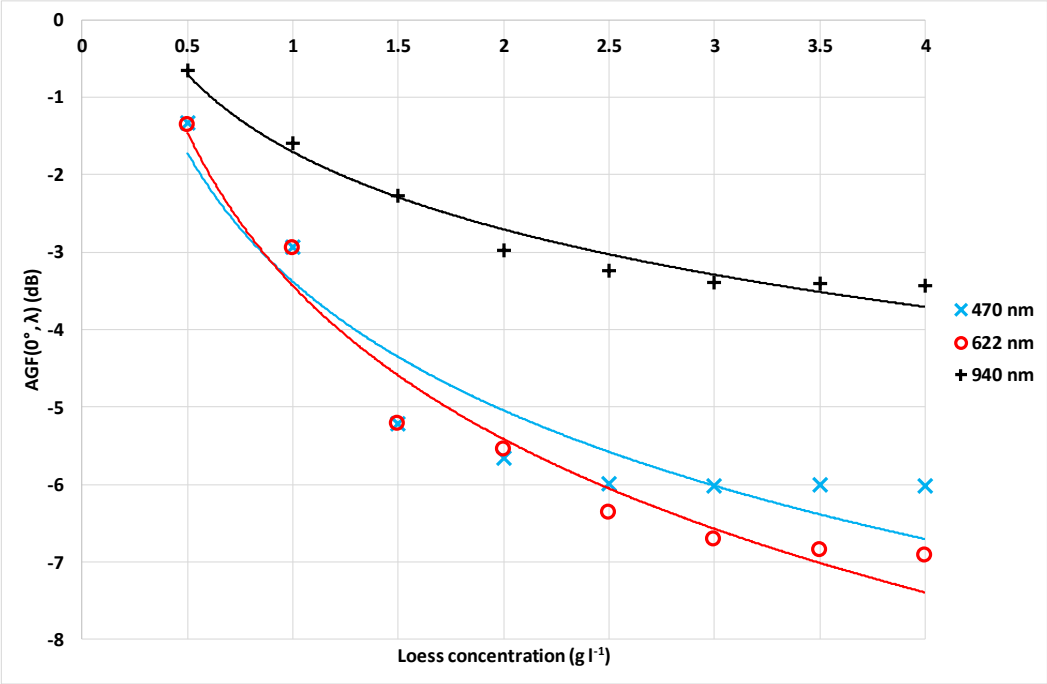

Figure 6-1. AGF(0°, λ), loess steady-state concentration.

Similarly, equations for SSC determination based on the AGF could be derived from the 10° detection angle data (Figure 6-2).

Table 6-2. Equations for calculating the loess concentration ρ_c given AGF(10°, λ).

Wavelength (nm)	R^2	p-intercept	p-slope	Concentration Calculation	
470	0.885	5.92 x 10^{-6}	0.000496	$\rho_c = e^{-(AGF(0°,470\ nm)+2.3790)/2.7527}$	*6-4*
622	0.967	0.000164	1.09 x 10^{-5}	$\rho_c = e^{-(AGF(0°,622\ nm)+1.1451)/4.6357}$	*6-5*
940	0.965	7.54 x 10^{-6}	1.38 x 10^{-5}	$\rho_c = e^{-(AGF(0°,940\ nm)+0.9020)/2.0506}$	*6-6*

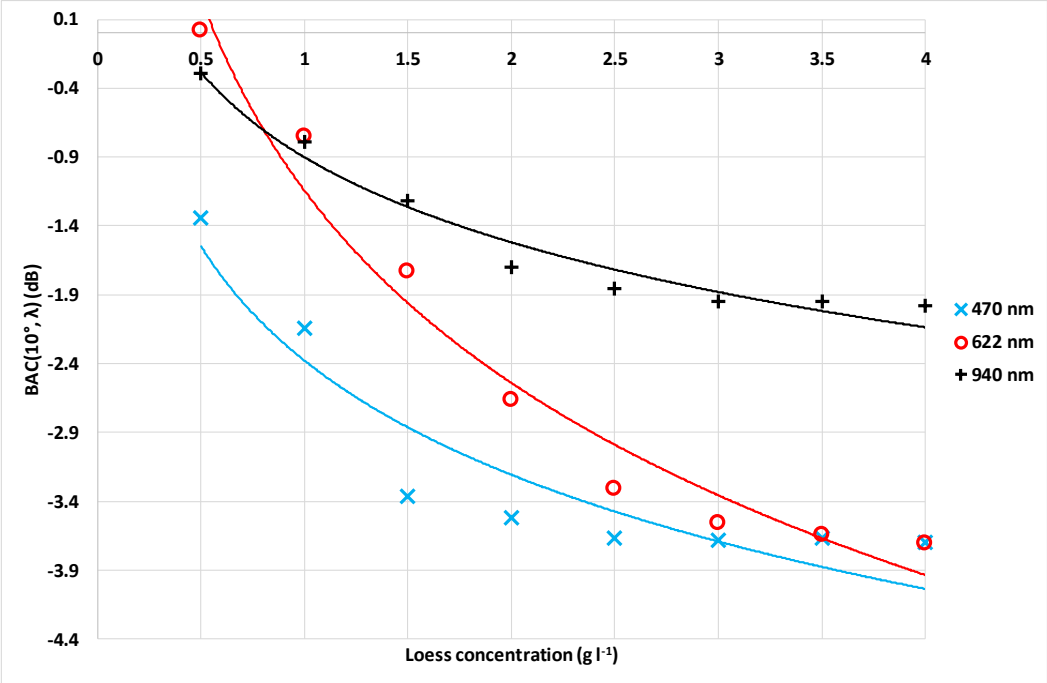

Figure 6-2. AGF(10°, λ), loess steady-state concentration.

As the detection angle increases from 20° through to 170°, the general shape of the AGF curves is similar to that depicted in the 90° data in Figure 6-3, i.e. there is little or no dependency on concentration. It is notable that at all of these detection angles, the increase in AGF value is not proportional to the corresponding decrease in wavelength from 940 nm to 470 nm. The red (622 nm) AGF values are higher than both the blue (470 nm) and infrared (940 nm) AGF values.

Hypothesis 1 (not tested): The colour of the loess sediment may be biasing the results of the steady-state suspended sediment experiments – assuming that there is not an undetected systematic calibration error.

Testing hypothesis 1: See section 6.3.1. for testing strategies.

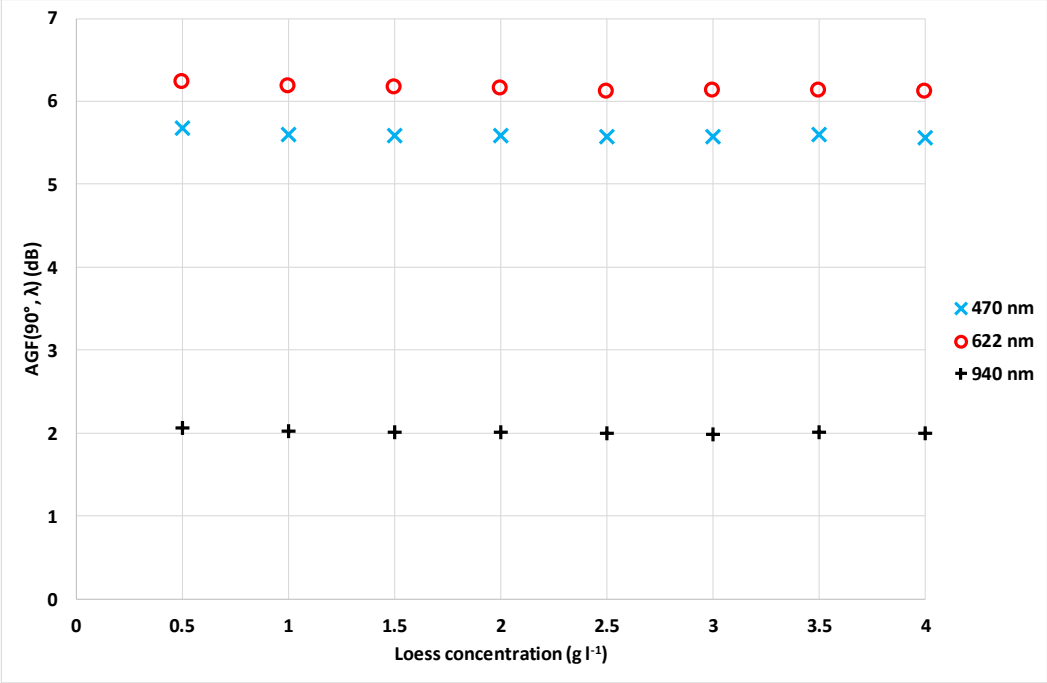

Figure 6-3. AGF(90°, λ), loess steady-state concentration.

6.1.2 A method for comparing different sediments via a standard suspension

The methodology described in this section relates to the PSDs of loess and kaolin sediments, and so a prior knowledge of them is useful. The data presented in Figure 6-4 (obtained using a Horiba LA950 particle size analyser) can be referred to throughout the following discussion.

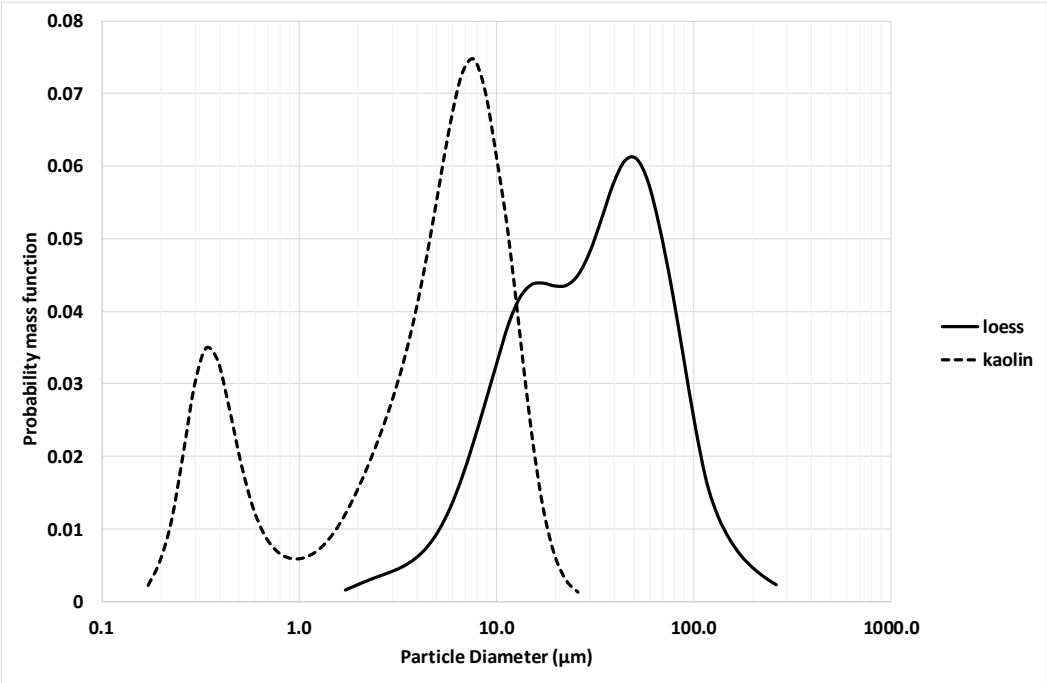

Figure 6-4. Probablity mass functions of loess and kaolin PSDs.

Considering the steady-state measurement method described in section 4.2.1., a hypothetical standard suspension S = [Kaolin @ 0.5 g l^{-1}] is defined. Kaolin is not the perfect choice for use as a calibration standard, since it has a bimodal PSD (there is some colloidal submicron material present – see Figure 6-4). However, it is readily available and has a relatively narrow primary PSD peak, centered on 7.5 µm.

The weighted angular gain function (Equation 4-10) of an unknown sediment is calculated, WAGF (θ=0° to 170° [step=10°], λ=622nm, S), in which the kaolin AGF is the reference value (the inclusion of a "step" angle indicates that the measurement positions are discrete rather than being continuous over the complete angular range). The hypothetical "unknown sediment" is in this case is actually loess for the sake of demonstration. Plotting the WAGF yields Figure 6-5. The 0.5 g l^{-1} data and the 2.0 g l^{-1} data both indicate that the loess exhibits a relatively larger degree of forward scattering than does the reference suspension, which drops off as concentration increases – to the point at which the relative forward scattering is less than for the reference suspension (4.0 g l^{-1}). A similar, but much smaller effect is observed in the backscatter signal centred on the 130° detection angle.

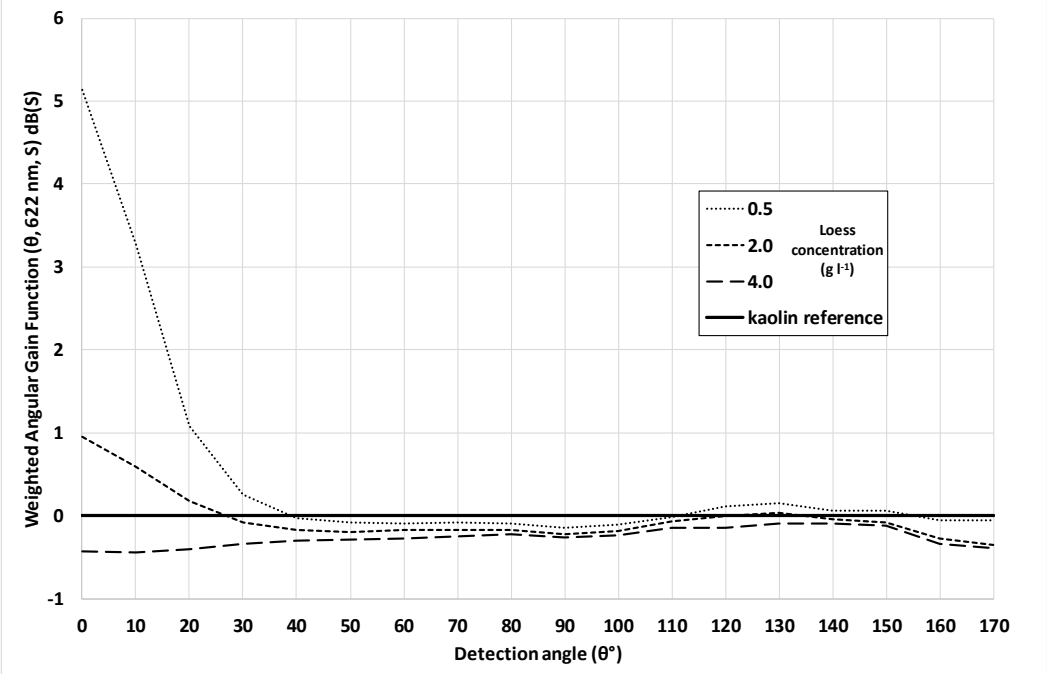

Figure 6-5. Loess WAGF (θ=0° to 170° [step=10°], λ=622nm, S).

The referencing of different unknown sediments to the same reference suspension could facilitate a standardised methodology for relative comparison. However, in order to be able to interpret the results of a comparison between two different materials with two different PSDs (Figure 6-5); it would be sensible to first understand the effects of performing a comparison of the reference

material with itself, i.e. keeping the PSD constant. Now, the effects due to changing the concentration can be examined in isolation. Figure 6-6 shows that an increase in the concentration of the kaolin suspension to values greater than the 0.5 g l^{-1} reference level manifests in general terms as a small increase in the backscatter signal by up to 0.6 dB(S), and a small reduction in the forward scattering signal down to -0.4 dB(S). These effects are attributable to the presence of an increased number of particles of approximately 7.5 μm mean diameter (up to a maximum diameter of approximately 20 μm – see Figure 6-4) as the concentration increases from 0.5 g l^{-1} to 4.0 g l^{-1}.

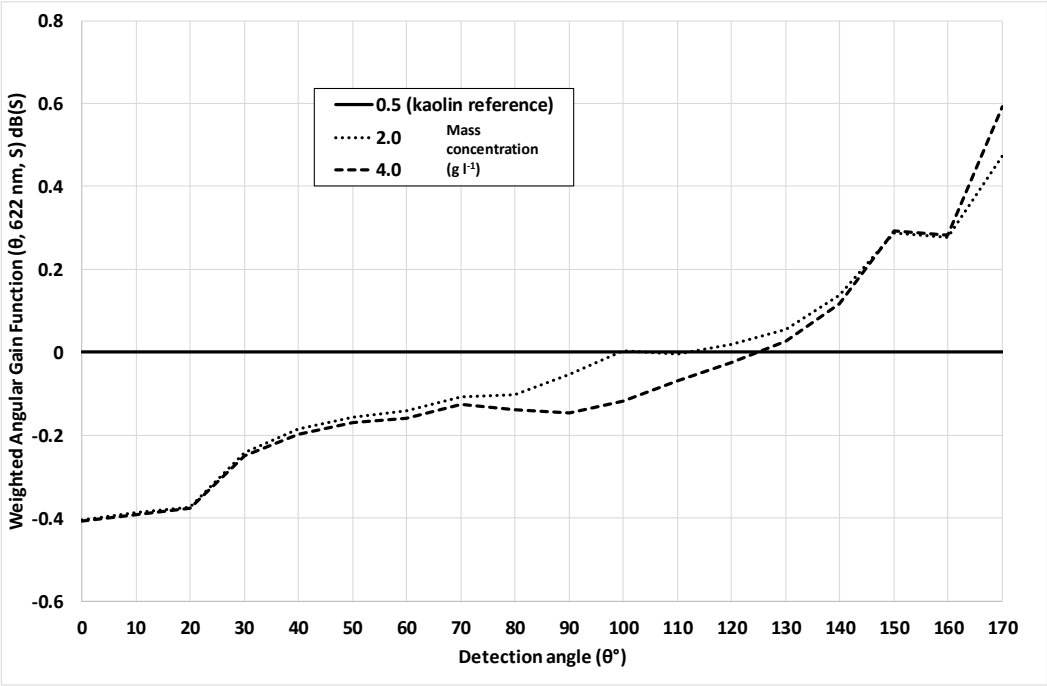

Figure 6-6. Kaolin WAGF (θ=0° to 170° [step=10°], λ=622nm, S).

6.1.3 Hypotheses to explain the AGF response to loess sediment

Hypothesis 2 (not tested): Reconsidering the loess AGF response (Figure 6-5) in light of the kaolin AGF response (Figure 6-6), it is notable that the kaolin does not give rise to a positive value of the AGF at detection angles of < 110°. This response suggests that the sediment particles of size ≅ 7.5 μm (corresponding with the primary kaolin PSD peak) manifest as an increase in the backscatter intensity signal as the concentration increases. The corresponding decrease in the AGF observed in the 0° to 100° detection positions corroborates this suggestion. Therefore, the positive AGF values observed in the loess AGF response (Figure 6-5) at concentrations of 0.5 g l^{-1} and 2.0 g l^{-1} cannot be attributed to these small particles.

Testing hypothesis 2: See section 6.3.1. for testing strategies.

Hypothesis 3 (not tested): The forward-angle loess AGF response is due to particles of greater diameter than those present in the kaolin PSD (i.e. greater than 27 μm, which represents the maximum size of the kaolin PSD.

Testing hypothesis 3: See section 6.3.1. for testing strategies.

Hypothesis 4 (not tested): As the loess concentration increases (Figure 6-5), the forward-angle increase in the AGF caused by the > 27 μm particles is damped by the proportional increase in the number of < 27 μm particles. This could be because the smaller particles are collectively more efficient at absorbing 622 nm light than the larger particles are at scattering it.

Testing hypothesis 4: See section 6.3.1. for testing strategies.

6.2 Sediment settling experiments

Using the same physical setup as the steady-state experiments of section 4.2.1, an initial loess concentration of 4.0 g l^{-1} was brought into steady-state suspension by agitation with the magnetic stirring rod. The stirrer was then switched off, and the sediment was allowed to settle freely for approximately five days. The TARDIIS response was recorded throughout the experiment.

6.2.1 Features present in the settling profile

The first observation to be made of the loess settling data, is the presence of intensity maxima in the settling profile (Figure 6-7). The largest maxima (primary peaks) occur early in the settling profile, and the times at which the peaks are placed within the settling profile appear to be directly related to the detection angle. Figure 6-7 shows the un-calibrated voltage signals for sensor positions 50° to 80°, with vertical dotted lines to emphasise the relative positions of the peaks.

The second observation is the presence of smaller intensity maxima (secondary peaks) which occur at around 10500 s into the settling profile. These secondary peaks appear at the same time, and are independent of the detection angle.

The third observation is that the relative slope of the tail (the profile to the right of the primary peak) decreases as the detection angle increases.

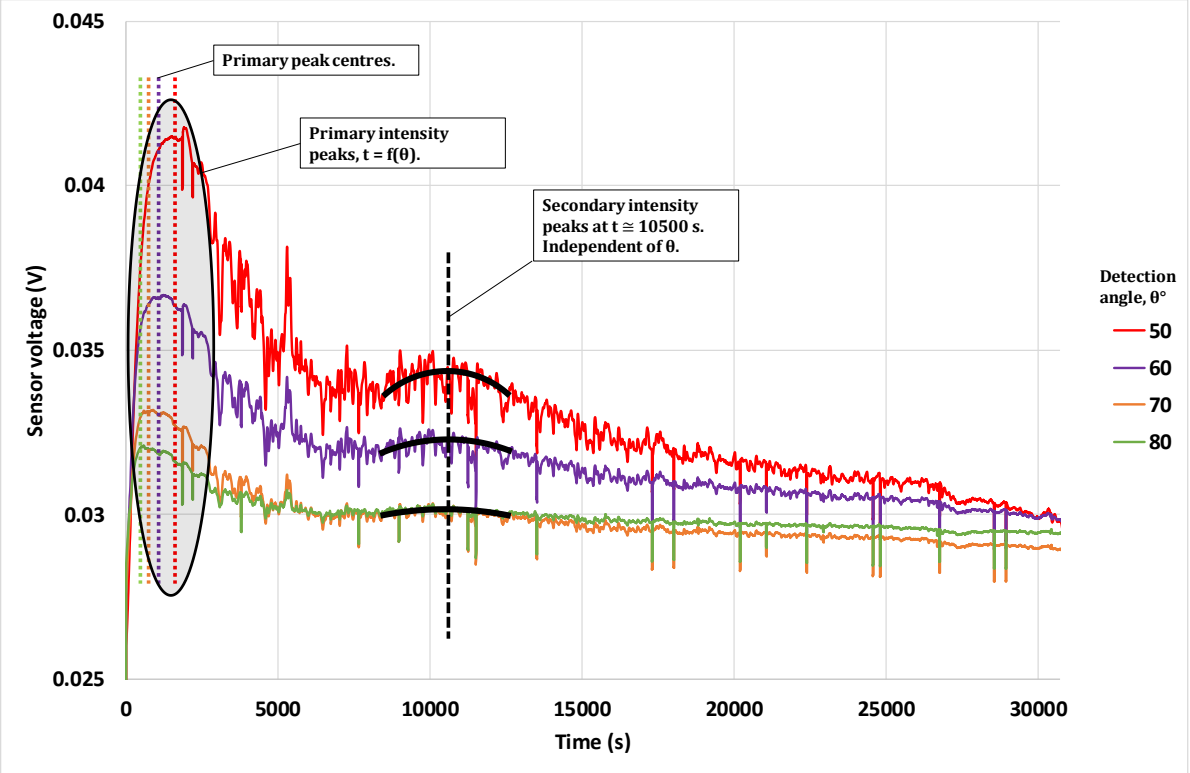

Figure 6-7. Intensity maxima in loess settling data at 622 nm wavelength, with initial concentration of 4.0 g l^{-1}. The first approximately 8.5 hours of the settling data are shown.

6.2.2 A Mie-Stokes graphical method to describe the form of the loess settling profile

The Mie-Stokes graphical method (MSGM) was developed to determine how the PSD of the loess gives rise to the sediment settling profiles, examples of which are shown in Figure 6-7. The PSD of the loess is defined as follows:

$$L = \sum_{n=1}^{n=38} d_n \gamma_n \qquad 6\text{-}7$$

where n is the number of the histogram bin pertaining to a categorical particle size class d_n (µm) in the distribution, as defined in Chapter 5, Figure 5-7, such that d_1 represents the smallest particle size class in the histogram (1.729 µm) and d_{38} represents the largest (262.376 µm). The normalised frequency of occurrence is defined as γ_n.

The first step is to determine the Stokes settling velocity for each particle size class d_n such that:

$$V_S(d_n) = \frac{g d_n^2 (\rho_p - \rho_m)}{18\mu} \qquad 6\text{-}8$$

where g is the acceleration due to gravity (9.81 m s^{-2}), ρ_p is the loess particle density (2.65 kg m^{-3}), ρ_m is the density of water (1.00 kg m^{-3}), and μ is the viscosity of water

(8.9×10^{-4} kg m^{-1} s^{-1}). The Stokes settling velocity is reinterpreted as a particle-size dependent Stokes settling time $t_S(d_n)$ (s) by the introduction of the Stokes scale parameter D_S (m), hence defining:

$$t_S(d_n) = \frac{D_S}{V_S(d_n)} \qquad 6\text{-}9$$

It is this quantity (Equation 6-9) that is plotted on the domain (horizontal axis) of the graph.

The second step in the development of the method is to determine the normalised angular scattering intensity for each particle size class in the distribution L, based on Mie theory (Mie 1908). A third-party software package called MiePlot (Laven 2018) was used to generate Mie scattering intensity data (normalised as $\bar{\mathbb{K}}_n$, Equation 6-10) for each of the 38 particle size classes at wavelength λ = 622 nm for detection angles θ = 40°, θ = 50°, θ = 60°, θ = 70°, and θ = 80°. The normalised Mie intensity distribution $I_{\bar{\mathbb{K}}}$ is defined in Equation 6-10.

$$I_{\bar{\mathbb{K}}}(d_n, \theta, \lambda) = \sum_{n=1}^{n=38} \bar{\mathbb{K}}_n \qquad 6\text{-}10$$

The next step is to apply a weighting function to the empirical loess distribution L, which accounts for the difference in absolute relative intensities as a function of detection angle θ. This weighting function is $I_{\bar{\mathbb{K}}}$. For specific values of θ and λ, a Mie-weighted loess empirical PSD is represented as the Loess-Mie (LM) intensity function:

$$L_{\bar{\mathbb{K}}}(d_n) = d_n \gamma_n^{\alpha_{\bar{\mathbb{K}},\theta} I_{\bar{\mathbb{K}}}(d_n)} \qquad 6\text{-}11$$

where $\alpha_{\bar{\mathbb{K}},\theta}$ is the Mie shape parameter. $L_{\bar{\mathbb{K}}}$ is plotted on the range (vertical axis) of the graph (Equation 6-11).

The Stokes scale parameter D_S is a constant, which is necessary for tuning the Stokes settling velocity to the same scale as the empirical data. Therefore, it will affect the position of the intensity peaks. Once the value of D_S has been determined, it can be ignored.

Experimentation has revealed that $\alpha_{\bar{\mathbb{K}},\theta}$ has a large effect on the shape of the simulated settling profile, and on the intensity peak positions. To demonstrate the effects of varying $\alpha_{\bar{\mathbb{K}},\theta}$, the simulated data is manually fitted to the normalised empirical settling profiles measured at the 40° to 80° positions. Manual optimisation suggests a constant value of $D_S = 0.000989$ m should be applied to all of the simulations. Figure 6-8 shows the θ = 40° data ($\alpha_{\bar{\mathbb{K}},\theta} = 95$), and Figure 6-9 shows the θ = 80° data ($\alpha_{\bar{\mathbb{K}},\theta} = 37$). The trailing slope of the simulated data becomes steeper as θ increases from 40° to 80°, thus it progressively diverges from the empirical data. This relationship is a power law (as would be expected from the form of Equation 6-11), such that:

$$\alpha_{\bar{\mathrm{K}},\theta} = 15857.77\theta^{-3.16345} \qquad 6\text{-}12$$

with p-slope = 0.000713, p-intercept = 0.00014, and R^2 = 0.9859.

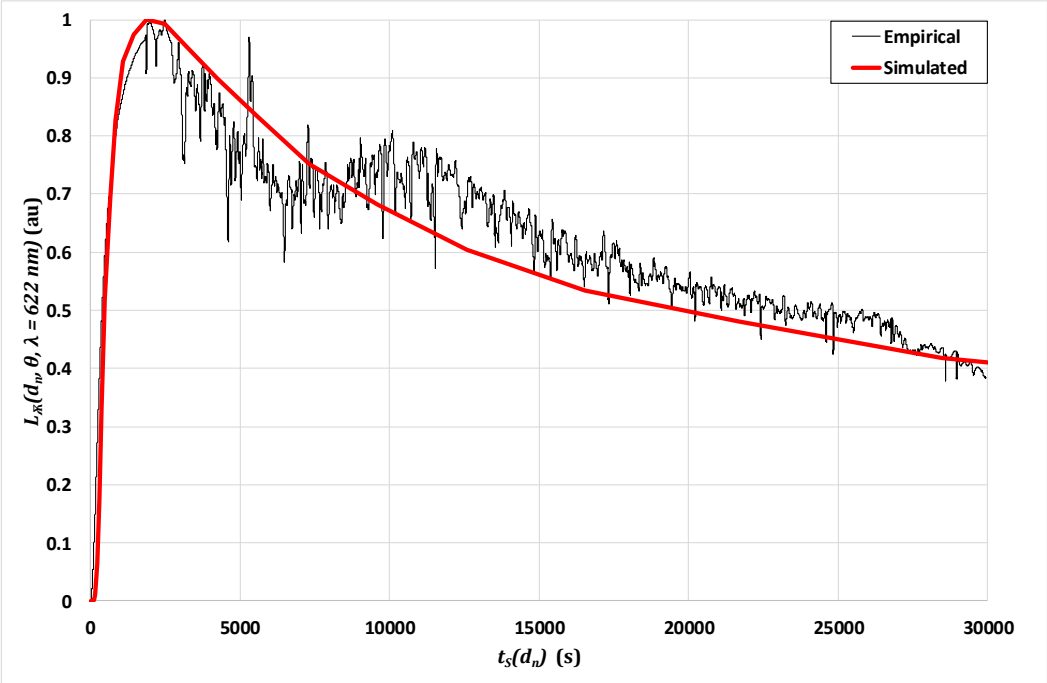

Figure 6-8. A Mie-Stokes graph showing empirical data measured at the 40° detection position (relative normalised intensity), which is plotted against settling time (s). On the same scale, the Loess-Mie intensity function is plotted against the Stokes settling time (simulated data). λ *= 622 nm.* D_S *= 0.000989 m.* $\alpha_{\bar{\mathrm{K}},40^\circ} = 95$.

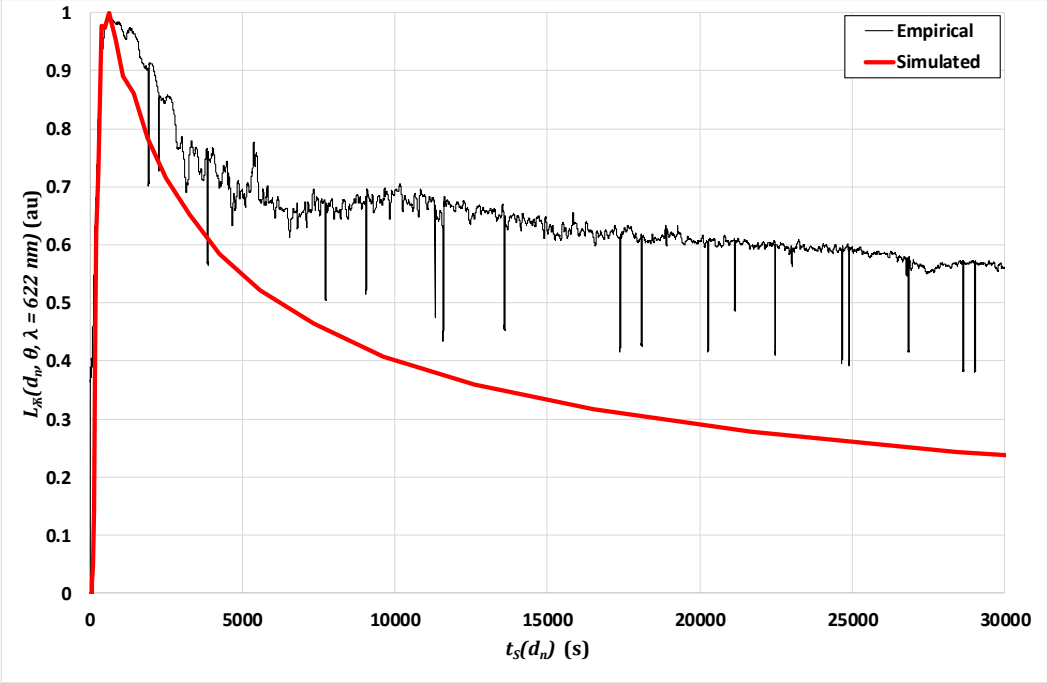

Figure 6-9. A Mie-Stokes graph showing empirical data measured at the 80° detection position (relative normalised intensity), which is plotted against settling time (s). On the same scale, the Loess-Mie intensity function is plotted against the Stokes settling time (simulated data). λ = 622 nm. D_S = 0.000989 m. $\alpha_{\bar{\lambda},80^\circ} = 37$. The narrow, downward-projecting spikes in the empirical data are due to instrumentation glitches.

Next, the relationship between the empirical peak position $P_{P,\theta}$ and the detection angle θ is determined. Equation 6-13 describes how the intensity peak position decreases (shifts to the left) as the detection angle increases:

$$P_{P,\theta} = 5991220\theta^{-2.08773} \qquad 6\text{-}13$$

with p-slope = 0.00145, p-intercept = 0.000239, and R^2 = 0.9774. By inspection, equation 6-12 has the same form as equation 6-13. The former represents a derived model (simulation) that has been tuned by the latter empirical model. Hence, there must be a direct relationship between $P_{P,\theta}$ and $\alpha_{\bar{\lambda},\theta}$. This relationship is tested by plotting $P_{P,\theta}/\alpha_{\bar{\lambda},\theta}$ versus detection angle θ. The response is shown to be linear (Equation 6-14, p-slope = 6.32×10^{-5}, p-intercept = 65.24×10^{-6}, R^2 = 0.9972). By first using equation 6-12 to find $\alpha_{\bar{\lambda},\theta}$, the peak intensity location $P_{P,\theta}$ can be predicted using equation 6-14.

$$P_{P,\theta} = \alpha_{\bar{\lambda},\theta}(-0.25872\theta + 36.599) \qquad 6\text{-}14$$

It is important to note that equation 6-14 is valid only for an initial loess concentration of 4.0 g l^{-1}, with a PSD as specified in Chapter 5, Figure 5-7 (reproduced in Figure 6-4).

6.2.3 Hypotheses about sediment settling and the Mie-Stokes graphical method

Hypothesis 5 (tested): The Mie shape parameter $\alpha_{\tilde{n},\theta}$ is a function of detection angle θ, and may be a function of sediment concentration.

Testing hypothesis 5: It is known that increasing $\alpha_{\tilde{n},\theta}$ will shift the primary intensity peak to the right on the Mie-Stokes graph. The same effect is also observed as the sediment concentration at the beginning of a settling experiment is increased. Figure 6-10 shows the results of three different settling experiments performed using kaolin clay. The initial concentrations of the experiments were 0.5 g l^{-1}, 2.0 g l^{-1}, and 4.0 g l^{-1}. This result shows that the primary intensity peak position increases with concentration, suggesting that $\alpha_{\tilde{n},\theta}$ does have a dependency on sediment concentration, since increasing it produces the same result.

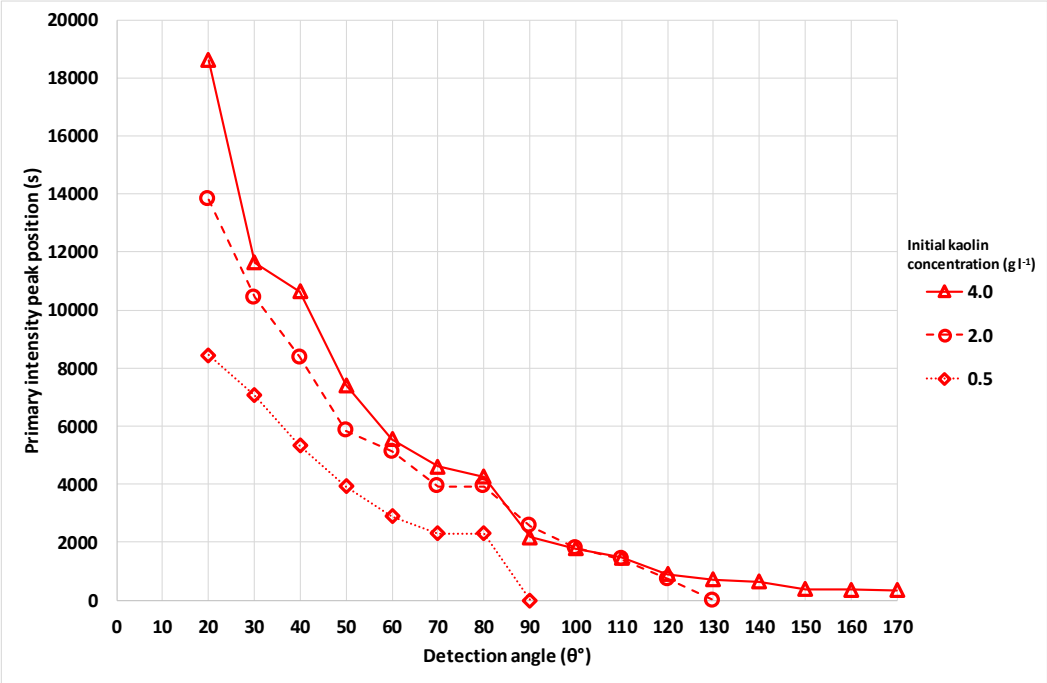

Figure 6-10. Sediment settling experiments at 622 nm and three concentrations of kaolin clay.

Hypothesis 6 (tested): The PSD of the loess changes dynamically during the settling process.

Testing hypothesis 6: This hypothesis can be tested in simulation via the Mie-Stokes graphical method. The method cannot show how the PSD may be evolving over time, but it does represent the situation as it is at the end of the observation period (30,000 s). By manually editing the loess PSD, it may be possible to obtain a better fit to the empirical settling profile. Figure 6-11 indicates that by changing the PSD of the loess, the Mie-Stokes graphical simulation does actually produce a better visual fit to the settling profile curve. The modified PSD is shown alongside the original

PSD in Figure 6-12, indicating the large relative abundance of particles in the 8.816 µm and 10.097 µm size bins, and an overall reduction in the relative abundance of all the other particle sizes in the distribution. These results suggest that the loess PSD does change dynamically throughout the settling process, although they have not been quantified fully.

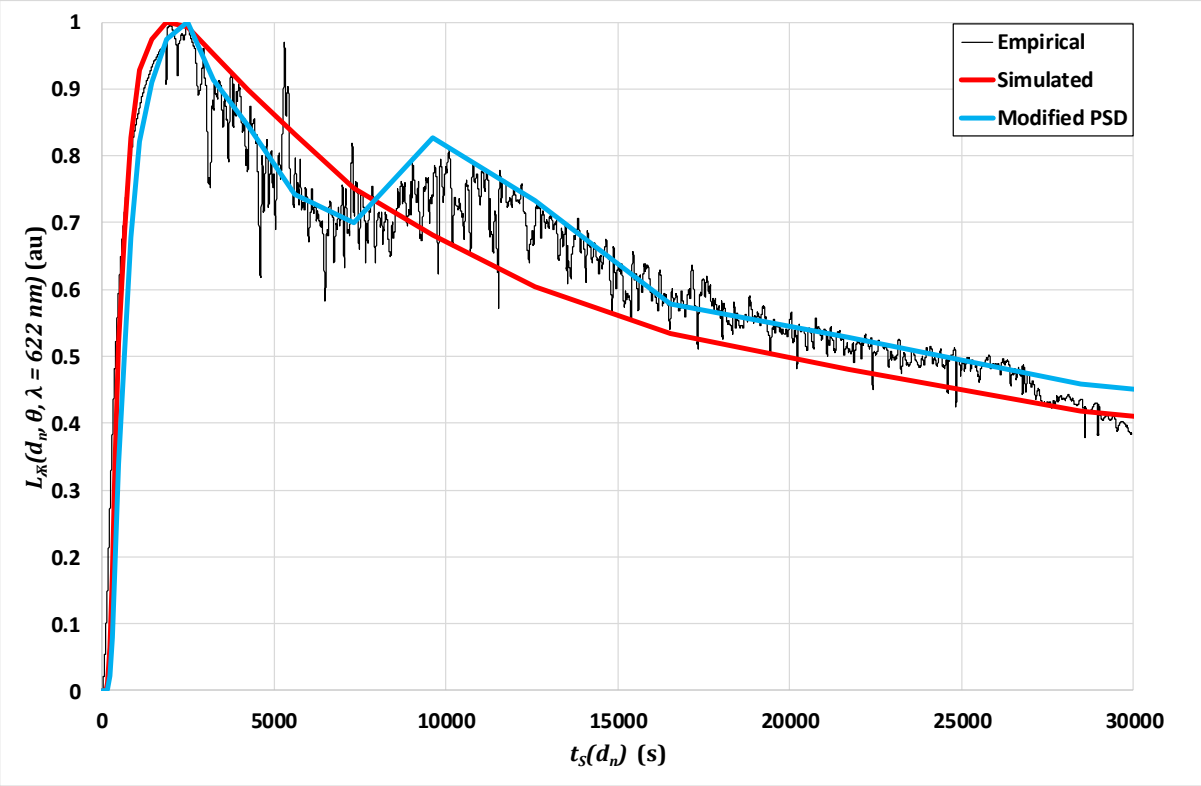

Figure 6-11. A Mie-Stokes graph showing empirical data measured at the 40° detection position (relative normalised intensity), which is plotted against settling time (s). On the same scale, the Loess-Mie intensity function representing the initial loess PSD is plotted against the Stokes settling time (red line), as is the representation of the final loess PSD (blue line). λ = 622 nm. D_S = 0.000989 m. $\alpha_{\bar{R},40^\circ} = 95$.

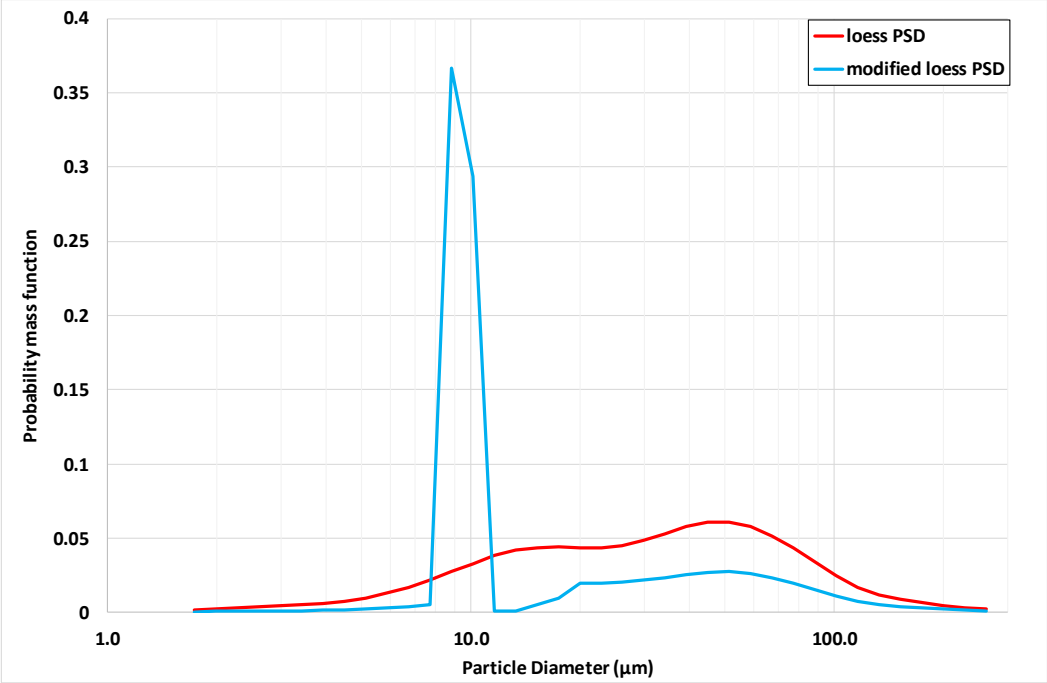

Figure 6-12. Probability mass functions of the loess PSD at the start of the sediment settling experiment (red line), and the manually modified PSD (blue line) suggestive of the eventual suspended PSD after 30,000 s settling time.

Hypothesis 7 (tested): The different detection angles have varying sensitivity to particle size, and hence respond differently to the same PSD. If this hypothesis is true, then the implication is that the PSD as determined by the Mie-Stokes graphical method (e.g. Figure 6-12) is actually a weighted PSD, and not the true PSD.

Testing hypothesis 7: This hypothesis can be tested in simulation via the Mie-Stokes graphical method, in the same way that hypothesis 6 was tested. The 80° detection angle empirical settling data was manually fitted by the MSGM to obtain Figure 6-13. The associated perceived loess PSD is plotted alongside the PSD as perceived by the 40° detection location. The original unmodified loess PSD is also plotted for comparison (Figure 6-14). If the peaks and troughs in the two angular PSD measurements are ignored, then there is a clear shift in the baseline PSD (expressed as a PMF) when they are compared to the original PMF. The discrepancy increases as the detection angle increases from 40° to 80°. For example, for a particle size of 1.729 µm, the perceived PMF at 40° is approximately 4.3 times lower than the unmodified PMF. At 80° the perceived PMF is 150 times lower than the unmodified PMF. The differences in peak response are clear: there is a strong oversensitivity centred on the 8.816 µm size bin at 40°, and an even stronger oversensitivity centred on 5.876 µm size bin at 80°. There is reduced sensitivity at 40° in the 11.565 µm to 19.904 µm particle size bins, and at 80° there is a severe reduction in sensitivity centred on the 11.565 µm bin, spanning a range from 7.697 µm to 44.938 µm. These results

suggest that more detailed calibrations of the TARDIIS instrument to a selection of carefully chosen narrow-band PSDs is required in order to understand fully the sediment settling profile. The results are also highly indicative of a detection angle-dependent sensitivity to particle size.

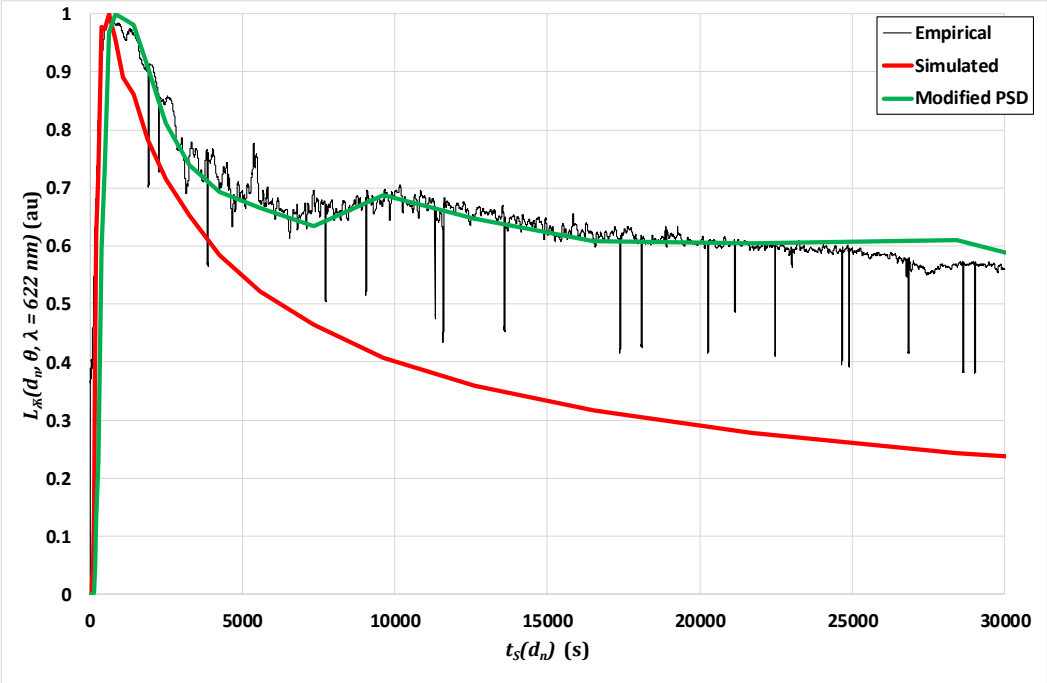

Figure 6-13. A Mie-Stokes graph showing empirical data measured at the 80° detection position (relative normalised intensity), which is plotted against settling time (s). On the same scale, the Loess-Mie intensity function representing the initial loess PSD is plotted against the Stokes settling time (red line), as is the representation of the final loess PSD (green line). λ = 622 nm. D_S = 0.000989 m. $\alpha_{\bar{\lambda},80^\circ} = 35$. The narrow, downward-projecting spikes in the empirical data are due to instrumentation glitches.

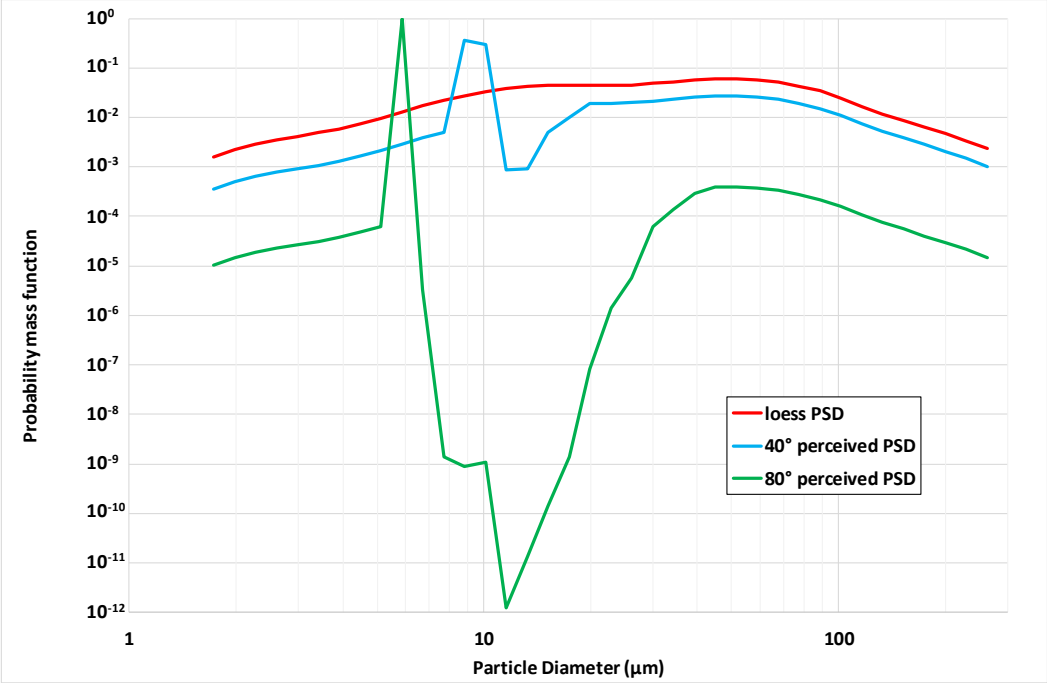

Figure 6-14. Probability mass functions of the loess PSD at the start of the sediment settling experiment (red line), the manually modified PSD (blue line) to fit the 40° empirical data, and the manually modified PSD (green line) to fit the 80° empirical data.

Hypothesis 8 (not tested): The secondary intensity peak (at approximately 10500 s for all detection angles) is due to a combination of four effects:

a. The fluid dynamics occurring in the sample cell as the result of the initial agitation are causing particles of size $d \leq 10$ µm to be deposited into the light beam over a period of time beginning at approximately t = 7500 s, peaking at approximately t = 10500 s, and ending at approximately t = 16000 s into the settling profile.
b. The TARDIIS detector system is disproportionately sensitive (with respect to θ) to particles in the size range $d \leq 10$ µm in the forward detection angles (0° to 90°), as suggested by the testing of hypothesis 6.
c. Non-Stokesian settling may be occurring.
d. The form of the Stokes settling equation (6-8) used in the Loess-Mie graphical method may be too simple.

Testing hypothesis 8: See section 6.3.1. for testing strategies.

6.3 Future work

The continuing development of TARDIIS as a turbidity research instrument should in the first instance focus on the improvement of the optical geometry of the device, and subsequently on the electronic instrumentation. Some aspects of turbidity have not been investigated in this thesis, for example:

- The effects on turbidity due to water colour.
- The polarisation of light in the context of turbidity.
- The effects of using coherent light sources (LASERs).

In order to enable a wider range of experiments to be performed in the future, the following key features are desirable to make the instrument more versatile or to improve its response:

1. Improved rejection of ambient light by the use of a bespoke enclosure.
2. Improved rejection of ambient light by improvements to the sensor electronics.
3. Optics to permit the focusing of the light beam.
4. The facility to insert ND filters into any of the sensor locations.
5. LASER diode modules to use in place of LEDs.
6. The facility to insert polarisation filters into any of the sensor positions, and in front of the light source.
7. Improvement of the light source brightness control system so that it can cope better with very low LED currents.
8. The development of a dedicated DAQ system with real-time (RT) signal processing capability, automatic calibration procedures, readout, and data-logging facilities. The system should be designed with the potential to incorporate AI algorithms for in-process information extraction (e.g. RT PSD estimation).

6.3.1 Testing the untested hypotheses

Eight hypotheses have been presented in section 6.2 which propose explanations for a number of phenomena observed in the steady-state suspended sediment experiments, and in the sediment settling experiments. Not one of the hypotheses relating to the steady-state experiments has been tested (hypotheses 1 to 4). These hypotheses can be in the future tested by comparing existing data, and further experimental data with the output of a refined version of the CLARITAS model. Hypotheses 5 to 7 which relate to the sediment settling experiments were tested with the Mie-Stokes graphical method, revealing that the sediment PSD changes dynamically throughout the settling process, and that the different detection angles have preferential sensitivities to different particle sizes. These hypotheses can be tested further (along with hypothesis 8) by CLARITAS,

but with the addition of a further modelling element. This new aspect to the CLARITAS model must deal with the sediment dynamics of particle settling (i.e. Stokes law), and the fluid dynamics occurring within the sample cell. These new requirements are suggested in response to the development and outcomes of the Mie-Stokes graphical method (section 6.2.2).

Chapter 7 Conclusions: *summary of the key findings*

7.1 Introduction

This concluding chapter summarises the findings of this thesis and elaborates on the key results. The summary (section 7.2) is structured around the original objectives identified in section 1.1. The main conclusions of this research are expanded in section 7.3, and the implications are considered in terms of turbidity measurement, the design of instrumentation, and the reporting of turbidity data in the wider research community.

7.2 Summary of the objectives

As stated in Chapter 1, the overall aim of this project was to provide a meticulous examination of turbidity measurement methodology, focusing on ways in which the fundamental parameters should be reinterpreted to improve our understanding of the relationship between turbidity and SSC, and to fully appreciate the limitations of the measurement techniques.

7.2.1 The state of the art

1. *Explain how turbidity measurement is done now, and how turbidity is related to SSC.*

The review conducted in Chapter 2 described the present state of the art with respect to turbidity measurement methodology and instrumentation. Advanced instruments that perform *in situ* particle characterization using laser diffraction techniques were discussed, although the focus of the conversation was on the development of turbidity instrumentation based on incoherent light sources such as LEDs, and how this development led to the evolution of the accepted turbidity units of measurement (FNU, NTU etc.). These measurement units were explained in terms of the measurement instrument geometries and the experimental conditions imposed by the turbidity measurement standards US EPA Method 180.1, ISO 7027, and GLI Method 2. The key point is that turbidity (or water clarity) is often used as a surrogate for SSC throughout the turbidity literature. This inconsistency has led to a plethora of different ways to report turbidity and SSC. More importantly, there is a deep-seated misunderstanding of what turbidity means within the physical sciences, due to the perpetuation of popular misconceptions about its relationship to SSC. There is a need within the turbidity research community to redefine turbidity in terms of correct physics, and to establish a new framework in which turbidity measurements can be compared consistently. By developing a new methodology for the reporting of turbidity, the

expectations of the researcher with regard to the turbidity-SSC relationship can be managed sensibly.

7.2.2 The problems with turbidity measurement

2. Explain what is wrong with these existing turbidity measurement methods.

The derivation of the accepted turbidity units of measurement (FNU, NTU etc.) was shown to be incorrect according to the underlying physics of light scattering and light absorption by particles suspended in water (Chapter 2). The root cause of this problem was the use of calibration standards which considered a *chemical concentration* of a substance (e.g. formazin) suspended in water to adequately and consistently produce the same particle size distribution under all experimental conditions. This assumption was shown to be incorrect in section 2.12. The problem is compounded by the broad range of acceptable measurement geometries and wavelengths of light sources specified in US EPA Method 180.1, ISO 7027, and GLI Method 2. These measurement standards do not place any emphasis on the calibration of the whole measurement system, including the sensor electronics and light source intensity. GLI Method 2 does make an attempt to compensate for the variability in light source intensity by the use of the beam-ratio method (US EPA 1992), however none of the methods consider the importance of the spatial distribution of the light beam as described in Chapter 4 (section 4.4.1). The divergence of the incident light beam is a function of light source intensity, and defines the fundamental baseline response of any turbidity instrument. The turbidity measurement methods described in US EPA Method 180.1, ISO 7027, and GLI Method 2 do not stipulate the characteristics of the light beam in terms of the spatial distribution or the nominal length of the light-path. The initial modelling work presented in Chapter 5 illustrated how defining correctly the spatial distribution function that describes the light beam is important for understanding the overall response of the measurement instrument (section 5.2.3). This understanding is of critical importance if a turbidity instrument is to be calibrated using a particulate suspension, since the beam divergence is also a function of the particle concentration. Therefore, an understanding of the beam geometry in the absence of suspended particles is vital to the understanding of how a suspended particle population will change the beam geometry. This holistic approach to instrument calibration is not considered in any of the existing methodologies. In addition to this problem, there is the issue of multiple, incommensurate turbidity measurement units. In order to enable the reporting of turbidity in a consistent way, it was necessary to define new measurement units that are based on the attenuation of light - since that is what is actually measured by a turbidity instrument - irrespective of the measurement angle to the incident light beam.

7.2.3 A new turbidity research instrument

3. Design a new turbidity research instrument from first principles.

Chapter 3 described the development of a turbidity research instrument. The device (TARDIIS) is intended for benchtop use in a laboratory setting. It features 18 sensor positions at 10° intervals, and a variable intensity light source with user-selectable wavelength options. It has been used successfully to demonstrate the importance of the calibration methodology, and it highlights the complexity of turbidity measurement. With hindsight, some other features would have been included in the design. The ability to insert neutral density (ND) filters into any of the sensor positions would be useful, as would a custom-built enclosure to ensure the complete rejection of stray light. However, even without these features the device performed very well, as described in Chapter 4.

7.2.4 Evaluation of the turbidity research instrument

4. Test and evaluate the new turbidity research instrument.

A basic evaluation of the new turbidity research instrument (TARDIIS) was performed in Chapter 3, in which the emphasis was placed on the assessment of individual photodiode amplifier sensors to specific intensities of light. ND filters were employed to select light intensity ranges that would be representative of operational conditions. The methodology for converting the sensor response voltage into a radiant intensity value was explained, and the concept of reporting the *beam attenuation coefficient* (BAC) for each angular sensor location was introduced. The instrument performance was discussed with regard to a number of steady-state suspended sediment experiments, in which the issues associated with the suspension agitation method were highlighted. These issues emphasised the need to model numerically the sediment agitation process in tandem with the light scattering and absorption processes. Also investigated were a number of sediment-settling experiments, in which previously suspended sediment (due to continuous agitation) was allowed to settle due to gravity. Once again, the complexity of the results emphasise the need to model numerically the sediment settling process. These settling experiments did show some interesting phenomena occurring in the time domain of the settling profile, which have the potential (with the aid of numerical modelling) to reveal information about the PSD (and possibly the particle shape characteristics) of the suspended sediment. The instrument is not perfect as it is a prototype, however it performed well and was fit for purpose.

7.2.5 Reporting turbidity data

5. Suggest a new and better way to report turbidity data.

Chapter 4 expanded upon the basic evaluation described in Chapter 3 by first reintroducing the concept of the *volume scattering function* (VSF). The concept that TARDIIS is actually making a direct measurement of the VSF is suggested. The VSF itself has a *shape* component called the *scattering phase function*, and an *amplitude* component called the *scattering coefficient*. These two concepts can be conceptually confusing, as the information contained in both is essentially the same. The scattering phase function can be viewed as a way to perform a normalisation of the VSF, which allows, for example, data collected at different wavelengths of light to be compared directly. This comparison accounts for the differences in sensor calibration at the different wavelengths, whereas the scattering coefficient does not.

It was shown that by plotting the scattering phase function, the light scattering response of a particular sediment can change as a function of concentration. This evidence shows that turbidity instruments that have different geometries will have different responses to light scattering from the same sediment at the same concentration. The effects of the wavelength of light were also evident as differences in the scattering phase function for a given sediment.

The scattering coefficient is also useful as a measurement parameter, as it leads to the definition of the *backscatter fraction*. The backscatter fraction is a single metric for the description of the shape of the VSF, which because it is a ratio, it has effectively been normalised – making it a suitable parameter for cross-comparisons between measurements made on the same sediment at different wavelengths, or with measurements made on other suspended sediments. This metric has been used as a way to score the success of the physical modelling (CLARITAS model) of light scattering from steady-state sediment suspensions in the TARDIIS device (Chapter 5, section 5.2.10) – modelling that is vital to the eventual understanding of the inherent optical properties (IOPs) of suspended sediments. This modelling has been supplementary to the major arc of this thesis; however, it will lead to improvements in turbidity instrument design and calibration procedures, especially where LED light sources are used. It has revealed the importance of the light beam geometry, and the requirement for geometric optics to be applied in future model development.

Returning to the idea of the BAC (which was first introduced in the literature review in Chapter 2), it was realised that this parameter is essentially the same as the VSF, i.e. it represents what TARDIIS actually measures. The breakthrough in the reporting of turbidity data occurred with the idea to report the baseline response of the turbidity instrument as a BAC, and then to compare

this baseline BAC (reference BAC) with the BAC measured for a sediment suspension, thus defining the *angular gain function* (AGF). The AGF effectively represents the absolute response of a measurement instrument to a sediment suspension, *independently to the instrument geometry*. However, in order to compare two turbidity measurements made using different instruments, the AGF is not effective, since it does not account for *differences* in instrument sensitivity. To state the necessary *relative* measurement, a further innovation was to define the *weighted angular gain function* (WAGF), which facilitates the comparison of two AGFs which have *the same reference BAC*. The implication of this interpretation is that it is *still necessary to use calibration standards* in order to compare effectively turbidity measurements made by the same/different instruments of the same/different suspended sediments. The invention of the WAGF provides a potential route for the development of turbidity reporting standards that are suitable to different sectors of turbidity measurement. It is sensible at this stage, to split the application of turbidity measurement into key research areas. For example, the assessment of drinking water clarity has a completely different set of measurement ranges than those of waste water assessment. It is therefore not likely that instruments optimised for use in the former application would be used in the latter, and *vice-versa*. Similarly, the calibration standards used for each application should be optimised for use in *that application only* (or for similar applications). This approach therefore requires the development of *application specific calibration standards*. These calibration standards should conform to the requirements set out in section 4.3.2. In addition to those requirements, the water used for the calibration should also be well-defined (i.e. tap water, de-ionised water etc.). It may be useful to define *coloured water standards* for some applications, for example the amount of dissolved humic substances in a sample could be measured using turbidity instruments.

For example, consider four potential calibration standards designed for different applications (all using non-coloured water): drinking water assessment (D); suspended sediment concentration (S); waste-water assessment (P); and general turbidity research (X). Each calibration standard should have an associated *method statement*, which describes how it should be made into a suspension and used for calibration, featuring the requirements laid out in section 4.3.2. Table 7-1 summarises the example measurement parameters.

Table 7-1. Examples of turbidity measurement applications requiring different calibration standards described by method statements D, S, and P.

Application	BAC	WAGF (Equation 4-10)	Measurement Units	Method Statement
Drinking water assessment	$BAC_{\boldsymbol{D}}(\theta,\lambda)$	$WAGF(\theta,\lambda,\boldsymbol{D})$	dB(D)	Method D
Suspended sediment concentration	$BAC_{\boldsymbol{S}}(\theta,\lambda)$	$WAGF(\theta,\lambda,\boldsymbol{S})$	dB(S)	Method S
Waste-water assessment	$BAC_{\boldsymbol{P}}(\theta,\lambda)$	$WAGF(\theta,\lambda,\boldsymbol{P})$	dB(P)	Method P
General turbidity research	$BAC_{\boldsymbol{X}}(\theta,\lambda)$	$WAGF(\theta,\lambda,\boldsymbol{X})$ $AGF(\theta,\lambda)$	dB(X) dB	Any method X, including new methods

This new methodology would ensure that turbidity measurements made using incommensurate methods are not compared with each other, i.e. it is only valid to compare measurements reported in units of dB(S) with other measurements that are also reported in dB(S). It is meaningless to compare turbidity measurements reported in dB(S) with turbidity measurements reported in dB(P) or any other units. It is also not possible, and therefore invalid to convert turbidity measurements from one WAGF unit into another WAFG unit (e.g. from dB(S) to dB(D)). It is important to remember that the WAGF encodes measurement geometry information in terms of the measurement angle θ and the wavelength λ. It is therefore not possible to compare directly WAGF(60°, 622 nm) measurements with WAGF(90°, 622 nm) measurements. The 90° $\pm$ 30° measurement angle stipulated by US EPA Method 180.1 (US EPA 1993) is therefore no longer valid in the new system of turbidity measurement and reporting. The standards pertaining to turbidity instrument design, therefore, should be reconsidered.

7.3 Research conclusions

The relationship between turbidity and SSC will probably always be subjective to some degree. However, there is good reason to be optimistic for the future of turbidity measurement. The innovations in the reporting of turbidity data that were explained in Chapter 4 and discussed further in section 7.2.5 could begin to untangle the web of imprecise and physically meaningless turbidity measurement units that have dominated the physical sciences for several decades. The drafting of new *application-specific* turbidity measurement standards would facilitate the development of mutually consistent turbidity instruments that will go on to collect data that can be compared *meaningfully* with other turbidity measurements from the *same application domain* (e.g. drinking water quality). The existence of the many different turbidity measurement units has arisen from the need to create *application specific* units of measurement that only encompass a small subset of relevant turbidity parameters. This requirement is not unreasonable, however the existing units have evolved haphazardly from incorrect physics principles, as explained in Chapter 2. The WAGF is the embodiment of an application specific turbidity measurement, with a solid foundation in metrology. The only class of instruments that will require *non-specific* measurement ranges are *research instruments* such as TARDIIS. This class of instrument will be used to inform the design of the other application specific types of turbidity instrument, and the parameters of the new classes of calibration reference standards (i.e. particle size distribution, mass density, refractive index, reflectivity etc.).

Research instruments have the capability to collect parameter-rich data sets which can be analysed to obtain particle characterisation information. The interpretation of this information does present further problems due to its complexity. The applications of TARDIIS described in Chapter 6 bear testiment to this assertion. Methods do exist for the extraction of useful information from complex data. These data-driven methods involve machine-learning techniques, and they require moderate to large amounts of data for the generation of useful models. Further studies are therefore needed to generate the necessary data.

In parallel to the data-driven modelling approach to particle characterisation, the process-based modelling approach is important for the understanding of light-particle interactions, and hence the characterisation of the suspended particles. In the case of suspended sediment research, key parameters such as the particle size distribution, the mass concentration, and the particle shape distribution can be estimated by both approaches to numerical modelling. However, the process-based model is essential to the understanding of the actual physical processes occurring within a *specific turbidity instrument*, with its *unique geometry*. The use of better, more developed versions of the CLARITAS model (Chapter 5) will allow turbidity instrument designs to be tested in a virtual environment and tuned to specific applications, before the physical design stage.

In simple terms, the data-driven approach to modelling turbidity will determine *what* the important factors are in the measurement of turbidity and its relationship to SSC; and the process-based approach will explain *why* they are important.

TARDIIS has been successful as a research tool. The concepts developed during this project should be useful to the turbidity research community for commercial and non-commercial applications. In order to develop further the ideas presented in this thesis, a substantial research programme is proposed which will:

- Develop multiple different narrow-band PSD calibration standards for use in WAGF measurements.
- Embark on a large-scale collection of steady-state AGF and WAGF data from many different types of sediment.
- Implement data-driven algorithms to determine the key turbidity instrument parameters.
- Refine the process-based modelling approaches described in chapter 5, incorporating the relationships discovered by the Mie-Stokes graphical method described in chapter 6. Fully developed models should involve the simulation of light scattering and sediment dynamics, giving useful information about the physical properties of unknown sediments.
- Disseminate and popularise these new approaches to turbidity measurement in the scientific community, and draft new turbidity standards that will facilitate a more scientifically balanced and precise approach to estimating the turbidity-SSC relationship.

References

Agrawal, Y.C., Whitmire, A., Mikkelsen, O.A. & Pottsmith, H.C., 2008. Light scattering by random shaped particles and consequences on measuring suspended sediments by laser diffraction. *Journal of Geophysical Research*, 113(C4), p.C04023. Available at: http://doi.wiley.com/10.1029/2007JC004403 [Accessed April 21, 2017].

APHA, 1971. Standard methods for the examination of water and wastewater (13th ed.): Method 2540 D, Total Suspended Solids Dried at 103°– 105° C. *American Public Health Association, American Water Works Association, and Water Pollution Control Federation*.

Arya, L.M. & Paris, J.F., 1981. A Physicoempirical Model to Predict the Soil Moisture Characteristic from Particle-Size Distribution and Bulk Density Data1. *Soil Science Society of America Journal*, 45(6), p.1023. Available at: https://www.soils.org/publications/sssaj/abstracts/45/6/SS0450061023 [Accessed May 29, 2019].

ASTM, 1998. ASTM D3977 - 97 Standard Test Methods for Determining Sediment Concentration in Water Samples. *American Society for Testing and Materials*, 11.02, pp.395–400.

Baker, E.T. & Lavelle, J.W., 1984. The Effect of Particle Size on the Light Attenuation Coefficient of Natural Suspensions. *Journal of Geophysical Research*, 89(C5), pp.8197–8203.

Banzi, M., Cuartielles, D., Igoe, T., Martino, G. & Mellis, D., 2012. Arduino. Available at: http://www.arduino.cc/.

Beer, 1852. Bestimmung der Absorption des rothen Lichts in farbigen Flüssigkeiten. *Annalen der Physik und Chemie.*, 86, pp.78–88.

Bilotta, G.S. & Brazier, R.E., 2008. Understanding the influence of suspended solids on water quality and aquatic biota. *Water research*, 42(12), pp.2849–61. Available at: http://www.ncbi.nlm.nih.gov/pubmed/18462772 [Accessed November 18, 2013].

Bilro, L., Prats, S.A., Pinto, J.L., Keizer, J.J. & Nogueira, R.N., 2010. Design and performance assessment of a plastic optical fibre-based sensor for measuring water turbidity. *Measurement Science and Technology*, 21(10), p.107001. Available at: http://stacks.iop.org/0957-0233/21/i=10/a=107001 [Accessed August 24, 2014].

Bouguer, P., 1729. Essai d'optique, Sur la gradation de la lumière. *Claude Jombert*, p.164 ff.

Burchard-Levine, A., Liu, S., Vince, F., Li, M. & Ostfeld, A., 2014. A hybrid evolutionary data driven model for river water quality early warning. *Journal of Environmental Management*, 143, pp.8–16. Available at: https://www.sciencedirect.com/science/article/pii/S0301479714002059 [Accessed May 29, 2019].

Buzoianu, M., 2000. Practical considerations on the traceability to conventional scales. *Accreditation and Quality Assurance*, 5(4), pp.142–150. Available at: http://link.springer.com/10.1007/s007690050433 [Accessed April 21, 2017].

Campbell, C.G., Laycak, D.T., Hoppes, W., Tran, N.T. & Shi, F.G., 2005. High concentration suspended sediment measurements using a continuous fiber optic in-stream transmissometer. *Journal of Hydrology*, 311(1–4), pp.244–253. Available at: http://www.sciencedirect.com/science/article/pii/S0022169405000326.

References

Clifford, N.J., Richards, K.S., Brown, R.A. & Lane, S.N., 1995. Laboratory and field assessment of an infrared turbidity probe and its response to particle size and variation in suspended sediment concentration. *Hydrological Sciences Journal*, 40(6), pp.771–791.

Collin, A., Archambault, P. & Long, B., 2011. Predicting Species Diversity of Benthic Communities within Turbid Nearshore Using Full-Waveform Bathymetric LiDAR and Machine Learners H. Browman, ed. *PLoS ONE*, 6(6), p.e21265. Available at: https://dx.plos.org/10.1371/journal.pone.0021265 [Accessed May 29, 2019].

Davies-Colley, R.J. & Smith, D.G., 2001. Turbidity, suspended sediment, and water clarity: a review. *Journal of the American Water Resources Association*, 37(5), pp.1085–1101.

Finlayson, B.L., 1985. Field calibration of a recording turbidity meter. *Catena*, 12(2–3), pp.141–147. Available at: http://linkinghub.elsevier.com/retrieve/pii/0341816285900062.

Fugate, D.C. & Friedrichs, C.T., 2002. Determining concentration and fall velocity of estuarine particle populations using ADV, OBS and LISST. *Continental Shelf Research*, 22(11–13), pp.1867–1886. Available at: http://linkinghub.elsevier.com/retrieve/pii/S0278434302000432.

Gibbs, R.J., 1978. Light scattering from particles of different shapes. *Journal of Geophysical Research*, 83(C1), p.501. Available at: http://doi.wiley.com/10.1029/JC083iC01p00501.

Gippel, C.J., 1989. The use of turbidimeters in suspended sediment research. *Hydrobiologia*, 176–177(1), pp.465–480. Available at: http://link.springer.com/10.1007/BF00026582.

Gray, J.R., Glysson, G.D., Turcios, L.M. & Schwarz, G.E., 2000. Comparability of suspended-solids concentration and total suspended solids data. In US Department, of the Interior, US Geological Survey.

Green, M.O. & Boon, J.D., 1993. The measurement of constituent concentrations in nonhomogeneous sediment suspensions using optical backscatter sensors. *Marine Geology*, 110, pp.73–81.

Guillén, J., Palanques, A., Puig, P. & Madron, X.D.D.E., 2000. Field calibration of optical sensors for measuring suspended sediment concentration in the western Mediterranean *. *Scientia Marina*, 64(4), pp.427–435.

Gumprecht, R.O. & Sliepcevich, C.M., 1953. Measurement of particle sizes in polydispersed systems by means of light transmission measurements combined with differential settling. *Journal of Physical Chemistry*, 57(1), pp.95–97.

Hale, G.M. & Querry, M.R., 1973. Optical Constants of Water in the 200-nm to 200-µm Wavelength Region. *Applied Optics*, 12, p.555.

Holliday, C.P., Rasmussen, T.C. & Miller, W.P., 2003. Establishing the relationship between turbidity and total suspended sediment concentration. , pp.1–3.

Hongve, D. & Akesson, G., 1998. Comparison of nephelometric turbidity measurements using wavelengths 400-600 and 860 nm. *Water research*, 32(10), pp.3143–3145.

Van De Hulst, H., 1957. *Light scattering by small particles*, Dover Pubns. Available at: http://books.google.co.uk/books?hl=en&lr=&id=PlHfPMVAFRcC&oi=fnd&pg=PA1&dq=light+scattering+by+small+particles&ots=Ge0bKwppIa&sig=QAVu3sO5nggAw_-4F51qDxF9ajs.

Instruments, N., 2018. National Instruments: Test, Measurement, and Embedded Systems - National Instruments. Available at: http://www.ni.com/en-gb.html [Accessed July 21, 2018].

ISO, 1999. *ISO 7027:1999 Water quality - determination of turbidity*, Available at:

www.iso.org/iso/catalogue_detail.htm?csnumber=30123.

ISO, 2006. ISO 80000-3:2006 - Quantities and units -- Part 3: Space and time. *International Organization for Standardization*, p.19. Available at: https://www.iso.org/standard/31888.html [Accessed July 20, 2019].

Jansson, M.B., 1992. Turbidimeter measurements in a tropical river, Costa Rica. In *Erosion and Sediment Transport Monitoring Programmes in River Basins (Proceedings of the Oslo Symposium, August 1992).* pp. 71–78.

Juntunen, P., Liukkonen, M., Lehtola, M.J. & Hiltunen, Y., 2013a. Dynamic soft sensors for detecting factors affecting turbidity in drinking water. *Journal of Hydroinformatics*, 15(2), pp.416–426. Available at: https://iwaponline.com/jh/article/15/2/416-426/3436 [Accessed May 29, 2019].

Juntunen, P., Liukkonen, M., Lehtola, M.J. & Hiltunen, Y., 2013b. Dynamic soft sensors for detecting factors affecting turbidity in drinking water. *Journal of Hydroinformatics*, 15(2), pp.416–426.

Kelley, C.D., Krolick, A., Brunner, L., Burklund, A., Kahn, D., Ball, W.P. & Weber-Shirk, M., 2014. An affordable open-source turbidimeter. *Sensors (Basel, Switzerland)*, 14(4), pp.7142–55. Available at: http://www.mdpi.com/1424-8220/14/4/7142/htm [Accessed August 8, 2014].

Kerr, S.J., 1995. *Silt , Turbidity and Suspended Sediments in the Aquatic Environment : an annotated bibliography and literature review.*,

Kim, Y.H., Im, J., Ha, H.K., Choi, J.-K. & Ha, S., 2014. Machine learning approaches to coastal water quality monitoring using GOCI satellite data. *GIScience & Remote Sensing*, 51(2), pp.158–174. Available at: http://www.tandfonline.com/doi/abs/10.1080/15481603.2014.900983 [Accessed May 29, 2019].

Kintel, M. & Wolf, C., 2018. OpenSCAD, The Programmers Solid 3D CAD Modeller. Available at: http://www.openscad.org/.

Kirk, J.T.O., 1985. Effects of suspensoids (turbidity) on penetration of solar radiation in aquatic ecosystems. *Hydrobiologia*, 125, pp.195–208.

Kitchener, B.G.B., Dixon, S.D., Howarth, K.O., Parsons, A.J., Wainwright, J., Bateman, M.D., Cooper, J.R., Hargrave, G.K., Long, E.J. & Hewett, C.J.M., 2019. A low-cost bench-top research device for turbidity measurement by radially distributed illumination intensity sensing at multiple wavelengths. *HardwareX*, 5.

Kitchener, B.G.B., Wainwright, J. & Parsons, A.J., 2017. A review of the principles of turbidity measurement. *Progress in Physical Geography*, 41(5), pp.620–642. Available at: http://journals.sagepub.com/doi/10.1177/0309133317726540 [Accessed September 14, 2017].

Lambert, J.H., 1760. Lamberts Photometrie : [Photometria, sive De mensura et gradibus luminus, colorum et umbrae]. *Leipzig : W. Engelmann*, p.433. Available at: https://archive.org/details/lambertsphotome00lambgoog [Accessed April 22, 2017].

Lambrou, T.P., Anastasiou, C.C. & Panayiotou, C.G., 2009. A Nephelometric Turbidity System for Monitoring Residential Drinking Water Quality. In *Sensor Applications, Experimentation, and Logistics : First International Conference, SENSAPPEAL 2009, Athens, Greece, September 25, 2009, Revised Selected Papers*. Springer Berlin Heidelberg, pp. 43–55.

Laven, P., 2018. MiePlot. Available at: http://philiplaven.com/mieplot.htm.

Lawler, D.M., 2005. Turbidimetry and Nephelometry. *Water*, pp.343–351.

Lawler, D.M. & Brown, R.M., 1992. A simple and inexpensive turbidity meter for the estimation of

suspended sediment concentrations. *Hydrological processes*, 6(May 1991), pp.159–168.

Lelli, L., 2014. Aerosol and Clouds WS2014 - Scattering Regimes. , p.47.

Liu, Y., Arnott, W.P. & Hallett, J., 1998. Anomalous diffraction theory for arbitrarily oriented finite circular cylinders and comparison with exact T-matrix results. *Applied Optics*, 37(21), pp.5019–5030.

Maxim, 2015. MAX1415/MAX1416, 16-Bit, Low-Power, 2-Channel, Sigma-Delta ADCs. , p.35. Available at: https://datasheets.maximintegrated.com/en/ds/MAX1415-MAX1416.pdf.

Maxim, 2014. MAX6225/MAX6241/MAX6250, Low-Noise, Precision, +2.5V/+4.096V/+5V Voltage References. , p.11. Available at: https://datasheets.maximintegrated.com/en/ds/MAX6225-MAX6250.pdf.

Microchip, 2008. MCP414X/416X/424X/426X, 7/8-Bit Single/Dual SPI Digital POT with Non-Volatile Memory. , p.88. Available at: http://ww1.microchip.com/downloads/en/DeviceDoc/22059b.pdf.

Microchip, 2012. MCP6491/2/4, 7.5 MHz, Low-Input Bias Current Op Amps. , p.50. Available at: https://www.microchip.com/wwwproducts/en/MCP6491.

Mie, G., 1908. Contributions to the optics of turbid media, particularly of colloidal metal solutions. *Ann. Phys.*, 25, pp.377–445. Available at: http://doi.wiley.com/10.1002/andp.19083300302.

Moosmüller, H. & Arnott, W.P., 2009. Particle optics in the Rayleigh regime. *Journal of the Air & Waste Management Association (1995)*, 59(9), pp.1028–31.

Morais, I.P. a., Tóth, I. V. & Rangel, A.O.S.S., 2006. Turbidimetric and Nephelometric Flow Analysis: Concepts and Applications. *Spectroscopy Letters*, 39(6), pp.547–579. Available at: http://www.tandfonline.com/doi/abs/10.1080/00387010600824629 [Accessed November 26, 2013].

National Instruments, 2018a. myDAQ Student Data Acquisition Device - National Instruments. Available at: https://www.ni.com/en-gb/shop/select/mydaq-student-data-acquisition-device [Accessed August 12, 2018].

National Instruments, 2018b. USB-6211 - National Instruments. Available at: http://www.ni.com/en-gb/support/model.usb-6211.html [Accessed August 12, 2018].

Novarm, 2018. DipTrace, schematic and PCB design software. Available at: https://diptrace.com/download/download-diptrace/.

Orwin, J.F. & Smart, C.C., 2005. An inexpensive turbidimeter for monitoring suspended sediment. *Geomorphology*, 68(1–2), pp.3–15. Available at: http://linkinghub.elsevier.com/retrieve/pii/S0169555X04002855 [Accessed November 26, 2013].

Osram, 2018. SFH213, Silicon PIN Photodiode. , p.13. Available at: https://dammedia.osram.info/media/resource/hires/osram-dam-5488355/SFH 213_EN.pdf.

Pavanelli, D. & Bigi, a., 2005. Indirect Methods to Estimate Suspended Sediment Concentration: Reliability and Relationship of Turbidity and Settleable Solids. *Biosystems Engineering*, 90(1), pp.75–83. Available at: http://linkinghub.elsevier.com/retrieve/pii/S1537511004001710 [Accessed November 26, 2013].

Pope, R.M. & Fry, E.S., 1997. Absorption spectrum (380-700 nm) of pure water. II. Integrating cavity measurements. *Applied optics*, 36, pp.8710–8723.

References

Ragworm, 2018. RAGWORM PCB FABRICATION. Available at: https://ragworm.eu/ [Accessed August 12, 2018].

Rice, E.W., Sethi, V., Patnaik, P., Biswas, P. & Clark, R.M., 1997. Evaluation of optical detection methods for waterborne suspensions. *American Water Works Association.*, 89(2), pp.98–112.

Sadar, M., 2004. Making Sense of Turbidity Measurements – Advantages In Establishing Traceability Between Measurements and Technology. In *National Monitoring Conference, Chattanooga, TN, USA*. p. 10.

Sadar, M., 1999. *Turbidimeter Instrument Comparison: Low-level Sample Measurements*, Available at: http://www.hach.com/asset-get.download-en.jsa?code=61798.

Sharpe, L.T., Stockman, A., Jagla, W. & Jägle, H., 2005. A luminous efficiency function, $V^*(\lambda)$, for daylight adaptation. *Journal of Vision*, 5(11), p.3. Available at: http://jov.arvojournals.org/article.aspx?doi=10.1167/5.11.3 [Accessed August 12, 2018].

Slattery, M.C. & Burt, T.P., 1997. Particle size characteristics of suspended sediment in hillslope runoff and stream flow. *Earth Surface Processes and Landforms*, 22, pp.705–719.

Solomatine, D., See, L.M. & Abrahart, R.J., 2009. Data-Driven Modelling: Concepts, Approaches and Experiences. In *Practical Hydroinformatics*. Berlin, Heidelberg: Springer Berlin Heidelberg, pp. 17–30. Available at: http://link.springer.com/10.1007/978-3-540-79881-1_2 [Accessed May 29, 2019].

ST Microelectronics, *LM317*, Available at: https://www.st.com/resource/en/datasheet/lm217.pdf [Accessed August 28, 2018].

Strutt, J.W., 1871. On the Light from the Sky, its Polarization and Colour. *Philoshopical Magazine*, XLI, pp.107–120, 274–279.

Sutherland, T.., Lane, P.., Amos, C.. & Downing, J., 2000. The calibration of optical backscatter sensors for suspended sediment of varying darkness levels. *Marine Geology*, 162(2–4), pp.587–597. Available at: http://linkinghub.elsevier.com/retrieve/pii/S0025322799000808.

THORLABS, 2018. *Radiometric vs. Photometric Units*, Available at: https://www.thorlabs.de/catalogPages/506.pdf.

US EPA, 1993. *Method 180.1 determination of turbidity by nephelometry*,

USGS, 2013. Units of Measurement for Turbidity Sensors. Available at: http://or.water.usgs.gov/grapher/fnu.html.

Vishay, 2017. TSAL6100, High Power Infrared Emitting Diode, 940 nm, GaAlAs, MQW. *VISHAY INTERTECHNOLOGY*. Available at: https://www.vishay.com/ir-emitting-diodes/list/product-81009/ [Accessed July 21, 2018].

Williams, N.D., Walling, D.E. & Leeks, G.J.L., 2007. High temporal resolution in situ measurement of the effective particle size characteristics of fluvial suspended sediment. *Water research*, 41(5), pp.1081–93. Available at: http://www.ncbi.nlm.nih.gov/pubmed/17215017 [Accessed November 26, 2013].

Xu, J.P., 1997. Converting near-bottom OBS measurements into suspended sediment concentrations. *Geo-Marine Letters*, 17(2), pp.154–161. Available at: http://link.springer.com/10.1007/s003670050021.

Yang, K.C. & Hogg, R., 1979. Estimation of Particle Size Distributions from Turbidimetric Measurements. *Analytical Chemistry*, 51(6), pp.758–763.

References

Ziegler, A.C., 2003. Issues related to use of turbidity measurements as a surrogate for suspended sediment. , (Circular 1250), pp.16–18.

Appendix 1 CLARITAS model description

A1.1 Model parameters

A1: Table 1. CLARITAS basic parameters.

Parameter	Description	Formula (units)	Range
r_c	Inner radius of the sample cell.	(mm)	49
R	The number of times a ray is permitted to internally reflect from the wall of the sample cell.	Angle of incidence = angle of reflection. (none)	0 to 100
H_s	The height of the sensor ring sensor centres above the base.	(mm)	32 to 485
θ_c	Angular position of the sensor bin for the determination of model convergence.	(degrees)	0 to 170 (multiples of 10)
I_c	The intensity value of the selected sensor bin required to signify convergence.	(mW sr^{-1})	0 to no limit
R_c	Number of rays fired from the LED to signify model convergence.	(none)	0 to no limit
ξ	The vertical beam emergence angle.	(degrees)	0 to 180
φ_{min}	Lower bound of the horizontal beam emergence angle φ.	(degrees)	0 to 90
φ_{max}	Upper bound of the horizontal beam emergence angle φ.	(degrees)	0 to 90
ε	The horizontal beam emergence angle.	(degrees)	0 to 90
d_r	The step-distance travelled by a ray during an iteration of the main calculation loop.	(mm)	1.0 for ray-tracing. 10^{-6} to 1.0 for scattering.

Parameter	Description	Formula (units)	Range
α_1	First shape parameter of the beta distribution.	(none)	
α_2	Second shape parameter of the beta distribution.	(none)	

A1: Table 2. CLARITAS extended model parameters.

Parameter	Description	Formula (units)	Range
ρ_m	Mass concentration of sample suspension	(gl^{-1})	0 to ~10
V_{PDF}	Total volume of the suspended particles as randomly sampled from the input PDF.	$V_{PDF} = f(C)$ (m^3)	0 to ~0.004
P_c	Probability that a ray will interact (collide) with a suspended particle	(none)	
A	Absorbance of suspended particles	(m^{-1})	0 to 1000
I_R	Initial user-defined intensity of the ray.	(mW sr^{-1})	0 to 1
M_d	Mie transition diameter. Particles with d>=M_d will behave as planar reflectors and will not induce Mie scattering.	(µm)	0 to 1000
M_p	Probability that particles with d<M_d will undergo Mie scattering rather than particle-planar reflection.	(none)	0 to 1

A1.2 Model geometry

A vector from the origin of the Cartesian system can describe any point with Cartesian coordinates. For example, *p(x, y, z)* can be expressed as vector **A***(α, β, γ)*, where *α*, *β* and *γ* are the angular distances from **A** to each of the coordinate axes *x*, *y* and *z* (A1: Figure 1). To convert between vector and Cartesian notation, the following identities are true:

$$p(x) = |\mathbf{A}| \cos \alpha \qquad A1: 1$$

$$p(y) = |\mathbf{A}| \cos \beta \qquad A1: 2$$

$$p(z) = |\mathbf{A}| \cos \gamma \qquad A1: 3$$

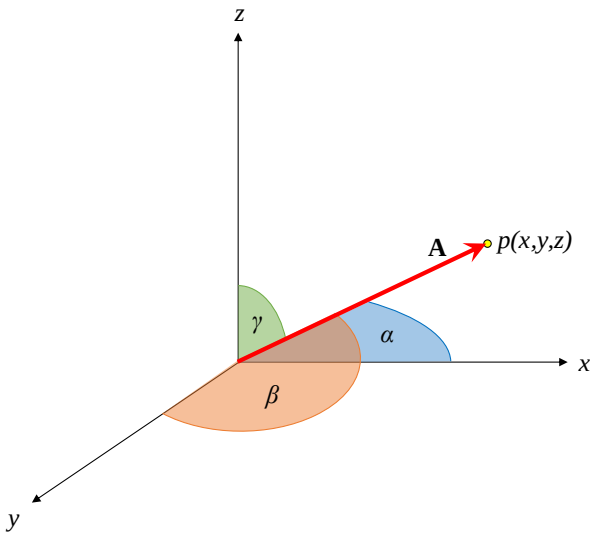

*A1: Figure 1. Coordinate system. Point p has Cartesian coordinates xyz, and is pointed to by a vector **A** which is anchored at the origin of the Cartesian axes. Angles α, β and γ are the angular distances between vector **A** and the x-, y- and z-axes respectively.*

In the CLARITAS model the plane of the sensor ring is located in the *+x* and *+y* quadrant of the *xy* plane. The diagonal vector **B** such that $\alpha = \beta = 45°$ and $\gamma = 90°$ denotes the *beam axis*. The LED and the 0° sensor (S_0) are located at opposite sides of the sample cell, aligned along the beam axis that passes through the centre of the sample cell (A1: Figure 2). A ray travelling two step-distances d_r through the sample cell is shown in A1: Figure 3. In this case an uninterrupted ray is shown. Notionally, at each distance-step, the ray could potentially encounter a suspended-sediment particle and have its direction altered by the application of Mie scattering codes (or by pseudo-geometric reflection).

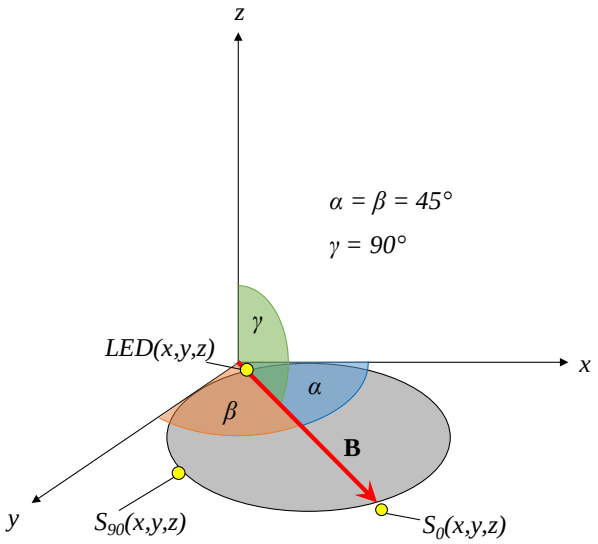

A1: Figure 2. Cartesian representation of the sensor ring (grey disk), and default values of alpha, beta and gamma in CLARITAS (α = β = 45°, γ = 90°). The vector **B** *represents the "beam-axis" position in the xy plane. All beam dispersion measurements are referenced to* **B**. S_0 *and* S_{90} *are the 0° and 90° sensor positions, and the LED position is indicated.*

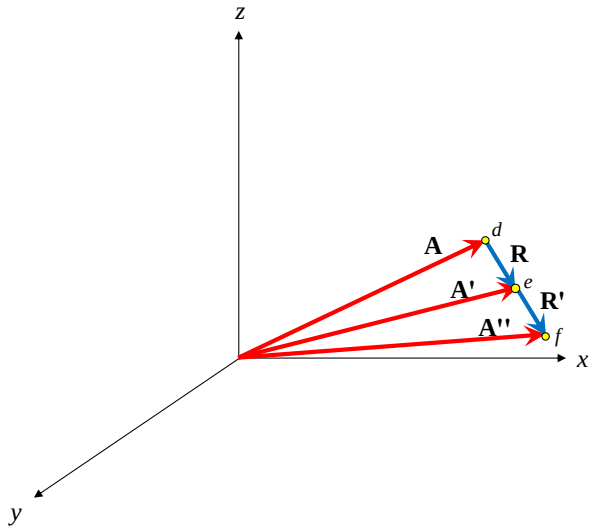

A1: Figure 3. A ray travelling through Cartesian space. Ray vector R *moves from point d to point e, and* R' *moves from point e to point f. The magnitude of* R, R' *etc. is equal to the step distance* d_r.

The geometry of the beam divergence (δ = horizontal, ξ = vertical) is described by A1: Figure 4. All of the modelling undertaken in this thesis used a vertical beam divergence of zero (ξ = 0), effectively reducing the complexity to two dimensions. In the LabVIEW GUI discussed in the next section, ξ is synonymous with the "z angle".

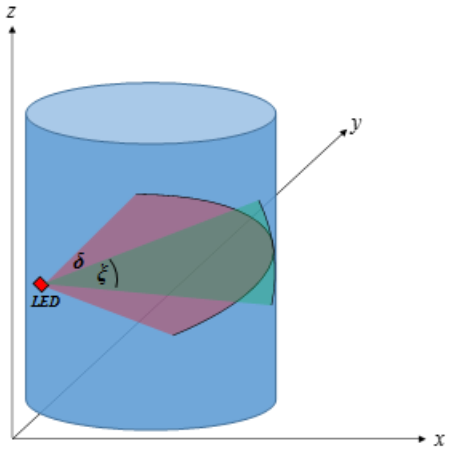

A1: Figure 4. Diagram showing total horizontal beam divergence δ in the xy plane of the sensor ring, and the vertical beam divergence ξ parallel to the z-axis.

The CLARITAS model works in three dimensions (3D). However, through experimentation it was discovered that when the sediment concentration is homogeneous, the simulation gives the same results when operated in only two dimensions (2D). The simulation now works in a notionally 2D (or 3D with infinitesimal thickness) circular plane, encompassing the virtual LED and all of the virtual sensors. This simplification has reduced the computation time significantly.

A1.3 LabVIEW GUI

LabVIEW is a powerful engineering application development language, which is very effective for rapid application development. It was chosen as the development platform for the CLARITAS model simply because the author is very familiar with it. It is not, however, easy to explain LabVIEW source code, since LabVIEW uses a graphical programming environment consisting of icons and interconnecting "wires" that represent the flow of data within a program. It would not be advantageous to document the CLARITAS program code here, since this initial attempt at process-based modelling needs considerable further work, which should be attempted in a language that is more accessible to the research community (e.g. C++, FORTRAN, R etc.). The author, in future work, will redevelop the CLARITAS model in a more accessible and sustainable format. This endeavour will have the added benefit of permitting the speed-optimisation of the CLARITAS code, since the LabVIEW application is not suited to this task. For the sake of completeness, some examples of the CLARITAS LabVIEW program output are shown in the following figures.

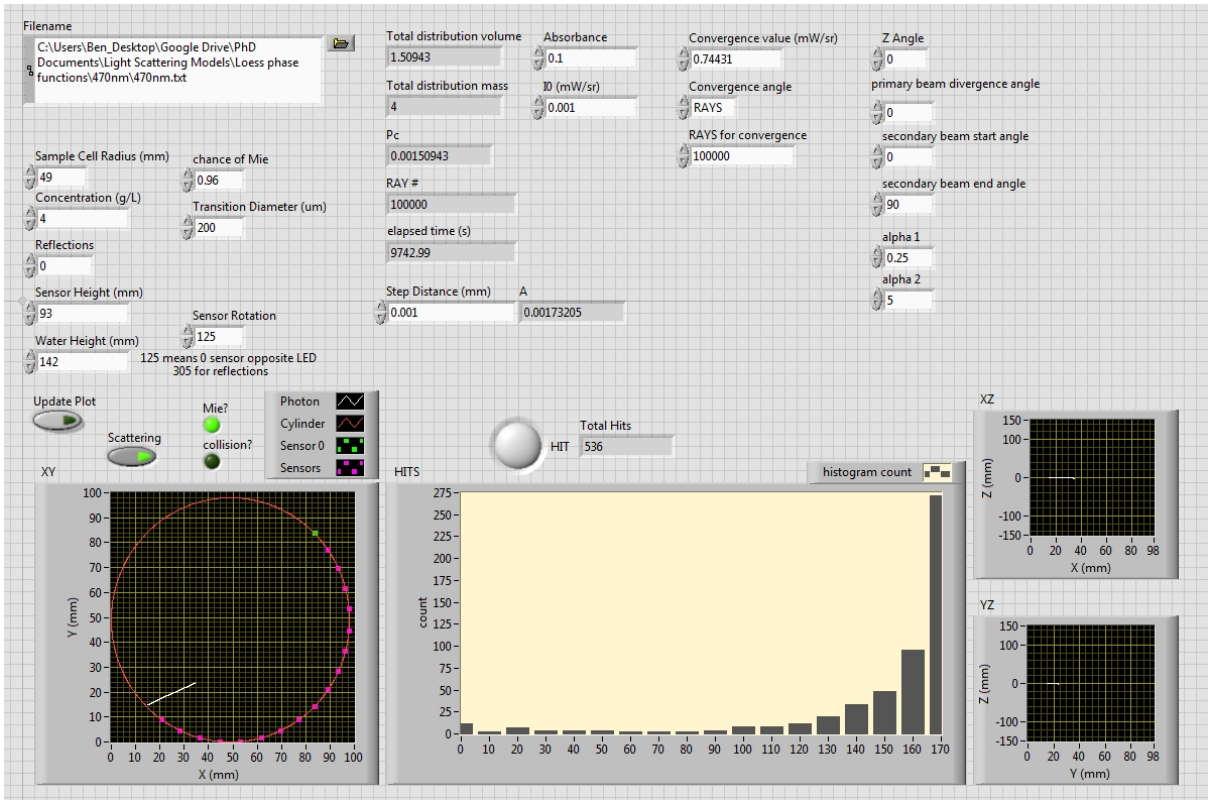

A1: Figure 5. CLARITAS main GUI. The controls and indicators in the top half of the panel are the program input parameters and calculated values. The panel in the bottom-left corner is a plan-view of the TARDIIS virtual sample cell (red circle). The pink dots on the circumference are the virtual sensors, with the green dot representing the 0° sensor. A "ray" (white line) can be seen emerging from a point on the circumference of the red circle at the position of the virtual LED. The large histogram (bottom-centre) indicates the number of "virtual hits" received by the virtual sensors (0° to 170°). The two panels at the bottom-right show the other Cartesian projections of the sample space (the light-ray is restricted to the z = 0° plane).

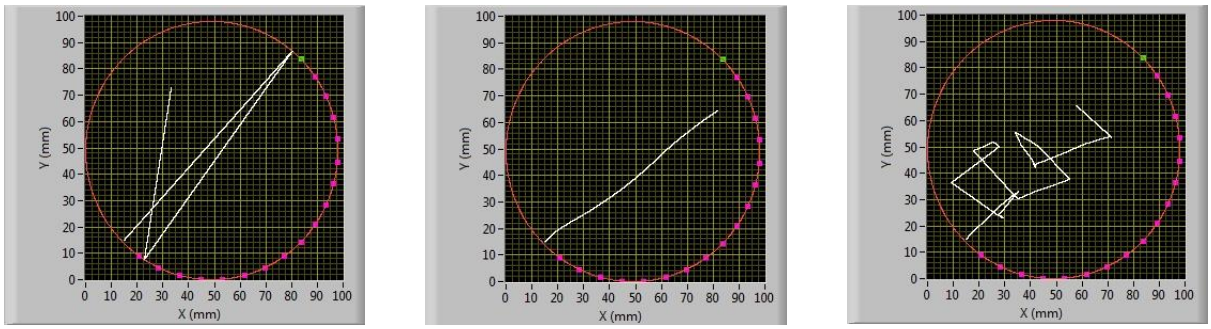

(a) (b) (c)

A1: Figure 6. Visualisations of a simulated light-ray in the CLARITAS model, illustrating the different modes of operation. a) Ray-tracing without scattering, including reflections from the sample cell wall. b) Mie scattering only. c) Mie scattering and pseudo-geometric reflections.